Compact Structure in Southern Peaked Spectrum Radio Sources

by

Edward Alander King, B.Sc.(Hons.)

Submitted in fulfilment of the requirements
for the Degree of
Doctor of Philosophy

University of Tasmania
Hobart

June 1994

Declaration

This thesis contains no material which has been accepted for the award of any other higher degree or graduate diploma in any tertiary institution. To the best of my knowledge and belief, this thesis contains no material previously published or written by another person, except where due reference has been made in the text of the thesis.

Edward Alander King

Thesis Summary

Data for a sample of forty three Southern radio sources is presented. The majority of the sources have spectra that are steep at high frequencies and that peak, or at least flatten markedly, below a few giga-hertz. The sources have been studied through both single dish observations and VLBI.

A dual frequency (2.3 and 8.4 GHz) flux density monitoring program lasting nearly two and a half years and comprising measurements of all sources at intervals of between one and three weeks has shown that the incidence of variability is systematically low in peaked spectrum sources. This observation is consistent with the assertion that the energy source powering the luminous cores in this type object is of a different nature to that driving the compact cores seen in many powerful flat spectrum radio sources. In order that the observations could be performed on a regular basis with minimum user intervention, an automated observing and data acquisition system was implemented. To stabilise the receiver gain, the system incorporates a versatile software implementation of a noise adding radiometer.

The recently established Southern Hemisphere VLBI Experiment (SHEVE) array is described and its capabilities and limitations discussed. The operational procedures and special difficulties inherent in the operation of the array are explained.

Images for nine sources made from observations with the SHEVE array are presented. For seven of the sources, images are available at both 2.3 and 8.4 GHz. The images have a mean dynamic range of 65:1 and provide accurate measurements of the detailed structure in these sources, including component sizes, flux densities and spectral indices. All of the peaked spectrum sources imaged are doubles and few show any evidence of significant extended structure. These data constitute the first high resolution observations for six of the sources.

Observations with a single baseline interferometer have provided the first survey of the compact structure in thirty eight of the sources in the sample. Simple models representing the basic source structures have been fit to the data for all objects detected in this survey. These models show that about two thirds of the sources surveyed have more than one component at milli-arcsecond resolution. A comparison of the models with the images is used to set limits on the reliability of the model fitting results.

A database of all the source properties obtained, both through the observations described, and compiled from the literature is presented. Numerous parameters intrinsic to the sources are calculated using these data and are briefly discussed.

Acknowledgements

There are three people to whom I would like to pay special tribute for the roles that they have played, for without them this thesis would not exist. Firstly, my associate supervisor, Dr. Dave Jauncey, has continually wound me up, pointed me in the right direction and let me go, intervening only when I was going round in circles (or if there was telescope time available). His knowledge, insight and wisdom were invaluable in providing a sense of purpose and a framework that gave meaning to my sleepless nights. Even though it was normally delivered by telephone at a range of not less than $30M\lambda$ [1], I have always found that Dave's infectious enthusiasm was sufficient to overwhelm the most intractable of problems. His sagacious advice during the writing of this thesis has contributed greatly to the final result. Secondly (and thirdly), I would like to pay tribute to my very good friends Tas (now Dr.) and Linda van Ommen who have given of their love, support and encouragement with a generosity I have never known elsewhere. As a colleague, Tas has always been a tremendous encouragement, a good source of advice, and a great sounding board.

The Astronomical Measurements Group at JPL, including Drs. Bob Preston, Dave Meier, Dave Murphy and Dayton Jones have given generously both of their advice and hospitality during my visits to Pasadena. I thank Bob in particular for exceptional hospitality, encouragement, and for letting me move in with his dog whilst he and his family were on vacation.

The SHEVE experiment is a web of collaborating institutions and astronomers. However it seems that all strands lead back, at some point, to Dr. John Reynolds. Apart from contributing much of the work that has ensured the success of SHEVE, through his patient explanations John has done more than anyone to transform my knowledge of VLBI into something approaching an understanding. I thank him not only for much organisation of SHEVE, but for personally supporting most of the single baseline observations at Tidbinbilla, for hospitality in Sydney, and also for many enjoyable days and nights in Pasadena whilst we were correlating SHEVE data.

Jim Lovell, a fellow student, has assisted with the flux density monitoring observations and has been a source of many stimulating discussions and helpful suggestions. He has also given generously of his time in the support of SHEVE observations.

My supervisor at the University of Tasmania, Dr. Peter McCulloch, has provided excellent support for the research described herein and has always been a

[1] $\lambda = 13\ cm$

source of sound advice. I would like to thank Peter and also Prof. Pip Hamilton for their work in establishing the Mt. Pleasant Observatory and making it the reliable instrument that it is. My thanks go also to the observatory manager, Mr. Gordon Gowland, whose technical assistance, always cheerfully given whatever hour of day or night, represents a tremendous contribution to the success of the observations.

I would like to thank the Block-II correlator manager, Dr. S.C. Unwin, for his advice and assistance with the use of the correlator, and for often flexibly rescheduling correlator time allocation to accommodate my requirements. The correlator operators, Tim Rogstad and Gerry Zandle, who between them have probably seen more SHEVE fringes than anyone else, were always models of efficiency and reliability. I am indebted to Dr. T.J. Pearson for his continuing development and support of the Caltech VLBI programs. The excellent imaging program Difmap, written by Martin Shepherd, is a wonderful recent addition to the package.

In addition to frequent advice and encouragement, Dr. Tasso Tzioumis, gave generously of his time to support the single baseline observations between Hobart and Mopra. I thank Duncan Campbell-Wilson for conducting the 843 MHz flux density observations at Molonglo.

The success of the SHEVE experiments depends on the diligent and generous contributions of many people at each of the observatories. I wish to express my gratitude to them all for their professional efforts and team spirit. I have been fortunate to have the company here in the Physics Department of other postgraduate students of cheerful demeanour and great generosity. I would like to thank Marco, Tas, Geoff, Jim, Jenny, and Simon for their friendship over the past years.

I am grateful to the Australian Government for a Postgraduate Research Award which provided financial support for much of the time that I worked towards preparing this thesis. I thank the director of the ATNF, Dr. R.D. Ekers, for the provision of airfares for two of the visits I made to correlate SHEVE data in Pasadena. This work has used data from the COSMOS/UKST Southern Sky Catalogue as provided by the Anglo-Australian Observatory and has made use of the NASA/IPAC Extragalactic Database (NED) which is operated by the Jet Propulsion Laboratory, Caltech, under contract with the National Aeronautics and Space Administration.

Lastly I would like to thank my family, particularly my parents, for their encouragement and support throughout the course of this project.

Contents

List of Tables

List of Figures

Chapter 1

Introduction

1.1 Background

Peaked spectra are believed to reflect the presence of synchrotron self absorption processes in radio sources. Synchrotron theory for relativistic electrons predicts a steep high frequency spectrum due to radiation losses, while at lower frequencies the radiation is re-absorbed (or self absorbed) by the radiating electrons themselves. Consequently, the observed flux density does not increase monotonically towards lower frequencies. Instead the spectrum is expected to flatten as progressively more radiation is self absorbed, and if the physical conditions allow, the flux density actually decreases for frequencies below some critical frequency ν_{max}, which usually lies near 1 GHz. Hence these objects are often referred to as Gigahertz Peaked Spectrum sources, or GPS sources.

Peaked spectrum radio sources have been attracting the attention of astronomers from as early as 1963. In that year, Slysh (1963) recognised the relationship between brightness temperatures and synchrotron self absorption processes in radio sources and consequently discovered a relationship linking the angular sizes of self absorbed sources with the magnetic field strength and flux density at the frequency of the peak. On the same page of the issue of Nature in which Slysh's article appeared, there was also a paper by Bolton, Gardner and Mackey (1963) announcing the discovery of a strong Southern radio source, 1934−638, possessing just the type of peaked spectrum that Slysh's conclusions concerned. The synchrotron radiation models assumed that the radiation was emitted by an expanding cloud of relativistic electrons and led some authors (Kellermann, 1966; Shklovsky, 1965) to predict secular variations in both the flux density and frequency of the peak for 1934−638. Kellermann used Slysh's expression to estimate an angular size for the source of only two milli-arcseconds, well below the angular resolutions of radio interferometers of the day. VLBI techniques were certainly emerging at the time, but only with a limited number of baselines and only in the Northern Hemisphere. It was not until 1969 that the first high resolution observations of 1934−638 were made (Gubbay *et al.*, 1971). However by then, the evolution of flux density predicted for a few of the peaked spectrum sources had failed to eventuate, and the focus of extragalactic radio astronomy at high

resolution in the north was turning towards the objects showing very high brightness temperatures and exhibiting dramatic flux density variability and internal motions on milli-arcsecond scales.

As a consequence, the study of peaked spectrum sources fell from the mainstream and relatively few investigators showed any interest in the field. Notable exceptions include Mutel, Phillips and Hodges (*e.g.* Phillips and Mutel, 1982; Hodges *et al.*, 1984; Mutel *et al.*, 1985 and Mutel and Phillips, 1987), and more recently, O'dea, Baum, Stanghellini and others (*e.g.* O'dea *et al.*, 1990; Baum *et al.*, 1990; Stanghellini *et al.*, 1993; O'dea *et al.*, 1991 and references therein). Mutel *et al.* postulated a link between peaked spectra and VLBI sources with two compact components of similar size and morphology (so-called compact doubles) and are responsible for much of the VLBI imaging of these sources in the north. O'dea *et al.* have begun to assemble and investigate a Northern sample of GPS sources at both radio (Stanghellini *et al.*, 1990b) and optical (O'Dea, 1990; Stanghellini *et al.*, 1993) wavelengths. O'dea *et al.* (1991) provides the most comprehensive review of the properties of GPS sources in the literature at present.

In the south, interest in these sources was rekindled in 1987 when a search for calibrators for the Australia Telescope Compact Array, using the Parkes–Tidbinbilla Interferometer, revealed the existence at 2.3 GHz of several strong subarcsecond scale double sources with very compact individual components (Jauncey 1988, private communication). These sources were found to possess peaked spectra and with their apparently simple basic structures, strong compact components, and angular sizes between a few milli-arcseconds and one arcsecond, were ideally suited to take advantage of the opportunity to make observations with the new SHEVE array that was just being commissioned at the time.

A particularly enigmatic feature of the GPS sources that was emerging was the presence of highly luminous, small, bright components that were, in all respects, other than their spectra and (seemingly) their variability, indistinguishable from the bright milli-arcsecond scale cores seen in variable flat spectrum sources. At the time, very few peaked spectrum objects had been investigated with high angular resolution in the Southern sky and it was apparent that a survey of such objects would yield much useful new data. The aim of the investigation described in this thesis is therefore to "revisit" the Southern peaked spectrum sources to establish a sizeable database from which general properties of the sample could be reliably inferred, and to try and gain some insight as to the properties of the compact cores.

This general survey thus involved selecting a sample of Southern sources that had, on the basis of the available flux density measurements, spectra with peaks distributed over as wide a range of frequencies as possible. The reason for choosing a wide range of peak frequencies is simply that the peak frequency depends on the conditions existing within the source, so that selecting a large range ought to result in the widest possible sampling of the potential parameter space. The observations envisaged involve three distinct approaches. Firstly, a flux density monitoring survey at a low and a high frequency ($\sim$1–2 GHz and $\sim$10 GHz) would be used to test for variability in the sources. The choice of widely differing frequencies enables the variability in the cores to be separated from that in the extended structure,

which is presumed to have the steeper spectrum. Secondly, a small number of the stronger sources known to have complex structure would be imaged with the full SHEVE array to obtain detailed information about component sizes, orientations and shapes, and the distribution of flux density with respect to angular scale. The large effort required to mount full imaging experiments with SHEVE precludes the possibility of making images of more than a small fraction of the total sample. Therefore, a third approach involves surveying as many of the sample objects as possible with a single baseline interferometer and to try and characterise the compact structure by fitting models to the data.

An investigation such as this should allow the fulfillment of several worthwhile astrophysical goals. The images obtained for the individual sources provide information about the spatial distribution of radio emission, leading to an understanding of the possible physical processes at work in each object. The single baseline data will make a very substantial contribution to the total body of data for GPS sources since, being mostly accessible only from the Southern Hemisphere, very few of the sources will have been observed previously. If the sample is large enough, it may be possible to draw meaningful statistical conclusions and to determine the correlations and relationships that exist between various objects, both within this class of radio source, and also with other types of objects.

1.2 Outline of the Thesis

This project has involved work in observing system and software development, observing, data processing and analysis. The chapters of this thesis describe aspects of this work and present the results. A brief synopsis of the thesis is given here:

Chapter 2: The selection criteria for the source sample are outlined and the sample is introduced. Difficulties with the source selection procedure are discussed. Complete radio spectra compiled from the literature, and also including data obtained during this investigation, are presented for all sources.

Chapter 3: The flux density monitoring survey conducted at frequencies of 2.3 and 8.4 GHz is described. Procedures adopted to minimise instrumental effects are explained. All the data are presented, analysed and discussed.

Chapter 4: The SHEVE VLBI array is introduced and its capabilities considered. The procedures involved in the processing and calibration of the VLBI data are explained.

Chapter 5: Difference mapping procedures and image analysis are described as a prelude to the presentation of images for nine sources in the present sample. Images at both 2.3 and 8.4 GHz are given for all but three sources. All images are examined in detail and source parameters are measured from them.

Chapter 6: Assumptions and techniques concerned with the fitting of models to visibility data are considered. An automated technique for correcting the

bias in incoherently averaged visibility amplitudes is described. All data from a single baseline interferometer survey of the source sample are presented. The parameters of the source models fit to these data are given, together with contour plots of the source brightness distributions so determined. A comparison of the models with the corresponding images in the previous chapter is used to establish the reliability of the source parameters measured through the model fitting analysis.

Chapter 7: Source parameters and properties determined from the observations in earlier chapters are compiled and summarised. Data from the literature, including all known optical identifications and redshifts, is compiled for all sources. This database of new results and earlier work is used to calculate intrinsic source parameters, including brightness temperatures, source sizes, component extents, and magnetic field estimates based on equipartition and synchrotron self absorption models.

Chapter 8: The investigation presented in the thesis and its results are summarised and briefly discussed. The future prospects for VLBI in the Southern Hemisphere, and Australia in particular, are considered.

Appendices: Two appendices follow the main body of the thesis. The first describes the equipment configuration used in the flux density monitoring observations. A new implementation of a noise adding radiometer is described and an analysis of its performance presented. A second appendix gives all the visibility amplitudes and closure phase data used in the making of the images presented in Chapter 5. Fits of the clean component models from the images to these data are shown.

Two Conventions

There are two alternative definitions of spectral index in common use, one for flux density as a function of frequency, and one as a function of wavelength. Throughout this thesis, the definition of spectral index is taken to be the former, so that a positive index α implies a flux density S increasing with frequency ν, that is $S \propto \nu^{\alpha}$.

The radio sources studied in this investigation are drawn from the Parkes catalogues of the Southern sky, and therefore are correctly identified by their Parkes catalogue names, including the prefix PKS and either a B or a J depending on the epoch of the coordinate system from which their names have been derived. In this thesis, for the sake of brevity, sources will always be referred to by their B1950 names and the PKS prefix will be omitted.

Chapter 2

Source Sample

2.1 Introduction

The numerous reasons why peaked spectrum sources are of astrophysical interest have already been discussed. The remainder of this thesis is concerned with an investigation of the properties of a southern sample of these objects. In Section 2.2 the source sample is introduced. The procedures whereby this sample was selected and the difficulties inherent in the selection process are explained. Radio spectra for all the sources in the sample, comprising flux density measurements compiled from both the literature, and also new data obtained in this study, are presented in Section 2.3. A more comprehensive database of other source properties appears later in the thesis (Chapter 7).

2.2 Selection Criteria

The candidate objects for this investigation were chosen from the Parkes catalogue of southern radio sources, based on the Parkes 2700 MHz survey (Bolton *et al.*, 1979, and references therein) and maintained by the CSIRO Division of Radiophysics. The objective of the selection process was to choose a group of sources with peaks in their spectra spread over a range of frequencies up to approximately 2 to 3 GHz. The types of observations envisaged, namely flux density monitoring with a 26 m antenna and interferometry with an adhoc VLBI array (which includes several small antennas), required that appropriate declination and flux density limits be set. Thus only objects south of declination 0° and having a 2.7 GHz flux density greater than 1.5 Jy were considered. Flux density measurements at at least four, and preferably five, different frequencies were required before a source was considered to be well enough sampled to be classifiable on the basis of the shape of its spectrum. In addition to sources with simple peaked spectra, objects having both a spectral peak in the 1 to 3 GHz range and an additional "optically thin" component with a steep spectrum at lower frequencies were also deemed acceptable.

Despite these simple criteria, the selection of a sample of peaked spectrum sources in the Southern Hemisphere is a difficult task because of the scarcity of

accurate flux density measurements at the lowest frequencies. Often, and particularly when few measurements are available, the classification of a spectrum as peaked, or otherwise, depends critically upon the flux densities at the ends of the frequency range. However, in the south there has been no equivalent of the Cambridge 3C or 4C surveys (which only extend to $\delta = -7°$) at 178 MHz. The only surveys at, or below, this frequency are the 80 and 160 MHz surveys made with the Radioheliograph at Culgoora by Slee and Higgins (Slee and Higgins, 1973; Slee and Higgins, 1975; Slee, 1977). While these surveys have limiting flux densities of approximately 2 Jy, the uncertainties associated with the measurements below 10 Jy are of the order 20% and 10–15% at 80 and 160 MHz respectively. Furthermore, the Culgoora instrument, designed to observe the sun, was unable to cover declinations south of about $-40°$ so the actual number of sources for which measurements exist is relatively small. The most extensive compilation of low frequency measurements is the 408 MHz Molonglo Reference Catalogue (Large *et al.*, 1981). Several less comprehensive surveys have also been made with Parkes at 635 and 960 MHz (Wills, 1975).

The consequence of this shortage of low frequency data is that considerable uncertainty surrounds the characteristics of the spectra of many sources much below a gigahertz. An object may not have a low frequency measurement because it is either too-weak (in which case it is almost certainly a peaked spectrum source), too far south, or because it is confused with nearby objects. For this reason, sources with a steep high frequency spectrum, and showing a continuous bending leading to a pronounced flattening close to 1 GHz or below, were also deemed acceptable for the purposes of this investigation. Although no data were available at lower frequencies to confirm the presence of a peak, its existence could be inferred from the similarity of the dominant trend in the spectrum to that seen in sources with well defined peaks. Inevitably this must lead to some contamination of the sample with sources that are not truly peaked. However this need not necessarily compromise the survey since these objects can always be removed from the sample, if desired, when considering the properties of the objects known to be truly peaked. As is always the case when selecting sources on the basis of their spectra, the possibility exists that source flux density variability can lead to erroneous classifications unless measurements at different frequencies are obtained closely spaced in time. It is important to note also that the lack of low frequency data renders the prospect of selecting a southern peaked spectrum sample of statistically significant size, that is in any sense complete, virtually impossible. Accordingly, the investigation presented in this thesis is not going to set firm statistical limits on the characteristics of these sources, but simply through the acquisition of the first data for them, will constitute a survey of the properties of objects of this type. Since the sample was selected and observations commenced, it has become apparent, on the basis of more complete spectra or new data, that a small number of sources that met the selection criteria had been excluded, and conversely, some that had no longer did. However, in view of the survey nature of these observations, it was not considered worthwhile adjusting the sample to accommodate these changes since to do so would leave less complete data sets for new sources, and waste data already collected for those rejected.

The sample of 43 sources eventually chosen is listed in Table 2.1. The sample includes two objects which did not meet the minimum flux density criterion but were known to have peaked spectra. These two, 1354−174 and 1937−101, are both high redshift ($z > 3$) quasars. The table gives the Parkes names, the radio positions and the flux densities at 80 MHz (Culgoora), 408 MHz and 843 MHz (Molonglo), 2700 and 8400 MHz (Parkes). The lack of low frequency data is evident. The 843 MHz Molonglo flux densities were obtained as part of this investigation in 1993 on my behalf by D. Campbell-Wilson. The radio positions listed in the table are the most accurate available at present and, with only one exception, all have sub-arcsecond accuracy. Nearly half of the positions are from our Tidbinbilla–Hobart VLBI astrometry program (Reynolds *et al.*, 1994) and are accurate to better than 5 mas. Galactic coordinates for all sources are also given in the table. Complete spectra for all of the sample objects are presented in the next section and their properties will be considered in greater detail in Chapter 7.

2.3 Radio Spectra

The radio sources selected for this investigation were chosen largely on the basis of four or five flux density measurements drawn from the Parkes reference catalogue. The source spectra shown here in Figure 2.1 include data taken from a much wider range of the literature and provide a more complete picture of the spectral properties of each source.

Most of the values come from either the PKSCAT90 compilation (Wright and Otrupcek, 1990) or from Kühr *et al.* (1981). PKSCAT90 is the most recent version of the Parkes Catalogue and comprises observations mostly from Parkes, Culgoora and Molonglo over several years at various frequencies. The flux densities in PKSCAT90 are unreferenced. However, the literature references can mostly be found by checking the references given in Kühr *et al.* for the corresponding frequency as there is considerable overlap. Kühr *et al.* adjusted the values drawn from their literature search to bring all data onto the flux density scale of Baars *et al.* (1977). It appears from these spectra that most of the PKSCAT90 values are two to three percent lower than those of Kühr *et al.*, however no attempt to rescale the data has been made here.

Additional flux density measurements from the literature were found by means of a search conducted via the NASA/IPAC Extragalactic Database (NED). These data are drawn from a wide range publications, and the references are best obtained by consulting NED itself. These data, indicated on the spectra by open circles, are not necessarily on the Baars *et al.* flux density scale. The 843 MHz values are all from the Molonglo observations by Campbell-Wilson, mentioned in the previous section, and have not been published previously.

Measurements at 2.3 and 8.4 GHz from the flux density monitoring program described in Chapter 3 are also plotted. For completeness, the 2.3 and 8.4 GHz flux densities of the compact structure in these sources derived from the VLBI observations in Chapters 5 and 6, are also shown on the graphs. All these data are on a flux density scale consistent with that of Baars *et al.*.

Source	Position (J2000)		Pos.	S_ν (Jy) (ν in MHz)					Galactic	
name	RA.	DEC.	ref.	S_{80}	S_{408}	S_{843}	S_{2700}	S_{8400}	l^{II}	b^{II}
0008-421	00 10 52.5201	-41 53 10.788	R		6.61	6.70	2.49	0.58	329.7	-73.1
0022-423	00 24 42.9903	-42 02 03.953	R		0.83	1.88	2.84	0.93	321.3	-74.1
0023-263	00 25 49.21	-26 02 12.8	M	20.00	17.00		5.44	2.20	42.3	-84.2
0159-117	02 01 57.159	-11 32 33.0	V	9.00	5.70	3.68	2.00	0.85	173.1	-67.3
0237-233	02 40 08.1747	-23 09 15.74	R		3.67		5.16	2.20	209.8	-65.1
0403-132	04 05 34.0037	-13 08 13.6909	R	8.00	7.20	5.15	3.15	2.57	205.8	-42.7
0405-123	04 07 48.425	-12 11 36.62	V	25.00	7.70	4.25	2.35	1.19	204.9	-41.8
0454-463	04 55 50.756	-46 15 58.39	JA	12.00	4.25	2.91	2.36	1.58	252.0	-38.8
0506-612	05 06 43.9887	-61 09 40.999	R		5.03	2.68	1.89	1.38	270.6	-36.1
0624-058	06 27 10.10	-05 53 05.0	P	96.00	44.70	27.75	11.30	3.76	215.4	-8.1
0704-231	07 06 33.470	-23 11 37.57	P	12.00	7.37	5.03	2.50	0.93	235.3	-7.2
0733-174	07 35 45.80	-17 35 48.4	U		3.90	2.52	2.64	1.42	233.6	1.4
0741-063	07 44 21.655	-06 29 35.95	V	3.00	12.20	11.48	4.70	1.43	224.9	8.7
0743-673	07 43 31.6129	-67 26 25.54	R		8.61	5.30	2.74	1.40	279.5	-20.1
0823-500	08 25 26.8695	-50 10 38.491	R		1.88	3.73	5.03	1.50	266.6	-7.1
0834-196	08 37 11.22	-19 51 56.4	U	4.00	10.80	7.10	2.70	0.71	243.3	12.6
0859-140	09 02 16.8312	-14 15 30.8766	R		3.93	3.47	2.90	1.65	242.3	20.7
1015-314	10 18 09.27	-31 44 14.2	U	16.00	9.67	5.72	2.22	0.85	268.6	20.7
1127-145	11 30 07.0524	-14 49 27.386	R	3.00	5.07	5.28	6.73	3.18	275.3	43.6
1148-001	11 50 43.8711	00 23 54.205	R	4.00	3.43		2.58	1.02	272.5	58.8
1151-348	11 54 21.57	-39 05 28.89	MO	7.00	10.90	7.65	4.18	1.92	291.0	22.5
1215-457	12 18 06.23	-46 00 28.6	MO	14.00	9.59	6.60	3.30	1.27	296.9	16.5
1221-423	12 23 43.64	-42 35 27	U	7.00	5.08	3.25	1.62	0.63	297.5	20.0
1245-197	12 18 06.2531	-46 00 29.014	R	4.00	8.61	6.70	4.09	1.36	296.9	16.5
1302-492	13 05 28.3	-49 28 04	PK		14.00	8.30	5.00	1.69	305.3	13.3
1306-095	13 08 39.16	-09 50 32.6	M	15.00	8.30	5.44	3.01	1.11	310.0	52.8
1320-446	13 23 04.25	-44 52 33.0	U		6.91	4.60	1.79	0.52	308.8	17.6
1323-611	13 22 58.20	-61 07 05.78	L				6.20	2.11	306.7	1.5
1354-174	13 57 06.080	-17 44 01.93	V		0.91	1.23	1.28	0.67	324.3	42.4
1514-241	15 17 41.8137	-24 22 19.4733	R		1.78	1.52	2.00	1.76	340.7	27.6
1549-790	15 56 58.8706	-79 14 04.276	R		7.95	6.84	4.02	2.60	311.2	19.5
1733-565	17 37 35.7710	-56 34 03.152	R		13.00	11.00	4.40	1.45	335.4	-13.0
1740-517	17 44 25.457	-51 44 43.70	R		5.38	7.50	4.60	2.37	340.2	-11.5
1827-360	18 30 58.90	-36 02 30.3	MO	13.00	25.80	13.79	2.90	0.59	358.3	-11.8
1830-211	18 33 39.91	-21 03 40.1	R		11.50	12.44	9.30	6.59	12.2	-5.7
1934-638	19 39 25.006	-63 42 45.68	JB		6.24	13.50	11.10	3.00	332.7	-29.4
1937-101	19 39 57.2568	-10 02 41.517	R		0.99	0.90	0.79	0.54	29.3	-15.3
2052-474	20 56 16.3601	-47 14 47.627	R	13.00	4.15	2.20	3.00	1.68	352.6	-40.4
2126-158	21 29 12.1762	-15 38 41.037	R			0.43	1.17	1.08	35.9	-41.9
2135-209	21 37 50.01	-20 42 31.64	M	7.00	9.76	5.45	2.49	0.76	30.3	-45.6
2149-287	21 52 03.733	-28 28 28.11	V	11.00	5.68	4.10	2.00	0.75	20.2	-50.5
2204-540	22 07 43.7336	-53 46 33.813	R		2.55	1.94	2.70	1.09	339.9	-49.9
2311-452	23 14 09.3838	-44 55 49.240	R		3.55	3.19	1.81	0.93	344.0	-63.7

Table 2.1: The 43 sample sources. The radio positions are the most accurate available. Key to position references is: R – Reynolds *et al.* (1994), V – VLA calibrator list, see White (1992), W – Wall and Peacock (1985), L – ATCA position, Lovell, priv. comm. (1993), JA – Jauncey *et al.* (1989a), JB – Jauncey *et al.* (1989b), P – Perley (1982), PK – Parkes, M – Morganti *et al.* (1993), MO – MOST calibrator list, see White (1992), RS – Rao and Subramanyan (1988) U – Ulvestad *et al.* (1981)

Preston *et al.* (1985) conducted a high resolution (typically 2–3 mas resolution) VLBI survey at 2.3 GHz which included observations of many objects in this sample. These data are are shown on the spectra with a star, or where the correlated flux density is either less than 0.1 Jy, or an upper limit was specified, with a star and arrow. The inclusion of these VLBI data permits a simple visual estimation of the lower limit of the contribution made by very compact structure to the total flux density.

Figure 2.1: Complete radio spectra for the 43 sources in the survey sample.

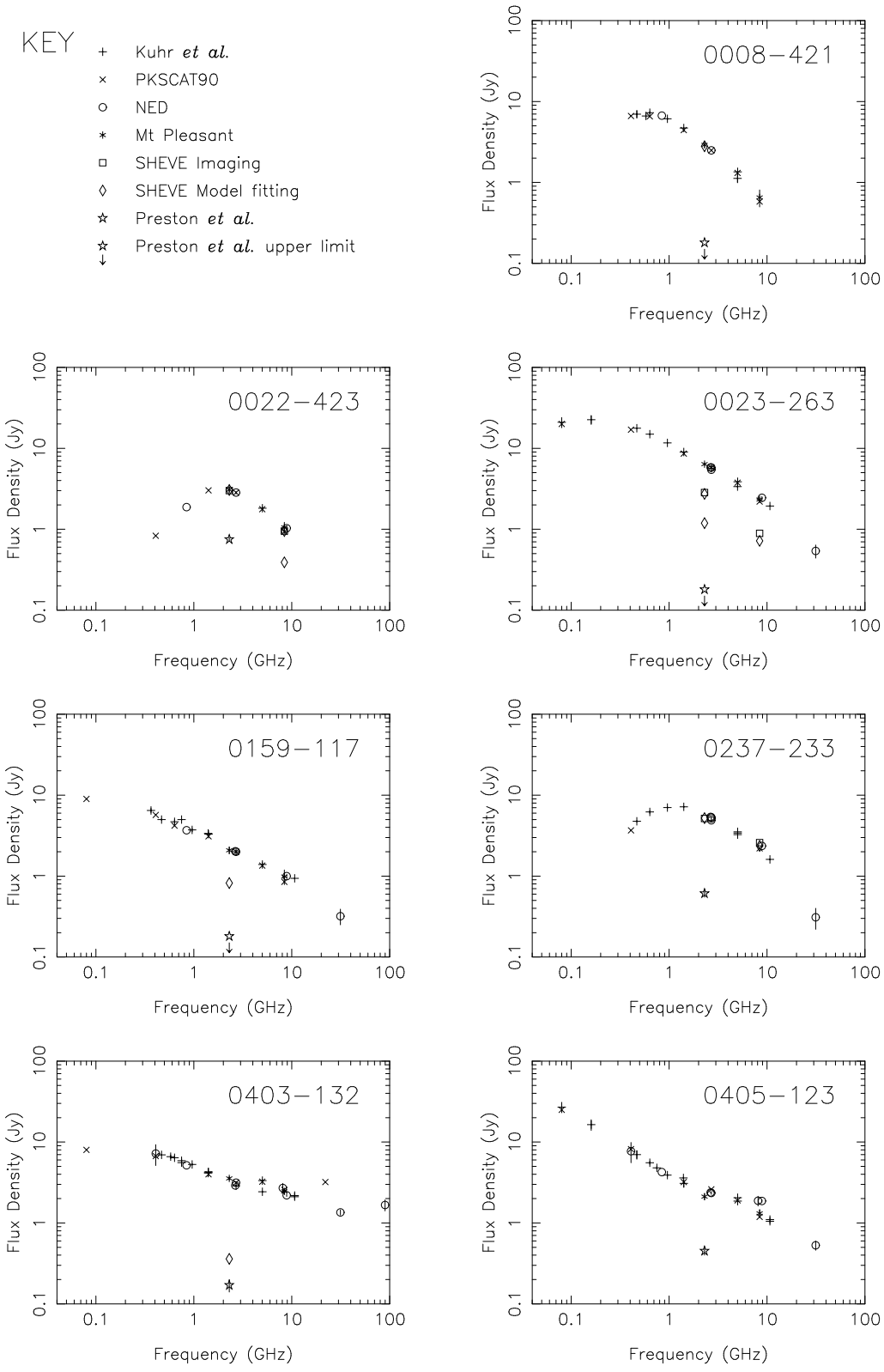

Source radio spectra continued...

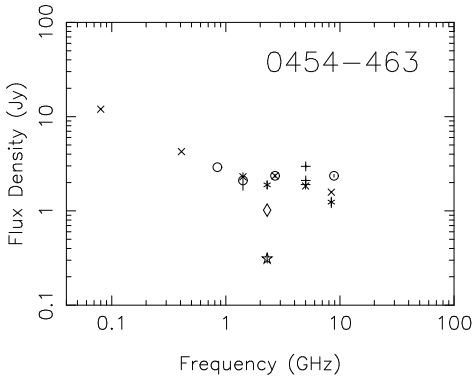

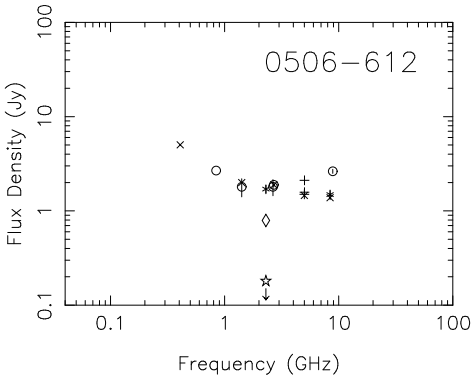

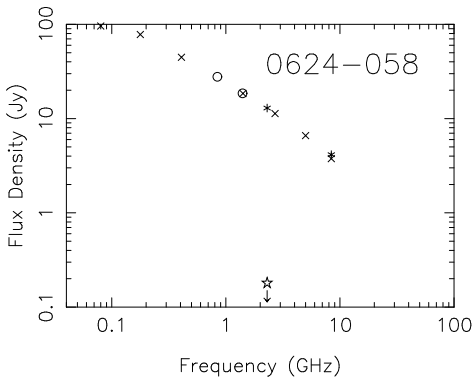

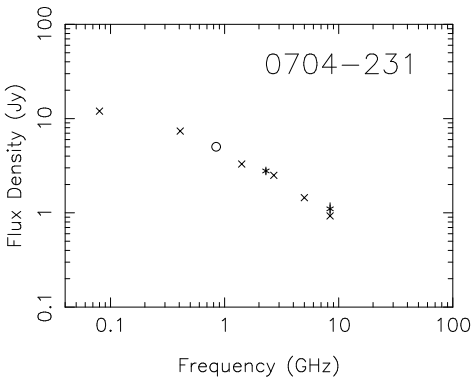

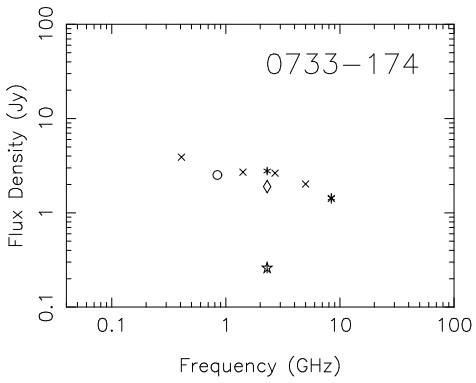

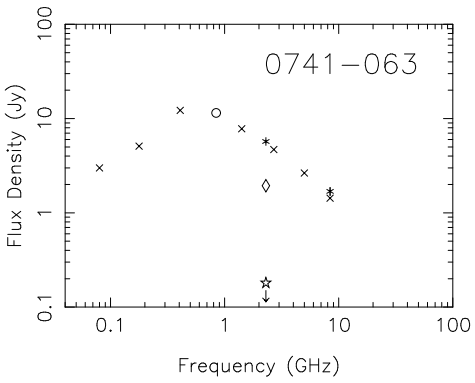

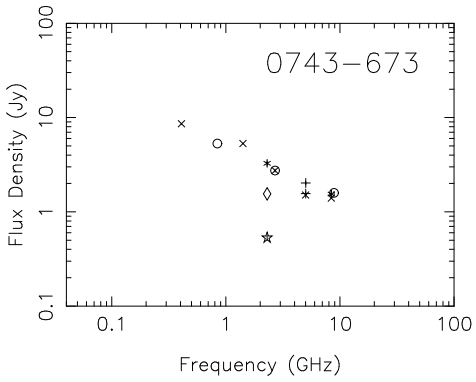

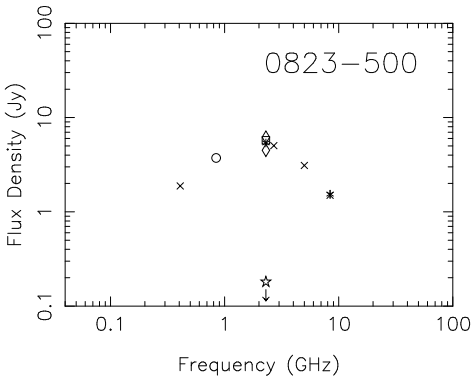

Source radio spectra continued...

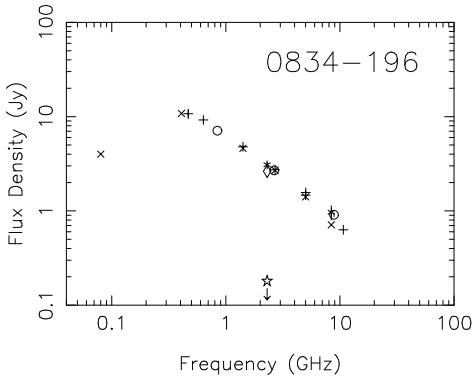

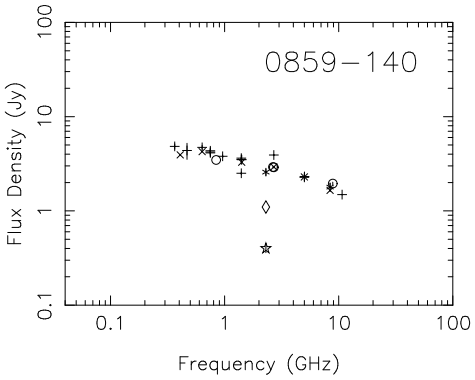

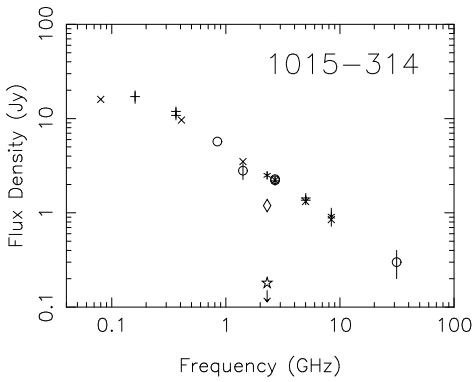

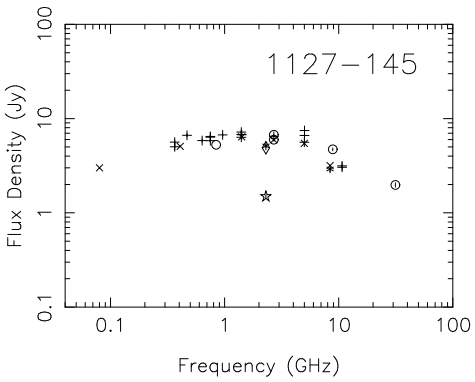

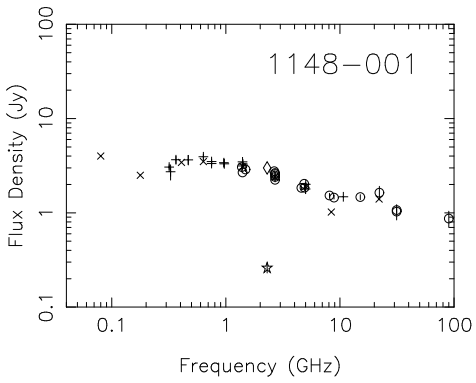

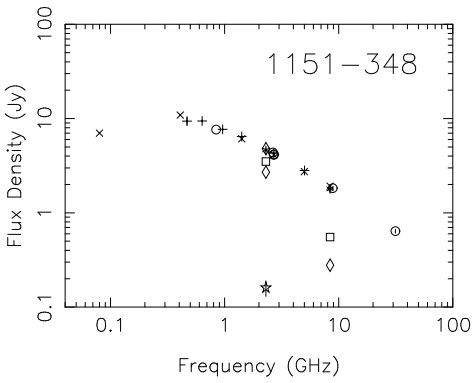

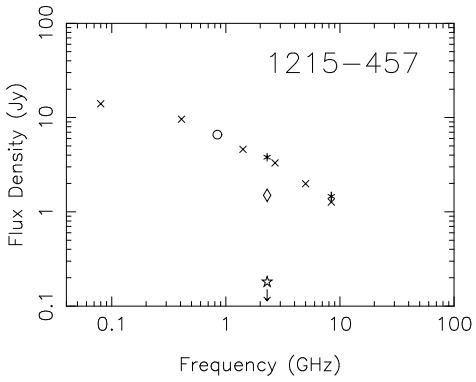

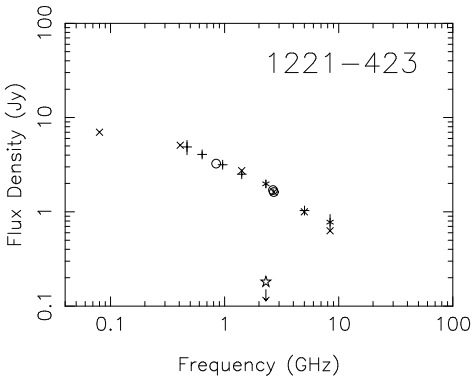

Source radio spectra continued...

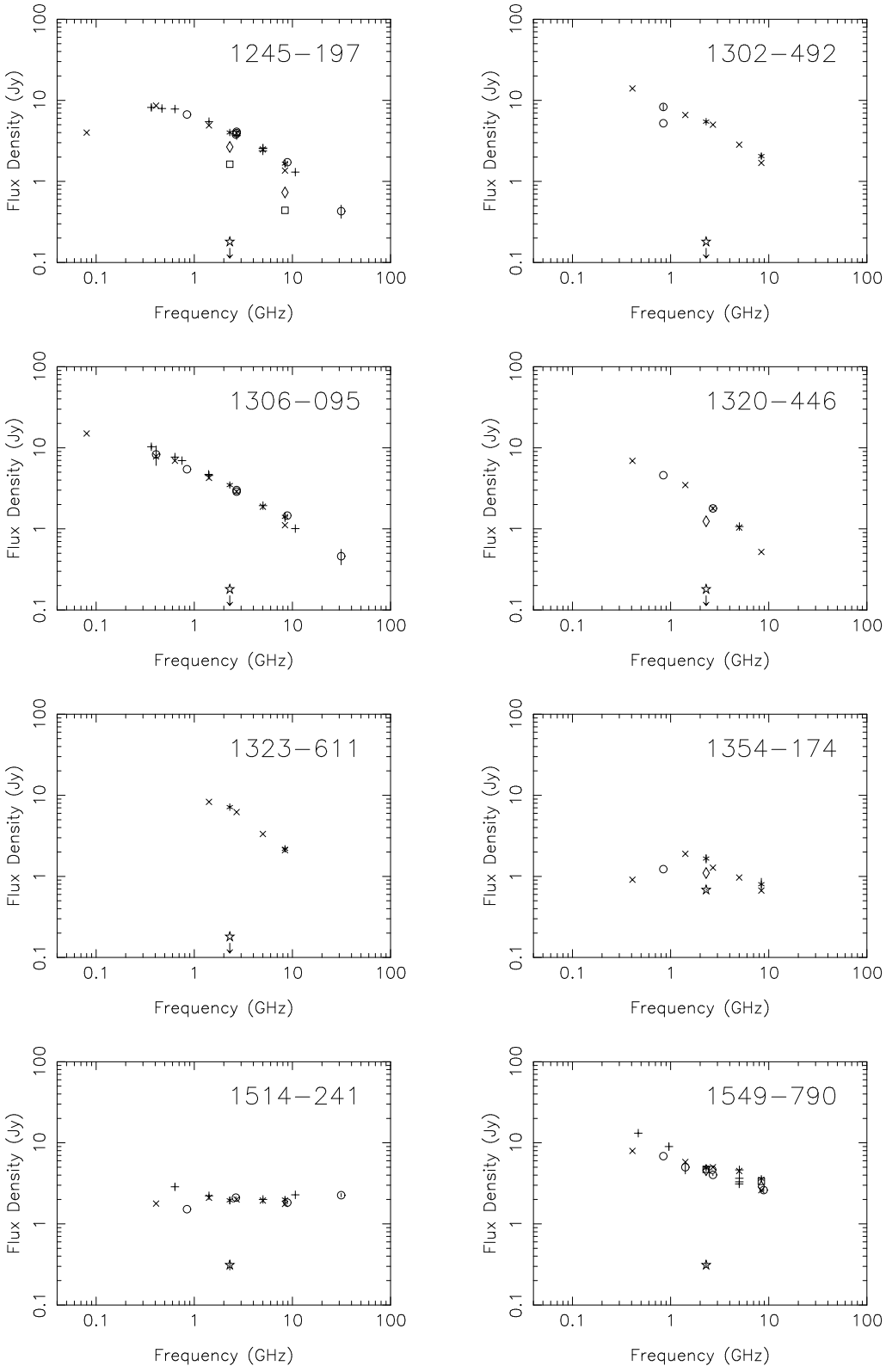

Source radio spectra continued...

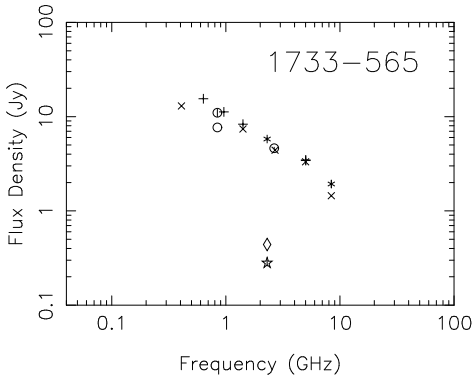

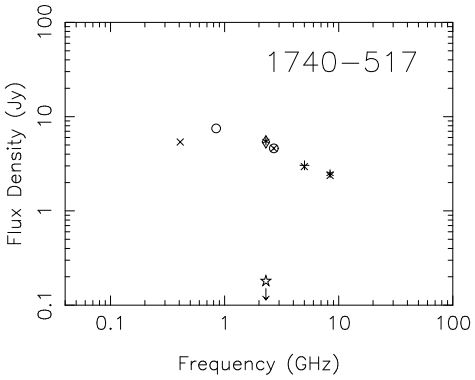

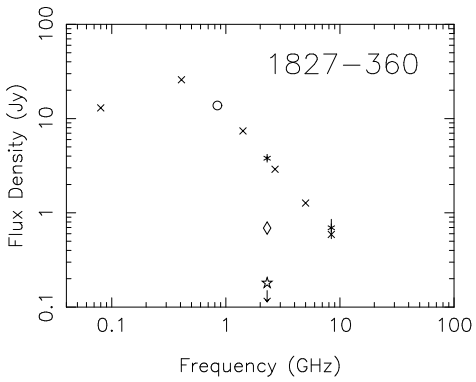

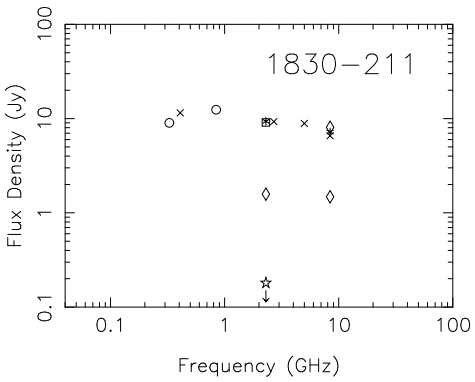

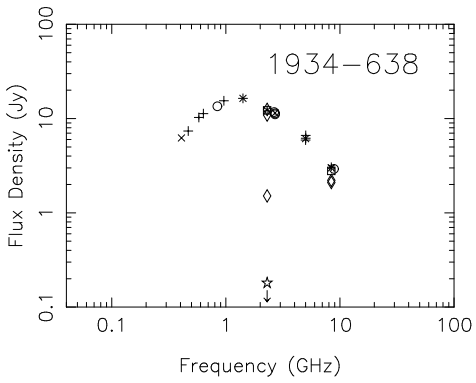

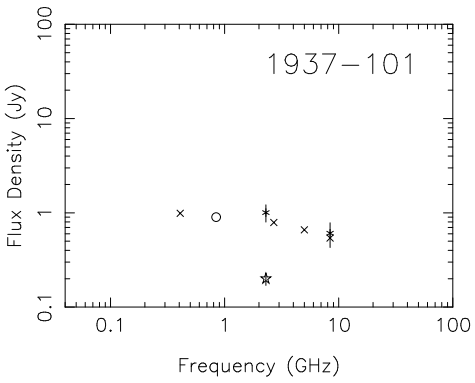

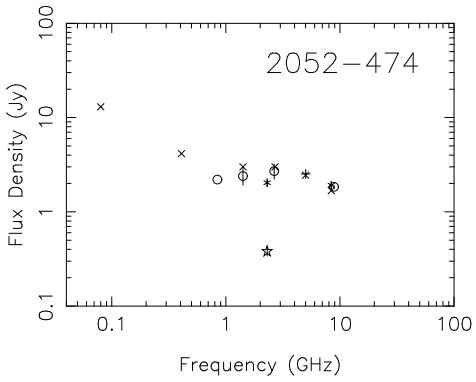

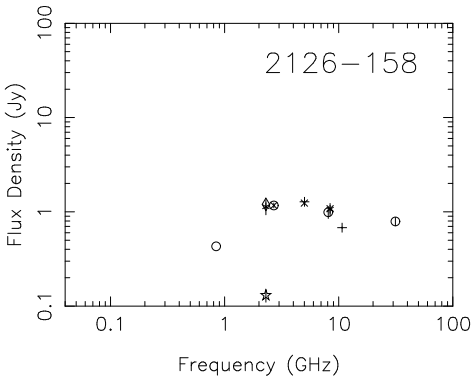

Source radio spectra continued...

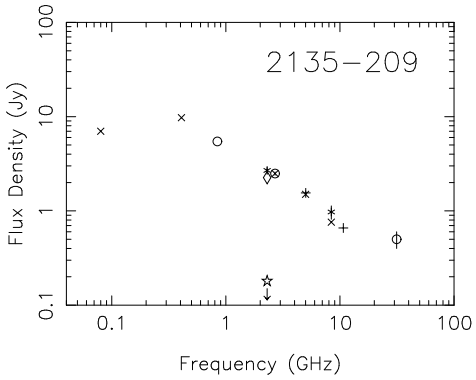
2135−209
Flux Density (Jy)
Frequency (GHz)
0.1
1
10
100

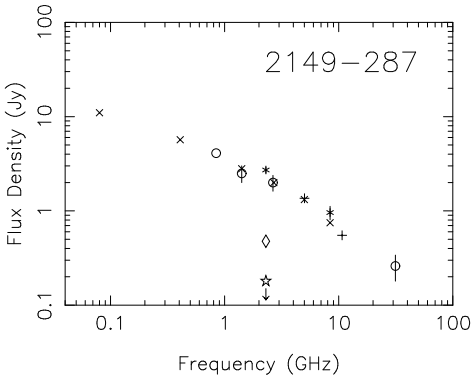
2149−287
Flux Density (Jy)
Frequency (GHz)
0.1
1
10
100

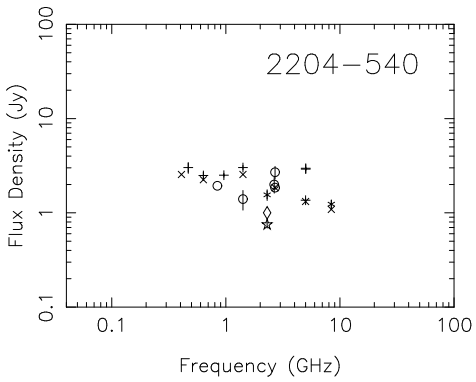
2204−540
Flux Density (Jy)
Frequency (GHz)
0.1
1
10
100

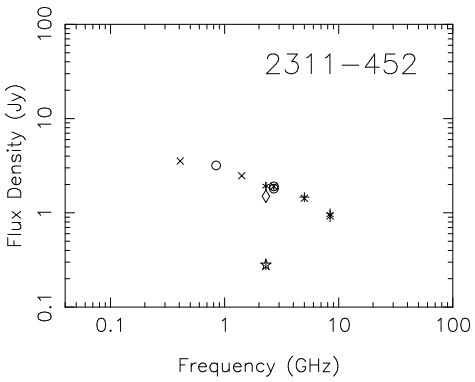
2311−452
Flux Density (Jy)
Frequency (GHz)
0.1
1
10
100

Chapter 3

Flux Density Monitoring

3.1 Introduction

Continuum flux density varibility at centimetre and decimetre wavelengths was detected in extragalactic objects soon after they were first discovered (Dent, 1965; Kellermann and Pauliny-Toth, 1967). Fractional flux density changes from only a few percent up to more than 100 percent occur over a broad range of timescales and frequencies. Whilst it is possible to find members of almost every spectral class that exhibit variability (Seielstad *et al.*, 1983; Kesteven *et al.*, 1977), the most active objects are those whose emission is dominated by milli-arcsecond scale flat or complex spectrum 'core' components, and the least active generally have steep spectra, often associated with extended emission. The variability timescale is a very useful probe of the emission physics of extragalactic radio sources since it places, via light travel time arguments, stringent constraints upon the physical extent of the regions from which the variability derives. This size can be used to derive an apparent brightness temperature without the need for imaging. For flat spectrum objects it is not uncommon for this quantity to be in excess of the 10^{12} K limit predicted by synchrotron radiation models (Kellermann and Pauliny-Toth, 1969; Jones and Burbidge, 1973; Kellermann and Owen, 1988; Fanti *et al.*, 1983). Furthermore, it is often the case that variability timescales are characteristic of the timescales upon which the angular structure of the cores change; that is, flux density variability is usually an indicator of spatially active sources.

Most Northern Hemisphere variability data for GPS sources comes from small samples of these objects that have been included in larger flux density monitoring surveys. In their survey at 5 GHz Rudnick and Jones (1982) found the least variability was exhibited by the peaked and steep spectrum objects. Fanti *et al.* (1983) and Seielstad *et al.* (1983) reported similar results for steep spectrum sources in particular, at 408 MHz and 10.8 GHz respectively. While some of these surveys have prompted VLBI studies of the *variable* CSS sources (Mantovani and Padrielli, 1990), and more recently, a consideration of the low frequency variability observed in the steep spectrum sources (Mantovani *et al.*, 1990), there is little evidence in the literature of any systematic attempt to monitor the flux densities of either CSS and GPS radio sources, particularly at centimetre wavelengths (Fanti, 1990).

It has been widely argued that the turnover in the spectra of GPS objects is due to synchrotron self absorption in compact components which become optically thick at low frequencies (*e.g.* Kellermann, 1966, Jones *et al.*, 1974 and Hodges *et al.*, 1984). Models of the processes underlying the flux density variability observed in extragalactic objects typically assume expanding clouds of relativistic particles possessing simple peaked spectra, similar to those seen in GPS sources. Invoking the self absorption mechanism, authors of these models predict an evolutionary decrease of both the flux density and peaks in the spectra of such clouds (Shklovsky, 1965; van der Laan, 1966). Flux density monitoring of GPS objects should therefore permit a direct test of the applicability of such models.

The presence of high brightness temperature milli-arcsecond components in GPS sources is well established and it is clearly important to determine whether these components are similar to the active cores seen in flat spectrum sources, being highly localised sites of transient energy release, or whether their small size is a consequence of youth, old age, or some other mechanism such as confinement by the surrounding medium of a stable but luminous energy source. Given the extensive flux density variability observed in flat spectrum sources, a quantification of the variability of GPS sources may well constitute a measure of the importance of the contribution, or even presence, of core components of this type. At present, the scarcity of variability data for GPS sources renders this question, if not unanswerable, then only conditionally so on the basis of the small number of objects observed in other surveys.

It is quite clear that there is much to be gained by systematically monitoring a sample of peaked spectrum sources, as a class, for evidence of variability. For many sources reliable flux density data can easily be obtained with a modest single dish antenna. This chapter describes a program of monitoring the present southern peaked spectrum source sample using the 26 m antenna operated by the Physics Department at the University of Tasmania. The observations were made at 2.3 GHz and 8.4 GHz between October 1990 and March 1993 at intervals ranging from a few days to several weeks. The first ten months of the data were analysed in 1991 by a student participating in an Honours program within the Physics Department and whilst reference is made in the text to aspects of this earlier work (Lovell, 1991), all the data, presented here in its entirety, has been independently processed and analysed by the author using his own computer software. The present author was also entirely responsible for the development of the data acquisition system and associated software which are described in greater detail in Appendix A.

3.2 Data Acquisition And Analysis

3.2.1 Contributions To A Flux Density Measurement

When an antenna is pointed at a radio source, the output power from the receiver contains a contribution due to the radiation received from the source. Unfortunately that contribution is superimposed over signals from a variety of origins and cannot be measured directly. Furthermore, it is modified and scaled by factors

arising from the media between the radio source and the antenna, and also properties of the antenna and receiver system itself. The causes of these contributions and factors that influence the output power measurement are summarised here:

- The sky surrounding the radio source, and confusing objects within the antenna beam, will contribute additional signal.
- The intensity of the radiation arriving at the antenna can be affected by scintillation in the interstellar and interplanetary medium giving rise to apparent flux density changes. This effect is most important at lower frequencies, and, in the case of interplanetary scintillation, at low solar elongations.
- A proportion of the radio signal can be absorbed by atmospheric water vapour leading to a reduced apparent flux density measurement. Thus cloud cover can cause inaccurate flux density measurements, particularly at higher frequencies.
- Radiation from the atmosphere and the ground will enter the receiver system via both the main beam and sidelobes, adding noise power. This effect is particularly severe at low elevations.
- Both terrestrial radio sources and the Sun are potential sources of strong interference and any observations affected by these need to be edited or rejected.
- If the antenna is incorrectly pointed so that the radio source lies in the centre of the beam, then the apparent flux density will be reduced.
- If the antenna surface distorts then the efficiency with which it gathers the radiation from the radio source will be affected leading to variations in the measured power.
- Components within the receiver contribute noise power of their own to the system which is independent of the source flux density.
- The amplifiers in the receiver are subject to gain fluctuations which affect the measurement of signal level.
- All measurements are made by means of comparison with a reference signal. This reference signal must be correctly calibrated and sufficiently stable that it does not vary significantly between calibrations.

The following sections describe the approaches and methods adopted to overcome or minimise these effects, either during observations, or in subsequent analysis.

3.2.2 Observing Techniques

The 26 Metre Antenna

The antenna used in these observations is a 26 metre diameter paraboloid located at the Mt. Pleasant Observatory in southern Tasmania. It was originally constructed as a tracking antenna by NASA at Orroral Valley near Canberra and was relocated to Mt. Pleasant in 1984. Unlike most antennas used in astronomy, it has an XY-mount with the X-axis running east-west below the Y-axis which is aligned in the north-south direction. This has the advantage that it can track sources either side of the zenith without having the 'wrap' problems associated with azimuth-elevation (az-el) mounted antennas. It is fully steerable in both axes and is operated under computer control. The receivers are located at the prime focus.

Receiver System

The observing frequencies of 2.3 GHz and 8.4 GHz were chosen primarily because of the availability at Mt. Pleasant of a dual-frequency receiver operating at these frequencies. Because these frequencies are essentially the same as those used for the majority of the VLBI observations, these data are directly comparable with the imaging data. 2.3 GHz is high enough that scintillation is minimal and low enough to be unaffected by absorption by atmospheric water vapour. However the latter effect is important at 8.4 GHz, necessitating careful inspection and editing of data obtained during periods of heavy cloud or wet weather. At both frequencies a single feed horn sensitive to right-circular polarization is used. Cryogenically cooled amplifiers are used to minimise and stabilise the contribution of receiver-intrinsic noise. Typical effective system temperatures in situ are 750 Jy and 650 Jy at 2.3 GHz and 8.4 GHz respectively. The corresponding pre-detection bandwidths are 55 MHz and 120 MHz for the two systems.

Temperature stabilised reference noise diode signals of approximately 100 Jy are injected into the receiver inputs at each frequency to provide calibration of the receiver and IF system. Software has been developed to rapidly switch this 'CAL' and digitally sample the detected signals throughout each observation. In this manner a software noise-adding radiometer (NAR) is implemented allowing continuous calibration of the system temperature and removal of receiver gain variations. The CAL noise sources are enclosed within the receiver package and extensive work by Lovell (1991) has demonstrated that they remain stable to better than 1.5 percent over periods of $\sim$24 hours when measured against standard celestial flux density calibration sources. The receiver system configuration and the NAR are described in greater detail in Appendix A.

Scanning

The signal due to the radio source is superimposed upon a background comprised of contributions from noise intrinsic to the receiver, local interference, and from other objects in the sky that fall within the antenna beam. The antenna is scanned

across the assumed source position, allowing trends in the background contributions to be modelled and removed. By making orthogonal scans, and fitting for the source position in each, the effects of antenna pointing errors can be quantified and allowance made in the calculation of the source flux density (see Section 3.2.3).

Each of the observations in this program is comprised of four scans, two at constant right ascension and two at constant declination, intersecting and centred at the assumed position of the object. The scan length is 2°, approximately six times the full-width at half maximum (FWHM) of the antenna beam at 2.3 GHz. This ensures that sufficient data, unaffected by the source, is available to enable the baseline effects to be adequately modelled and subtracted. All observations are made under the control of a computer which schedules the observations, moves the antenna, samples the detected signals, and stores the digital data on disk for subsequent analysis. This enabled the overwhelming majority of the data to be obtained in absentia, human intervention being required only to set up and start the observations and to retrieve the data afterwards. Limitations of the computer system make it impractical to perform any analysis of the data on-line, so it is not possible to detect and repeat, in real time, scans which have been corrupted by transient interference. However, the method for correcting pointing errors requires that satisfactory scans in both directions be obtained and the practice of scanning twice in each direction provides some measure of protection against interference causing the rejection of all the data in one of the scan directions. In the absence of interference, the sensitivity of each observation is increased by combining the data from each of the scan pairs.

Antenna Gain And Scheduling

Changes in antenna orientation cause gravitational deformations which are manifested as variations in antenna gain. With a conventional az-el mounted antenna, common in radio-astronomy, these gain variations are generally independent of azimuth and can usually be characterised simply by measuring the gain as a function of elevation. However for an XY mounted antenna, the gain is a function of both coordinates, a surface in X and Y. Therefore to describe this function accurately a family of strong sources of known flux density 'uniformly' spaced over the range of declinations of interest is required. Even if such a family of sources existed, the observations required to perform this task effectively would be substantial. However because the objective of the monitoring program is to determine not the absolute flux density of the objects observed, but the variations thereof, we are not concerned with the exact flux density scale used. That is, it is important that all the observations for a given source be on a self-consistent scale but it is not necessary that the same scale be used for all sources. This fact allows us to ignore the effect of gain variations by simply ensuring that all observations of any given object are made at close to the same X and Y each time.

Lovell (1991) has determined several gain curves (as a function of hour angle) for the 26 metre antenna using sources over a range of declinations at both frequencies. They demonstrate that the gain is typically 'flat' to better than one percent within a range of about $\sim$1.5 hours either side of the meridian, beyond

which the gain decreases. Because our source sample is distributed over the full range of right ascension it is straightforward to schedule the antenna so that each object is observed when close to transit. A complete sequence of observations thus requires approximately 24 hours to complete. Since the observing program commenced, the order of the observations has not significantly changed and care is taken to ensure that the schedule is always synchronised at close to the same phase with respect to the local sidereal time.

It is possible that distortion of the antenna structure by excessive wind loading could also cause transient gain fluctuations. Although strong winds are not uncommon at the observatory this is unlikely to be a problem since the antenna is unusually robust, a legacy of its satellite tracking pedigree, and is not operated at wind speeds in excess of 65 kmh^{-1}.

Reference Calibration

Calibration of the reference signal is essential if source flux densities are to be determined accurately. In the same way that the program source flux densities are measured by comparison with the CAL, the CAL can be measured by comparison with sources of known flux density. Several observations of intrinsically stable strong sources are incorporated into the standard schedule for this purpose.

3.2.3 Analysis Methods

Preliminary Data Reduction

As described in Appendix A, the data acquired at the observatory are in the form of a sequence of samples of the detector outputs for successive CAL-off and CAL-on states, together with information relating sample number to the antenna position on the sky. The first stage of the off-line analysis of each scan involves the automatic removal of any data corrupted by transient interference (less than 0.5 seconds in duration), and the calculation of the system gain by differencing successive points to enable the application of the NAR. In order to reduce its volume, this data is averaged into bins of approximately 1 second duration, with the bins separated by 0.5 arcminutes on the sky (any variation in the bin-to-bin integration time resulting from slight non-uniformities in the antenna scan rate). The product of this initial processing for each scan then is a sequence of system temperatures, expressed in units of the CAL signal, corresponding to uniform increments in angular position.

Fitting And Editing

The extraction of the source flux density contribution from the background effects in a scan is achieved by modelling the scan with a function which expresses the two contributions in a separable form. Representing the background part of the scan with either a linear or quadratic polynomial and the source convolved with the antenna beam as a Gaussian function

$$f(x) = Ae^{-\frac{(x-B)^2}{2C^2}} + D + Ex + Fx^2 \tag{3.1}$$

proves very successful. A non-linear least squares method is used to derive the parameters A–F, or A–E if only a linear baseline fit (F=0) is required. Wherever possible a linear baseline fit is preferred to a quadratic.

A first attempt to fit all the data is made automatically by the analysis software. Each scan and fit is then inspected and any scans affected by interference or bad weather are excluded from subsequent processing. A substantial proportion ($\sim$25$-$30%) of the 8.4 GHz data is rejected because of the effects of inclement weather at this stage. The fits to the data can frequently be improved by excluding parts of the baseline most distant from the source, and in some cases it is possible to recover a good fit from interference-affected scans by prudent editing. Typical fits are illustrated in Figure 3.1.

Considerable difficulty is experienced with the fitting of the strong calibration sources at 2.3 GHz (*e.g.* 0915$-$118 in Figure 3.1) because the signal strength is sufficient to expose the presence of the antenna sidelobes. Attempts to model the sidelobe contribution to the scan are unsuccessful, largely because of the difficulty of separating the sidelobes from the baseline; there is an interplay between the two leading to unrealistic background estimates in the vicinity of the source. Lengthening of the scans to provide more data to fit the polynomial component of the baseline also fails to provide a satisfactory solution since the data so far from the source do not lead to reasonable representation of the baseline in the vicinity of the source. The approach eventually adopted involves judicious editing and fitting of every scan so that the majority of the main beam is well fit and the baseline passes through the first nulls of the beam pattern.

To minimise the effects of antenna gain variations and to keep a fixed sidelobe pattern on the sky for each source, it is important that the observations of any given source are not widely separated in hour angle. It is convenient at this stage of the analysis to reject data points that lie far from the mean X and Y of all the observations for each source. The typical distribution of observations as a function of X and Y is illustrated for two sources in Figure 3.2. For each of the survey sources, observations are discarded if they lie outside a circle of diameter 25° in the XY plane, though for most objects the points are more tightly distributed. The centres of these circles almost always fall within a few degrees of the meridian where the antenna gain changes least rapidly.

Pointing Corrections

If the antenna is not pointed directly at the source then a reduced flux density will be measured. However for an unresolved source, if the shape of the beam and the true location of the source with respect to the track of the scan is known, then a correction can be made for the pointing errors. The following analysis, based on the assumption of a circular Gaussian beam and two perpendicular scans, demonstrates this.

Consider a rectangular coordinate system coincident with the two scans in which the radio source is offset from the origin and lies at position (x_0, y_0) (Figure 3.3). The two scans are one-dimensional slices through the surface formed by the convolution of the beamshape with the source (we ignore the background,

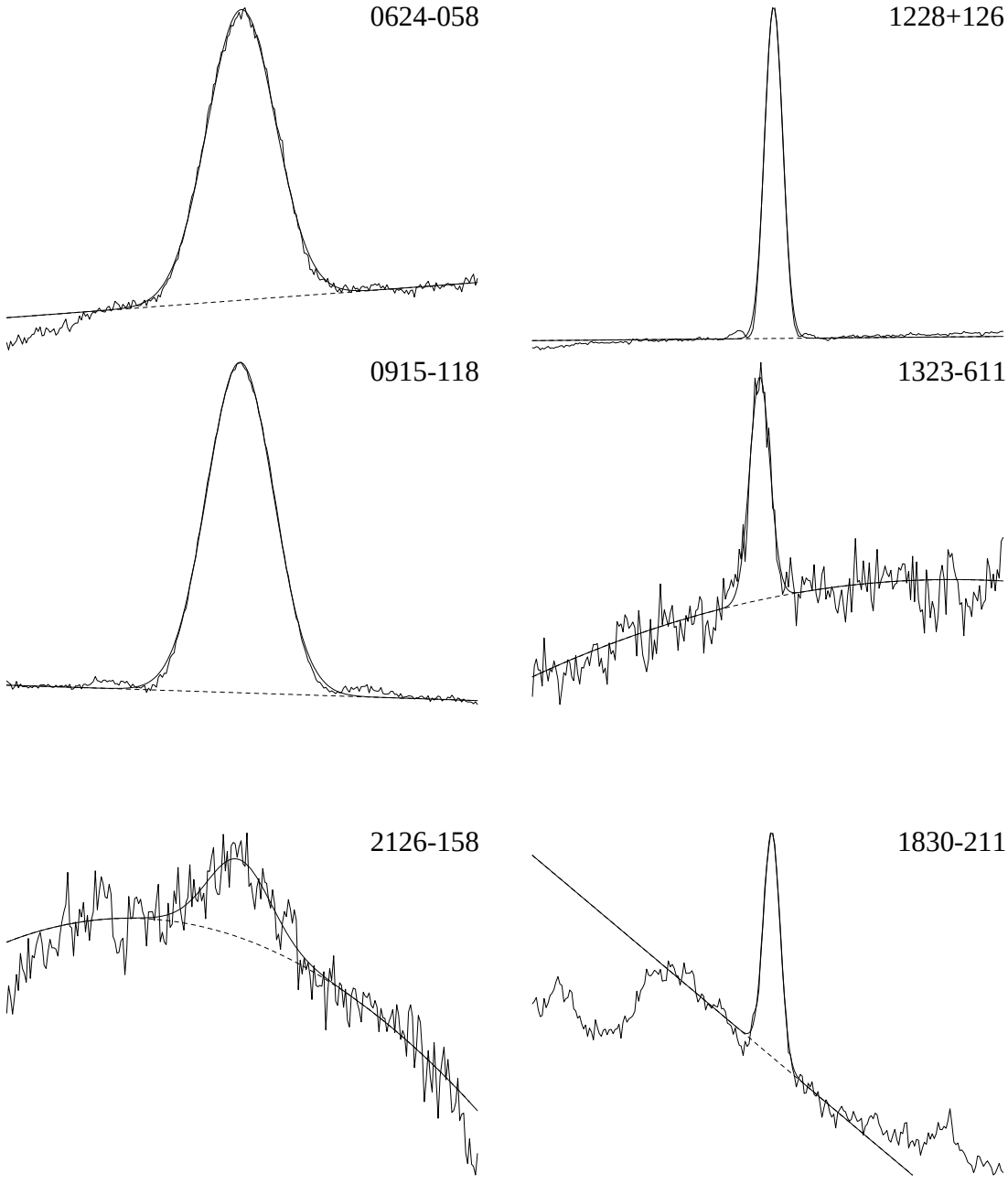

Figure 3.1: Examples of six scans and the fits of Equation 3.1. The dashed line represents the polynomial component (either linear or quadratic) of the fitted function. The three scans on the left were obtained at 2.3 GHz, the remainder at 8.4 GHz. None of the scans are shown to the same vertical scale. The curves diverge markedly from the data at the scan extremities where the data were excluded from the fitting procedure.

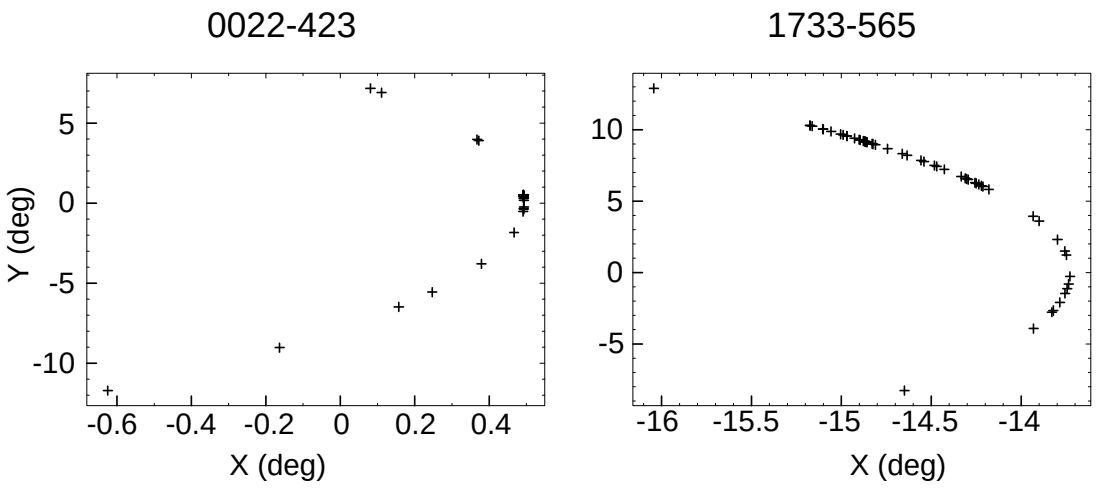

Figure 3.2: Distribution of observations of 0022−423 and 1733−565 as a function of antenna X and Y illustrating typical scatter due to scheduling variations. The number of observations of each object is 63 for 0022−423 and 58 for 1733−565.

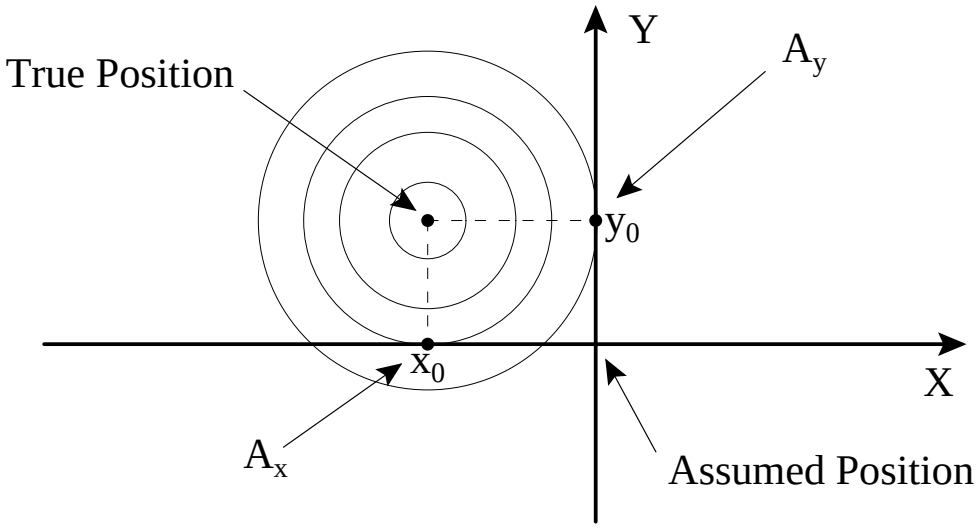

Figure 3.3: The coordinate system used for the discussion of the pointing corrections. The scans lie along the axes X and Y, and the concentric circles represent contours of the surface created by the convolution of the source with the antenna beam.

assuming it has been successfully removed by the fitting procedure). This surface is described in terms of the pointing offsets (x_0, y_0), the true source flux density A, and the beamwidth parameter C, by the following function:

$$f(x,y) = Ae^{-\frac{((x-x_0)^2+(y-y_0)^2)}{2C^2}} \tag{3.2}$$

The beamwidth parameter C, and the quantities x_0 and y_0, together with the (reduced) apparent flux densities A_x and A_y, are determined as part of the scan fitting process previously described. Substituting these values into Equation 3.2 yields two expressions

$$A_x = Ae^{-\frac{y_0^2}{2C^2}} \quad and \quad A_y = Ae^{-\frac{x_0^2}{2C^2}}$$

which are trivially solved to yield two estimates of the true flux density *viz.*

$$A = A_x e^{\frac{y_0^2}{2C^2}} \quad and \quad A = A_y e^{\frac{x_0^2}{2C^2}} \tag{3.3}$$

Note that while either expression can provide an independent estimate of the true flux density, it is essential that there is a scan in each direction to allow determination of the pointing errors, x_0 and y_0.

Examination of the beamwidth parameters obtained from fitting Equation 3.1 reveal no systematic differences between R.A. and Dec. scans for either observing frequency, justifying the assumption of a circular beam. If some sources were partially resolved by the antenna then we would expect the fitted beamwidths for those sources to be larger than for unresolved objects (recall that the beamwidth parameter actually characterises the width of the beam *convolved* with the source brightness distribution). However a plot of the average beamwidths for each source reveals no significant deviations from the mean, except possibly for two reference sources 0915−118 and 1228+126, allowing us to conclude that the survey objects are all unresolved, or at least nearly equally resolved (though still quite adequately modelled by a circular Gaussian). There is no evidence of any evolution of the beam shapes over the duration of the entire observing program. This permits the use of a mean value for the beamwidth when applying Equations 3.3, thereby reducing the contribution to the uncertainty in the final flux density estimate.

Treatment Of Errors

The uncertainty σ_A in the flux density derived from the first of Equations 3.3 and expressed in terms of the input parameters and their corresponding uncertainties (A_x, σ_{A_x}), (y_0, σ_{y_0}) and (C, σ_C) is

$$\sigma_A = A_x e^{\frac{{y_0}^2}{2C^2}} \left[\left(\frac{\sigma_{A_x}}{A_x} \right)^2 + \left(\frac{y_0 \sigma_{y_0}}{C^2} \right)^2 + \left(\frac{y_0^2 \sigma_C}{2C^3} \right)^2 \right]^{\frac{1}{2}} \tag{3.4}$$

A good estimate of the error in A_x is the root mean square (RMS) deviation of the fit to the data. In fact the correct value to use is $\sqrt{2}$ times the RMS since A_x is derived from the difference of the fits to the baseline and the Gaussian, the

subtraction being implicit in the fitting process. This error estimate is doubled for the primary calibrator objects at 2.3 GHz in order to provide a measure of protection against errors associated with the fitting of the antenna sidelobes.

For almost all the observations at 2.3 GHz, and the majority at 8.4 GHz, we have two scans in each of the two coordinate directions. The difference between the two source positions obtained from each pair of scans is an indicator of the uncertainties, σ_{x_0} and σ_{y_0}, in the pointing errors. This quantity varies markedly depending on the strength of the source (that is, the signal to noise ratio) and the antenna beamwidth. For all the observations of each source at each of the two observing frequencies, this quantity is calculated and the mean used as the estimate of the pointing uncertainty for that source and frequency. Typical values are approximately 1 and 0.5 arcminutes at 2.3 GHz and 8.4 GHz respectively.

As described above, the beamwidth parameters are derived by taking the mean fitted beamwidths of many observations of several sources. The RMS scatter of the data points about these means is taken as the standard error in the beamwidth estimates. Only the five strongest sources have been used to calculate these values which are listed in Table 3.1.

Frequency	C	σ_C	FWHM
2.3 GHz	8.48	0.25	20.0
8.4 GHz	2.22	0.15	5.22

Table 3.1: Average values and standard errors in arcminutes for the beamwidth parameters (C, σ_C) used in Equation 3.4. The corresponding half power beamwidths (FWHM) are also shown.

Calculation Of Source Flux Densities

Flux density and error estimates, calculated using Equations 3.3 and 3.4, from up to four scans are combined by taking a weighted mean to yield a single estimate of the source flux density and a corresponding formal error expressed in units of the reference calibration signal. For each set of these measurements of a program source, a value for the calibration signal is obtained by calculating the weighted mean of all observations of the calibration sources that lie within some specified time interval of the program source observation. If no calibrator observation exists within that time interval then the program source observation is excluded from further analysis.

3.3 Radio Light Curves and Results

Approximately 25000 individual scans have been obtained in about 65 observing sessions over a period of 27 months until March 1993. These data were subjected to the analysis procedures described in the previous sections. Not all of the observing sessions ran to completion, due to reasons such as excessive wind, equipment

failure, or other observing commitments for the 26 metre antenna, so there is some variation in the number of data points for each object. Data obviously corrupted by interference or, at 8.4 GHz particularly, bad weather, have also been removed.

3.3.1 Absolute Flux Density Calibration

The sources chosen as flux density calibrators are 0915−118 and 1228+126. The flux densities of these objects at each of the observing frequencies used in this investigation are obtained from an interpolation of the values published in Klein *et al.* (1987) and are presented in Table 3.2. These flux densities were corrected in a similar manner to that followed by Klein and Stelzreid (1976) to take into account the slight resolution of the objects by the 26 m antenna beam. A further correction is required to account for the difference in antenna gain between the two XY positions at which each was observed. This is done by calculating a nominal equivalent flux density for the calibration signal from each calibration source observation independently. A scaling factor α is then determined so that the quantity

$$\sum_{i=1}^{n}(\alpha U_i - V_i)^2$$

is minimised, the U_i and V_i being the two values of the calibration signal derived from the two sources in the $i'th$ observing session. The U_i are all scaled by α to bring both sets of observations onto the same flux density scale.

It is difficult to adjust the measurements of the program sources onto a common flux density scale because of the problems involved with accurately determining the antenna gain as a function of source declination (Section 3.2.2). Therefore, although the axes of the light curves in the next section are labelled as Jansky, the absolute scale is only accurate to within a few percent. The magnitude of the effect can be gauged from the rescaling computed for the two calibration sources which were typically observed at elevations of 35°and 60°. The scale factors α at each frequency were both close to two percent so it appears that the gain is not a strong function of the antenna X position, *provided* Y is close to zero (source close to meridian transit). In general, objects with similar declinations are on the same scale since they have been observed at close to the same XY position.

Frequency	0915−118	1228+126
2.3 GHz	27.7	140.0
8.4 GHz	8.3	46.0

Table 3.2: Assumed flux densities (in Jy) of the two calibration objects. These values were derived from Klein *et al.* (1987).

Figure 3.4: The radio light curves at 2.3 GHz and 8.4 GHz for the sources in the flux density monitoring survey. Wherever the flux densities for a given source are similar at the two observing frequencies, the data for each frequency are plotted separately. If two or more data points are available for a source on a given day, then only the weighted mean value for that day is plotted.

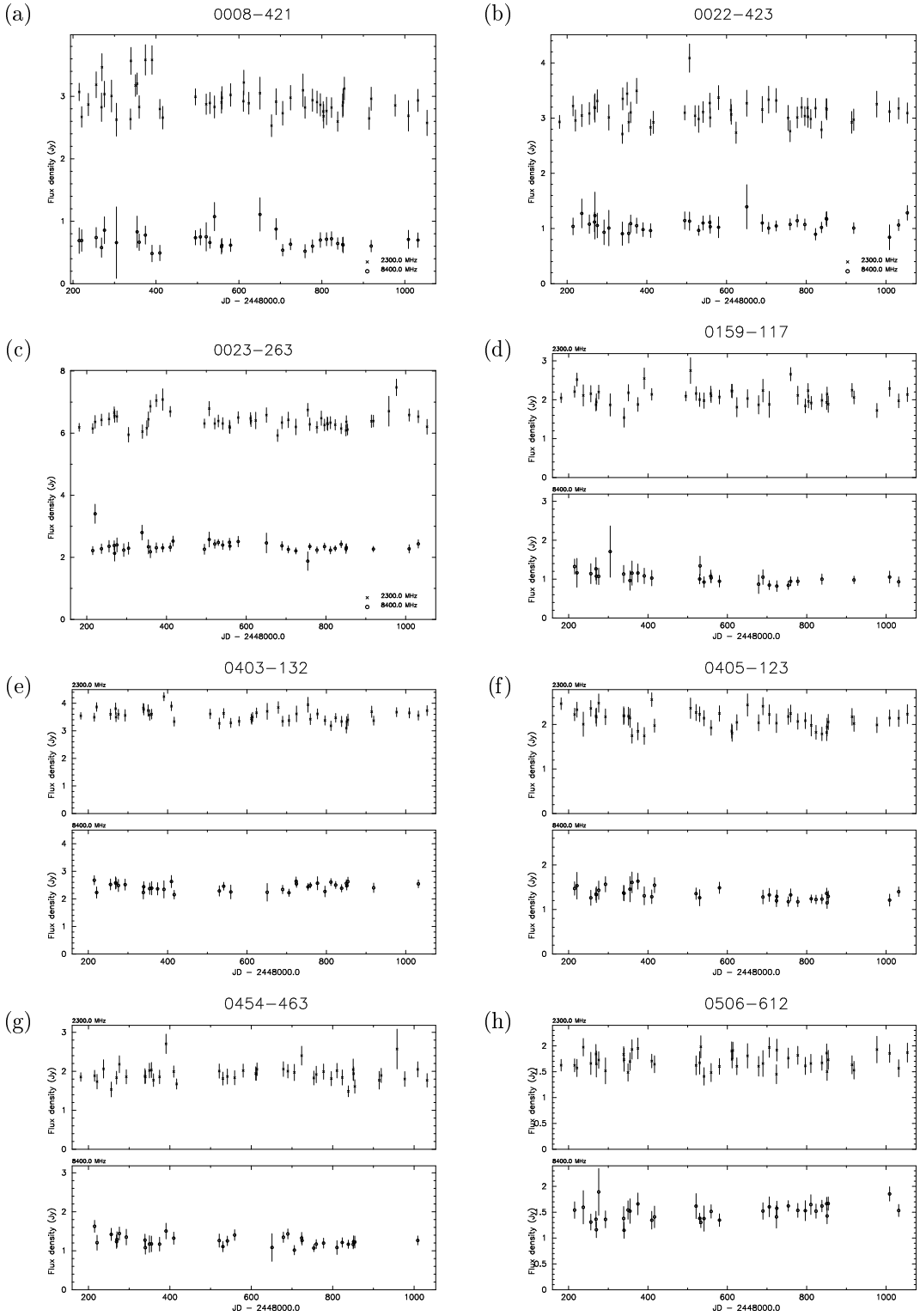

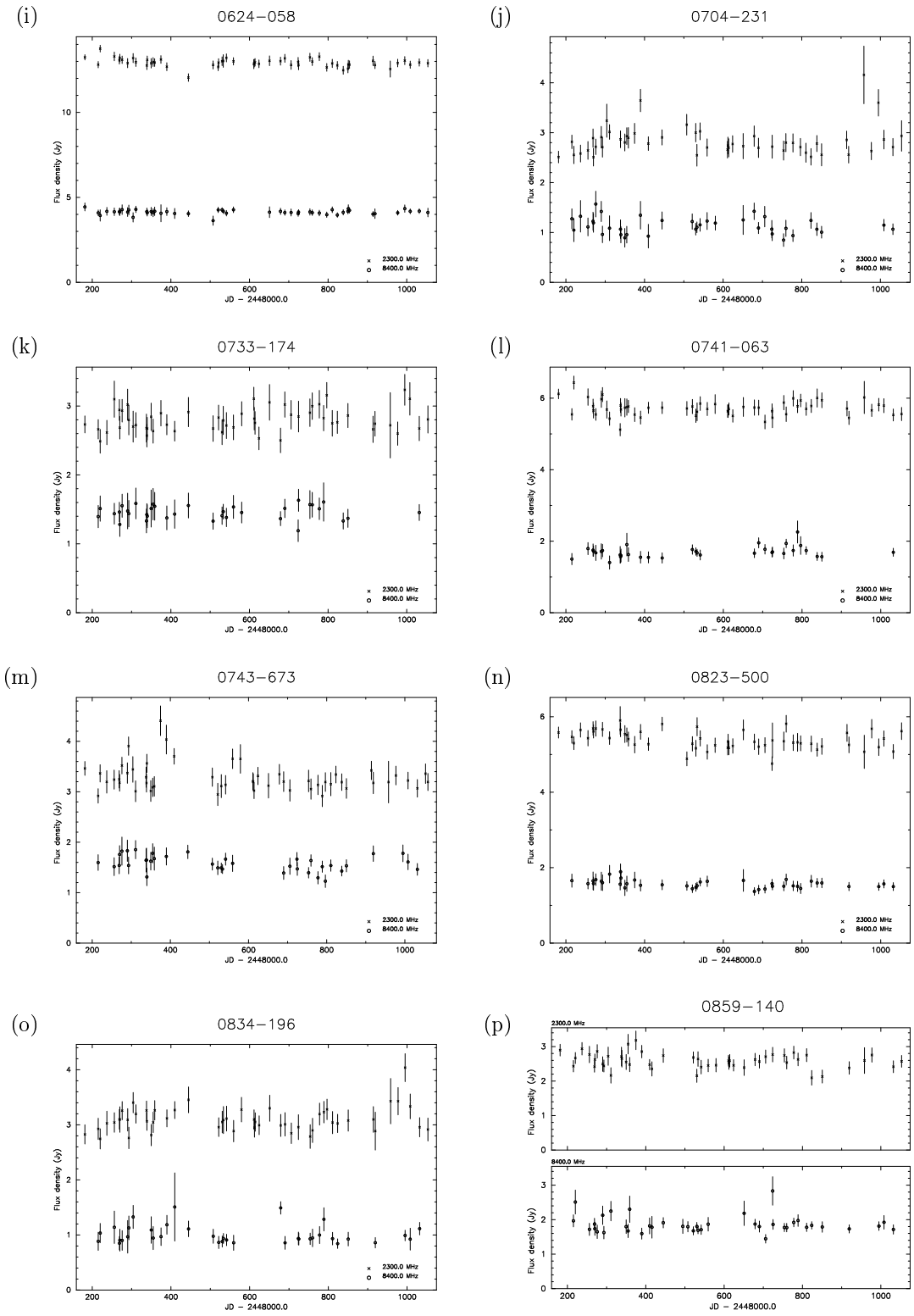
(i)
0624−058
(j)
0704−231
(k)
0733−174
(l)
0741−063
(m)
0743−673
(n)
0823−500
(o)
0834−196
(p)
0859−140
Flux density (Jy)
JD − 2448000.0
2300.0 MHz
8400.0 MHz

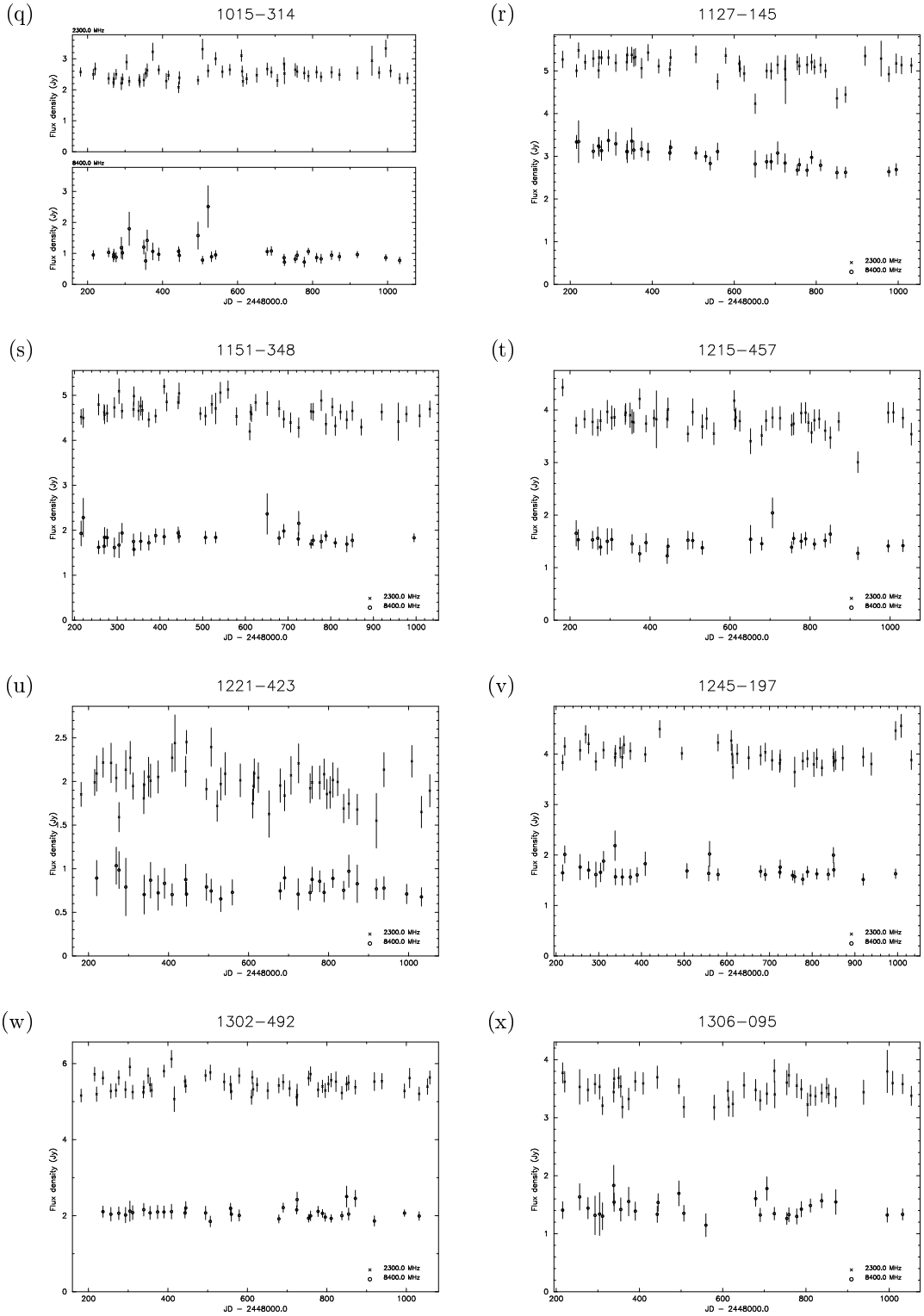
(q)
1015−314
2300.0 MHz
8400.0 MHz
Flux density (Jy)
JD − 2448000.0
(r)
1127−145
2300.0 MHz
8400.0 MHz
(s)
1151−348
(t)
1215−457
(u)
1221−423
(v)
1245−197
(w)
1302−492
(x)
1306−095

(y) 1323−611

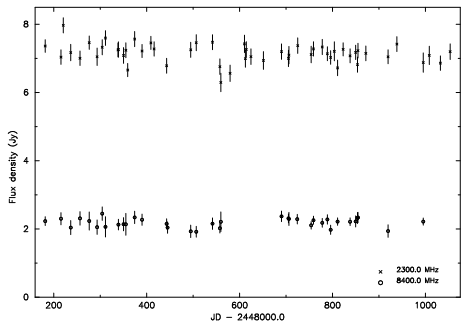

(z) 1354−174

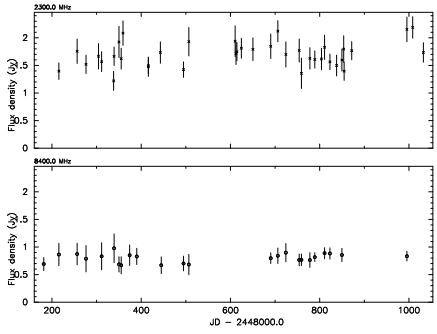

(aa) 1514−241

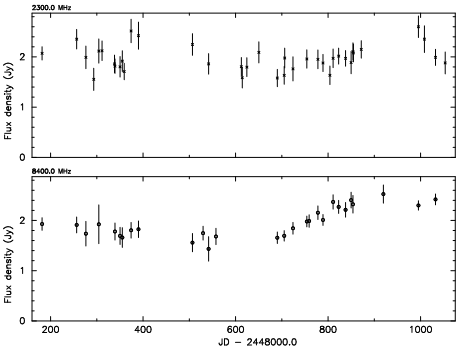

(ab) 1549−790

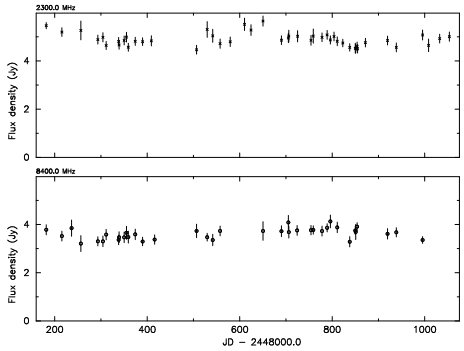

(ac) 1733−565

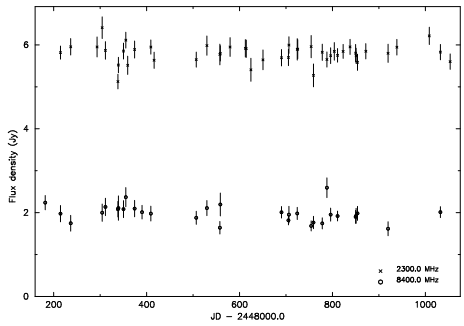

(ad) 1740−517

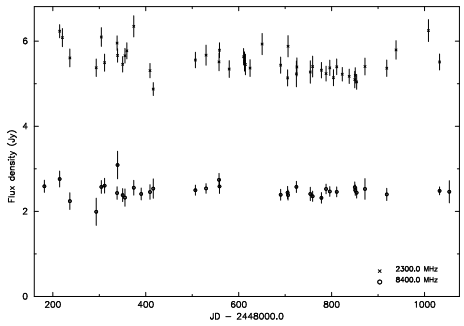

(ae) 1827−360

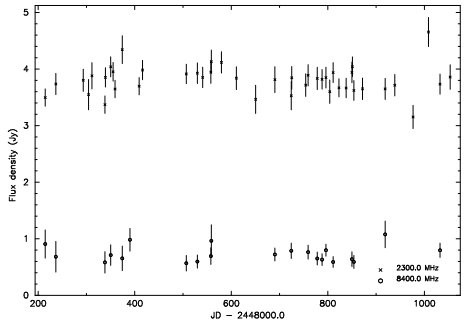

(af) 1830−211

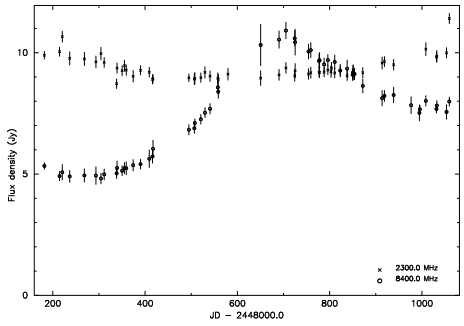

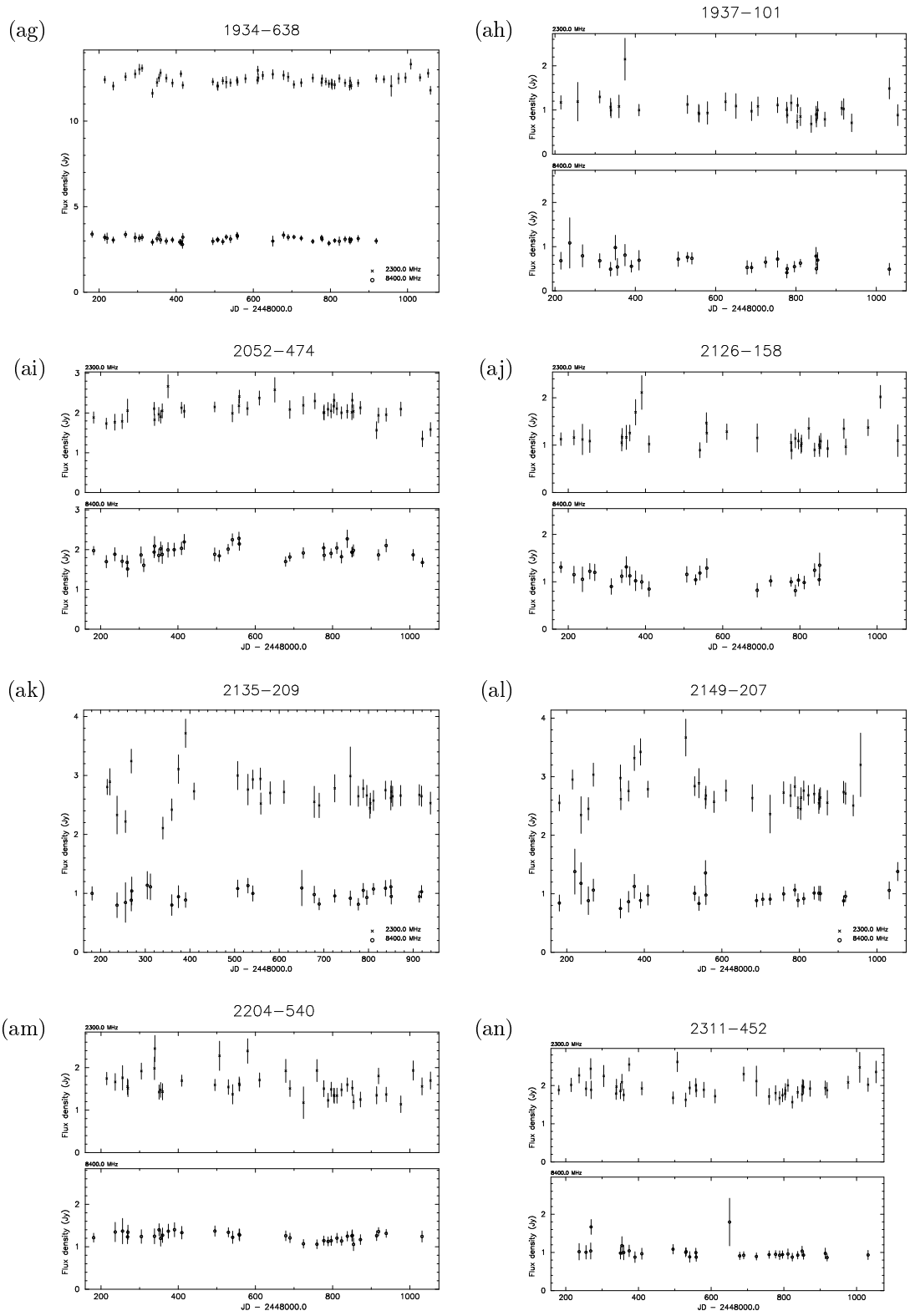

3.4 Classification Of Variability

An analytic test of the flux density variability of each of the sources was performed following the method of Kesteven *et al.* (1976). Given n flux densities S_i, each

having standard error σ_i, we can compute the quantity

$$x^2 = \sum_{i=1}^{n} \frac{(S_i - \overline{S})^2}{\sigma_i^2} \tag{3.5}$$

where $\overline{S}$ is the weighted mean flux density. If the dispersion in the S_i is due solely to the underlying distribution of measurement errors, then x^2 should be distributed as χ^2 with $n-1$ degrees of freedom. The probability $p(x^2)$ that x^2 should equal, or exceed the value computed, is readily calculable from tabulations of the χ^2 distribution. The probability that x^2 should equal a given value, is the probability that the source is intrinsically non-variable. Adopting the same criteria as Kesteven *et al.*, we classify a source as variable if $p < 0.1\%$ and 'possibly variable' for $0.1\% \leq p \leq 1\%$. The results of this test for the sources at both observing frequencies are presented in Table 3.3. It should be noted that strictly the χ^2 test applies only if all the data points have errors drawn from the same parent distribution. It is clear from the light curves in the preceeding section that there is some variation in the size of the errors for individual points. However analysis of the measurement errors shows that the occurrence of errors lying more than two standard deviations from the mean error is low and that the error distributions are neither bimodal nor broad and flat, indicating that the χ^2 test is applicable for this data.

The x^2 value is not an ordered statistic so it is not able to detect slow trends in the flux density measurements. A good example of this is 1127-145 for which the test is inconclusive with a probability of 0.002 (Table 3.3). However a visual inspection of the data reveals the obvious systematic decrease in the 8.4 GHz flux density immediately. With a longer data span, and assuming the trend continues, the χ^2 test would no doubt reclassify the source unambiguously. Nevertheless, it is clearly important that the χ^2 test not be relied upon as the sole detector of variability, a visual test is also justified.

3.5 Sensitivity Limits

The uncertainties in a flux density measurement can be attributed primarily to three sources; system sensitivity, pointing errors, and uncertainty in the antenna beamwidth, corresponding to the three terms in the summation in Equation 3.4. The expected sensitivity of a NAR system can be calculated using an appropriate form of the radiometer equation and for these observations is approximately 0.20 Jy and 0.12 Jy at 2.3 GHz and 8.4 GHz respectively (Appendix A). For a typical program source, with flux densities at each frequency of 6 and 2 Jy and mean pointing errors of 1.5 arcminutes, the ratio of the system noise term in Equation 3.4 to those due to antenna pointing errors and beamwidth uncertainty is about $1 : 0.5 : 0.01$ at 2.3 GHz and $1 : 3 : 0.3$ at 8.4 GHz. The contribution of system sensitivity to the final uncertainty at 2.3 GHz is thus about twice as large as that due to pointing errors. However at 8.4 GHz, with the narrower antenna beam, the uncertainty is dominated by the pointing component. Uncertainties for a source with 2.3 and 8.4 GHz flux densities of 6 and 2 Jy, after all four scans are averaged, are ~ 0.12 Jy (2%) and ~ 0.20 Jy (10%) respectively.

Program Source	2.3 GHz				8.4 GHz			
	n	x^2	p	var.	n	x^2	p	var.
0008−421	52	74.6	0.017	N	34	20.8	0.951	N
0022−423	50	56.7	0.211	N	36	15.3	0.998	N
0023−263	52	84.3	0.002	?	40	34.9	0.656	N
0159−117	45	52.5	0.178	N	30	16.1	0.975	N
0403−132	46	70.9	0.008	?	35	22.3	0.939	N
0405−123	48	63.2	0.058	N	33	22.7	0.887	N
0454−463	45	46.1	0.387	N	34	27.8	0.723	N
0506−612	47	33.6	0.912	N	35	37.2	0.324	N
0624−058	53	64.4	0.117	N	50	18.1	1.000	N
0704−231	49	67.8	0.032	N	37	28.7	0.802	N
0733−174	53	43.8	0.783	N	35	12.5	1.000	N
0741−063	55	71.7	0.054	N	34	23.8	0.881	N
0743−673	52	84.1	0.002	?	38	40.7	0.310	N
0823−500	52	71.4	0.031	N	40	18.2	0.998	N
0834−196	51	52.3	0.384	N	36	41.9	0.197	N
0859−140	49	56.6	0.184	N	40	37.3	0.550	N
1015−314	53	77.2	0.013	N	35	31.1	0.608	N
1127−145	47	72.4	0.008	?	34	61.0	0.002	?
1151−348	51	60.3	0.151	N	32	17.6	0.974	N
1215−457	50	63.1	0.085	N	28	16.2	0.949	N
1221−423	50	61.9	0.103	N	30	11.1	0.999	N
1245−197	42	47.0	0.240	N	31	23.2	0.809	N
1302−492	55	62.1	0.210	N	35	25.0	0.869	N
1306−095	44	36.0	0.768	N	29	21.7	0.797	N
1323−611	53	79.0	0.009	?	36	22.6	0.948	N
1354−174	38	49.9	0.076	N	24	7.3	0.999	N
1514−241	38	55.4	0.026	N	28	107.9	< 0.001	Y
1549−790	46	91.4	< 0.001	Y	37	39.6	0.313	N
1733−565	45	49.9	0.251	N	31	38.6	0.136	N
1740−517	46	133.6	< 0.001	Y	35	22.2	0.940	N
1827−360	43	62.2	0.023	N	21	13.3	0.862	N
1830−211	55	267.5	< 0.001	Y	55	2782.1	< 0.001	Y
1934−638	55	92.6	< 0.001	Y	44	28.6	0.955	N
1937−101	33	31.9	0.471	N	25	16.4	0.875	N
2052−474	42	64.2	0.012	N	39	46.6	0.161	N
2126−158	33	45.7	0.055	N	25	24.0	0.460	N
2135−209	35	63.1	0.002	?	27	15.0	0.958	N
2149−287	37	50.3	0.057	N	28	22.1	0.730	N
2204−540	42	67.0	0.006	?	36	19.8	0.982	N
2311−452	43	59.7	0.037	N	32	22.4	0.869	N

Table 3.3: Results of the χ^2 test for variability discussed in the the text. Key: Y=variable, ?=possible variable, N=non-variable.

One further contribution to the measurement errors is that due to the presence of numerous weak sources lying within the antenna beam. This ensemble of confusing sources places a fundamental limit on the precision with which any source flux density can be determined since they imbue the sky with an inherent roughness which can be reduced only by improving the antenna resolution. Klein and Stelzreid (1976) estimate that the magnitude of this effect for a 26 metre antenna operating at 2.27 GHz is ~ 0.12 Jy. Taking this into account in the above calculations raises the expected uncertainty at 2.3 GHz to ~ 0.14 Jy. Because the antenna confusion limit depends so strongly on beam size this effect is negligible at 8.4 GHz despite the increased bandwidth and lower system temperatures.

Similar calculations to those described above, and performed for several of the non-variable sources in this program, yield uncertainty estimates that are in close agreement with the RMS deviations of the individual flux density measurements about the mean for each source. This indicates that the calculation of the measurement uncertainties includes all significant contributing factors and that the quoted uncertainties for each data point are representative of the true uncertainties, a condition which must hold if the χ^2 test is to be a valid test of source variability. An additional test of the internal consistency of these measurements can be performed by expressing the flux density of one of the calibrator objects in terms of the other. When this is done for 0915−118 and 1228+126 (Figure 3.5) the χ^2 test indicates that these two sources are indeed mutually non-variable.

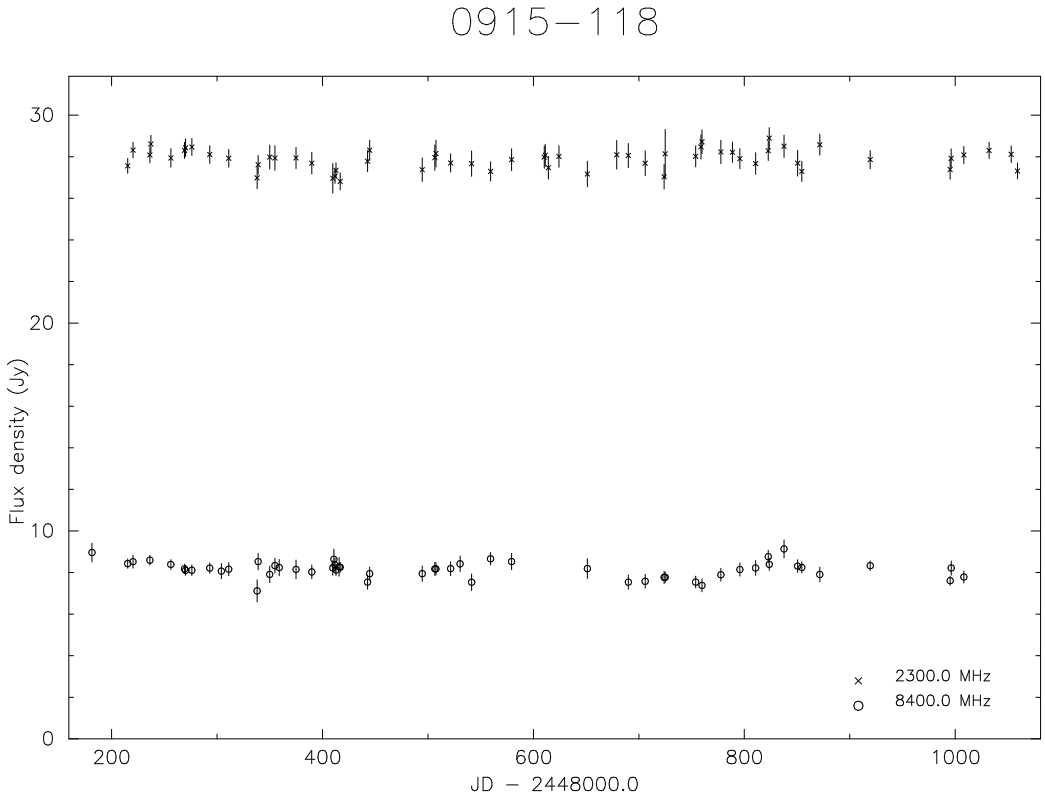

Figure 3.5: The flux density of 0915−118 derived from the measurements of 1228+126. The chi-squared test finds this object to be non-variable at both 2.3 GHz and 8.4 GHz.

3.6 Variable Sources

General Comments

The first and most obvious conclusion that can be drawn from the data presented in this chapter is that, within the errors, most of the sources are intrinsically non-variable (as defined by the χ^2 test). The implications of this general result will be discussed in Section 3.7, while the objects for which it does not hold (those exhibiting variability) are discussed below.

In general the probability that a source is non-variable is less for the 2.3 GHz data than for 8.4 GHz and there are several possible observational causes of this. Because the antenna beamwidth is greater at 2.3 GHz there is a greater chance that the baseline model derived from the scan fitting process is in error, leading to an error in the source flux density estimate. Extreme examples of this problem should be removed in the inspection process but it is less likely that the more marginal cases will be detected simply because of the reduced amount of the scan that is unaffected by the source. Several of the objects in this survey are highly compact and have the potential to exhibit the effects of interstellar scintillation. While this effect should be small, even at 2.3 GHz, it is important for this reason that very short timescale flux density variations (of the order of a few days) not necessarily be interpreted as source intrinsic.

One further cause for concern with the data presented in Figure 3.4 is the presence of a weak apparent periodicity in the 2.3 GHz light curve for 1934−638. The fact that this effect has a period close to one year suggests that it is very unlikely to be intrinsic. If the data for several of the non-varying sources are taken and used to determine the strength of the CAL signal over the duration of the survey then an annual periodicity is observed. This feature has the same phase regardless of the right ascension of the source so it appears to be a genuinely annual effect. However the light curves for several of the stronger (nominally) non-variable sources, such as 0624−058 and 1323−611, demonstrate that it is being successfully removed by the calibration process. The observed variation may, alternatively, originate in a diurnal effect involving the CAL and/or the antenna gain. This is possible because each object is always observed at close to the same local sidereal time throughout the year so that a diurnal effect would be aliased and appear in the light curve as an annual feature, at a phase dependent on the source right ascension. This can be tested by taking the calibrated data for a source not exhibiting obvious variability and calculating a mean flux density, for the whole of the data span, which is used to normalise all the individual observations for that source. By plotting these normalised flux densities as a function of the solar time at which they were obtained, any diurnal effect should be evident. However, when this is done, no such effect is apparent. An alternative approach, calculating normalised flux densities for many objects and then examining the evolution over a year of a plot of normalised flux densities for a particular observing session versus source right ascension, also fails to explicitly demonstrate the effect. If it is assumed that this effect is observational in origin then it can only be concluded that it is so weak that 1934−638 is the only object strong enough to reveal it unequivocally. This could be the case for a diurnal effect in particular, for which

objects observed at close to the same time as the primary calibrators 0915−118 and 1228+126 are relatively unaffected (*e.g.* 0624−058), while those more distant (*e.g.* 1934−638) demonstrate it. The present quantity of data, comprising observations of mostly weak objects (relative to 1934−638) over two and a half years, is simply insufficient to attribute the effect conclusively to a particular cause. However the apparently annual nature of the effect suggests very strongly that the variation is extrinsic to 1934−638.

0023−263

This object exhibits a single, symmetric event of approximately 100 days duration. There appears to be a brief decrease in the 2.3 GHz flux density immediately preceeding a steep rise of magnitude ∼1.5 Jy which is followed by a slower return back to the pre-outburst flux density. There is no significant evidence of any corresponding variation in the 8.4 GHz flux.

1127−145

Changes in the flux density of this object are apparent at both frequencies. A smooth decrease at a rate of 0.33 Jy per year persists throughout the observation span at 8.4 GHz. The variations at 2.3 GHz are equivocal, depending largely on three low measurements close to Julian days 2448650 and 2448850.

1514−241

There is a pronounced and steady increase in the 8.4 GHz flux density of 1514−241 of duration approximately 200 days and magnitude 0.7 Jy. There appears to be a weak decrease over the preceeding 600 days though the data are marginal. Some trace of the high frequency event towards the end of the data span is visible in the 2.3 GHz observations.

1549−790

Weak variations are present in the 2.3 GHz data for this object. The VLBI imaging in Chapter 5 show that this source has a classical core-jet morphology with a compact flat spectrum core which is most probably the origin of the variability.

1740−517

There is evidence of weak decreasing trend of nearly 1 Jy in the 2.3 GHz flux density of this source in the ∼ 700 days prior to Julian day 2448850. No corresponding effect is apparent in the 8.4 GHz data.

1830−211

The most dramatic variable in the sample, 1830−211 shows substantial changes at both frequencies, including a pronounced peak of 11 Jy, more than double the initial flux density, at 8.4 GHz. VLBI observations of this source lead eventually

to its identification as a gravitationally lensed core-jet, including a complete Einstein ring (Jauncey *et al.*, 1991; Kochanek and Narayan, 1992). The 2.3 GHz flux density, after decreasing by about 1 Jy is now slowly increasing and continued monitoring suggests that a new increase is beginning at 8.4 GHz. Our multiple epoch VLBI observations at 8.4 GHz (Chapter 6) indicate that the variation occurs in the compact components and not the ring, consistent with the behaviour expected of the lensed core. The strength of this object and well defined peak in the light curve mean that it is likely to be possible in future to measure the time delay between the two compact components.

2135−209

The larger scatter in the 2.3 GHz data for this source early in the survey is the basis for the claim of the detection of variability in this source. The behaviour is unsystematic, apart from the dramatic increase of nearly 2 Jy near Julian day 2448360, and uncharacteristic when compared with the remainder of the data span.

2204−540

The variability in the 2.3 GHz data of 2204−540 indicated by the chi-squared test depends largely on three widely separated data points that are substantially displaced from their nearest neighbours and is probably a false detection.

3.7 Conclusions

The flux density monitoring program described in this chapter has demonstrated that, with very few exceptions, the sources in this sample are non-variable, or at best, marginally variable. This places on a firm foundation the result that the incidence of variability in these objects is systematically low. It is therefore unlikely that the highly luminous compact structure observed in peaked spectrum sources is either powered by, or similar to the milli-arcsecond cores that dominate the emission in the active flat spectrum objects. Both the quiescent spectra, and the transient behaviour are different, despite the apparent morphological similarities. This does not preclude the possibility that GPS sources are either progenitors of the more active objects that have not yet 'turned on', or else remnants.

Alternatively the low variability may simply indicate that the flat spectrum cores are very weak and contribute so little of the total flux that their variability is undetectable. If this were so then it would be natural to associate the bulk of the emission, the component giving rise to the peaked spectrum, with matter ejected from the core, as appears to be the case in many core-jet sources containing active nuclei. However, if the peak in the spectrum is due to synchrotron self absorption then this material must be sufficiently dense to remain optically thick at frequencies below the spectral peak. Two ways in which this can occur are if the source is either very young (*e.g.* Mutel *et al.* 1985) or else confined or otherwise impeded by the surrounding medium (O'Dea *et al.*, 1991).

The absence of variability detected among these sources means that they are potentially excellent flux density calibrators for arcsecond scale synthesis arrays at centimetre wavelengths. Indeed two of the objects in this survey, 1934−638 and 0823−500, are primary and secondary calibrators respectively for the ATCA. However the suitability of a particular source for this purpose depends upon not only lack of variability, but also the proportion of the total flux density not contained within the compact components. This information is most easily obtained by means of the VLBI observations described in the next three chapters. It is also necessary to continue monitoring the flux density for evidence of the emergence of variable components.

This flux density monitoring survey also serves to emphasise the potential for doing worthwhile observations with only a 26 m antenna. The accuracy of the observations is certainly compromised by both reduced sensitivity and radio source confusion. However these can be largely overcome by taking care to minimise the change in sidelobe pattern on the sky between observations, and by more frequent sampling. Demand for small antennas is often substantially less than for larger more sensitive instruments so they are ideal tools for undertaking the type of exploratory surveys such as that described in this chapter.

Chapter 4

SHEVE Observations

4.1 Introduction

The VLBI observations presented in subsequent chapters of this thesis were obtained with the Southern Hemisphere VLBI Experiment (SHEVE) array. This array, comprising antennas at seven Australian locations and one in South Africa, is a descendent of the original array used in the first SHEVE experiment in April 1982 (Preston *et al.*, 1989). SHEVE is a collaboration between the various institutions that own and run the individual antennas, and does not operate as a "national facility" in quite the same way that the US or European VLBI networks do.

Not all sites are capable of supporting every frequency used by SHEVE. However observations with sub-arrays of three or more antennas have been made at 0.843, 1.6, 2.3, 4.85, 8.4 and 12.2 GHz. Rubidium vapour frequency standards were used initially at all observatories except Tidbinbilla, where a Hydrogen maser was installed. Parkes, Hobart and Hartebeesthoek have subsequently been equipped with Hydrogen masers. All sites are instrumented with the MK-II VLBI recording system and the four observatories with Hydrogen masers also support MK-III observations. The continuum data are normally correlated at the CIT/JPL Block-II VLBI Processor in California though some MK-III observations have been processed with the correlator at Haystack Observatory in Massachusetts. Subsequent processing and analysis utilise the NRAO AIPS software and the Caltech VLBI package (Pearson, 1991a).

The array has changed substantially since 1982 and the purpose of this chapter is to describe the current state and capabilities of the array and to detail the correlation and post-correlation stages of the data analysis, particularly as they apply to the 2.3 GHz and 8.4 GHz data that appear in subsequent chapters.

4.2 Antennas

Following the initial 1982 experiment, there was a lull in which no observations were made until October 1987. During this time a more versatile and sensitive antenna was acquired by Hobart and a new antenna at Perth became available

so that, although the antenna at Fleurs was lost, the overall capability of the array was substantially enhanced. The array has continued to evolve since the first observations with the new SHEVE in 1987 with the commissioning and participation of elements of the Australia Telescope located at Culgoora and Mopra. A small number of experiments have also utilised the Molonglo Synthesis Telescope (MOST) and more recently, a 27.5 m antenna at Perth. However as these two antennas did not contribute to the observations described in this thesis their description below is accordingly brief relative to the others. Except for Parkes, Hobart and Alice Springs, which are prime focus instruments, the parabolic antennas are all equipped with cassegrain feed systems. All of the 2.3 GHz and 8.4 GHz observations have been made using right-circular polarization. The basic parameters of the most commonly used SHEVE antennas and their receivers at 2.3 GHz and 8.4 GHz appear in Table 4.1.

			2.3 GHz				8.4 GHz		
Antenna	Size (m)	Mount	Receiver Type	T_{sys} (Jy)	T_{sys} (K)	DPFU (K/Jy)	Receiver Type	T_{sys} (Jy)	T_{sys} (K)	DPFU (K/Jy)
DSS 43	70	Az-El	TWM	15	16	1.025	TWM	20	18	0.921
DSS 45	34	Az-El	HEMT	165	38	0.225	TWM	130	31	0.240
DSS 42	34	HA-Dec	TWM	100	20	0.19	TWM	130	20	0.152
PRKS	64	Az-El	HEMT	90	50	0.538	HEMT	90	40	0.45
HOBT	26	XYEW	HEMT	750	77	0.1025	HEMT	650	65	0.1
CULG	22	Az-El	HEMT	400	22	0.0549	HEMT	400	72	0.090
MOPR	22	Az-El	HEMT	400	33	0.0813	HEMT	400	40	0.096
ALSP	9	Az-El	FET	45000	305	0.00676	FET	–	–	–
PRTH	15	Az-El	FET	3300	124	0.0375	FET	6000	–	–
HART	26	HA-Dec	HEMT	400	40	0.102	HEMT	950	60	0.062

Table 4.1: Parameters of SHEVE antennas and receivers. The T_{sys} columns give the approximate system temperatures in both Jy and Kelvin. The ratio of these quantities is the parameter DPFU (degrees per flux unit).

4.2.1 Tidbinbilla (DSS 43, DSS 45, DSS 42)

The Tidbinbilla antennas are all located at the Canberra Deep Space Communications Complex and are part of the NASA Deep Space Network (DSN), operated by the Jet Propulsion Laboratory (JPL). Time not allocated to spacecraft tracking is often available for radio-astronomy. With the exception of DSS 45 at 2.3 GHz, all three antennas are equipped with cooled travelling wave maser (TWM) receivers operating at 2.3 GHz and 8.4 GHz. Active subreflectors on each antenna compensate for the first-order effects of variations in the gain with elevation. MK-II and/or MK-III VLBI terminals at the station can record data from any of the three antennas. A Hydrogen maser is used as a time and frequency standard. The three antennas have participated in numerous SHEVE observations since 1987, though they are not often used simultaneously.

DSS 43

This azimuth-elevation (Az-El) mounted antenna had a diameter of 64 m at the time of the 1982 SHEVE experiment. It was enlarged to 70 m in 1986 to support the Voyager Uranus and Neptune encounters and is now the largest fully steerable antenna in the southern hemisphere. With 1.6 GHz and 12 GHz receivers, DSS 43 is the only Tidbinbilla antenna equipped to observe at other than 2.3 GHz and 8.4 GHz. The antenna has a slew rate of 12°per min and an elevation limit of 6.7°. The antenna gain and pointing are determined regularly as part of the normal operation of the DSN and are usually monitored in the course of SHEVE observations.

DSS 45

DSS 45 is a 34 m Az-El antenna located approximately 500 m west of DSS 43. The antenna has an elevation limit of 8° and a slew rate of 23°per min. At 2.3 GHz the gain is flat and it has been accurately measured at 8.4 GHz. The pointing behaviour of the antenna is accurate to between 15 and 20 arc-seconds rms.

DSS 42

DSS 42 is a HA-Dec antenna (HA limit $\pm 6.7 hrs$) 200 m north of DSS 43. Originally a 26 m antenna, subsequently enlarged to 34 m, DSS 42 is the oldest operational antenna at Tidbinbilla and has a poorer surface which degrades both the pointing and gain performance at 8.4 GHz. The pointing is accurate to between 0.5 and 1 arc-minute.

4.2.2 Parkes

The 64 m antenna operated by the Australia Telescope National Facility (ATNF) at Parkes is a conventional Az-El instrument and has an elevation limit of 30°. Numerous receivers are available for observations over a wide range of frequencies and, together with Hobart, the Parkes antenna provides the greatest frequency diversity available within SHEVE.

When SHEVE observations resumed in 1987, a MK-II recording system and rubidium frequency standard were installed. In 1991, a Hydrogen maser and MK-III recording system for collaborative US-Australia astrometric VLBI program (Reynolds *et al.*, 1994) were sent to Parkes and these are now available for SHEVE experiments.

It is normal practice to monitor the performance and to recalibrate the pointing whenever necessary during an observing session. This can usually be done without interfering with observations because the 30° elevation limit means that sources generally rise later (and set earlier) at Parkes than at the other antennas, leaving gaps in the Parkes schedule.

4.2.3 Hobart

The 14 m HA-Dec antenna used at Hobart for the 1982 SHEVE observations has been modified and relocated to the Mt. Pleasant Observatory several kilometres north of the former site. However it has been replaced for VLBI by the main instrument at the new observatory, a 26 m diameter XY-mounted antenna (Section 3.2.2). Both instruments and the observatory are operated by the Physics Department at the University of Tasmania.

As discussed in Section 3.2.2, the XY-mount suffers from a more complicated relationship between antenna orientation and gain than the Az-El antennas that are more common in radio-astronomy. Ideally it is necessary to determine antenna gain curves as a function of HA for a range of declinations in a manner similar to that required for HA-Dec antennas. Fortunately the antenna structure is sufficiently robust that the gain decreases significantly only at the lowest elevations and highest frequencies and modelling of the antenna behaviour with only a few generic gain curves has proved sufficient for the SHEVE VLBI observations.

The 26 m antenna has an elevation limit of approximately 6° and in 1991 the drive motors were upgraded to increase the slew rates in both axes from 20 to 40°per min. The pointing performance of the antenna is accurate to about one arc-minute. Although this is becoming significant at 8.4 GHz, tests demonstrate that the computer controlled tracking is stable to within approximately 15 arc-seconds so that systematic flux variations attributable to antenna pointing errors are generally beyond the limits of detectability with the available receivers.

When SHEVE observations first commenced with the 26 m antenna in 1987 a 2.3 GHz FET receiver with an effective system temperature of 1300 Jy was used with a rubidium frequency standard. In 1989 this system was upgraded to a cooled HEMT, concentric 2.3/8.4 GHz feed receiver which was provided for geodetic observations. At the same time a Hydrogen maser frequency standard and MK-III VLBI terminal were installed. Numerous other receivers are available for use with the 26 m antenna, the major constraint for VLBI being the frequencies that can be supported by other antennas in the SHEVE array.

4.2.4 Culgoora

The Australia Telescope Compact Array (ATCA) at Culgoora consists of six 22 m Az-El antennas on a 6 km east-west baseline. The first SHEVE observations at Culgoora took place in 1988 and used antenna 5. Subsequent observations used antenna 1 until mid-1991, antenna 6 has been used exclusively since then. It is anticipated that it will be possible to use all of the antennas as a phased array in the near future.

All ATCA antennas are equipped with cooled dual-frequency HEMT receivers and feeds operating at 1.6/2.3 GHz and 5.0/8.4 GHz. The 8.4 GHz observations presented in this thesis were made using a FET receiver with a system temperature of approximately 800 Jy. The new receivers have a system temperature about half this value. A MK-II recording unit and a rubidium frequency standard provide support for SHEVE observations.

The antenna pointing is monitored as part of the regular operation of the ATCA, and it is always calibrated whenever the array is reconfigured. The pointing is generally good to within 15 arc-seconds. Modelling of the variation of antenna sensitivity with elevation as a constant has proven satisfactory. The antenna elevation limit is 12°.

4.2.5 Mopra

The 22 m Az-El ATNF antenna at Mopra was commissioned as part of the SHEVE observations that took place in November 1991. It has nearly identical receiver and VLBI instrumentation to the compact array antennas. Until the receiver upgrade at Culgoora, the Mopra 8.4 GHz system was substantially better and provided a much lower system temperature of 400 Jy.

There is no detectable variation in the antenna gain at Mopra as a function of elevation and the pointing is comparable to that of the compact array antennas. The slew rates are 40°per min in azimuth and 20°per min in elevation. The structural elevation limit of 12° is slightly lower than the limits imposed by the hills to the south-west of the antenna site.

4.2.6 Perth

The 15 m antenna at Perth is a satellite ground station operated on behalf of the European Space Agency by the Australian Overseas Telecommunications Corporation (AOTC). The Az-El mount has a 5° elevation limit and a slewing speed of 900°per minute. The antenna pointing is better than 0.5 arc-minutes rms and the variation of sensitivity as a function of elevation is dominated by the contribution due the atmosphere and is barely detectable. A MK-II VLBI system is normally used in conjunction with a rubidium frequency standard. An experimental sapphire-crystal based oscillator developed at the University of Western Australia has been successfully tested as a frequency standard for this antenna in several SHEVE observations.

In 1992 a 27.5 m Az-El antenna operated by OTC in New South Wales was relocated to the Perth site. This instrument is equipped only with a 5 GHz feed and receiver and has recently participated in SHEVE observing sessions.

4.2.7 Alice Springs

The 9 m antenna at Alice Springs is operated by the Australian Centre for Remote Sensing and is a ground station for the LANDSAT satellites. The SHEVE observations utilise the 2.3 GHz satellite receiver, which is based on ambient temperature FET amplifiers, and the system has an effective system temperature of approximately 45000 Jy. The auto-track servo system is bypassed for the VLBI sessions and the Az-El mounted antenna is controlled by a dedicated microprocessor based system.

Because of the high system temperature, it has been very difficult to detect, let alone measure, the pointing and gain characteristics of this antenna. However

being a small antenna, built to withstand slew rates in excess of 100°per min, neither of these effects are likely to be significant. A MK-II VLBI recording system and rubidium frequency standard are taken to the station whenever it is used for SHEVE.

4.2.8 Molonglo

The Molonglo Synthesis Telescope (MOST) is operated by the University of Sydney Phyysics Department and is located approximately 40 km east of Canberra. It consists of the east-west arm of the former Mills-Cross antenna and has a collecting area equivalent to a 150 m diameter antenna. The MOST operates only at a frequency of 843 MHz. Only two other SHEVE antennas, Parkes and Hobart, can readily observe at this frequency and consequently its participation in SHEVE has been limited to three observing sessions, for each of which a MK-II recording system and rubidium frequency standard were specially installed.

4.2.9 Hartebeesthoek

The 26 m HA-Dec antenna at the Hartebeesthoek Radio Astronomy Observatory (HRAO) participates regularly in numerous VLBI experiments both with SHEVE, as well as the EVN, US-Network, and geodetic sessions. Accordingly it is well instrumented and observations are possible at most frequencies supported by other antennas. The VLBI instrumentation includes both MK-II and MK-III recording systems and a Hydrogen maser frequency standard.

The antenna has a ± 6.5 hr limit on the hour angle axis and slew rates of 22 and 28°per min on the hour angle and declination axes respectively. The pointing and gain performance of the antenna are well understood.

4.3 The SHEVE Array

4.3.1 Introduction

The SHEVE array is an ad-hoc VLBI array comprised of a variety of instruments. The purpose of this section is to describe facets of the organisation and operation of the array and to explain the constraints affecting the observations presented later in the thesis. Two common observing modes are used by SHEVE. Besides the "full array" experiments with four or more antennas that are the basis of the VLBI imaging effort, numerous experiments have been conducted using just Hobart and one of the antennas at Tidbinbilla (usually DSS 45). The different characteristics and capabilities of the array experiments and these single-baseline observations are described separately below.

4.3.2 Organisation

The antennas which participate in SHEVE are owned and operated by a diverse group of institutions based both within Australia and from overseas. The primary

collaborators are the ATNF and JPL who contribute four of the observatories, the correlator and most of the VLBI recording equipment. A substantial role is played by the Universities of Tasmania, Sydney, Western Australia and the HRAO. Time is allocated on the ATNF antennas on a competitive basis in a manner typical of "national facility" instruments elsewhere. However, there is no specific funding support for the other antennas and the remainder of the array is provided through a collaborative effort by the other participants. Astronomers wishing to observe with SHEVE therefore need not only to satisfy the requirements of the AT time assignment committee, but also to contribute directly in the collaboration. This often involves assisting with the observing and/or correlation, in addition to the data analysis.

4.3.3 Frequencies

Between 1987 and 1989 all observations were made at a frequency of 2.3 GHz. The choice of this frequency was influenced mostly by the fact that, being a standard spacecraft communication band, it was available on all the antennas. Since then the provision of Hydrogen maser frequency standards at Parkes and Hobart, and the availability of more receiver-antenna combinations capable of 8.4 GHz observations, has lead to increasing use of the higher frequency. Culgoora, Mopra and Perth have only rubidium frequency standards so the observations at 8.4 GHz are restricted because the lower coherence time affects the minimum flux source that can be successfully fringe-fit (Section 4.6). At the end of 1992, the availability of the 27 m Perth antenna with a 5 GHz receiver only provided the impetus to commence observations at that frequency.

4.3.4 Array Experiments

Scheduling Constraints

Because several of the SHEVE antennas are not operated primarily as radio-astronomy research instruments and are normally involved with spacecraft tracking it is often difficult to schedule observations that utilise all the possible antennas. Typically the array observes three to four times a year with each session lasting between four and ten days. These sessions involve all the ATNF antennas and Hobart. One or more of the Tidbinbilla antennas and Perth participate though subject to their tracking commitments. It is often possible to arrange in advance for observing time at these antennas.

Although the Alice Springs antenna is involved in tracking LANDSAT for only two or three hours a day, the poor sensitivity means that it is really only useful for the strongest sources, and then only at 2.3 GHz on baselines to the more sensitive antennas. Furthermore, a significant logistical effort is required to configure and operate the Alice Springs station so it is seldom worthwhile now that the full complement of ATNF antennas is available.

Both Hobart and Hartebeesthoek are involved in geodetic VLBI experiments unrelated to SHEVE which can affect their participation. However the location of Hartebeesthoek, far to the west of the Australian array (Figure 4.1), constitutes

a far more severe restriction on its ability to contribute because of the limited mutual visibility. Nevertheless, where the sources are sufficiently far south that they can be tracked by the Australian antennas for long enough, Hartebeesthoek makes a sensitive and valuable contribution.

UV-Coverage

The locations of all the SHEVE sites are are shown in Figure 4.1. Examples of the *uv*-coverage achievable with the array can be found accompanying the images in Chapter 5. The minimum fringe spacings achievable on all SHEVE baselines at both 2.3 GHz and 8.4 GHz are presented in Table 4.2.

Figure 4.1: Locations of the antennas that participate in SHEVE.

The five sensitive antennas located in eastern Australia provide a reasonably uniform *uv*-coverage for most sources with minimum fringe spacings of 20 mas and 5 mas at 2.3 GHz and 8.4 GHz respectively. However because these antennas lie almost on a north-south line, there are few observations for which *uv*-tracks cross, making accurate *a priori* calibration imperative. The spacing of these eastern antennas is such that for sources north of declinations around -30° the *uv*-tracks are so close to being equally separated that the synthesised beam possesses severe grating-type sidelobes (for example Figures 5.3 and 5.4).

In addition to improving the achievable resolution by a factor of two, the antennas at Perth, and to a lesser extent Alice Springs (because of its relative insensitivity), serve to fill out the *uv*-coverage in the east-west direction and provide numerous crossing points in the *uv*-plane thereby facilitating improved relative calibration of the eastern antennas. With minimum fringe spacings of less than 3 milli arcseconds, the intercontinental baselines to Hartebeesthoek provide the highest resolution available for southern objects. However the absence of any antennas with baselines intermediate between Perth and South Africa leads to large unsampled holes in the *uv*-plane and consequently difficulties in the imaging process.

The small number of antennas (6 in a typical experiment) means that there are few closure relations available for use in imaging. This, combined with the limitations of the *uv*-coverage, means that the SHEVE array is not amenable to a 'snapshot' observing mode. Imaging experiments generally comprise long scans of target sources separated by observations of strong compact objects which serve the dual function of being good fringe finders at the correlation stage and enabling relative calibration of the antenna gains.

	DS43	DS45	DS42	PRKS	HOBT	CULG	MOPR	PRTH	ALSP	HART
DS43				26.7	8.8	13.0	16.0	2.4		0.8
				19	52	58	41	151		63
DS45				26.8	8.8	13.0	16.0	2.4		0.8
				49	133	147	104	386		160
DS42				26.8	8.8	13.0	16.0	2.4		0.8
				49	133	147	104	386		160
PRKS	98.3	98.5	98.4		6.7	22.8	35.4	2.4		0.8
	17	56	43		110	122	87	321		133
HOBT	32.5	32.5	32.5	24.8		5.3	5.7	2.4		0.8
	48	161	125	119		329	233	863		359
CULG	47.7	47.7	47.7	83.7	19.4		63.6	2.3		0.7
	35	117	91	87	250		258	957		398
MOPR	58.9	59.0	58.9	130.2	21.0	234.0		2.4		0.8
	35	117	91	87	250	183		677		281
PRTH	8.8	8.9	8.8	9.0	9.0	8.5	8.7			0.9
	102	337	262	249	718	524	524			1043
ALSP	13.9	13.9	13.9	15.6	11.1	15.8	15.8	13.7		
	375	1244	968	919	2652	1936	1936	5562		
HART	2.8	2.8	2.8	2.8	2.9	2.7	2.8	3.5	2.9	
	35	117	91	87	250	183	183	524	1936	

Table 4.2: SHEVE baseline resolutions and sensitivities. The upper quantity in each entry is the minimum fringe spacing in milli-arcseconds for that baseline and the lower quantity is the minimum detectable correlated flux in mJy for a two minute integration ($5\Delta S_{ij}$ from Equation 4.1). The figures in the lower triangle are for 2.3 GHz while those in the upper are for 8.4 GHz.

Sensitivity and Imaging Capability

The noise in either the real or imaginary component of a visibility on an interferometer baseline is given by

$$\Delta S_{ij} = \eta_b \sqrt{\frac{T_i T_j}{2\Delta t \Delta \nu K_i K_j}} \tag{4.1}$$

(Walker, 1989) where the T_i and K_i are the system temperatures and sensitivities of each antenna and Δt and $\Delta \nu$ are the integration time and pre-detection bandwidth respectively. The factor η_b accounts for various losses in the recording and processing system and is ~ 2 for MK-II VLBI data. The value of $5\Delta S_{ij}$ has been calculated for all SHEVE baselines using an integration time of 2 minutes and a 2 MHz bandwidth and is given in Table 4.2. Clearly, correlated fluxes of the order of 100 mJy are readily detectable with good signal to noise ratios on all the baselines between the eastern Australian antennas.

The longer baselines to the ESA 15 m antenna are approximately a factor of three less sensitive and to be useful require stronger sources with a significant proportion of their flux in compact components. Table 4.2 also demonstrates the limited usefulness of the Alice Springs antenna for any but the strongest objects.

Despite the sensitivity constraints imposed by Perth and Alice Springs, the greatest impediment to high dynamic range imaging with SHEVE is the limited *uv*-coverage with its concomitant high sidelobes in the synthesised beam. Typical dynamic ranges (ratio of image peak to peak in residual map) are of the order 50 : 1, though for some far southern objects with long *uv*-tracks, images with dynamic ranges exceeding 100 have been produced.

4.3.5 Single-Baseline Surveys

As a full SHEVE imaging experiment requires a great deal of organisation, coordination and personnel at all stages it is only feasible to run three or four such sessions each year. It is therefore desirable to make preliminary observations with a single baseline to survey sources for the presence of compact structure suitable in intensity for imaging with the full array. Single baseline observations of several hours duration are capable of providing a wealth of information about the gross structure of sources and constitute an economic and efficient means of surveying a large number of objects, despite the inherently limited *uv*-coverage.

Short periods of time (6 to 24 hours) are often available on one of the antennas at Tidbinbilla, and whenever possible, these are utilised by forming a single baseline interferometer with Hobart which can usually be scheduled at very short notice. This interferometer is ideal for the types of test observations and surveys just described. The achievable resolution on the Tidbinbilla–Hobart baseline is sufficient to reveal the presence of structure suitable for imaging observations. Both sites are equipped with sensitive receiver systems and Hydrogen maser frequency standards allowing the detection of most objects that would be considered for imaging observations (see Table 4.2). After set-up, routine operation at Tidbinbilla is handled largely by the regular station staff, while observations at

Hobart are automated to the extent that personnel need only be present every four hours for the tape changes. The stable clocks and generally reliable systems installed at each of these observatories mean that the correlation procedures are straightforward and the subsequent analysis is standardised and simplified.

Most of the objects in the peaked spectrum sample described in this thesis were observed with this instrument at 2.3 GHz (Chapter 6). Where these data indicated the presence of complex structure, followup imaging observations were made with the full SHEVE array where time permitted (Chapter 5). The astrophysical observables are extracted from the single baseline data by the fitting of simple models to the correlated amplitudes. Short gaps in these data tend not to severely reduce the information that can be reliably obtained so a common observing mode often involved tracking two nearby sources alternately with a cycle time of 20 to 30 minutes each.

In addition to the Tidbinbilla-Hobart interferometer, two days of observations were made between Hobart and Mopra at 2.3 GHz in February 1993. While Mopra is not as sensitive as the Tidbinbilla antennas and has only a rubidium frequency standard, these data still provide useful information about the ten objects observed.

4.4 Correlation

All of the MK-II continuum VLBI data obtained with SHEVE is correlated at the CIT/JPL Block-II VLBI processor located at the California Institute Of Technology in Pasadena, California. This correlator was originally designed as a four station MK-III processor but was upgraded to process MK-II experiments with as many as 16 stations in a single pass. In production mode the correlator generates eight delay lags of 250 ns each for each baseline. In fringe searching mode 256 lags (64 μs) can be generated for up to four stations simultaneously. In both modes the correlator control computer provides an on-line display of the data from a (user) selected baseline enabling verification of correct operation. The correlator is in principle straightforward to operate, requiring a control file describing the station and source positions, scan times, the observing frequency and sideband, and the clock offsets and rates for each station. The Block-II control software accounts for the geometric delays, the effects of the motion of the observatories (due to the rotation of the earth) and of signal delay in the troposphere. The frequency offsets caused by measured clock rates can also be compensated for. The correlator output consists of the data for each lag coherently averaged for two seconds.

Although the Block-II correlator is routinely used for the processing of large US-Network experiments, there are several features of SHEVE that conspire to make the procedure considerably more difficult. When SHEVE observations resumed in 1987 only two of the stations, Tidbinbilla and Parkes, had antennas at the same locations as for the 1982 experiment. Consequently extensive effort was required with each of the new stations to determine accurate positions. The *a priori* positions, obtained through conventional surveying methods, were often accurate to little better than 100 m. A number of the rubidium standards used at

the stations since 1987 had substantial frequency offsets relative to the maser at Tidbinbilla (up to $\sim \pm 7\mu$s per day). Several of the MK-II data formatters were antiquated and prone to causing discontinuities in the times recorded on the tapes of several microseconds as often as several times daily. Furthermore, the positions of numerous southern radio sources were not known with the few-arcsecond accuracy needed to achieve correlation within the accessible lag windows. Because the correlator lag window is only two microseconds wide in production mode, the margin for error in any of the timing or position parameters is stringent and extensive fringe searching campaigns, often involving measurements every few hours throughout multi-day experiments, were required before correlation could be successfully accomplished. A computer program, written by John Reynolds, was used to analyse the residual fringe delays and rates determined in the fringe searching to refine the uncertain station positions prior to production correlation.

Since 1987 the formatting and recording equipment at most stations has been progressively upgraded leading to more reliable and consistent performance and data quality. The poorest of the rubidium frequency standards have been replaced as the Hydrogen masers became available at Parkes and Hobart and the availability of GPS receivers has facilitated the accurate monitoring of the clock behaviour during the experiment itself. The station positions are now all determined with accuracies better than 1 m and the advent of astrometric VLBI programs (*e.g.* Russell *et al.* 1994 and Reynolds *et al.* 1994), together with the commencement of operation of the Australia Telescope Compact Array, has lead to substantial improvement in the source position uncertainties. As a consequence, correlation of the more recent SHEVE experiments is considerably simplified and is a relatively routine procedure compared with effort required for the earlier data sets.

The Block-II correlator host computer (a VAX/VMS system) produces output PCR files (Post-Correlation Records) amounting to some 15 Mbytes per hour. Because of the way the MK-II tape playback units are interfaced to the processor, several baselines are correlated more than once simultaneously, leading to redundancy in the PCR files. The Caltech VLBI package program B2FITS reads these files and selects the best data (in terms of the number of valid bits used in calculating the correlation coefficients) from each baseline for each source and two second interval. Thus reduced in volume, these data are written to a FITS format file suitable for importing into AIPS.

4.5 Fringe Fitting

Fringe fitting of SHEVE data has all been undertaken within the NRAO AIPS data analysis software system and has utilised the global fringe fitting algorithm (Schwab and Cotton, 1983) as implemented in the task CALIB, and more recently, FRING. Global fringe fitting is a self calibration (self-cal) technique based on the fact that the residual phase gradients are separable into station based components and satisfy closure relations around baseline triangles, thereby allowing the phase corrections for each station to be determined using all the baselines in which it participates. It is a powerful method of improving the detectability of

fringes on insensitive baselines since the phase corrections can be computed from the solutions determined on the more sensitive baselines. This is particularly advantageous for SHEVE where fringes between the weaker antennas may not be detectable were it not possible to solve for the rates and delays using the more sensitive Tidbinbilla and Parkes baselines for that station. Because the solutions are determined from all baselines involving a given station, global fringe fitting also provides a means for ensuring the correct application of residual delays and rates during the amplitude nulls caused by source structure on a baseline, thereby enabling more stringent limits to be imposed on the depth of those nulls. Since it is a phase self-cal method, global fringe fitting requires a rudimentary model to predict the astronomical component of the phase on each baseline, and also the absolute source position is lost because the instrumental phase for one (reference) station is set arbitrarily to zero.

4.6 Oscillator Coherence

An important concept in the detection of fringes and coherent integration of VLBI data is that of coherence time. Phase noise, introduced primarily by the frequency standards used at each station, but also by propagation effects, causes a loss of amplitude when the data are coherently integrated. Coherent integration is a practical necessity in VLBI, both to achieve an adequate signal to noise ratio and to reduce the data volume to manageable proportions, so it is important to be able to quantify the extent of the amplitude reduction due to phase incoherence. Ultimately phase noise limits the sensitivity of an interferometer by imposing an upper bound on the coherent integration time beyond which no further improvement in signal to noise ratio is achieved.

An estimate of the coherence time τ_c of an interferometer pair is the time for which the rms phase error is one radian,

$$2\pi\nu\tau_c\sigma_y(\tau_c) \simeq 1 \tag{4.2}$$

where ν is the observing frequency in hertz and $\sigma_y(t)$ is the two-sample Allan variance (see, for example, Thompson *et al.*, 1986, sec. 9.4). To characterise the coherence behaviour of the frequency standards used in SHEVE observations it is important to obtain the Allan variance from the data before it is fringe fit since global fringe fitting, being a self-cal technique, modifies the phases and can mask the effects of poor oscillator coherence. To this end a program was developed to read the data from strong compact sources before fringe fitting, and to solve for and remove the phase gradients due to the residual *delays*, and then average together the separate frequency channels. These averaged data were then used to compute the Allan variance. The top panels of Figure 4.2 illustrate examples of these calculations for two representative SHEVE experiments at 2.3 GHz in November 1988 and 8.4 GHz in November 1991 using data from unresolved or barely resolved sources showing strong fringes. The line $(2\pi\nu\tau)^{-1}$ plotted on each graph emphasises the broad variation in the quality of the different frequency standards, particularly at 8.4 GHz where the Mopra rubidium standard has a

coherence time of only a few seconds compared with the masers which are good to more than ten minutes.

In an attempt to quantify the losses due to poor coherence, Rogers and Moran (1981) defined the following coherence function for an integration time T

$$C(T) = \left| \frac{1}{T} \int_0^T e^{i\phi(t)} dt \right| \tag{4.3}$$

where $\phi(t)$ is the phase difference measured between the two stations. While numerical evaluation of this expression provides a direct measurement of the coherence losses, it reveals nothing about the extent of the loss incurred in the unavoidable two second coherent average performed by the correlator. However for the regime in which σ_y is proportional $\tau^{-0.5}$, corresponding to the first several hundred seconds in Figure 4.2, Rogers and Moran showed that

$$< C^2(T) >= \frac{2(e^{-aT} + aT - 1)}{a^2 T^2} \tag{4.4}$$

where $a = 2\pi\nu^2\tau\sigma_y^2(\tau)$. The results of evaluation of this expression for each of the baselines in Figure 4.2 is presented in the middle panels of that figure. The losses after two seconds of coherent integration are negligible for all except the DSS43–MOPRA baseline in the 1991 8.4 GHz experiment, for which the amplitude reduction is nearly seven percent. For experiments in which such severe coherence losses were evident, the above measurements were made at several times throughout the experiment to ensure that the effects were consistent and would not constitute a source of time dependent calibration errors. With only one exception this proved to be the case, the exception being the November 1991 experiment for which the Mopra system exhibited two different and clearly defined modes. One mode is shown in the figure and the second mode is similar to that shown for Culgoora in the same experiment.

The residual delays and rates which fringe fitting is intended to remove change slowly with time and best results are obtained when the solutions derived from the data are smoothed over tens of minutes. However many instrumental and propagation induced phase errors occur on comparatively short timescales (tens of seconds) and it is advantageous to follow the fringe fitting with another phase self-cal stage to align the phases. Since oscillator introduced phase errors are station dependent, their effect can be substantially diminished by this step, provided always that the fringes are detected in the self-cal solution time (usually 15 or 20 seconds). In fact this procedure arrests the coherence losses completely at about three to four percent for the worst stations for averaging times beyond about twice the solution time. The lower panels of Figure 4.2 show the results of evaluating the coherence function (Equation 4.3) using the same data as for the other panels, this time *after* the final phase self-cal stage. To minimise coherence losses the solution interval should be as short as possible. However care must be taken that it is long enough to achieve a detection, otherwise the losses due to coherent integration can vary as a function of signal to noise ratio. Tests with SHEVE data, made by comparing coherent and incoherent averages of the same

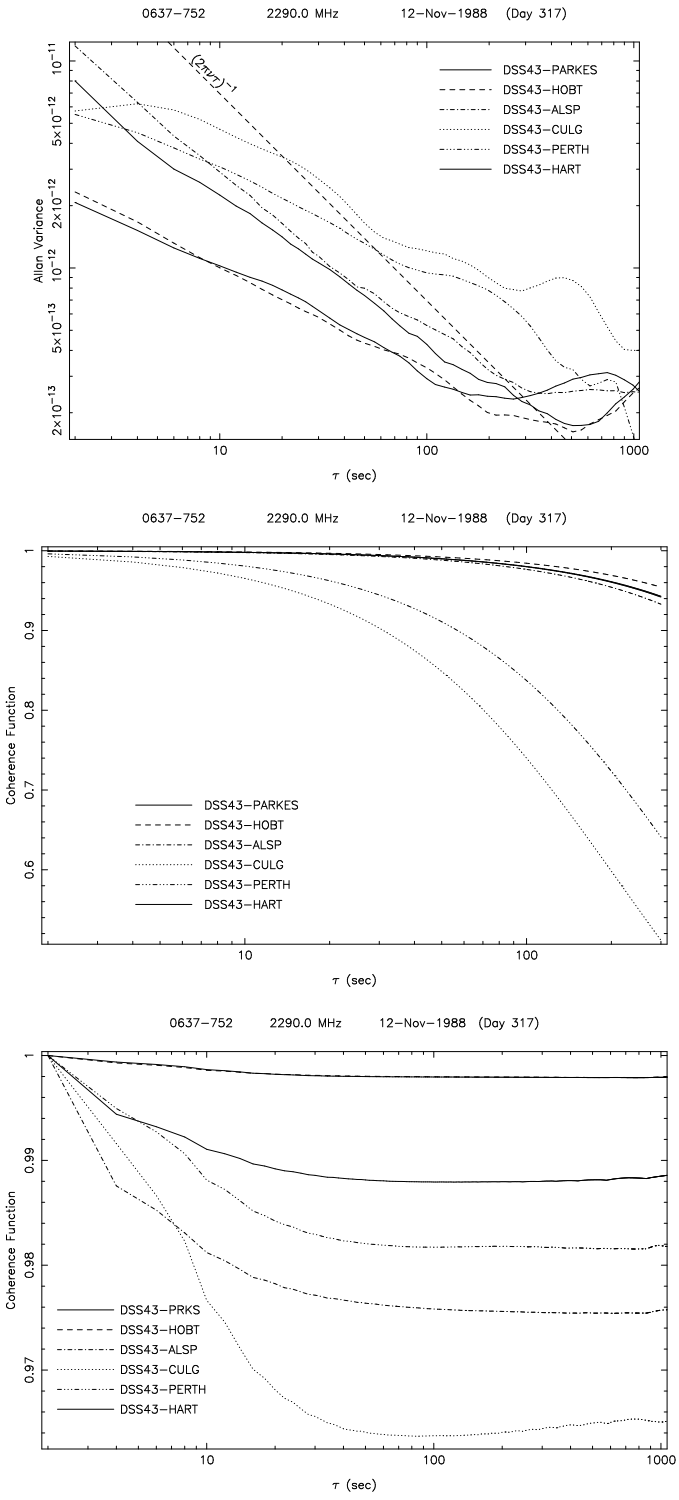

Figure 4.2: Examples of the performance of frequency standards in two SHEVE experiments at 2.3 GHz (this page) and 8.4 GHz (next page). The top panels show the Allan variance for each baseline involving DSS 43 derived from the correlator output before fringe fitting. The diagonal dashed line labelled $(2\pi\nu\tau)^{-1}$ intersects the Allan variance curves at the nominal coherence time τ_c defined by Equation 4.2. The middle panels show estimates of the coherence function computed from Equation 4.4 using the data in the top panels as described in the text. The lower panels show values of the Equation 4.3 evaluated on the data after it has been fringe fit and self calibrated.

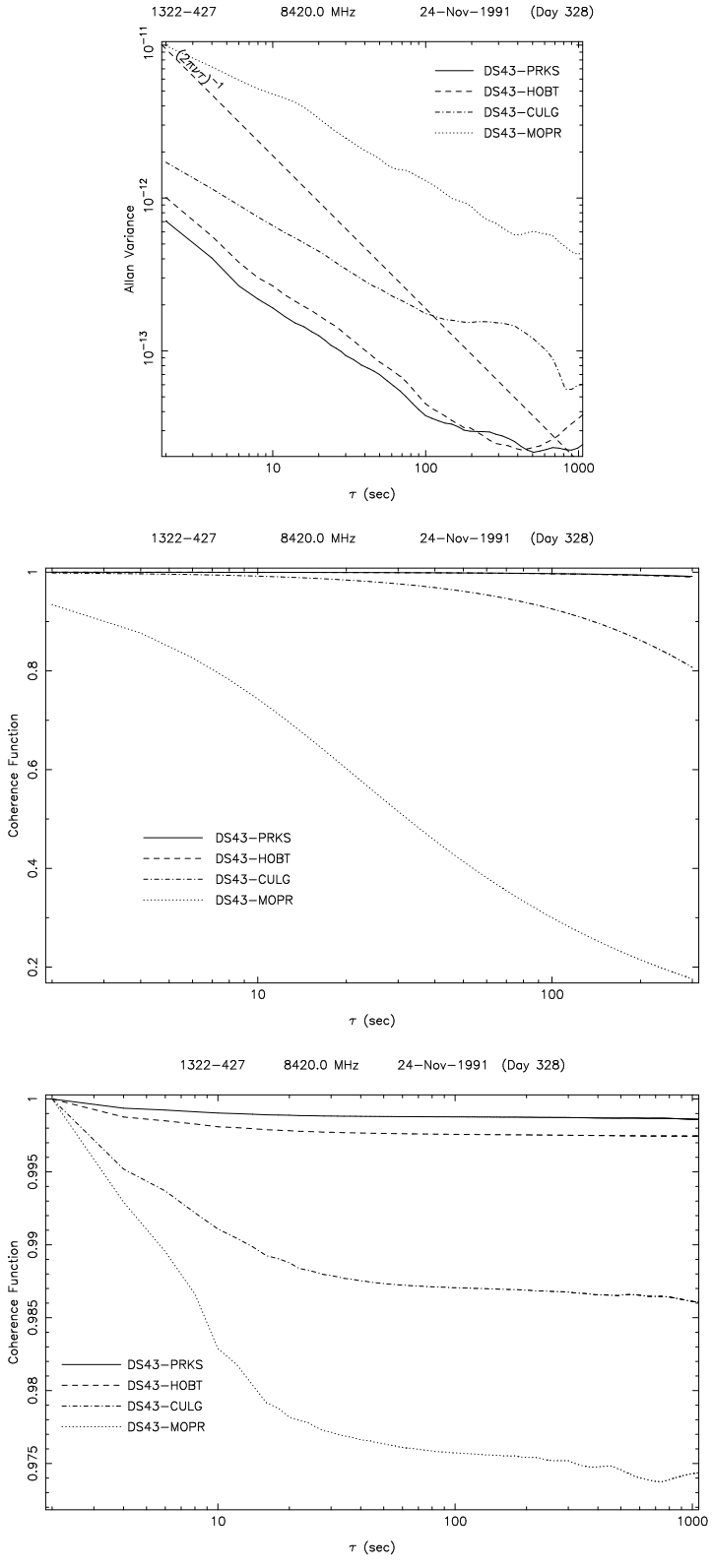
1322−427 8420.0 MHz 24−Nov−1991 (Day 328)
Allan Variance
10^{-11}
10^{-12}
10^{-13}
$(2\pi\tau)^{-1}$
DS43−PRKS
DS43−HOBT
DS43−CULG
DS43−MOPR
10
100
1000
τ (sec)
1322−427 8420.0 MHz 24−Nov−1991 (Day 328)
Coherence Function
1
0.8
0.6
0.4
0.2
DS43−PRKS
DS43−HOBT
DS43−CULG
DS43−MOPR
10
100
τ (sec)
1322−427 8420.0 MHz 24−Nov−1991 (Day 328)
Coherence Function
1
0.995
0.99
0.985
0.98
0.975
DS43−PRKS
DS43−HOBT
DS43−CULG
DS43−MOPR
10
100
1000
τ (sec)

two-second visibilities, demonstrate that the onset of this effect is sudden and that it only becomes significant at the very low signal to noise ratios where the data are of such dubious quality that they would normally be discarded anyway.

Since the correlation coefficients output from the correlator are coherently averaged for an interval of two seconds, any residual fringe rate present in the data, manifesting as a continuous winding in phase, will lead to a loss of fringe amplitude. The estimate of the fringe rate determined by the fringe fitting procedure enables a correction to be applied to the data to compensate for this effect. The finite number of delay lags produced by the correlator means that the measured cross-correlation function approximates the true cross-correlation well only if the fringes are centred in the lag window. A further correction, dependent on the residual delay, is applied to correct the fringe amplitudes when the separate frequency channels (corresponding to the lag-domain bins) are averaged. Although small for low residual rates and delays, both of these corrections benefit from the smoothing of the delay and rate solutions.

4.7 Post-Fringe Fit Processing

The data for each source are fringe fit separately and the resultant dataset is exported from AIPS and converted to the MERGE file format recognised by the programs of the Caltech VLBI package which was used for all subsequent analysis. This processing involves the editing and averaging of the data, calibration, model fitting and imaging analysis. The calibration is discussed in the next section while the model fitting and imaging procedures are described in the next two chapters.

All available information, including both the station logs from each experiment and the logs from the correlator, are used to rigourously exclude any data that may have been corrupted by equipment malfunction, antenna slewing delays, or the various calibration procedures performed at each station during the observations. This is done prior to the fringe fitting to minimise the potential for this largely automated procedure to be compromised by such data.

If the fringe fit data are destined for imaging, then they are normally coherently averaged for an interval consistent with the signal to noise ratio, oscillator coherence, the rapidity of variation of the visibilities and the desire to produce a dataset of a size practical for convenient analysis. Generally the coherent averaging times chosen are between thirty seconds and two minutes.

A different averaging procedure was adopted for the single baseline data obtained using the Tidbinbilla–Hobart and Mopra–Hobart interferometers. Since a single baseline provides no useful phase information and only the amplitudes were to be used in the analysis, these data were incoherently averaged. The procedure, and implications of this approach are discussed in Section 6.4.

No attempt was made to further edit the two-second data points before the averaging procedure since it would involve manually inspecting an inordinate number of points. Furthermore, the relatively low signal to noise ratio of the individual points threatens to compromise any attempt to be objective in the process. Having been carefully flagged before the fringe fitting, the averaged datasets generally

required little extra editing. Bad data was easily recognisable either as individual points that were significantly lower (more than about twice the size of the error bars) than their neighbours, or as simultaneous sections of anomalous visibilities on all baselines to a particular antenna. Very low signal to noise ratio data were rejected if the phases were random and distributed uniformly between $\pm 180°$.

The exceptionally poor phase coherence exhibited periodically by the Mopra rubidium frequency standard and LO chain during the November 1991 experiment required some modification to the above procedures to enable recovery of sufficient data. The data were first coherently averaged for ten seconds and then edited by hand. These edited data were then averaged for thirty seconds to produce a dataset of manageable size which, where necessary, was edited further prior to calibration and imaging. In this manner the worst affected data were eliminated before the second average, thereby permitting retention of a much greater proportion of the total dataset.

4.8 Calibration

Ideally calibration of a VLBI array should require only the application of corrections to compensate for the attributes of each of the individual antenna and receiver elements. However, in practice, the procedures used at each antenna to determine these corrections will differ so that extra effort must be expended to ensure consistency amongst the different baselines. Furthermore the gain of the instrument as a whole must be determined to allow the measurements to be expressed as correlated flux densities consistent with an external, or absolute, flux density scale. The techniques used to perform these calibration steps with SHEVE are described here.

4.8.1 A priori Calibration

The raw correlation coefficients produced by the correlator and subsequent processing have amplitudes dependent upon not only the fringe visibility, but also the sensitivity of the various receiver systems used at each station. The expression relating the correlated flux S_{Cij} to the correlation coefficient ρ_{ij} on baseline $i-j$ for a source with total flux S_T is (Cohen *et al.*, 1975)

$$S_{Cij} = b\rho_{ij} S_T \sqrt{\frac{T_{Si}}{T_{ai}} \frac{T_{Sj}}{T_{aj}}} = b\rho_{ij} \sqrt{\frac{T_{Si}}{g_i} \frac{T_{Sj}}{g_j}} \tag{4.5}$$

where T_s and T_a are the system and antenna temperatures respectively, g is the antenna sensitivity or gain (T_a/S_T), and b is a factor characterising the recording system, correlator and fringe-fitting software and is discussed further in Section 4.8.3. For an unpolarized source the antenna gain is

$$g = \frac{\eta A}{2k_B}$$

where η is the antenna efficiency, A the area and k_B is Boltzmann's constant. The antenna efficiency η normally depends on elevation or hour-angle in a regular and

repeatable manner and it is convenient to separate the contributions to the gain as a product of a normalised (with respect to the zenith) polynomial describing this dependence, and a constant factor, the degrees per flux unit (DPFU).

Calibration of the correlation coefficients therefore consists of monitoring the system temperatures at each station during the observations and the determination of the gain polynomials. The calibration program in the Caltech package (CAL) implements Equation 4.5 and applies the gain polynomials, DPFU factors and system temperature data. Originally the program accepted the system temperatures tabulated as a function of time for each antenna and performed a linear interpolation when values were required between measurements. At most antennas the system temperature is only measured at the beginning and end of scans, and hourly in between, so there is potential for erroneous values severely affecting the calibration over periods of an hour or more. This was a significant problem in several of the earlier SHEVE experiments for which the calibration procedures at some stations were then unrefined and prone to generating noisy system temperature measurements. The CAL program was modified by David Meier to accept a low-order polynomial describing the variation of the system temperatures as a function of elevation or hour angle in a manner similar to the antenna gains. A separate program was written to determine the polynomial coefficients by means of a least-squares fit to the system temperature measurements. This permitted the application of calibration data that varied smoothly with time and which reflected the underlying trends in the measurements rather than point to point fluctuations. A potential disadvantage of this method is that it assumes a symmetric variation of system temperature about the meridian. In practice the data usually exhibited such symmetry, however where significant differences between rising and setting were apparent either the original measurements were used directly, or polynomials were fit to the two segments separately and used to generate smoothed measurements that were applied as tables. A progressive improvement in the accuracy and reliability of the calibration techniques at each station has meant that the individual system temperature polynomials for each experiment are rarely necessary for the more recent SHEVE imaging experiments, the tabulated measurements proving satisfactory.

For a small number of the single baseline experiments between Tidbinbilla and Hobart little or no calibration data were available at one of the stations due to either failure or unavailability of equipment. The collection of system temperature polynomials determined in other experiments permitted the recovery of much of this data through the application of a system temperature curve for a source at a nearby declination which reflected a similar variation to that which would be expected for the source for which no data were available. This method compensates only for the variation of system temperature as a function of antenna elevation or hour angle but does not necessarily calibrate the data to the correct flux scale. If no calibration measurements at all were available for Hobart then it was usually possible set the scale to within about ten percent by using a system temperature value determined from the most recent flux monitoring observations of that source (Chapter 3). At Tidbinbilla the procedure was less certain, depending on

the weather, since rain falling on the exposed cassegrain feeds caused system temperatures to fluctuate between experiments, and because of the greater sensitivity of the Tidbinbilla antennas these fluctuations were generally more important.

4.8.2 Internal Calibration

Before the data from several baselines can be combined and used for imaging or model fitting, it is essential that all data are calibrated to a common flux scale internally consistent within the VLBI array. However the procedures for determining the system temperatures and antenna gains vary from station to station and some differences between antennas are inevitable. All the methods used to obtain estimates of the relative gains of the antennas are based on the assumption that the observed visibilities $V_{ij,obs}$ can be factorised, in the absence of noise, into terms representing the the true visibilities $V_{ij,true}$ and the individual antenna gains g_i so that

$$\frac{V_{ij,obs}}{V_{jk,obs}} = \frac{g_i g_j V_{ij,true}}{g_j g_k V_{jk,true}} = \frac{g_i V_{ij,true}}{g_k V_{jk,true}}.$$

A traditional means of achieving correct internal calibration of a VLBI array is to use the ratios of the calibrated visibility amplitudes at points in the uv-plane where two tracks with a common antenna cross to determine the difference in scaling between the other two antennas since the visibility amplitudes must be equal at such points. Unfortunately this approach is of little value with SHEVE because, being a predominantly north-south array, the only crossing points almost always involve either Alice Springs or Perth as the common antennas and since these are insensitive stations the visibilities tend to have a low signal to noise ratio and are of limited usefulness.

A second method relies upon the property of unresolved sources that they should yield the same correlated fluxes on all baselines simultaneously, thereby obviating the need for crossing points. This technique is not as robust as the crossing point method since it is necessary to know *a priori* that the objects used are indeed unresolved, there being no means of testing this independently. Furthermore, there are few strong sources which are not at least partially resolved by the longest VLBI baselines.

Two criteria were used in selecting sources for this purpose. First, with the best possible *a priori* calibration, the visibility amplitudes were required to be constant with time, indicative of a point source, and not more than about twenty percent lower (the largest plausible calibration error) on the longest baselines. Secondly the closure phases were examined for any evidence of source structure; it should be noted that this test is not as stringent as the first since, although unresolved sources must have zero closure phases, the reverse is not necessarily always true. Once it has been established that a source meets these criteria the ratios of each antenna scale with respect to all others can be determined by using different pairs of baselines, each with a different antenna in common. If for a given pair of antennas these ratios are equal, to within the limits set by the noise

intrinsic to the data, for several different baseline combinations then this is further evidence that the source is unresolved on the baselines concerned.

Three sources which meet these criteria, at least within the Australian baselines, are 0537−441, 1610−771 and 1921−293. These objects have proven satisfactory internal calibrators for the antennas in Australia at 2.3 GHz and 8.4 GHz. Typically the scatter in the corrections computed for pairs of stations using different baseline combinations and these sources is about five percent, and it rarely exceeds ten percent. At 2.3 GHz 0537−441 begins to show evidence of structure to Hartebeesthoek and has a fringe visibility (S_{corr}/S_{total}) of approximately 0.6. However, by assuming that this visibility reduction progresses uniformly with increasing baseline length, it has still been possible to use this object to derive corrections accurate to within about ten percent for Perth since the intercontinental baselines are nearly four times as long as the longest within Australia. At present there are no objects known that are unresolved to Hartebeesthoek (Preston *et al.*, 1989) and calibration of that station relies entirely upon accurate *a priori* calibration. A small number of other objects are unresolved on the baselines in eastern Australia and provide a useful crosscheck on the corrections computed from the primary sources.

The third means of estimating the relative gains of the SHEVE antennas is that of amplitude self-calibration used in hybrid mapping (for example, Cornwell and Wilkinson (1981)). This method is applicable only when the imaging procedures have reached an advanced stage and a good model of the source is available. As such it is useful as a further gauge of the accuracy of the *a priori* calibration and the scaling factors derived from the unresolved sources as described above. Typically the self-cal gain corrections were found to be less than five percent and only very rarely do they exceed ten percent. By combining the consistent correction factors calculated from imaging several sources in a single experiment, it is possible to refine the antenna flux scales so that they have a relative accuracy better than five percent.

4.8.3 External Calibration

The internal calibration of the SHEVE array is carried out carefully to ensure that the antenna gains are all set to a scale consistent with a particular reference antenna, usually one of the Tidbinbilla antennas. Provided the *a priori* calibration of this antenna is correct, the correlated fluxes obtained with the array will be tied to an external flux scale. The present flux scale was set through single-dish total flux density observations of 0915−118 and 1228−126 (Hydra-A and Virgo-A) (Klein and Stelzried, 1976) at both Tidbinbilla and Parkes. Flux density measurements of secondary objects using these antennas demonstrate agreement to within one percent (Reynolds, 1993, private communication).

Despite this apparent accurate calibration, several strong sources, including 0022−423, 0237−233, 0537−441, 0823−500, 1549−790, 1921−293 and 1934−638 exhibit fringe visibilities on the short baselines exceeding unity by as much as twenty percent at both 2.3 GHz and 8.4 GHz. This problem has persisted throughout all the SHEVE experiments undertaken since 1982 and is indicative of a scaling

error common to all the data. The most likely cause of the effect is the use of an incorrect value for the b-factor in Equation 4.5. This quantity is experimentally determined and for the Block-II correlator and fringe fitting in AIPS the accepted value has been 13.53. However two recent MK-II observations, one with the VLBA, and another with an interferometer comprising DSS 45 and DSS 43, both suggest that this value is significantly in error and that it is too large by a factor of between ten and twenty percent (Reynolds, 1993, private communication).

The procedure for deciding an appropriate b-factor for the SHEVE observations involves consideration of the errors in the visibilities contributed by both the total flux densities and the correlated flux densities. As stated above, the independent flux density measurements from Parkes and DSS 43 are in close agreement. The program source flux density measurements were obtained at either Parkes or Tidbinbilla during the VLBI experiments so any intrinsic variability should have negligible effect upon the visibility calculations, provided of course that the objects are truly unresolved so that the VLBI and total fluxes are indeed equal. However the relative error in the calibration of the VLBI stations is of the order of five to ten percent so it is reasonable to expect scatter of this magnitude in the visibilities of several sources, all of which are unresolved. After examination of the fringe visibilities for all of the strong sources a scaling factor of 0.85, corresponding to a b-factor of 11.50, was chosen and applied to the entire SHEVE data set. This value results in most observations of the objects without significant VLBI structure (0537−441, 1921−293, and 0237−233 on the short baselines) yielding fringe visibilites within three percent of unity. After this scaling no object has a fringe visibility in excess of 1.05, the highest being 1934−638 at 2.3 GHz from the November 1988 experiment with a value of 1.05, consistent with the estimated accuracy of the internal calibration of the array.

The flux scale of Klein and Stelzreid (1976) is calibrated to that of Baars and Haartsuijker (1972) which is the same as that of Baars *et al.* (1977) over the range of frequencies of interest. Therefore the overall calibration of the SHEVE correlated fluxes is believed to be accurate to within about five percent on the flux density scale of Baars and Haartsuijker and consistent at this level with observations obtained with other instruments.

4.9 Acknowledgements and Author's Contribution

The brief description of the experiment and procedures given in this chapter belies the immense amount of painstaking work that is involved at each stage. The SHEVE experiment is obviously a large undertaking involving many people and it is appropriate in a thesis such as this to outline the author's contribution to the project. I have been involved in all stages of the data acquisition, reduction and analysis process. In particular, I was responsible for the organisation and support of practically all SHEVE observations at Hobart between 1988 and 1992, including all the single baseline experiments in addition to the imaging. I implemented the

automatic antenna control and calibration procedures at the Mt. Pleasant Observatory. I gratefully acknowledge the generous contribution made by numerous fellow graduate students in assisting with the operation of the observatory during the long imaging experiments. Special thanks are due to Dave Jauncey, John Reynolds and Tasso Tzioumis for supporting the Tidbinbilla and Mopra ends of the single baseline observations.

During four visits to the Jet Propulsion Laboratory, totalling in excess of ten months, I played a central role in the correlation of SHEVE data including fringe searching and determining the positions of new stations, Whilst big contributions to SHEVE correlation and fringe fitting have been made by Don Hoard, Dave Meier, John Reynolds, and Tas van Ommen, I was personally responsible for the processing of at least ninety percent of the data presented in this thesis, in addition to a substantial volume of data which does not appear here. The overwhelming weight of responsibility for the calibration of SHEVE has fallen on the shoulders of John Reynolds. Nevertheless I was responsible for calibration of all the single baseline experiments and have also been closely involved in the calibration of several of the large experiments and am familiar with all the procedures used. The imaging and model fitting presented in the next two chapters is entirely my own work.

Chapter 5

VLBI Imaging

5.1 Introduction

Imaging provides a natural means by which to incorporate all available visibility data simultaneously in the process of reconstructing source brightness distributions. Images provide a more complete picture of source morphologies than can be derived from the fitting of models to the visibility data. Furthermore, imaging does not depend on the source actually resembling the elements from which the models are constructed and so is better able to accurately represent the true brightness distribution. Nine sources in the peaked spectrum sample have been observed in SHEVE experiments using antennas at up to seven sites in Australia and South Africa. The images derived from these visibility data are presented and analysed in this chapter.

Seven of the objects were observed at both 2.3 GHz and 8.4 GHz. The resulting pairs of images permit characterisation of the spectral properties of the different regions of the sources. This significantly constrains the models of the physical processes that give rise to the emission observed.

5.2 Methods and Analysis

Imaging Techniques

All the visibility data used to create the images were subjected to the correlation, fringe fitting, averaging, editing and calibration procedures described in Chapter 4. Images were formed using the self-calibration algorithms of Readhead and Wilkinson (1978) and Cornwell and Wilkinson (1981), and the deconvolution procedure CLEAN (Högbom, 1974), as implemented in the Caltech VLBI package. Initially most of the images were derived using the separate programs (AMPHI, INVERT, CLEAN) to perform each stage of the iterative imaging loop, as described by Pearson (1991b). However, upon the release of the difference mapping program Difmap (written by Martin Shepherd), as part of the Caltech package all the data were reprocessed and the images so formed are the ones presented here.

Difference mapping consists of a process of progressive cleaning of a *residual* dirty image, that is, the difference between the source model and the visibilities.

This differs from the usual image formation method in which the whole of the visibility data are inverted, self-calibrated and cleaned repeatedly with each (completely new) set of clean components being used in the next self-calibration stage. In difference mapping the set of clean components is built up more gradually and is used to self-calibrate the visibility data periodically as it becomes more complete. The method has the advantage that structure already cleaned no longer appears in the residual (dirty) map, so that it is possible to concentrate on the *differences* between the model and the data rather than searching for those differences in the presence of strong components. This allows considerably more control over the cleaning process since once structure due to strong unresolved components has been removed from the residual map, the clean windows can be reset to prevent further components being subtracted from those regions.

Like conventional self-calibration imaging methods, difference mapping is not a 'one-pass' technique. A sequence of iterations is usually stopped when negative clean components are found, or when clean components smaller than some experimenter-defined threshold are removed. For a good image the residual map would contain only random noise and no systematic structure. The model derived from one complete set of iterations is used to self calibrate the original data and is discarded, whereupon the process begins again. The final image from each set of iterations is constructed by convolving the clean components with a clean restoring beam in the usual way, and adding the residual map. Difmap incorporates the entire procedure, including image display, into a single program resulting in computational efficiency and great convenience. A brief description of Difmap and difference mapping can be found in Taylor (1993).

For the images presented below, the decision regarding what constituted a good final image was based on the following two criteria, that (a) the transform of the clean model must agree well with the visibility amplitudes and closure phases, and (b) that the images created by successive sets of iterations, each beginning with an empty clean model and concluding with a featureless residual map, differ only at the level of the residual noise. That is, the process must both fit the data and converge. In the case of SHEVE observations, the small number of antennas means that the final image quality is limited more by incomplete *uv*-coverage and amplitude calibration errors than by sensitivity. The residual map tends to be dominated by sidelobes caused by image reconstruction errors rather than thermal noise, as can be seen in the images of 0023−263 and 1830−211 (Figures 5.4, 5.5 and 5.18).

The imaging algorithms are not constrained to try and fit the source structure with any particular functional forms, such as Gaussians, lines and disks. Therefore the use of windows to clean only 'real' source structure is crucial, otherwise the final image is unlikely to bear much resemblance to the genuine brightness distribution. Real source structure ought not move about the image from one self-calibration stage to the next and should appear consistently in the images. By constraining the clean procedure to operate in only these regions, and keeping the regions as small as possible, the final model is less likely to contain spurious components. If the clean model contains only real structure then a natural definition for the image dynamic range is the ratio of the peak brightness in the restored image to the

maximum level of the features in the residual map. The images presented in this chapter have been contoured at a level sufficiently low to permit assessment of the magnitude of the residual noise. It is important to note, however, that although difference mapping works by subtracting the bulk of the emission from an image, and thereby focussing attention upon minimisation of the "underlying" residual noise, the residual noise is not necessarily a reliable guide to the accuracy of the on-source reconstruction which can depend on the *uv*-coverage, true brightness distribution and characteristics of the imaging and cleaning algorithms.

Measurement of Physical Parameters

The locations and sizes of the separate components in the images were obtained through the use of the AIPS program JMFIT which allows Gaussian models to be fit to the features present in the image. The program deconvolves the clean restoring beam from the fit and reports the estimates of the component size. Conway *et al.* (1992) investigated the sensitivity of the parameters derived by JMFIT to errors in image reconstruction by generating simulated data sets resembling their actual data, using specific source models. These data were then subjected to the same imaging and fitting procedures and the results compared with the original models. Although the results of such tests might be expected to vary with UV coverage, such a huge task is beyond the scope of the investigation presented here and rather than perform similar tests, only their conclusions are summarised. It was found that component positions were accurate to between five and fifteen percent of the beamwidth, depending largely upon the UV coverage. Six of the nine observations described by Conway *et al.* involved between four and six antennas, comparable to most of the SHEVE observations presented below. It is therefore reasonable to expect that the errors in parameters derived from the SHEVE images are probably similar. The relative flux densities of components were accurate between ten and fifteen percent. Component sizes are generally in error by less than twenty percent, provided they are larger than half the beam width. For components smaller than this, the size measurement depends entirely, and sensitively, on the correct amplitude calibration of the longest baselines. Many components with such small measured sizes are probably unresolved. At some level, the errors in the component parameters derived by JMFIT will depend on the applicability of Gaussians to represent the source structure. There is no *a priori* reason to expect that the sources should have a Gaussian form. The importance of this assumption is best gauged by examination of the residuals to the fit.

The total flux density of each discrete component was measured with one of the AIPS routines IMEAN or TVSTAT which calculate the flux densities within rectangular (IMEAN) or polygonal (TVSTAT) regions. These programs were preferred over JMFIT since they do not make assumptions about the source components resembling particular functional forms (such as Gaussians) and therefore are not subject to the systematic biases that can occur when an inapplicable model is used.

5.3 VLBI Observations

5.3.1 Introduction

The data presented here were obtained from five separate SHEVE experiments at 2.3 GHz and/or 8.4 GHz over a five year period from November 1988 through March 1992. Images of seven sources have been made at both frequencies, and images of another two sources have been made only at 2.3 GHz. The observations are summarised in Table 5.1. Additional low resolution images of three sources (0237−233, 1549−790 and 1934−638) were made from subsets of the data by excluding the baselines involving Hartebeesthoek. The fits of the clean component models to the amplitude and closure phase data for all except the three low resolution images are presented in Appendix B. The peak flux density, contour levels as a percentage of the peak, and the size and orientation of the clean restoring beam are shown beneath each image. The restoring beam dimensions are determined by a fit to the main lobe of the dirty beam. An abbreviated listing of the antennas participating in each observation appears at the top of each image and should be interpreted according to the following schema: D,Dt=Tidbinbilla; P,Pk=Parkes; Hb=Hobart; Cg=Culgoora; M=Mopra; A=Alice Springs, Pr=Perth; E=Hartebeesthoek. Preliminary 2.3 GHz images using these data for 0237−233, 1549−790 and 1934−638 have been published by Murphy *et al.* (1993). However the images presented here represent a new and independent analysis of these data.

Source	Epoch	Freq. (GHz)	Duration (hours)	No. of Ants.	Max. Baseline $M\lambda$	Dynamic Range	AF	Figure Ref.
0022−423	89.93	2.29	10.75	5	73.6	70:1	1.43	5.1
0022−423	91.90	8.42	13	5	39.1	45:1	1.07	5.2
0023−263	91.34	2.29	11.5	5	10.5	60:1	2.16	5.4
0023−263	91.90	8.42	11	5	29.9	40:1	1.19	5.5
0237−233	88.86	2.29	11	7	75.2	90:1	1.34	5.6
0237−233	88.86	2.29	11	6	24.2	100:1	1.96	5.7
0237−233	91.90	8.42	10	5	38.0	45:1	0.95	5.8
0823−500	89.93	2.29	11	4	13.3	80:1	2.19	5.9
1151−348	91.34	2.29	11.75	4	10.7	70:1	1.62	5.10
1151−348	92.24	8.42	11	5	30.3	35:1	1.28	5.11
1245−197	91.34	2.29	11.25	4	10.2	75:1	1.29	5.12
1245−197	92.24	8.42	10.5	5	29.1	35:1	1.06	5.13
1549−790	88.86	2.29	9.5	7	75.2	120:1	1.31	5.14
1549−790	88.86	2.29	9.5	6	24.2	115:1	1.64	5.15
1549−790	91.90	8.42	11	5	29.2	85:1	0.99	5.16
1830−211	91.34	2.29	11.5	4	10.3	25:1	5.62	5.18
1934−638	88.86	2.29	15.5	7	75.2	35:1	1.87	5.19
1934−638	88.86	2.29	15.5	6	24.2	40:1	2.53	5.20
1934−638	91.90	8.42	13.5	5	35.11	60:1	1.45	5.21

Table 5.1: Observations and images presented in this chapter. Epochs are expressed as years since 1900. The dynamic range indicates the ratio of the peak brightness in the image to the peak in the residual map. The agreement factor (AF) is the reduced χ^2 of the clean component model with respect to the visibility data and quantifies the extent to which the model represents the data (6.2.2). Entries in the last column refer to the figure in which each image appears.

5.3.2 0022−423

The source 0022−423 is a magnitude 20.6 (V) galaxy with a redshift of 0.661 (Wall and Peacock, 1985). The 2.3 GHz and 8.4 GHz images in Figures 5.1 and 5.2 show the simple double structure of this source. The phase self-calibration used in the imaging process means that the absolute positions of the components in the two images are unknown. However the relative positions are accurate and since at both frequencies the two components are separated by 28 mas at a position angle (PA) of -62°, it is reasonable to assume that they are identified with one another. The 2.3 GHz data includes baselines with Perth and Hartebeesthoek and has a resolution comparable to that of the 8.4 GHz image, although in a nearly orthogonal direction.

Table 5.2 gives the results of the Gaussian model fits to the two images. Component A is unresolved at 8.4 GHz and is resolved at 2.3 GHz in the east-west direction only. The 2.3 GHz image shows that component B is extended towards the east and the Gaussian model, which was fit only to the western part of the component, also indicates that the component is well resolved in the east-west direction but not in the north-south direction. It is unresolved at 8.4 GHz. All the model components are roughly aligned with the overall PA of the source, though for the 8.4 GHz image this may reflect the alignment of the restoring beam with the extended source structure rather than the components themselves.

The two components, including the extension of B, contribute 3.0 Jy of the total 2.3 GHz flux density of 3.1 Jy so any structure not seen in this image must be very weak. Similarly the total flux density at 8.4 GHz (1.0 Jy) is almost completely accounted for by the 0.95 Jy in the image. These results are consistent with the absence of emission on the few-arcsecond scale at 5 GHz reported by Morganti *et al.* (1993). Assuming that the flux densities have not changed significantly in the two years between these two observations, the spectral indices of both components are found to be very similar (Table 5.2). If the extended structure seen in B at 2.3 GHz is omitted from the calculation, then the spectral index of the compact component is even closer to that of A.

In both images there is evidence of some weak emission lying directly between the two strong components. However the relative positions differ in the two images and these features are not stable between successive mapping iterations. The two images have been convolved with larger restoring beams to search for bridges or cores in this region but nothing reliable was found.

Component	Frequency (GHz)	Flux Density (Jy)	Maj (mas)	Min (mas)	PA (°)	$\alpha_{2.3}^{8.4}$
A	2.3	2.209	3.76	0.68	-67	-0.86
A	8.4	0.726	3.49	0.85	-63	
B	2.3	0.764	5.40	1.14	-54	-0.93
B	8.4	0.228	2.94	1.73	-29	

Table 5.2: Gaussian fitting of 0022−423.

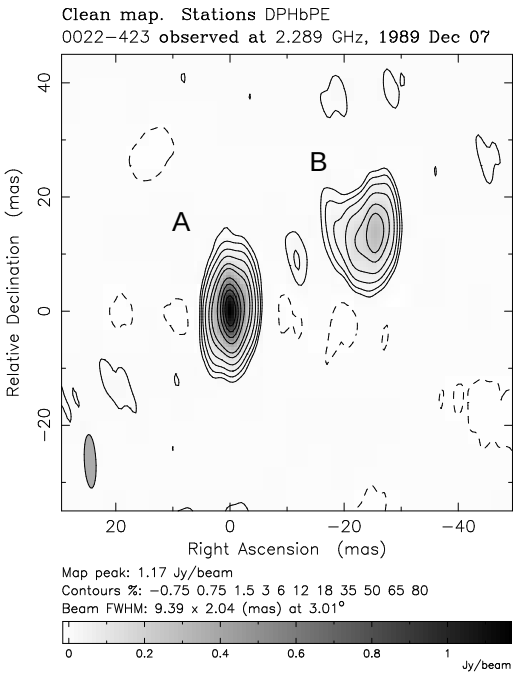

Figure 5.1: 2.3 GHz image of 0022−423.

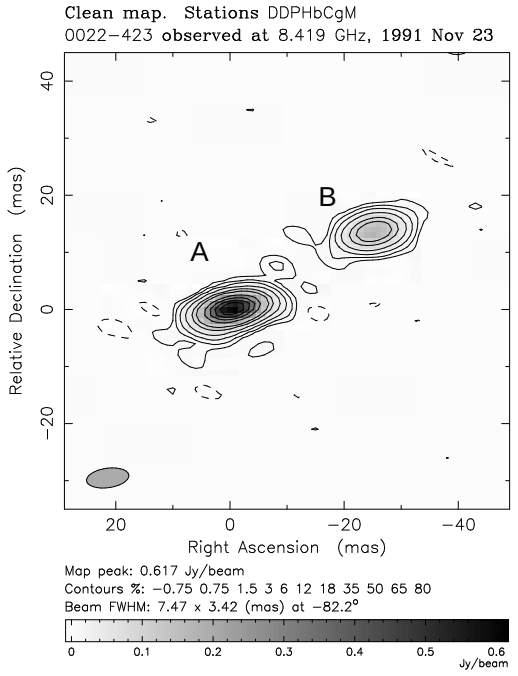

Figure 5.2: 8.4 GHz image of 0022−423.

5.3.3 0023−263

Wall and Peacock (1985) identify 0023−263 with an m_V=19.5 galaxy. The redshift is 0.322 (Tadhunter *et al.*, 1993). Both of the images, presented here in Figures 5.4 and 5.5, show the basic double structure of the source, and also show that neither of the components is simple. At a declination of -26°, the *uv*-coverage obtained from the eastern Australian array comprises a series of almost equally spaced tracks (Figure 5.3) that result in large regularly spaced sidelobes in the dirty beam, making deconvolution difficult. Traces of these sidelobes are visible as arcs in the low level contours and grey-scales of both images. Consequently all the features in the images away from the two main components are most probably artifacts. In the discussion below the *compact* part at the north of the north-west component (at 2.3 GHz) is referred to as A, and the south-east component is component B, and is comprised of B1 and B2 as shown on the images.

The angular separations of A and B1 are 655 mas at 2.3 GHz and 652 mas at 8.4 GHz. The position angle of A relative to B1 is -34° at both frequencies. The spacings and position angles of B2 relative to B1 are 33 mas and -37° and 31 mas and -52° at 2.3 GHz and 8.4 GHz respectively. The differences in these values are easily accommodated, given the different resolutions and signal to noise ratios, allowing the three components seen at one frequency to be unambiguously associated with the three at the other.

Gaussian models were fit to each of the components at both frequencies; the parameters of the resultant models are shown in Table 5.3. The fit to B2 at the high frequency was unreliable and only the integrated flux density is shown in the table. Component A is slightly resolved in the north-south direction at both frequencies. The extension seen at 2.3 GHz is almost absent in the 8.4 GHz image, some asymmetry just being visible. Since A is so marginally resolved, little weight should be attributed to the apparently orthogonal orientations at the two frequencies. The two components in B are quite distinct and the Gaussian models fit the data well at the lower frequency. B1 is probably unresolved while B2 is well resolved and has angular dimensions 38×23 mas. Both B1 and B2 are substantially weaker in the 8.4 GHz image and are certainly resolved at this resolution. The misalignment of B1-B2 compared with B-A is approximately 18° at the high frequency and could indicate that component B is the terminus of a jet with B1 and B2 hotspots (shocks?) caused by the disruption of the jet.

Within the calibration uncertainties (five percent), components A and B1 have the same spectral index (∼-0.5). In contrast B2 has a very steep index of -2.1, though the low signal to noise ratio means that this value is very uncertain (±50%). The total 2.3 GHz flux density of the whole northern component (including both A and the extension) is 1.62 Jy and is denoted in the table as A′. Similarly, the entire southern component has a comparable flux density of 1.22 Jy. The sum of these, 2.84 Jy, is only about forty percent of the total flux density (7.1 Jy). Although the difference between A and B1+B2 is much greater at 8.4 GHz the ratio of VLBI flux density to total flux density is almost identical at both frequencies. Evidently the substantial extended structure not seen in either of these images has a similar spectral index to the components that are visible here.

A 5 GHz MERLIN image of this object, with a resolution of approximately 100 mas, shows the presence of a bridge of emission lying between the two compact components (Muxlow *et al.*, private communication). However low resolution images, made by convolving the VLBI data here with larger restoring beams, give no indication of this structure. The absence of any structure on few-arcsecond scales (Morganti *et al.*, 1993) suggests that all emission in this object originates either in, or between, the two compact components.

Component	Frequency (GHz)	Flux Density (Jy)	Maj (mas)	Min (mas)	PA (°)	$\alpha_{2.3}^{8.4}$
A	2.3	1.349	12.1	10.4	-46	-0.58
A	8.4	0.638	5.27	4.42	45	
B1	2.3	0.354	18.7	5.08	52	-0.52
B1	8.4	0.180	17.3	9.95	59	
B2	2.3	1.134	37.8	22.8	-8	-2.11
B2	8.4	0.074				
A′	2.3	1.622				
B	2.3	1.223				

Table 5.3: Gaussian fitting and component flux densities of 0023−263. The flux densities of B1 and B2 at 2.3 GHz are derived from the Gaussian model fits because they are too close to each other to accurately measure with IMEAN or TVSTAT. The last three lines of the table give flux densities obtained by integrating components that were not amenable to fitting with JMFIT (explained in the text).

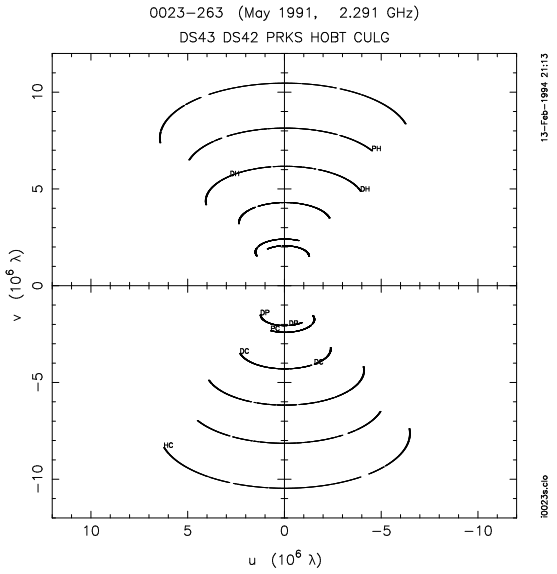

Figure 5.3: 2.3 GHz *uv*-coverage of 0023−263.

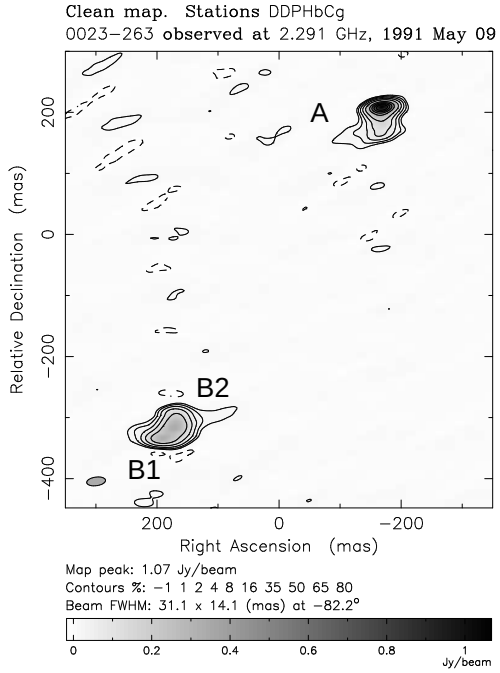

Figure 5.4: 2.3 GHz image of 0023−263.

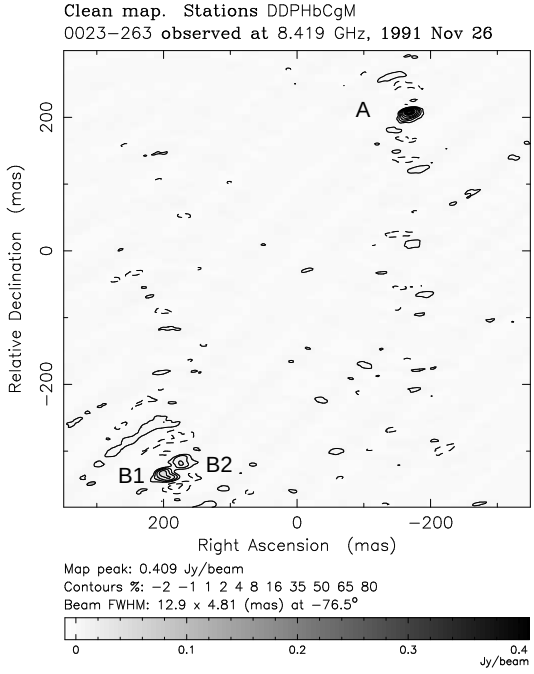

Figure 5.5: 8.4 GHz image of 0023−263.

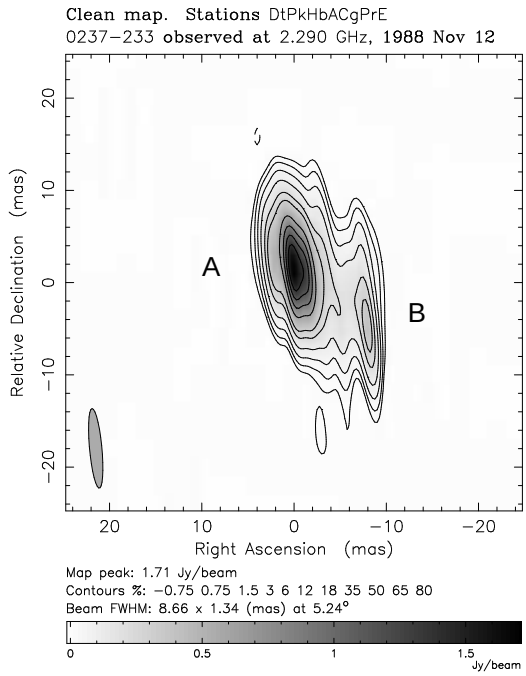

Figure 5.6: 2.3 GHz image of 0237−233 including the Hartebeesthoek baselines.

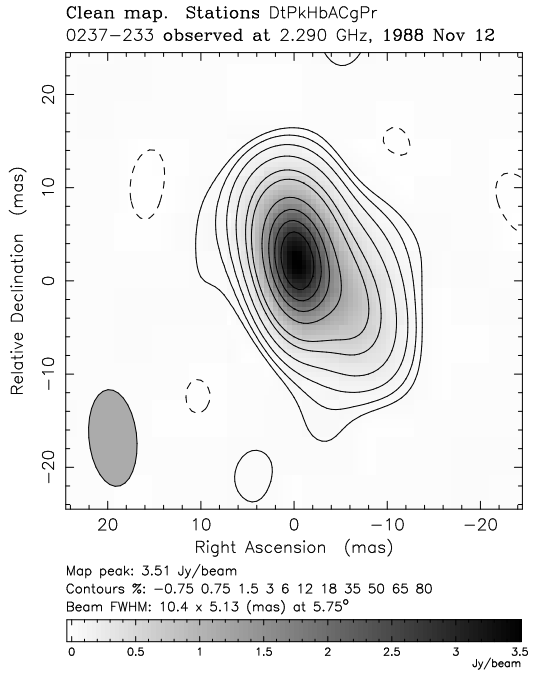

Figure 5.7: 2.3 GHz image of 0237−233 without Hartebeesthoek data.

5.3.4 0237−233

The redshift of the m_V=16.6 quasar 0237−233 is 2.223 (Burbidge and Burbidge, 1969). Three images were made of this object, two at 2.3 GHz with and without the South African baselines (Figures 5.6 and 5.7), and one at 8.4 GHz (Figure 5.8). The source is clearly a very compact double at both frequencies. The separations and relative position angles of the two components are 9.3 mas and 52° at 2.3 GHz, and 9.9 mas and 53° at 8.4 GHz. The difference between the two 2.3 GHz images clearly demonstrates the value for some sources of the extra resolution provided by Hartebeesthoek. The lower resolution image only indicates the presence of some extension towards the south-west of the otherwise unresolved source, and does not show that this structure is due to a distinct component, as can be seen in the full resolution image. Although the image in Figure 5.6 has a dynamic range of 100:1, some significant imaging artifacts are visible in the image as elongated structures running in a north-south direction between the two main components. The clean component model fits the visibility data very well (AF=1.34) but fitting Gaussian models to the *visibility* data (a technique described in detail in Chapter 6) shows that the source can be adequately represented with only two components. This false structure is more likely to result from difficulties associated with properly deconvolving the dirty beam (there is a large hole in the *uv*-coverage between the Australian and South African baselines) rather than calibration errors.

The results of the Gaussian model fits to the components in the full resolution 2.3 GHz image and the 8.4 GHz image are listed in Table 5.4. At 2.3 GHz component A is just resolved in only the south-west direction. The component is better resolved at 8.4 GHz where it has an angular size of 5.5×3.0 mas and a similar orientation (within 20°) to that found at 2.3 GHz. The south-west component B is unresolved at the high frequency and probably is at 2.3 GHz also.

The high and low resolution 2.3 GHz images have total integrated flux densities of 5.22 Jy and 5.16 Jy respectively, values which bracket the total flux density of 5.17 Jy measured with the 70 m antenna at Tidbinbilla during the experiment. The integrated flux density of the 8.4 GHz image is 2.59 Jy compared with the approximate measured total flux density of 2.4 Jy. Clearly all the emission in this object comes solely from the two milli-arcsecond size components seen in these VLBI observations. This result is consistent with VLA observations at 1.4, 1.6, 5.0 and 23 GHz that show no evidence of structure on scales from about 100 mas to several arcseconds (Stanghellini *et al.*, 1990a).

The 2.3 GHz emission is dominated by the steep spectrum ($\alpha = -0.7$) component which contributes more than seventy percent of the total flux density. However the very compact component B with a spectral index of +0.6 contributes almost half the flux density at the high frequency. Component B is thus likely to be a compact core separated from the more diffuse component A. The difference in component separation (0.6 mas) detected between the images at the two epochs is not sufficient to claim a detection of relative motion since it is less than half the maximum resolution achieved by the *uv*-coverage and furthermore, because the images are at different frequencies, the unknown spectral dependence of the morphology means that it is not possible to align the components with any

certainty.

Component	Frequency (GHz)	Flux Density (Jy)	Maj (mas)	Min (mas)	PA (°)	$\alpha_{2.3}^{8.4}$
A	2.3	3.758	4.15	1.93	47	-0.70
A	8.4	1.52	5.45	2.96	66	
B	2.3	0.490	6.14	1.30	13	0.60
B	8.4	1.07	0.00	0.00	–	

Table 5.4: Gaussian fitting of 0237−233. The 8.4 GHz flux densities are from the model fitting, not integration. However their sum is equal to the total flux density found by integrating the whole source, and the models fit the data very well, so the values are probably reliable.

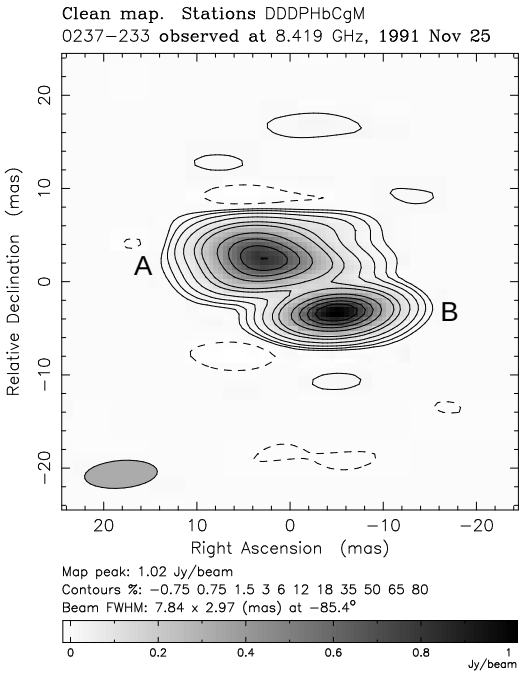

Figure 5.8: 8.4 GHz image of 0237−233.

5.3.5 0823−500

This object has a very pronounced peak in its spectrum near 2 GHz but unfortunately there is no optical identification. Only a 2.3 GHz image (Figure 5.9) is available from the SHEVE observations to date. No emission is apparent apart from the two simple components. The double structure is resolved on all but the shortest baseline (Appendix B) and shows that the two components have an angular separation of 24 mas at a position angle of -56°.

The results of Gaussian fits to the two components, designated A and B as shown in the figure, are listed in Table 5.5. The resolution of both components

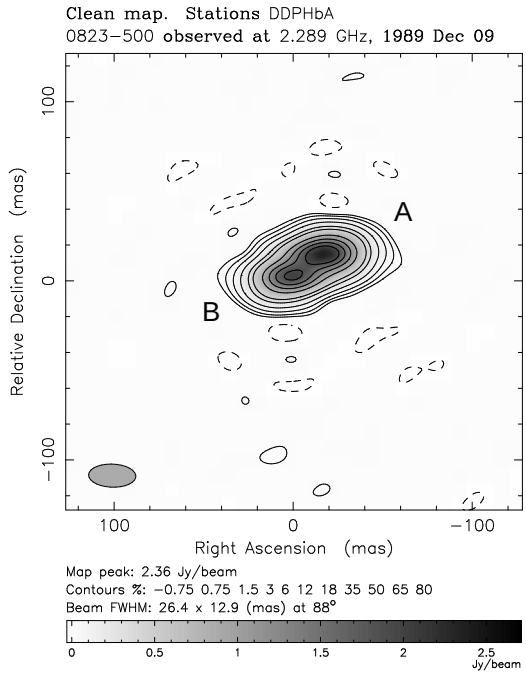

Figure 5.9: 2.3 GHz image of 0823−500.

is marginal and depends mostly upon the longer baselines involving Alice Springs that are relatively insensitive and difficult to calibrate accurately. Consequently component sizes are not very reliable. Both components appear to be aligned with the overall position angle of the double structure. However these measurements are very uncertain and really more resolution is needed, either from observations at a higher frequency, or involving the Perth antenna.

The integrated flux density of the two components is 5.75 Jy, three percent less than the total flux density of 5.95 Jy so there is unlikely to be any extended emission associated with this object. The components A and B contribute to the total flux density in ratio 3:2. The absence of any observations at other frequencies prevents determination of any spectral properties of the components in this source.

Component	Frequency (GHz)	Flux Density (Jy)	Maj (mas)	Min (mas)	PA (°)
A	2.3	3.56	17.5	10.6	-72
B	2.3	2.23	10.7	7.5	-69

Table 5.5: Gaussian fitting of 0823−500.

5.3.6 1151−348

The radio source 1151−348 is identified with an $m_V = 18.0$ quasar having a redshift $z = 0.258$ (Jauncey *et al.*, 1978). The 2.3 and 8.4 GHz images (Figures 5.10

and 5.11) show two components, labelled as A and B, with a relative position angle of 72° and an angular separation of 91 mas. At the high frequency the two components are distinct. However there appears to be a weak bridge of emission running between them at 2.3 GHz. The reality of this feature was investigated by convolving the image with smaller restoring beams to test for the presence of extensions between the main components. These images show that there is indeed some weak extended structure present, however not at a level that can be regarded as convincing. Other images, made at the same resolution as the one presented here, do not show the bridge at the same level but do indicate the extension in the south-west of component A. Although the clean component model is a good fit to the data (Appendix B), further processing with tighter clean windows may give a better indication of how real this bridge actually is; in the interim it should be regarded with some suspicion.

The results of fitting Gaussian models to each component at both frequencies are listed in Table 5.6. At 2.3 GHz both A and B are slightly resolved along the north-south dimension. This becomes more pronounced at the higher frequency with both components well resolved along position angles -27° (A) and 40° (B), or roughly orthogonal and parallel to the overall source orientation respectively. The measured component separations at the two frequencies differ by only half a milli-arcsecond, permitting unambiguous association of each 8.4 GHz component with its corresponding lower frequency counterpart, and hence, calculation of the spectral indices of each component. Component B is the steeper of the two with $\alpha = -1.1$.

At both frequencies, the milli-arcsecond components seen in these images contribute only about seventy percent of the total flux density. However, save for the tenuous bridge in the 2.3 GHz image, there is no evidence of any emission on larger scales. Morganti *et al.* (1993) find the source unresolved when observed at 5 GHz with the VLA (resolution 3 arcseconds). Using the total flux densities at the low and high frequencies (4.6 and 1.8 Jy respectively) and assuming that the structure giving rise to the missing flux density is homogeneous, its spectral index can be computed. This calculation yields a value of -0.7, very similar to component A, possibly indicating that the emission is simply resolved, diffuse, extensions of the components seen here.

Component	Frequency (GHz)	Flux Density (Jy)	Maj (mas)	Min (mas)	PA (°)	$\alpha_{2.3}^{8.4}$
A	2.3	2.20	14.06	9.38	-70	-0.68
A	8.4	0.909	9.07	6.38	-27	
B	2.3	1.32	17.2	14.0	-79	-1.12
B	8.4	0.310	12.5	8.9	40	

Table 5.6: Gaussian fitting of 1151−348.

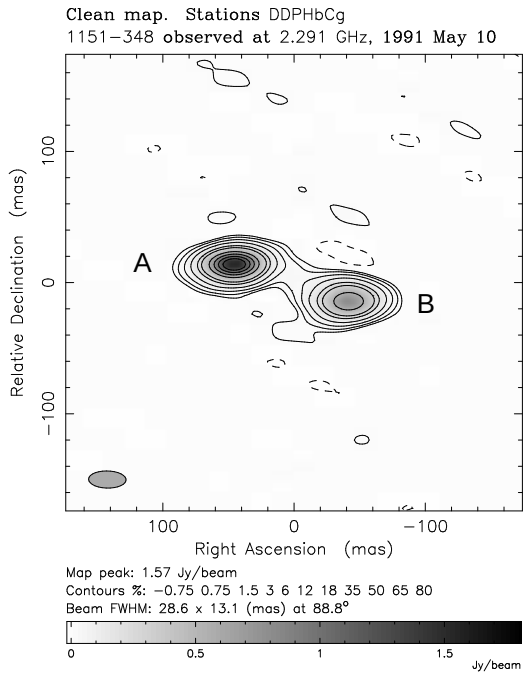

Figure 5.10: 2.3 GHz image of 1151−348.

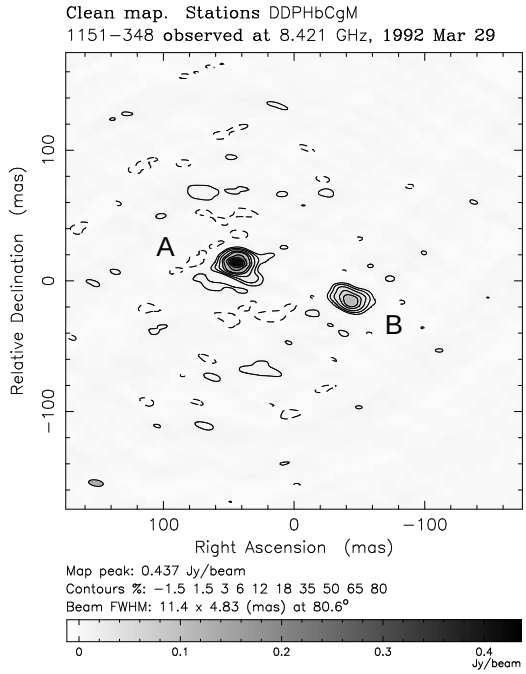

Figure 5.11: 8.4 GHz image of 1151−348.

5.3.7 1245−197

With $z = 1.275$ (Mantovani *et al.*, 1992), 1245−197 has the highest redshift of any of the galaxies in this survey. The digitised UK Schmidt plate (from the COSMOS database, Yentis *et al.*, 1992(1992)) gives the J magnitude as 21.6. The 2.3 GHz SHEVE image (Figure 5.12) shows two distinct components separated by 130 mas at position angle 88°. The stronger of the two is elongated in a north-easterly direction and there is also extension towards the north-west. Restoring the image with a clean beam one third smaller than that shown resolves the stronger component enough to demonstrate that it is composed of two very compact components, designated A1 and A2 in the figure. These are quite distinct in the higher resolution 8.4 GHz image (Figure 5.13) and have an angular separation of 17 mas at PA=55°, consistent within the uncertainties with the 19 mas and 55° measured at 2.3 GHz. Component B is very weak at the high frequency. Attempts to window only component A when cleaning the image failed to remove component B from the residual map and the fit of the clean component model is significantly improved by its inclusion, particularly on the DSS43–Hobart baseline (Appendix B). Gaussian model fits are inappropriate for this component, however the emission above the one percent contour shown in the image has a centroid lying only 5 mas to the west of the location predicted from the 2.3 GHz measurements, assuming that the components labelled A1 in each figure can be associated without ambiguity.

Component	Frequency (GHz)	Flux Density (Jy)	Maj (mas)	Min (mas)	PA (°)	$\alpha_{2.3}^{8.4}$
A1	2.3	1.311	12.5	5.8	81	-0.60
A1	8.4	0.600	5.17	3.55	67	
A2	2.3	1.726	19.9	8.90	82	-0.91
A2	8.4	0.528	16.75	4.41	70	
B	2.3	0.363	20.4	8.46	76	-1.44
B	8.4	0.056	–	–	–	

Table 5.7: Gaussian fitting of 1245−197. The flux densities for A1 and A2 at 2.3 GHz are the results of the Gaussian fitting because the two components are too close to be accurately separated for integration. The fit for component B at 8.4 GHz was unreliable and only the integrated flux density is given.

The results of the component size measurements from Gaussian fitting of all components, together with the integrated flux densities, are listed in Table 5.7. At the low frequency A1 is probably unresolved, though some extension towards B is apparent in profiles through the component in an east-west direction. The nearby A2 is certainly resolved in a similar direction. Component B is slightly extended towards the south-west but otherwise unresolved. The extension of A2 is more obvious at 8.4 GHz, but A1 may still be unresolved, although there is evidence of extension in the south-west. Despite being almost completely resolved at the higher frequency, the remnant of component B is oriented in the direction of the extension seen at 2.3 GHz.

The spectral indices of all three components are steeper than -0.5, with the flattest being the unresolved component A1 ($\alpha = -0.6$). The more extended A2, which contributes as much of the total VLBI flux density as the other two components combined at 2.3 GHz, is weaker than A1 alone at 8.4 GHz and has a steeper spectrum. The flux density of B at 8.4 GHz is uncertain and while the spectral index is very steep, the value given in Table 5.7 could be in error by as much as ± 0.8.

The sum of the flux densities of all the components seen in these VLBI images is less than the total flux density of 1245−197 at either frequency, the fractions being 85 percent and 75 percent at 2.3 GHz and 8.4 GHz respectively. In a VLBI survey at 2.3 GHz with a resolution of 2.6 mas Preston *et al.* (1985) reported an upper limit to the correlated flux density for this source of only 6 mJy, indicating an absence of highly compact structure on angular scales much smaller than those resolved by the 8.4 GHz SHEVE image. VLA observations at 5 GHz with three arcsecond resolution show no extended structure (Morganti *et al.*, 1993) and Mantovani *et al.* (1992), using the same instrument and frequency with a resolution of 450 mas, report 96 percent of the total flux density is located in an unresolved core on which they placed an upper limit on the angular size of 150 mas. It would seem therefore that the two SHEVE observations shown here cover the range of angular scales present in this object and that there is not a great deal of structure remaining undiscovered.

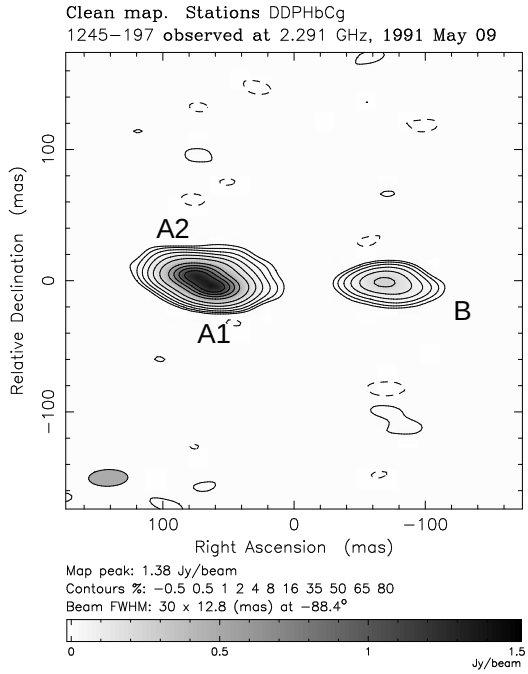

Figure 5.12: 2.3 GHz image of 1245−197.

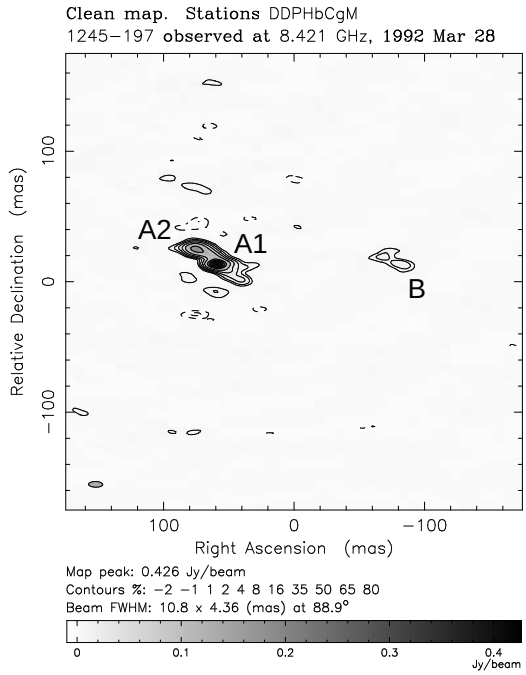

Figure 5.13: 8.4 GHz image of 1245−197.

5.3.8 1549−790

This z=0.149, m_V=18.5 galaxy (Véron *et al.*, 1990; Prestage and Peacock, 1983) has the most extended radio structure of any source shown in the SHEVE images presented in this chapter. All three images, Figures 5.14, 5.15 and 5.16, show the same overall features, comprising a strong compact component with a short extension pointing towards the north-east, and a long elongated structure at PA=120° about 80 mas further to the east. The elongated feature is much weaker at 8.4 GHz and a natural interpretation of this morphology is of a flat spectrum core with a one sided steep spectrum jet that bends through approximately 60°. Several components can be distinguished in the far-jet (beyond the bend) at 2.3 GHz and the near-jet also shows complex structure in Figure 5.14. Both jet components are either weak or resolved at 8.4 GHz and only a small remnant is visible in Figure 5.16. The image in Figure 5.15 is made from the same data as in Figure 5.14 but without the baselines involving Hartebeesthoek. The core region and extended jet are discussed separately below. The brightest part of the core in each image is designated component A1, as shown, and it is assumed that all three images can be aligned with one another at this point, that is, the core serves as a common reference point between the two frequencies and epochs.

Core and Near-jet

Considering first the lower resolution 2.3 GHz image (Figure 5.15), the core is resolved into two distinct components (A1 and A3) separated by 19 mas at position angle 64°. The results of Gaussian fits to the core components are given in Table 5.8. The strongest component, A1, appears to be resolved towards A3, but

Component	Frequency (GHz)	Flux Density (Jy)	Maj (mas)	Min (mas)	PA (°)	$\alpha_{2.3}^{8.4}$
A1	2.3	3.102	7.67	2.36	64	0.00
A1′	2.3	2.161	3.61	0.73	52	
A1	8.4	3.132	4.73	1.09	46	
A2′	2.3	0.985	5.30	3.95	-72	
A3′	2.3	0.163	10.90	6.98	89	steep

Table 5.8: Gaussian fitting of 1549−790. Components are labelled as shown in the figures and those measurements made from the high resolution 2.3 GHz image are denoted with a ′.

is unresolved perpendicular to the jet. Component A3 is resolved.

The image made by including the trans-oceanic baselines to South Africa (Figure 5.14) permits a more detailed examination of the core region and shows the very bright, and unresolved, component A1 lying at the western extremity. The fits of models to the components in this image are also listed in Table 5.8 but are distinguished there from the measurements made using the lower resolution image by a ′ (*e.g.* A1′). The near-jet, which has a peak brightness of about 25 percent that of the core, begins immediately to the east and its intensity diminishes gradually before terminating in a component identified with A3 from the lower resolution image ($\Delta\theta$ and PA relative to A1 of 20.5 mas and 62° respectively). The jet is very narrow, only becoming resolved transversely when it reaches A3.

Between A1 and A3, two uniformly spaced blobs, or ripples, can be seen in the jet. The parameters of the strongest of these, A2, are given in the table. However the reality of both these features is uncertain. The inclusion of the Hartebeesthoek data creates a large unsampled gap in the *uv*-plane between 25 and 60 Mλ, leading to substantial sidelobes in the dirty beam, so these apparent knots may actually result from a combination of the placement of the clean windows and a failure of the clean process to deconvolve the dirty beam accurately. To investigate whether or not these features are genuine, or only a consequence of the imaging procedures, models were fit to the visibility data. This approach has the advantage that simple models with basic components (such as points and lines) can often meet the demands of the visibility data by direct Fourier inversion, without the need for complicated deconvolution and self-calibration procedures, and are therefore often able to provide a more reliable, if somewhat less detailed, description of the overall source brightness distribution. The results of fitting such models to the data from baselines including the South African station (∼3 mas resolution) showed that only a single point and a linear component are needed. When the baselines between the eastern Australian antennas and Perth are added (∼10 mas resolution), a third linear component is required to account for the slight bend in the near-jet. A sequence of two or three point source model components is unable to account for the behaviour of the visibilities nearly as well so it is likely that the blobs seen in the image are artifacts or, at the very least, the near-jet is dominated by linear structures rather than knot-like components.

Another subtle indication of the care needed when interpreting these images is that although components A1 and A3 have the same relative locations in the two 2.3 GHz images (which, incidentally, have the two highest dynamic ranges of all the images presented here), the near-jet appears to kink in opposite directions between them. Convolving the high resolution image with the low resolution beam shows that this is, in part, an illusory effect caused by the emergence of the near-jet slightly to the north of A1 (rather than due east). However this does not entirely account for the difference seen and indicates that there is some uncertainty ($\sim$5 mas) in the actual position of the near-jet in the direction of least resolution (north-south).

The 8.4 GHz image (Figure 5.16) shows the core component but the near-jet is practically absent. This image has more surface brightness sensitivity than the high resolution 2.3 GHz image (almost twice the beam area and comparable antenna system temperatures) so the near-jet is not just resolved, it must have a steep spectral index. The core component is slightly elongated along PA=49° (Table 5.8), close to the position angle of the near-jet seen at the low frequency. Comparison of the integrated flux densities of the component A1 at the two frequencies shows that it has a flat spectrum; within the errors the flux densities are identical at the two epochs and frequencies. This is true for the high resolution 2.3 GHz data also, provided the flux densities of A1 and A2 are combined. Without more resolution at the high frequency, it is not possible to comment separately on the spectra of the components A1 and A2 seen in the high resolution 2.3 GHz image.

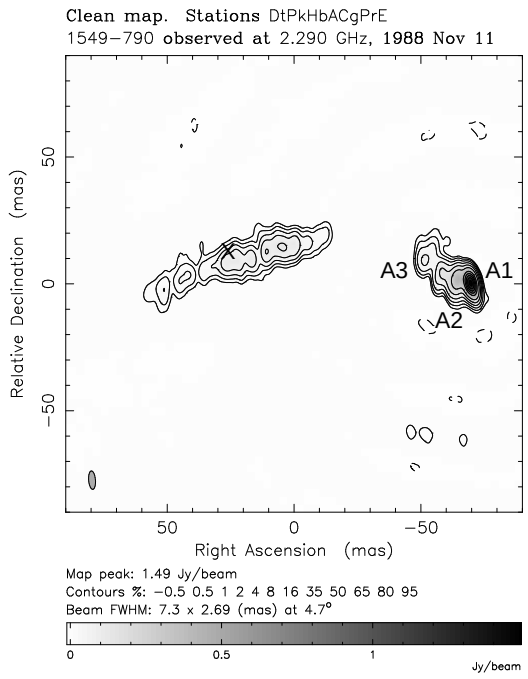

Figure 5.14: 2.3 GHz image of 1549−790. The X marks the location of the jet component seen in the 8.4 GHz image.

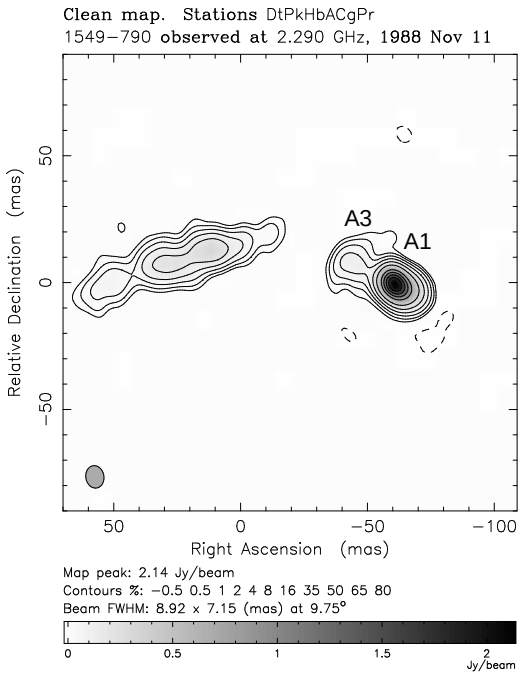

Figure 5.15: 2.3 GHz image of 1549−790 without Hartebeesthoek data.

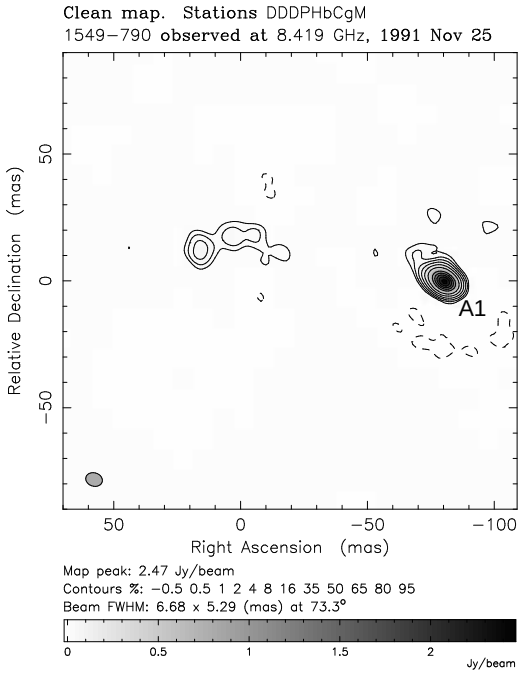

Figure 5.16: 8.4 GHz image of 1549−790.

Jet

Beyond component A3, no emission is detected in the 2.3 GHz images until approximately 20−30 mas (depending on the beam size) further east, where the long (∼80 mas) jet structure appears. The jet undergoes a bend of more than 60° towards the south whilst traversing this region where it is not detected. The absence of emission from this area indicates that the jet is either very weak, diffuse, obscured or otherwise occluded here. Unless obscuration is the cause, this suggests that there are no hotspots or tightly confined structures in the bending region so it might be reasonable to infer that the bending is caused not by collision or deflection with some entity such as the external medium, but rather by a change in orientation of the near-jet over time as the jet material is ejected. If this were the case then the apparent gap in the jet could arise from either orientation effects, or it may indicate that the core emission processes are episodic, a hypothesis possibly supported by the segmented nature of the jet.

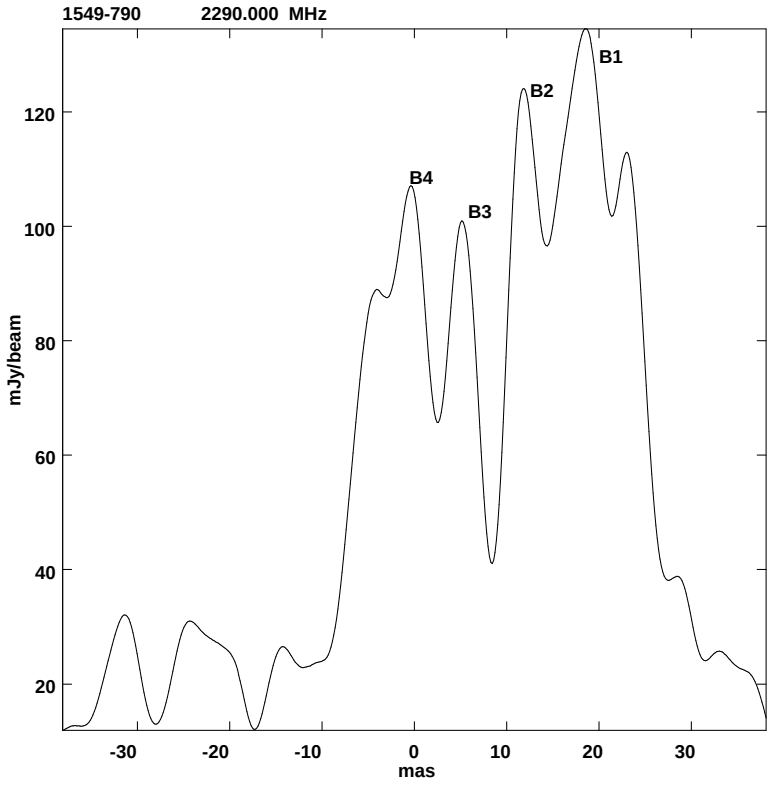

Figure 5.17: A profile of surface brightness along the length of the jet of 1549−790 at 2.3 GHz. The abscissa increases towards the west and the components B1 and B2 correspond to the two highest contours in the jet in Figure 5.14

Both of the 2.3 GHz images show the same basic structure in the jet. It is composed of three segments, each about 20 to 30 mas long, and essentially lying in a straight line. At no point along its length is the jet resolved across its width. The slight "S-bending" visible in the high resolution image cannot be considered significant given the resolution and sensitivity achieved. Less easy to discount, however, are the series of compact features located within the two

strongest jet components. These components are most clearly shown, labelled B1–B4, in Figure 5.17 which is a profile of the surface brightness along the length of the jet shown in Figure 5.14. The profile shows that, with the exception of B1, all of these features are unresolved, the restoring beam width in this direction being approximately 3 mas FWHM. It could be argued that these apparent hotspots are actually another artefact of the deconvolution process. However, examination of the visibility amplitudes on the Perth baselines (Appendix B) indicates that one or more weak components some distance from the core are present. An extension of the visibility model fitting, described above, shows that at least two point-like components lying near the axis of the jet are needed to do this, but the data do not constrain either their position or number well. Furthermore, the approximate location of the peaks seen in the image do not seem to depend on the windows used in the cleaning, although their relative strengths can vary. However more imaging tests using different tapering and weighting schemes are required to establish the reality of these components beyond doubt.

The 8.4 GHz image shows only a fraction of the jet structure visible at 2.3 GHz. Clearly the whole of the jet, including the hotspots, has a steep spectrum. The strongest component that can be seen in the jet at this frequency is well resolved and while the position of all the jet structure in the image is very uncertain simply because it is weak, the location of this component relative to A1, can be measured ($\Delta\theta$=97 mas, PA=83°). This position is marked on the high resolution 2.3 GHz image (Figure 5.14) by an X and clearly does not lie on the centre of the jet. Whether this results from uncertainties associated with the imaging procedures, or reflects either a spectral or temporal effect within the jet remains unknown. By permitting quantification of any component motion, a second epoch image of this source, at either frequency, should provide some indication of the cause of this effect. A second epoch at 2.3 GHz would also be helpful for investigating the hotspots in the jet.

The core to jet flux density ratio is almost 2:1 at 2.3 GHz and nearly an order of magnitude greater, 20:1, at the higher frequency. Nevertheless, the proportion of the total flux density contained within the VLBI structure is high (∼95 percent) at both frequencies. Therefore there is unlikely to be much diffuse emission beyond the eastern end of the jet.

5.3.9 1830−211

This strong radio source has been identified as an Einstein ring by Jauncey *et al.* (1991) but, to date, has no optical counterpart. The 2.3 GHz SHEVE image presented here (Figure 5.18) shows the compact components believed to be the two images of the core of the lensed source (Kochanek and Narayan, 1992). These two components are separated by 973 mas along position angle 42.2°. With only four antennas and a low declination, these data show severe arc sidelobes similar to those seen for 0023−263 (*cf* Figure 5.3). Strong fringes are obtained on all baselines except Hobart–Culgoora (Appendix B) so the poor dynamic range (25:1) of this image results, not from a lack of sensitivity, but mostly from difficulties associated with deconvolving the dirty beam and detecting the substantial amount

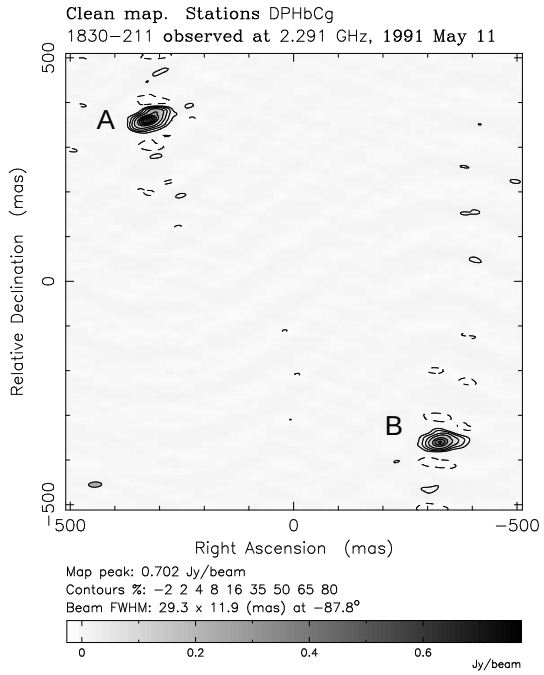

Figure 5.18: 2.3 GHz image of 1830−211.

of extended structure known to exist in this object (*e.g.* Jauncey *et al.*, 1991).

The results of Gaussian model fits to the components seen in the image, denoted A and B, are listed in Table 5.9. Both components are well resolved and have similar angular sizes of 35×13 mas and 25×17 mas. Component A is the more elongated of the two and is oriented at a position angle of -55°. Although B is more circular, it clearly has a different orientation. Comparison with the lower resolution MERLIN and VLA images presented by Jauncey *et al.*, suggests that this difference is significant and shows that the SHEVE image is sensitive to the "tails" on the compact components that merge into the lensed ring structure.

Component	Frequency (GHz)	Flux Density (Jy)	Maj (mas)	Min (mas)	PA (°)
A	2.3	1.683	34.72	12.76	-55
B	2.3	0.988	24.54	16.50	-71

Table 5.9: Gaussian fitting of 1830−211.

At the time of the observation, the total 2.3 GHz flux density of this variable source was 9.1 Jy. The sum of the flux densities in the two components is nearly 2.7 Jy, still less than thirty percent of the total. The bulk of the difference is probably accounted for by the diffuse ring structure upon the circumference of which these components lie. However, as can be seen from the fit of the clean model to the visibilities (Appendix B), there remains unmodelled approximately 0.5 Jy in structure to which these observations are sensitive. Component A has

almost sixty five percent of the flux density in the compact structure though this ratio must necessarily remain uncertain until enough time can be expended to improve the fit of the clean component model to the visibilities. Without an image at another frequency it is not possible to comment on the spectral indices of the components. In any case, the dramatic variability found in this object (Chapter 3) requires that any calculation of the spectral properties be made on the basis of measurements separated by no more than a few weeks.

5.3.10 1934−638

The compact radio source 1934-638 was identified as an m_V=18.4 galaxy by Kellermann (1966) and the redshift was first measured by Peterson and Bolton (1972). An improved redshift determination ($z = 0.183$) was subsequently made by Penston and Fosbury (1978). Each of the three SHEVE images presented here (Figures 5.19, 5.20 and 5.21) shows the same basic near-equal east-west double structure reported by earlier observers (Gubbay *et al.*, 1971; Tzioumis *et al.*, 1989). The image in Figure 5.20 is made from the same data as was used for that in Figure 5.19, but without the baselines involving Hartebeesthoek. However it has resolution comparable to the 8.4 GHz image because it includes baselines involving Perth and Alice Springs. The relative component positions from these two images are $\Delta\theta$=41.3 mas at PA=89° at 2.3 GHz, and 42.3 mas at 88° at 8.4 GHz. The higher resolution 2.3 GHz image resolves the western component into three subcomponents (B1, B2 and B3 shown in the figure). The separation of A and B2, the strongest of these, is 42.0 mas at PA=89°. Thus all three measurements agree to within a milli-arcsecond, substantially less than the resolution for the two images made using the Australian baselines only, and the measurement from the high resolution image is bracketed by the other two. The three images all show that component A is extended in an east-west direction and that component B has a nearly orthogonal north-south orientation.

Gaussian models have been fit using JMFIT to all components seen in the three images and the parameters of these fits are given in Table 5.10. Considering first the two images based upon data from the Australian baselines, all the components are resolved at both frequencies. The angular sizes at the low frequency are approximately 7×3 mas (A) and 8×6 (B). The dimensions measured at the higher frequency for component A are about 75 percent less than those at 2.3 GHz. Similarly, the size of component B is about 65 percent less at 8.4 GHz. The values obtained for the component orientations are consistent to within about 20° between the two images. The high resolution 2.3 GHz image yields almost identical parameters for component A (labelled A′ in the table) as the low resolution image.

As described above, the structure in the western component can be described by three components which are indicated in Figure 5.19. The residuals of the three-Gaussian fit to this ensemble of components are approximately ten percent of the peak brightness so the parameters derived ought to be regarded more as a guide to the component sizes and orientations rather than precise measurements. Components B1 and B2 are almost coincident (within 0.5 mas east-west) and

Component	Frequency (GHz)	Flux Density (Jy)	Maj (mas)	Min (mas)	PA (°)	$\alpha_{2.3}^{8.4}$
A	2.3	5.429	6.76	3.32	94	-1.04
A	8.4	1.409	4.83	2.40	85	
B	2.3	6.900	7.93	5.96	11	-1.28
B	8.4	1.320	5.24	3.94	32	
A′	2.3	5.300	6.13	3.14	94	
B1	2.3	1.823	4.87	1.59	-30	
B2	2.3	3.411	8.00	3.33	28	
B3	2.3	1.089	3.43	2.07	44	

Table 5.10: Gaussian fitting of 1934−638. The east component in the high resolution 2.3 GHz image is denoted A′ to distinguish it from the component measured in the lower resolution image. The flux densities of B1, B2 and B3 listed are from the Gaussian fitting and sum to 6.32 Jy, less than 1.5 percent more than the 6.24 Jy obtained by integration.

lie at the western extremity of B. Both are oriented in an approximately north-south direction and are resolved in both directions. The third component, B3, lies directly between A and B1 only 5 mas to the east of B1. It too is resolved and, although only slightly elongated, is oriented towards the north-east. Two other weak features are visible in the image in Figure 5.19, a slender component running north-south just west of component A, and a small circular lobe on the west side of B. These components were excluded from the windows used in the cleaning but their presence persisted, even after many iterations of the self-calibration and cleaning cycle. The circular component is probably an artefact caused by the more complicated deconvolution required for component B. However the elongated feature seems to be associated with a broad tongue of very weak emission present in the residuals that originates from A and extends for about 20 mas at a position angle of about -80°. The component seen here lies almost on top of a sidelobe from component A, so while it is certainly worthy of more extensive investigation, it is inappropriate to regard it as real at present.

The spectral indices of the two main components (A and B), calculated using the flux densities obtained by integration from the two images without Hartebeesthoek data, are also given in Table 5.10. They are very similar but *not* identical, with the larger component B having a significantly steeper spectrum. For the spectral indices to be the same, it is necessary to contrive errors well in excess of five percent in the flux densities of all components, and not only is this beyond our estimated calibration uncertainties (Chapter 4), but the errors need to be of opposite sign for the two components at the same frequency. Given the high signal to noise ratio in these data, the possibility of random errors of this magnitude can be considered remote. Of course with such a strong source the potential to underestimate the systematic errors associated with the imaging process is increased. However if the flux density ratios of the two components were substantially in error then the clean component models would not fit the visibilities, particularly in the amplitude maxima and minima. Examination of the data in Appendix B

shows that this is clearly not the case.

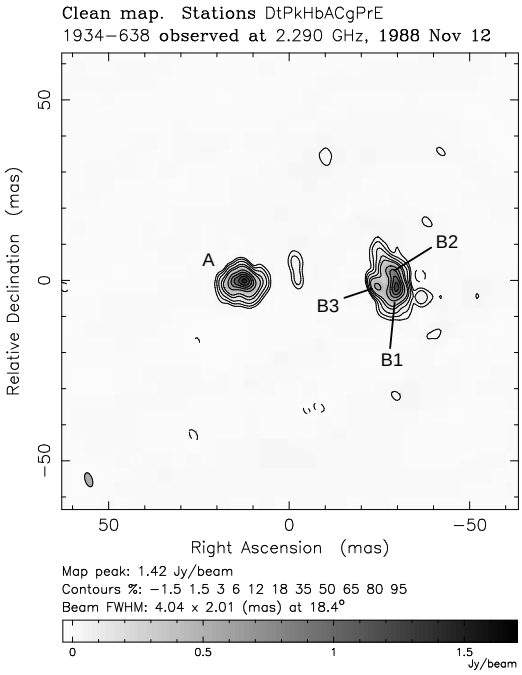

Figure 5.19: 2.3 GHz image of 1934−638.

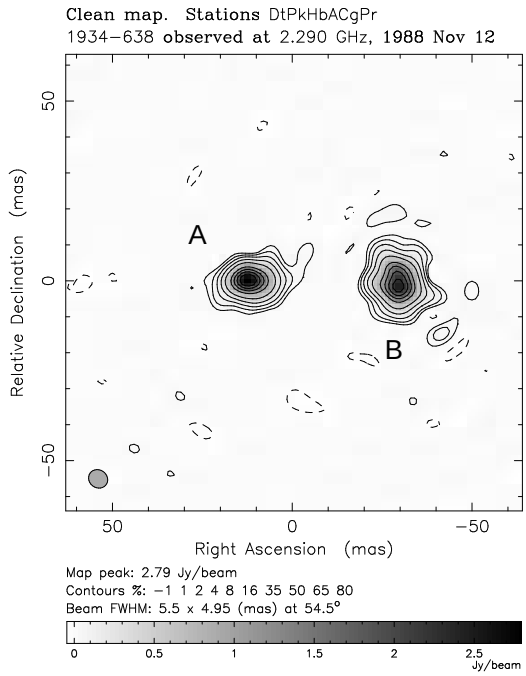

Figure 5.20: 2.3 GHz image of 1934−638 without Hartebeesthoek data.

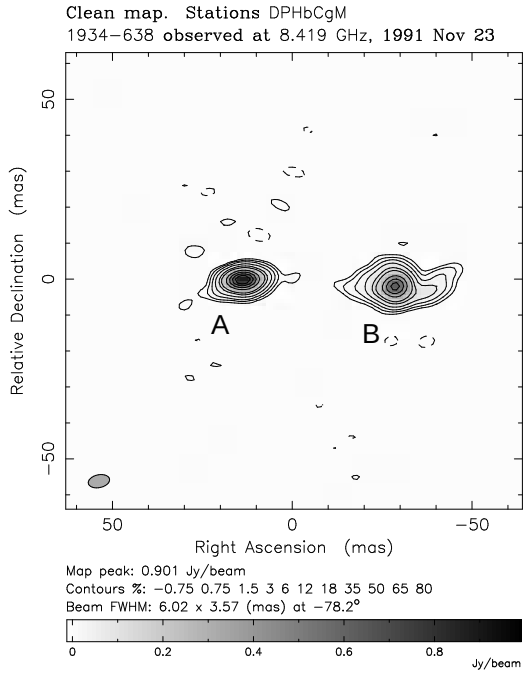

Figure 5.21: 8.4 GHz image of 1934−638.

The 2.3 GHz images contain the whole of the total flux density of 12.2 Jy while the 8.4 GHz image accounts for 88 percent of the 3.1 Jy total at that frequency. Thus these VLBI images most likely include all the structure that contributes significantly to the total emission. This source has been used as the primary calibrator for the Australia Telescope Compact Array for six years and there is no evidence for even weak emission from structure on arcsecond scales between 1.4 and 8.4 GHz.

5.4 Summary

Nineteen VLBI images of nine radio sources made from data at two frequencies have been presented and described in this chapter. With a mean dynamic range of 65:1, these images demonstrate the unique capacity of the SHEVE array, often operating with only four or five antennas, to produce useful information about the milli-arcsecond scale structure of southern radio sources. Measurements of the angular sizes and separations of components detected in the images have been made by fitting Gaussian models to the images, wherever such models are appropriate. Integrated flux densities calculated from these components have been used to calculate spectral indices and/or infer the extent and properties of any extended structure.

The objective of the discussion and evaluation of these data has been to focus upon the measurement of parameters that can be deduced from the images without the need for assumptions about underlying physical models, such as an appropriate cosmology (which permits calculation of linear sizes) or specific emission mechanisms (relevant to energy densities and magnetic fields). As such, this chapter has established a database of reliably determined source properties which are not likely to change with advances in physical understanding, but from which physical parameters can be calculated using models of current interest. Such calculations, using both these data and the other new data presented in Chapters 3 and 6, appear later in the thesis.

Chapter 6

VLBI Survey Model Fitting

6.1 Introduction

The objective of the single baseline VLBI survey between Tidbinbilla and Hobart, and later Mopra and Hobart, was to determine rudimentary information about the presence, extent and form of compact structure in as many of the sample sources as possible. Because of the substantial logistical overheads involved in the organisation, running, and correlation of full SHEVE array experiments, it is simply not practical to make imaging observations of all the sources in the peaked spectrum sample. Furthermore, when so little is known about these objects, there is little point in investing valuable array time to discover that they are either unresolved or completely resolved. However the single baseline interferometer is a reliable, convenient, efficient and effective tool with which to probe the sub-arcsecond structure of southern radio sources, both as a filter to find the objects for which imaging observations are worthwhile, and in its own right as means of investigating basic source structures.

Being only a solitary track in the aperture plane, and therefore providing a highly restricted and selective sample of the potential spatial information present, there are limits to the capability a single baseline observation has in the reliable determination of source structure. Attempts to derive the brightness distributions of sources from single baseline data by direct Fourier inversion of the visibilities are often confounded by the masking effects of the contorted beamshapes associated with such sparsely sampled data. A far more fruitful approach is to represent the radio source in the image plane by simple models which are transformed into the aperture plane and refined through direct comparison with the visibility data. However this is a potentially hazardous procedure because it permits the observer to "guess" the source structure, and also because many structures can be consistent with the same set of visibilities (*e.g.* Bracewell and Roberts, 1954). It is therefore essential that the process be governed by a set of rules which encourage the generation of simple models rather than more complex models which, because of their inherently greater capacity to accommodate the visibility data, are less likely to represent the true brightness distribution of the source.

This chapter discusses the mechanics of model fitting, sets out the rules that

were applied to control the process, and presents the single baseline survey visibility data and fits from the source models produced according to the rules outlined.

In addition to the single baseline survey, a small number of experiments were conducted between Tidbinbilla, Hobart, and one other station, either Alice Springs or Hartebeesthoek. Also, some two or three antenna data is available from the earlier less successful imaging experiments. Several of these imaging experiments, particularly in 1988 and 1989, were plagued by equipment malfunctions at two or more stations, and often the resultant data set was sparse. All of these data, which are almost as resistant to conventional imaging as are single baseline observations, were also analysed by modelling and appear in this chapter.

The success or failure of the model fitting procedures adopted below, must be judged on the basis of a comparison between the models and more complete images constructed from multi-baseline array observations. Thus a third source of data presented here derives from the Tidbinbilla-Hobart baselines of the imaging data sets that appeared in Chapter 5. These data were subjected to the same modelling procedures as the remainder of the data in this survey and, through a comparison with the full array images, demonstrate the capability of the modelling to accurately reproduce source structure (Section 6.7). Altogether, a total of 52 data sets, comprising 2.3 GHz and/or 8.4 GHz observations of 34 sources have been modelled with the procedures described below and appear here.

6.2 Methods of Model Determination

6.2.1 Inspection

The approximation of visibility data by models in the inverse Fourier domain is a non-trivial undertaking. However, armed with a basic understanding of the properties of the Fourier transform and a little experience, it is usually possible to discern from an inspection of the visibility data and *uv*-coverage some of the overall characteristics of some sources. Bracewell (1986) provides an extensive pictorial catalogue of Fourier transform pairs which is useful in the formulation of initial models. Another helpful dictionary is that of Fomalont and Wright (1974) which gives the visibilities that would be expected from a variety of one and two component models.

The types of parameters that can be estimated easily, with varying degrees of accuracy, are the orientation of solitary elongated components or doubles, the flux ratio of doubles, and sometimes the relative angular size of two components. This is possible because these characteristics generally produce well defined localised features in the *uv*-plane, such as distinct maxima and minima.Determination of source structure by inspection quickly becomes more difficult with increasing source complexity and *uv*-coverage, and to obtain a model for even a source with only three distinct components by this method often constitutes a challenge.

6.2.2 Analytic Model Fitting

Although inspection can provide qualitative insights into the structure of radio sources, a more quantitative approach involves the actual representation of the visibility data by analytic models. Provided they are composed of simple components, an analytic form can be found for the transform of these models and if these are formulated appropriately, numerical methods can be used to adjust the model parameters to maximise the agreement between the transformed models and the visibility data. A useful function for these purposes is an elliptical Gaussian, parameterised by the location of the centroid, the position angle and length of the major axis, an axial ratio and a flux density. This function has the advantage that it has an elementary analytic form and several simpler structures, such as points, circular Gaussians and lines, can be represented as special cases of the more general form.

These simple objects are the basic building blocks from which source models are constructed. Model fitting only works because most sources that have been imaged have been found to be describable by these types of basic structures. The procedure can fail completely when applied to a source that cannot be represented by a small number of such components (for example, extended regions of uniform brightness) and it is essential that the observer remain constantly alert to this possibility.

The Caltech package program MODELFIT implements a non-linear least-squares method to compute model parameters that best fit the visibility data. The "goodness" of the fit of the models to the data is quantified by the χ^2 statistic defined as

$$\chi^2 = \sum_{i=1}^{N} \left\{ \frac{[y_i - y(x_i; a_j)]^2}{\sigma_i^2} \right\}$$

where N is the number of independent data points, (x_i, y_i) are the visibility measurements (x=uv-position, y=visibility amplitude or closure phase), σ_i is the error (uncertainty) associated with each y_i and $y(x; a_j)$ is the fitting function parameterised by the a_j. The objective of the MODELFIT program is to minimise the value of χ^2 by varying either a subset, or all, of the a_j.

The program reports its progress through a quantity termed the "agreement factor" (AF) which is the square root of the reduced χ^2, that is

$$AF = \sqrt{\frac{\chi^2}{\nu}}$$

where ν is the number of degrees of freedom, defined by $\nu = N - n$, n being the number of parameters in the model. For a good fit the deviation of the model from the data is, on average, comparable to the uncertainties, and so $\chi^2 \to \nu$ and the agreement factor decreases towards unity.

The fitting procedure requires an initial model as input. The observer incorporates the essence of the structure determined from inspection of the visibilities into this initial model to start the numerical process in a region of parameter space that is (hopefully) close to the global minimum in χ^2. The numerical procedure then progresses in two separate iterative stages, the first being a gradient

search controlled by the partial derivatives of χ^2 with respect to the parameters a_j, and then secondly a grid search in which the fit is fine-tuned by stepping each parameter in small increments to minimise χ^2 once the gradient has "levelled out".

6.2.3 Parameter Uncertainties

The MODELFIT program permits the computation of models that best-fit the data in a least squares sense. However it provides no numerical estimates of the uncertainties or acceptable ranges of the parameter values calculated via this method. To calculate such values in any general way is a formidable task. In fact it is not always possible since the source may, in reality, be quite different in structure from the model which has been fit to the restricted visibility data. Furthermore, because there is often a strong correlation between the different parameters in a model, the uncertainties in one parameter are very sensitive to the specific value of another. The strength of this correlation varies from model to model and data set to data set. Also, some model parameters may simply be poorly constrained by the data, depending on such factors as the *uv*-coverage and signal to noise ratio and it is unclear how to quantify this in a general fashion.

To produce meaningful results, formal statistical approaches to the problem of uncertainty computation rely on the data points, and their associated uncertainties, being truly independent. This is rarely true in the case of VLBI data, there being correlations between adjacent points on an hourly timescale due to calibration errors, and possibly throughout an experiment because of antenna scaling calibration errors. In such cases, the data points themselves are not only related, but the error bars are quite probably systematically wrong also. A bias caused by a subset of corrupt data in fringe-fitting can also lead to an error which is correlated between data points within a solution interval, or even longer, depending on the extent to which the fringe fitting solutions have been smoothed.

In spite of these obstacles, the program ERRFIT in the Caltech package attempts to implement a formal calculation of the parameter uncertainties to estimate confidence limits. It requires a user input estimate of the number of degrees of freedom and ignores the uncertainties associated with each data point, calculating them instead from the scatter in the data themselves. The program help file suggests that the number of degrees of freedom is the number of stations times the number of hours of data (assuming calibration is applied hourly). The calculated parameter uncertainties scale with the inverse square of this number, which for the single baseline survey observations is often relatively small, and given the concocted nature of the calibration procedures for some of the experiments (in terms of the use of T_{sys} versus elevation curves from other observations) is difficult to estimate objectively. Thus the parameter uncertainties derived via this method are themselves uncertain and prone to systematic error. In the light of these difficulties, and considering the effort required to correctly, though always at best subjectively, estimate the number of degrees of freedom for each experiment independently, it was decided that this method of error estimation was inappropriate for the data presented here.

Another semi-numerical approach to the estimation of confidence limits in the

fitted parameters is that of boundaries of constant χ^2. This method involves taking the best fit model, perturbing a parameter away from its best fit value, and then holding it constant at this value while the other parameters are varied until the model once more is the best fit to the data (in the sense that χ^2 is minimised subject to the constancy of the parameter of interest). This procedure is repeated until the χ^2 of the fit has increased by some specified amount, usually one, and then the amount by which the parameter has been displaced is related to its confidence interval. Once again this procedure depends crucially upon the extent to which the error bars really represent the uncertainties in the data and so it is difficult to apply to VLBI data. Also it is not a simple process to automate, since it requires repeated refitting of the data, and is therefore obviously very labour intensive.

In view of the dependence of model parameters both upon one another, and on the peculiarities of each data set, it is not feasible to compute by any automated procedure meaningful uncertainties for all the parameters obtained through the model fitting process. Any procedure for uncertainty estimation needs to incorporate the experimenter's knowledge of the behaviour and sensitivities of each model with respect to the data used in its formulation. A method which does this, and adopted for these data, is modelled on the ideas of the boundaries of constant χ^2 method just discussed, but relies upon as a measure of the quality of the fit, not the χ^2, but a purely visual assessment of the agreement between the data and the model. This procedure, described by Tzioumis *et al.* (1989), involves stepping the parameter of interest away from the best-fit value and repeatedly refitting until the model no longer appears to be in agreement with the data. In this manner the range of acceptable values for the parameter of interest can be explored with due regard being given to the influence of its particular value on the (subjective) quality of the fit. Also the experimenter has the discretion of placing extra emphasis on the ability of the model to represent particularly sensitive features in the data, such as the location of amplitude minima for a double source or discontinuities in the closure phases. Although this method does not formally incorporate the measurement errors associated with the data, they can be taken into account by the experimenter in assessing the quality of the fit. The range of parameter values obtained is thus a reasonable estimate of the uncertainty since it indicates the scope of variation in each parameter that can be accommodated by the data. Because it is also a very labour intensive procedure, this method was only used to estimate the acceptable ranges of parameters of particular interest, for example, the separations of two components at different epochs.

6.3 Model Fitting Strategy

Model fitting is clearly a subjective procedure, the experimenter having control over both the initial model and the choice of which parameters are free to vary in the fitting procedure. In an attempt to make the process of fitting these data as objective as possible, so that all data are treated equally, a scheme consisting of a set of simple rules for deciding which parameters could be varied, and the

circumstances under which new parameters could be added, was chosen and then adhered to throughout the process for all the data.

The objective of the model fitting is to construct the "simplest" models consistent with the available visibility data and the types of structure that has been found in other high resolution VLBI observations of radio sources (since this is what our model building blocks are good at representing). It is quite easy to fit almost any data just by allowing the model sufficient freedom in terms of the number of components and free parameters. However, such over-parameterised models are unlikely to be unique, and many of their parameters will be poorly constrained by the data. In the event that the experimenter allows this to occur, the whole procedure becomes meaningless since the model is free to fit any one of a number of local minima in χ^2, few of which will be in the vicinity of the global minimum, or in other words, the chance that the model reflects the true source structure becomes small. By restricting the number of free parameters the capacity of the models to represent false structure is limited.

The simplest models are composed of the most rudimentary components (such as points, lines, circular and elliptical Gaussians) and the minimum number of these components required to accommodate the visibility data are used. Such models are usually well constrained by the data because, in addition to fitting the visibilities well, they are "rigid" in the sense that they have insufficient residual flexibility (or freedom) to assume other configurations without severely degrading the quality of the fit. The model fitting strategy described below is thus a set of rules designed with the objective of keeping the number of parameters (and components) low and preventing elementary models from evolving to more complex forms in excess of what can be justified by the visibility data.

1. A model with fewer but more elaborate components is favoured over a model with more distinct components. For example an elliptical Gaussian would be preferred over a coincident point and circular Gaussian unless a substantially better fit could be achieved by the latter.

2. Because component sizes are not easily separated from flux densities, point sources are preferred over circular Gaussians, and similarly lines ahead of elliptical components. This leads to the derivation of minimum possible component flux densities rather than actual values.

3. When adding new components, they are first tried coincident with those already in the model so that the location of the centroid does not require two extra parameters immediately.

4. When it is necessary to permit a component of a double model to become elongated, or to add a third component, every effort is made to try and keep the position angles in common, and the components collinear, so that the elongation is aligned with the orientation of the double, or the third component lies along the position angle defined by the other two components.

The procedure for the fitting of models begins then with inspection of the data, and with the above rules borne in mind, models consisting of either a point source,

or an equal double point source if the data show obvious beating characteristic of doubles, are tried. These point sources are allowed to vary in flux, and relative position in the case of doubles. If necessary they are then permitted to become circular Gaussians. If it is then apparent that component orientation is significant a line is tried, and only as a last resort, a full elliptical with six free parameters. Only when this stage is reached, if the model is clearly still inadequate, is consideration of an additional component entertained. The procedure for adding new parameters then is driven solely by the demands of the data in the aperture plane, and not the desire to produce some particular type of model in the image plane (subject to the constraint that only a limited variety of image plane component types are available to achieve this).

If an extra component is added, then an attempt is made to pare back the previous model so that it consists of the simplest possible components. For example, if an elliptical Gaussian did not fit well, then rather than try a coincident point and elliptical, a coincident point and line would be tried. In this manner, adding the new component effectively increases the degrees of freedom within the model by less than would otherwise be the case.

When more than one baseline is present in the data, the approach followed is to try and fit the longest baselines first. This is simply because the longest baselines are sensitive to only the most compact structure whereas the shorter baselines "see" both these components and larger more extended features. That is, larger components will be resolved out and need only fit the short baselines. An example of this in these data is 0454−463, in which a line component fits the trans-oceanic baselines quite adequately, but is not sufficient to explain the shorter Australian baselines.

6.4 Treatment of the Visibility Amplitudes

For the single baseline observations only the amplitudes are used when fitting models to visibility data. It is therefore sufficient to average the two second data output by the fringe fitting incoherently, rather than coherently (Section 4.7). This approach has the benefit of eliminating the loss due to any phase noise present in the observing system (beyond the initial two second integration performed by the correlator). Unfortunately the procedure is complicated by virtue of the visibility amplitudes, in the presence of noise, following a Rice distribution which has a mean that is systematically higher than the true mean (Moran, 1976; Thompson *et al.*, sec. 9.3). It is necessary to correct the amplitudes for this bias if incoherent averaging is to be used.

The effect was simulated by generating a large number of visibility vectors of a fixed amplitude V and adding Gaussian noise vectors with amplitude standard deviation σ. The mean amplitudes of the resultant vectors were then evaluated. The results of this simulation for signal to noise ratios (V/σ) between zero and twenty is shown in Figure 6.1. Thompson *et al.* suggest that a good estimate of the true visibility amplitude is $V \simeq \sqrt{Z^2 - \sigma^2}$, where Z is the measured amplitude of the resultant vector. However, as the authors point out, this estimate deviates

substantially for signal to noise ratios less than about three (Figure 6.1). To describe the bias effect at low signal to noise ratios, a degree six polynomial was fit to the simulated data and is also shown in Figure 6.1.

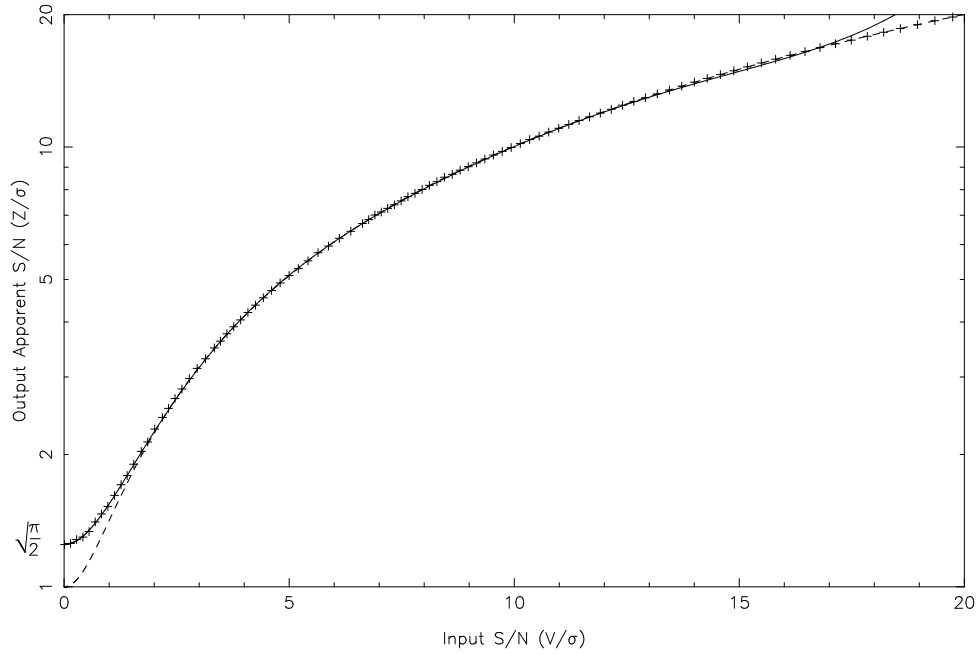

Figure 6.1: The apparent signal to noise ratio (Z/σ) of a visibility amplitude measured in the presence of an additive random (Gaussian) noise vector. The crosses indicate the simulation data discussed in the text, and the solid line is the degree six polynomial fit to these data. The dashed line is the correction $Z/\sigma = \sqrt{(V/\sigma)^2 + 1}$.

A program was written to correct this bias by applying the analytic correction at high signal to noise ratios, and using the polynomial at lower signal levels. The step in the correction function at the changeover point between these two methods was minimised by making the changeover at an apparent signal to noise ratio of 15 where the two methods are in close agreement. Note that these corrections are based on mean amplitudes and assume that we never measure an amplitude (Z/σ) less than $\sqrt{\frac{\pi}{2}}$ (Figure 6.1)[1]. In practice of course, at low signal to noise ratios, the measured amplitudes will be distributed right down to zero, though even for zero signal to noise ratio their mean will be greater than or equal to $\sqrt{\frac{\pi}{2}}$. The program overcomes this difficulty by first computing a running mean of the amplitudes with a user specified averaging time. The correction is then calculated from the value of this running mean, but is applied to the individual visibilities. This ensures that neighbouring visibilities, whose amplitudes ought to be correlated, are corrected by similar amounts, and prevents wild fluctuations in the magnitude of the correction applied when the mean of the data lies close to

[1]The value of $\sqrt{\frac{\pi}{2}}$ is the mean value of a Rayleigh distribution with unit mode. A Rayleigh distribution is the special case of a Rice distribution which applies for a signal to noise ratio of zero (see Figure 6.2 and accompanying text).

the asymptote in the correction function $Z/\sigma \sim \sqrt{\frac{\pi}{2}}$.

The program requires an estimate of the amplitude of the noise in order to apply the bias correction. Before calibration of the visibility amplitudes, the noise amplitude is dependent solely on the characteristics of the recording system, correlator and fringe fitting software. Any two uncorrelated signals will always produce the same distribution of correlation coefficient amplitudes for a given one-bit recording system and correlator because there is no amplitude information encoded in the two recorded bitstreams, the signal amplitudes arising only from the degree of correlation between the two. The properties of the noise distribution were measured by taking the raw fringe-fit two second amplitudes from an experiment in which the source was undetected (phases random) and fitting a Rayleigh distribution function,

$$p(Z) = \frac{Z}{\sigma^2} e^{-\frac{Z^2}{2\sigma^2}}$$

as shown in Figure 6.2. The mode of this distribution (σ) is the standard deviation of the underlying Gaussian noise amplitude distribution (Thompson *et al.*, 1986). This value is used by the bias correction program to normalise the uncalibrated visibility amplitudes so that the required corrections can be calculated from either the analytic estimate or the polynomial discussed above.

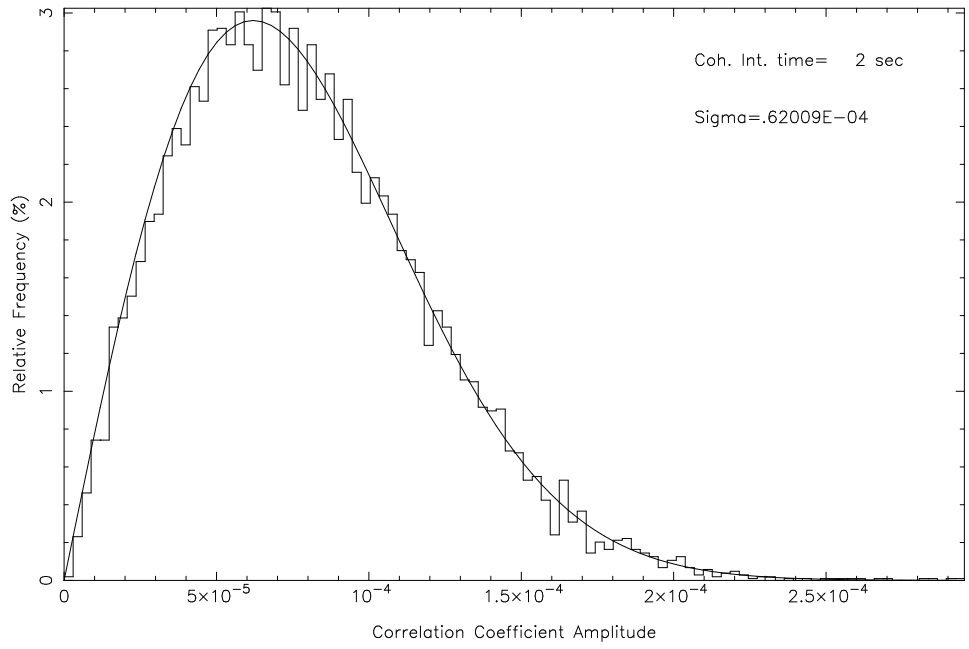

Figure 6.2: The amplitudes of of the correlation coefficients computed by the correlator for two uncorrelated input signals follow a Rayleigh distribution with mode $\sigma = 6.2 \times 10^{-5}$ and mean $\sqrt{\frac{\pi}{2}}\sigma = 7.8 \times 10^{-5}$.

The effectiveness of the correction procedure is illustrated in Figure 6.3 which shows the results of a test of the method using a simulated data set. The top panel of the figure shows the uncorrected two second visibility amplitudes and the model

visibility function. The data is generated with the Caltech program FAKE and the amplitude noise is produced by adding noise vectors with standard deviation 0.1 Jy to the model visibilities. The middle panel shows the result of incoherently averaging these data into thirty second intervals and the presence of the bias is evident in the amplitude nulls, particularly the cusp. The effect of applying the bias correction program to the two second data and then averaging incoherently is shown in the bottom panel and demonstrates how much better the data reflect the true visibility amplitudes. The reduction in the error bars at the very lowest amplitudes is a consequence of the "pinching" of the noise distribution that occurs because the correction is mono-directional (the error bars in the averaged data are computed from the scatter in the data input to the averaging). As an indication of how important this bias correction can be, simple two component models, based on the model used to generate the data, were fit separately to the two averaged data sets shown in the figure. The original model was composed of a point source and a linear component of equal flux density. For the uncorrected data, the best fit model components differed in flux density by nearly twenty percent, for the corrected data the difference was less than one percent.

It was necessary to modify the Caltech program AVERAGE in order to perform the incoherent average correctly. Originally the program, in addition to coherent averaging, only provided incoherent averaging in which the errors of output points are calculated from the errors associated with the input data. However the two second visibilities output by the fringe fitting are not accompanied by meaningful errors and in the case of the coherent average, the errors are calculated from the scatter intrinsic to the input data points. The program was modified so that it can calculate a hybrid average in which the amplitudes were averaged incoherently and the phases coherently, with the errors in both computed from the scatter in the data in a manner similar to that used for the coherent average. In addition to producing realistic uncertainties for the output data and permitting an incoherent average, this has the benefit that phase closure relations are preserved so that the closure phases can be calculated and used in the model fitting if multiple baselines are present in the data set. Except where otherwise stated, all the visibility data presented in this chapter has been subject to this averaging procedure, and the bias correction described above.

6.5 Results

The results of the model fitting for the peaked spectrum survey sources are presented in Table 6.1 and Figures 6.4 and 6.5. Peculiarities of the individual models will be discussed in the next section. General features of the models and the problems encountered in their formulation are discussed below.

Of the 49 models, 15 have a single component, 27 have two components and only seven consist of three components. Most of the parameters in the models that are zero, or in the case of the axial ratio, either zero or one, were not permitted to vary in the fitting procedure. Thirty nine of the models have agreement factors less than two indicating good agreement with the data. A further nine have agreement

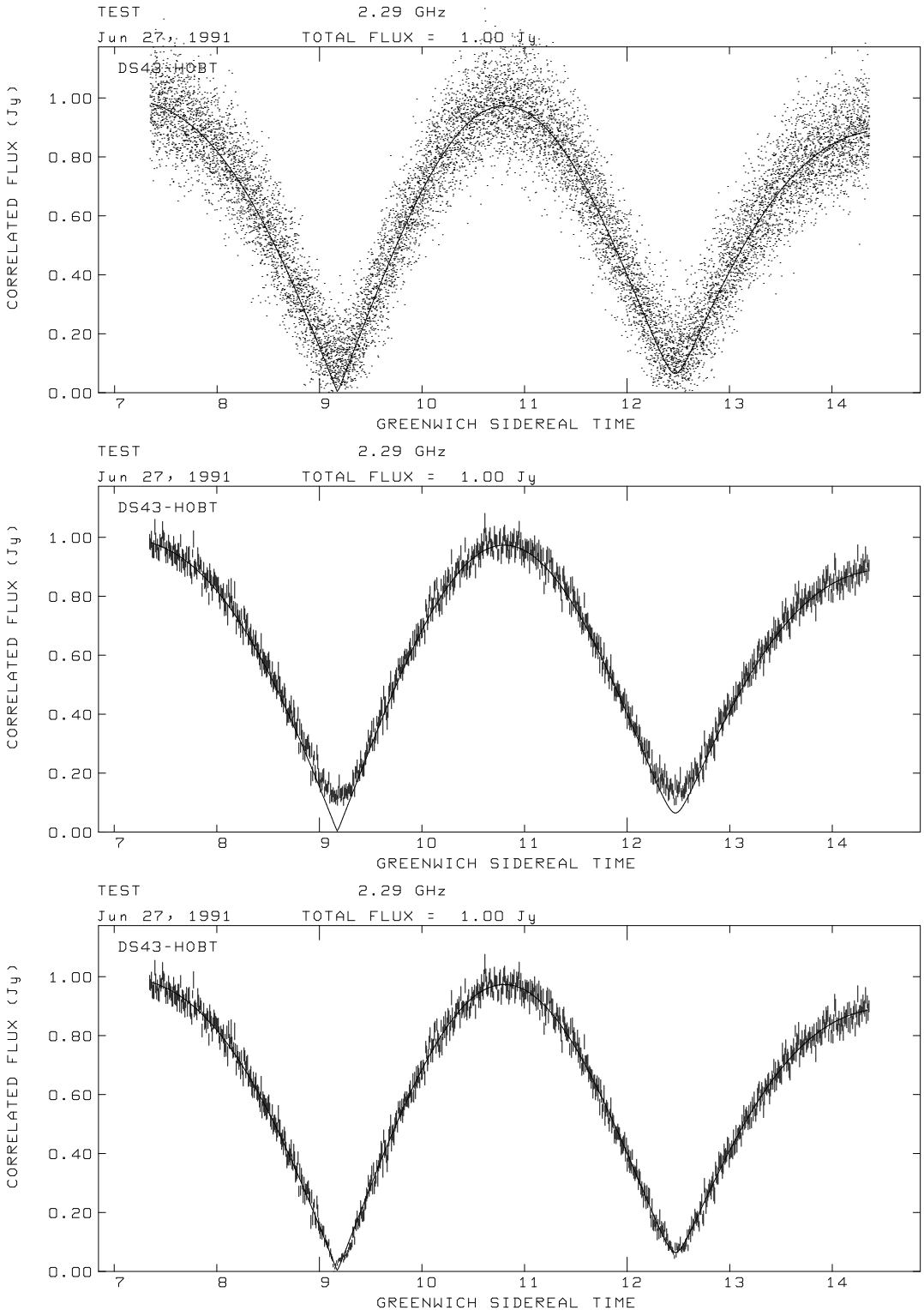

Figure 6.3: The top panel shows the uncorrected two second visibility amplitudes. The middle panel and bottom panels show the results of incoherently averaging for thirty seconds the uncorrected and corrected amplitudes respectively. The solid line in each graph is the visibility amplitude of the model used to generate the data.

factors between two and four, and only one is worse than this.

The poorer fitting models were all tried with more free parameters and more components. However when this led to only slight improvements in the agreement factors, the best fitting simpler model was chosen since the extra parameters were either unjustified by the improvement in the fit or very poorly constrained. In all cases these simpler models reflect the overall characteristics of the data well and, though lacking in detail, can be confidently regarded as representing the essence of the source structure.

It is pertinent that several of the models with the worse agreement factors involve a baseline including the 70 m antenna DSS 43. High signal to noise ratio continuous data can be very demanding on a source model since they can require a very accurate model to fit perfectly, yet they generally provide insufficient spatial information to give any confidence that such a model is unique. Thus in these cases it was also considered more appropriate to choose the poorer fitting simple model, rather than a more complicated one in which one or more of the components is quite possibly completely wrong. A further hazard associated with fitting the most sensitive baselines is that the error bars reflect only the scatter in the two second data points that were averaged, and do not take into account calibration errors. Therefore, attempts to fit these data very well may result in source models that are more representative of the pointing and calibration nuances of the antennas rather than the sources themselves. An extreme example of this is the model of 1934-638 designated (an) in the table and figures. This model has the poorest agreement factor of 7.3, yet it appears to fit the data very well. The error bars on these data are so small that any discrepancies between model and data make a huge contribution to the χ^2. However it is not possible to differentiate between systematic observational effects (pointing, calibration etc) and subtle changes in the visibilities due to source structure. If the error bars associated with this data were to be inflated to account for pointing and calibration errors then a lower value of the agreement factor would result, though the fit itself ought not change.

Experience during the fitting process indicates that the minimum component flux densities, and for the doubles, the spacing and relative component position angles, are all well determined (in the sense that the quality of the fit of the model is sensitive to changes in these parameters). Where the *uv*-tracks are long enough ($>\sim 6-8^{hrs}$) the position angles of elongated components are usually reliable. Component sizes are mostly unreliable. This is hardly surprising since measurement of a component size requires data obtained at widely different spacings in the *uv*-plane. A single baseline can be approximated by an arc of a circle centred at the origin, at least over a limited hour angle range, so any determination of the size is very sensitive to the visibility amplitudes and can easily be substantially in error. Even in the cases where a single baseline does cover a wide spacing range, the effect of the change in baseline orientation can affect the size measurement unless the component is circular. Given this uncertainty in the sizes and the difficulty of separating component size and flux, the decision to prefer minimum flux densities and point or line components would appear justified.

The degree of complexity of these models is dependent partly upon the amount and quality of the data. For example, the source 0403-132 (model-k) has so little

data that only a point source is justified, whereas for 1934-638 (model-ap) the high signal to noise ratio and long *uv*-tracks (16^{hrs}) permit, and in fact call for, a more complex three component model. Almost certainly all the sources for which data are presented below are more complicated than the accompanying source models imply, but it is not possible to say so for certain on the basis of the available *uv*-coverage. Where a model has obvious shortcomings when compared with the visibility data it is in principle possible to infer something of the additional structure but with little confidence. By favouring the simplest models with minimum structure it is probable that the maximum *reliable* structure has been determined.

Table 6.1: Parameters of models derived from fits to visibility data. The letter entries in the first column refer to the corresponding plots in Figures 6.4 and 6.5. Note that the agreement factors apply to the best fit model. However the values presented in this table have been rounded so that the flux densities are quoted with a precision appropriate to the calibration uncertainty and the parameters describing the relative positions and orientations of the components are sufficient to reproduce the best fit model with an accuracy of one milli-arcsecond, which is always finer than the best resolution achievable given the *uv*-coverage. Where closure phases have been used in the fitting process, the phase closure agreement factor is quoted separately and appears in braces immediately beneath the accompanying amplitude agreement factor. The epoch is the fractional year since 1900.

Fig. ref.	Source name	Obs. freq. (GHz)	Epoch	Total f.d. (Jy)	Cpt. f.d. (Jy)	Centroid Radius (mas)	Centroid Angle (°)	Major axis (mas)	Axial ratio	Posn. angle (°)	Agr. Fac. Ampl. (Clo.Ph.)
(a)	0008-421	2.3	89.93	2.9	1.7	0	0	12.5	0	90	3.559
					1.1	124	89.9	29.2	0	90	(2.696)
(b)	0022-423	2.3	89.93	3.1	2.22	0	0	0	1	0	1.035
					0.84	28	119	0	1	0	
(c)	0022-423	8.4	90.05	1.0	0.303	0	0	3.9	0	-62	1.151
					0.087	28	119	0	1	0	
(d)	0022-423	8.4	91.90	1.0	0.69	0	0	4.0	0	-70	1.667
					0.26	28	119	3.2	0	15	
(e)	0023-263	2.3	90.30	6.1	1.1	0	0	17.0	0	-60	1.658
					1.64	657	145.9	25.5	0	29	
(f)	0023-263	2.3	91.34	7.1	0.90	0	0	8.0	0	-78	2.981
					0.29	654	145.9	13.6	0	53	
(g)	0023-263	8.4	91.90	2.2	0.72	0	0	5.1	0.8	46	1.879
(h)	0159-117	2.3	91.91	2.1	0.70	0	0	13.2	0	-40	1.228
					0.12	1594	-4.12	0	1	0	
(i)	0237-233	2.3	88.86	5.2	5.2	0	0	7.8	0	53	1.232
(j)	0237-233	8.4	91.90	2.4	1.61	0	0	4.5	0	21	1.496
					0.75	10	-127	0	1	0	
(k)	0403-132	2.3	93.15	3.5	0.36	0	0	0	1	0	1.267
(l)	0454-463	2.3	89.93	1.7	0.61	0	0	1.2	1	0	1.604
					0.41	22	77	17.4	0	89	(1.139)
(m)	0506-612	2.3	89.86	1.6	0.38	0	0	0	1	0	1.244
					0.24	107	35	50.8	0	83	
					0.17	144	50.3	59.6	0	-65	
(n)	0733-174	2.3	93.15	2.7	1.9	0	0	8.5	0	34	1.094
(o)	0741-063	2.3	93.15	5.6	1.14	0	0	0	1	0	1.301
					0.80	141	84.9	22.6	0	-73	
	0743-673	2.3	88.56	3.2	0.99	0	0	48.0	0	-86	1.132
					0.61	0	0	0	1	0	
	0743-673	2.3	89.93	3.2	0.81	0	0	52.8	0	-87	1.575
					0.71	0	0	0	1	0	
(p)	0743-673	2.3	both	3.2	0.86	0	0	52.5	0	-86	1.651
					0.69	0	0	0	1	0	

Source model parameters continued...

Source model parameters continued...

Fig. ref.	Source name	Obs. freq. (GHz)	Epoch	Total f.d. (Jy)	Cpt. f.d. (Jy)	Centroid Radius (mas)	Centroid Angle (°)	Major axis (mas)	Axial ratio	Posn. angle (°)	Agr. Fac. Ampl. (Clo.Ph.)
(q)	0823-500	2.3	88.77	5.7	2.0	0	0	0	1	0	1.990
					2.5	21	127	8.5	1	0	
(r)	0823-500	2.3	89.93	5.7	2.0	0	0	0.0	1	0	1.921
					4.2	22	130	12.7	1	0	
(s)	0834-196	2.3	91.48	3.1	0.63	0	0	13.8	1	0	1.622
					0.56	104	149	59.1	0	-55	
					1.44	104	139	15.2	1	0	
(t)	0859-140	2.3	91.48	2.6	1.1	0	0	9.6	0	-68	1.026
(u)	1015-314	2.3	91.48	2.4	0.249	0	0	0	1	0	1.078
					0.864	0	0	35.1	0	2	
					0.080	71	93	33.4	0	-80	
(v)	1127-145	2.3	93.15	5.1	4.9	0	0	7.4	0	26	1.208
(w)	1148-001	2.3	93.15	2.6	3.0	0	0	13.1	0	23	1.004
(x)	1151-348	2.3	89.93	4.6	1.8	0	0	10.7	0.76	-48	1.614
					1.0	93	-108	13.4	0.85	-33	(1.788)
					2.0	46.5	-108	77.1	1	0	
(y)	1151-348	2.3	91.34	4.6	1.6	0	0	10.1	0	-57	1.934
					1.1	92	-108	12.8	1	0	
(z)	1151-348	8.4	92.24	1.8	0.248	0	0	2.7	0	-37	1.237
					0.030	88	-104	0	1	0	
(aa)	1215-457	2.3	88.75	3.6	1.5	0	0	12.0	0	50	1.185
(ab)	1245-197	2.3	91.34	4.0	1.16	0	0	0	1	0	2.577
					1.18	19	56	0	1	0	
					0.32	148	87	22.0	0	74	
(ac)	1245-197	8.4	92.24	1.6	0.36	0	0	4.9	0	-78	1.276
					0.37	21	55	6.8	0	29	
(ad)	1320-446	2.3	89.83	2.1	0.77	0	0	0	1	0	1.362
					0.47	33	72	45	0	83	
(ae)	1354-174	2.3	91.48	1.7	1.1	0	0	10.3	0	-86	1.672
(af)	1549-790	2.3	88.86	4.9	3.1	0	0	12.3	0	76	2.823
					1.5	83	83	41	0	-73	
(ag)	1549-790	8.4	91.90	3.6	2.9	0	0	4.2	0	46	1.837
(ah)	1733-565	2.3	91.51	5.6	0.44	0	0	0	1	0	1.152
(ai)	1740-517	2.3	89.93	5.2	4.3	0	0	6.7	0.86	67	1.663
					1.1	52	13	10.2	0	24	
(aj)	1827-360	2.3	90.30	3.7	0.69	0	0	74.2	0	0	1.998
(ak)	1830-211	2.3	91.34	9.1	0.44	0	0	8.8	0	-37	3.286
					1.14	974	-137.7	21.6	0	-38	
(al)	1830-211	8.4	90.51	5.8	0.85	0	0	6.6	0	-60	1.945
					0.63	972	41.7	8.7	0	-60	
(am)	1830-211	8.4	92.24	10.8	3.1	0	0	4.4	0.39	-64	2.001
					5.0	971	41.6	4.9	0.34	-25	(1.640)
(an)	1934-638	2.3	88.86	12.2	5.8	0	0	0	1	0	7.262
					5.1	42.2	91	0	1	0	
(ao)	1934-638	2.3	92.05	12.2	5.7	0	0	10.1	1	0	1.483
					6.8	41.2	89	8.8	1	0	
(ap)	1934-638	2.3	92.05	12.2	0.27	0	0	1.3	0	-58	3.106
					0.81	43.7	91	4.1	0	-66	
					0.43	42.3	89	1.9	0	70	
(aq)	1934-638	8.4	90.08	3.1	0.77	0	0	2.9	0	5	3.355
					1.33	42.4	87	4.9	0	88	
(ar)	1934-638	8.4	91.90	3.1	1.80	0	0	4.7	0	43	1.478
					0.41	41.1	86	0	1	0	
	2126-158	2.3	88.93	1.1	1.0	0	0	0	1	0	1.327
	2126-158	2.3	93.15	1.1	0.79	0	0	0	1	0	1.026
(as)	2126-158	2.3	both	1.1	1.2	0	0	7.4	1	0	1.203
(at)	2135-209	2.3	91.48	2.6	0.88	0	0	9.2	0	11	
					0.75	167	52.0	24.7	0	-20	1.809
					0.62	149	53.0	21.8	0	-7	
(au)	2149-287	2.3	91.48	2.7	0.073	0	0	15.3	0	-22	1.526
					0.404	396	30.9	33.6	0	62	
(av)	2204-540	2.3	91.50	1.5	1.0	0	0	5.8	0	24	1.103
	2311-452	2.3	88.72	1.9	1.3	0	0	4.9	0	-21	2.067
	2311-452	2.3	93.15	1.9	1.1	0	0	7	0	-22	1.216
(aw)	2311-452	2.3	both	1.9	1.5	0	0	9.3	0.8	-46	1.666

Figure 6.4: Contour plots of the source models in Table 6.1. The images have been created by convolution of the models with a gaussian beam (shown shaded) appropriate to the *uv*-coverage of the data used in the fitting process. The contour levels are at 1, 5, 10, 20, 35, 50, 65, 80, 95 percent of the peak value. The antennas contributing to the visibilities from which these models were derived are denoted by the letters at top of each plot as follows: D=Tidbinbilla (DSS 42, 43 or 45), P=Parkes, H=Hobart, M=Mopra, E=Hartebeesthoek and Pr=Perth.

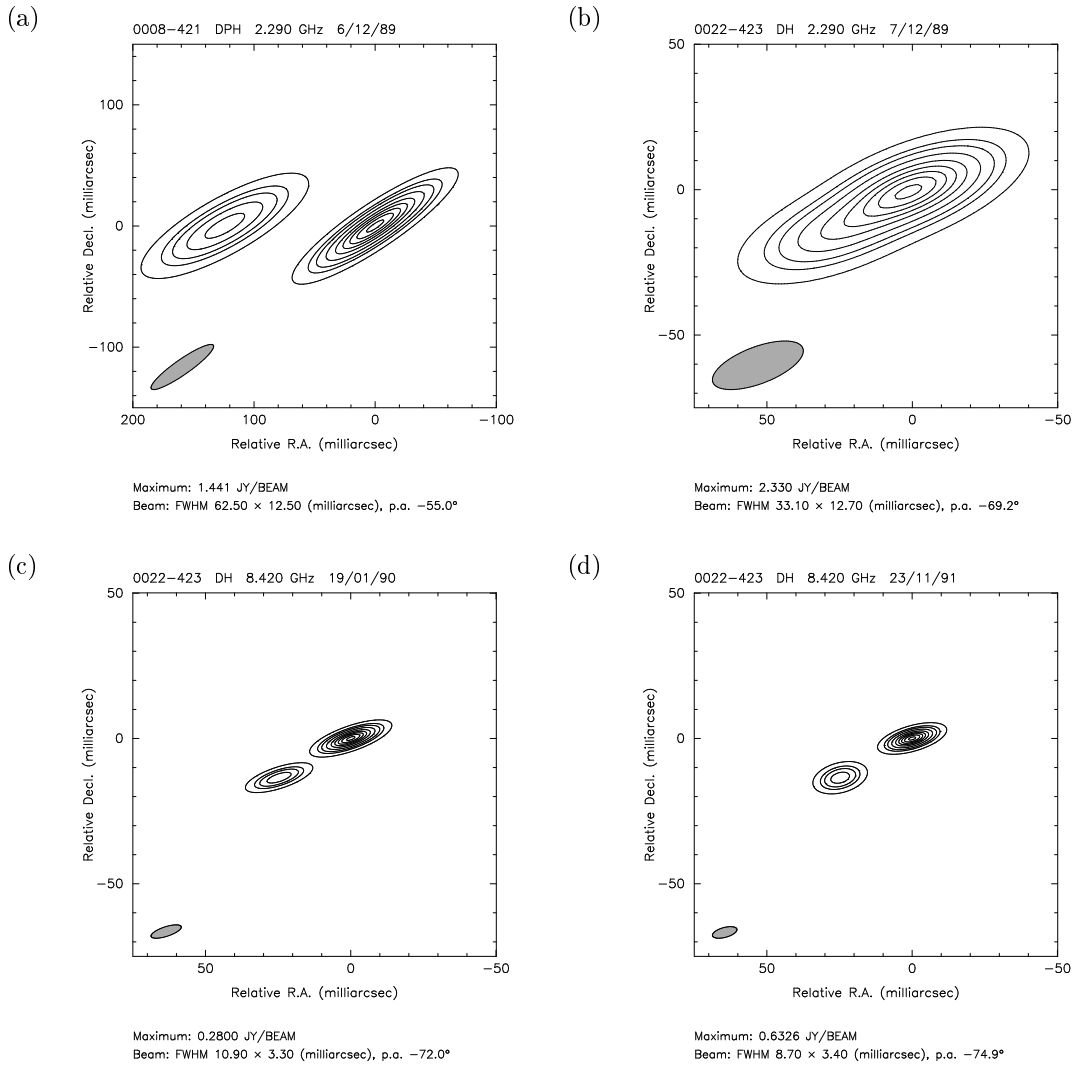

Source model contour plots continued...

(e)

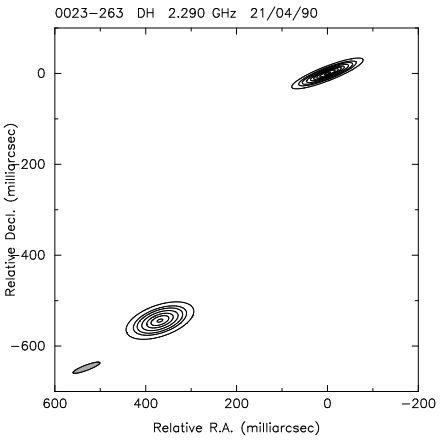

Maximum: 1.038 JY/BEAM
Beam: FWHM 63.10 × 11.80 (milliarcsec), p.a. −69.4°

(f)

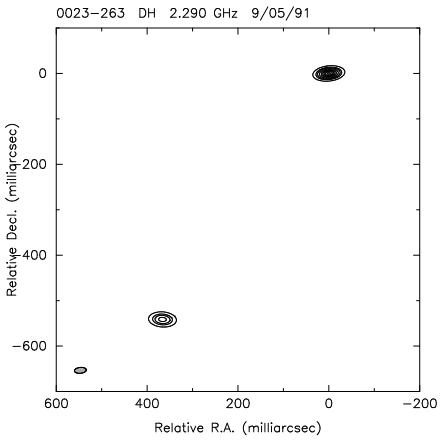

Maximum: 0.8614 JY/BEAM
Beam: FWHM 26.20 × 12.90 (milliarcsec), p.a. −84.6°

(g)

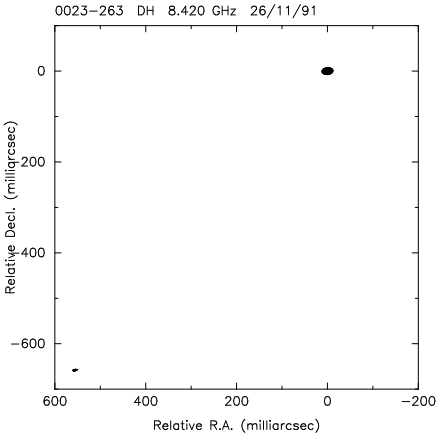

Maximum: 0.3668 JY/BEAM
Beam: FWHM 8.30 × 3.40 (milliarcsec), p.a. −80.0°

(h)

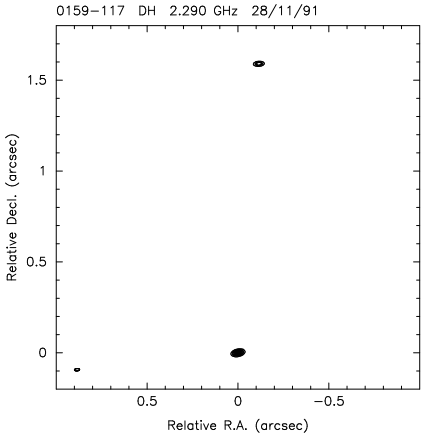

Maximum: 0.5556 JY/BEAM
Beam: FWHM 0.03 × 0.01 (arcsec), p.a. −85.9°

(i)

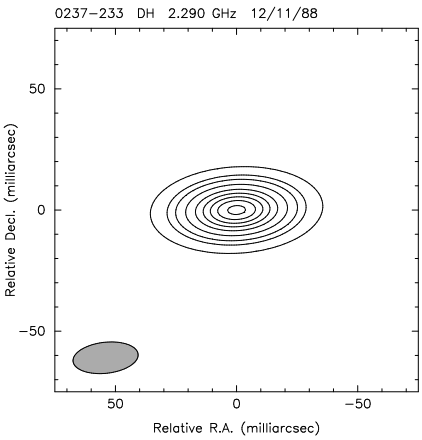

Maximum: 4.736 JY/BEAM
Beam: FWHM 27.00 × 12.80 (milliarcsec), p.a. −83.6°

(j)

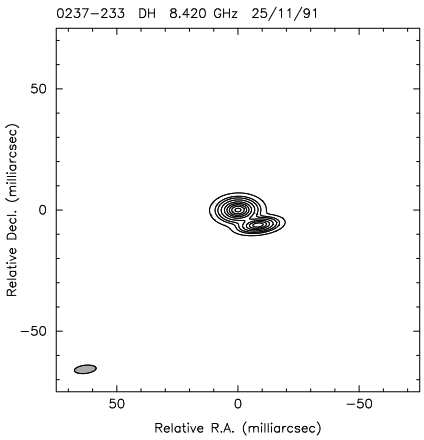

Maximum: 0.9922 JY/BEAM
Beam: FWHM 9.00 × 3.40 (milliarcsec), p.a. −83.5°

Source model contour plots continued...

(k)

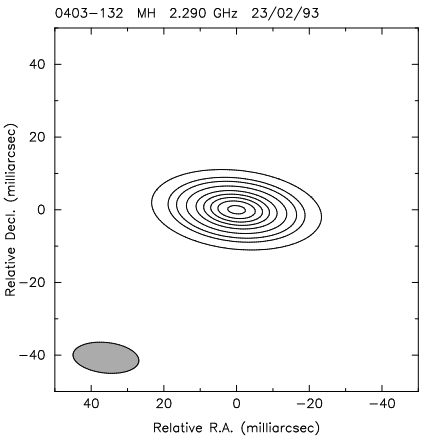

Maximum: 0.3642 JY/BEAM
Beam: FWHM 18.20 × 8.40 (milliarcsec), p.a. 83.9°

(l)

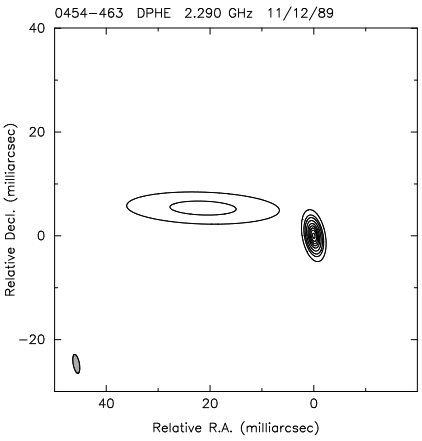

Maximum: 0.4011 JY/BEAM
Beam: FWHM 3.70 × 1.20 (milliarcsec), p.a. 10.4°

(m)

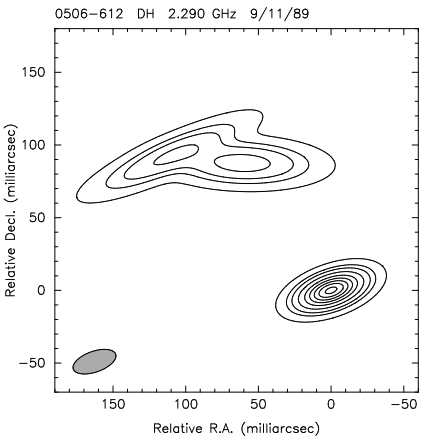

Maximum: 0.3786 JY/BEAM
Beam: FWHM 30.90 × 14.30 (milliarcsec), p.a. −70.7°

(n)

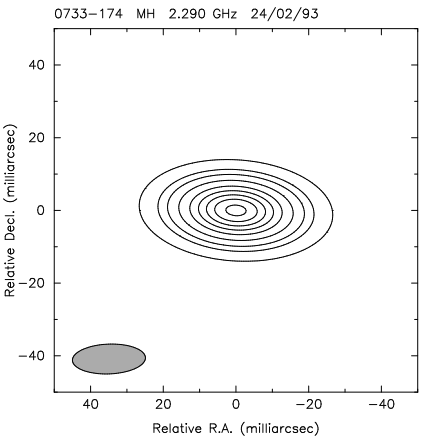

Maximum: 1.380 JY/BEAM
Beam: FWHM 20.10 × 8.20 (milliarcsec), p.a. −87.8°

(o)

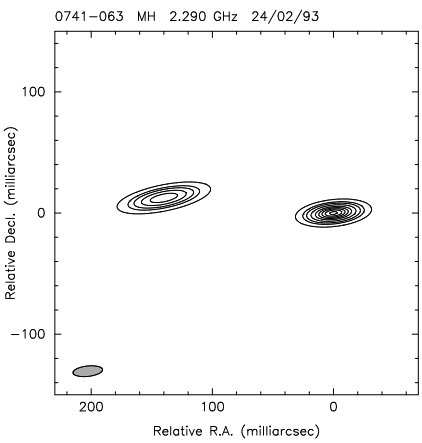

Maximum: 1.142 JY/BEAM
Beam: FWHM 24.50 × 8.60 (milliarcsec), p.a. −83.7°

(p)

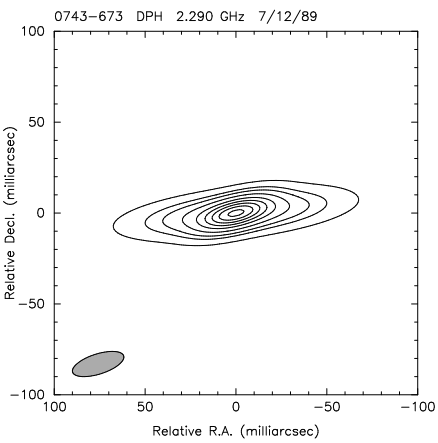

Maximum: 1.059 JY/BEAM
Beam: FWHM 29.50 × 11.10 (milliarcsec), p.a. −72.3°

Source model contour plots continued...

(q)

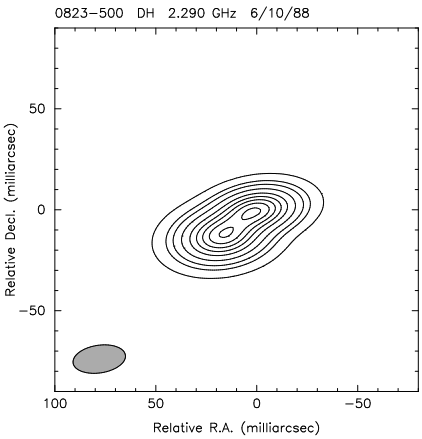

(r)

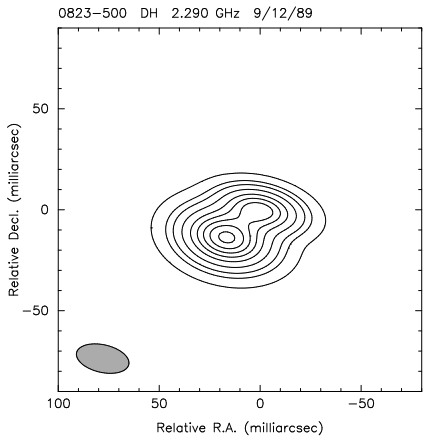

(s)

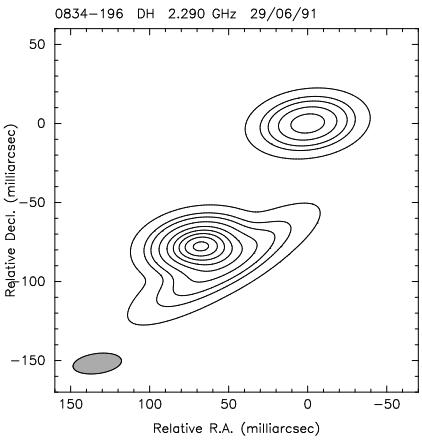

(t)

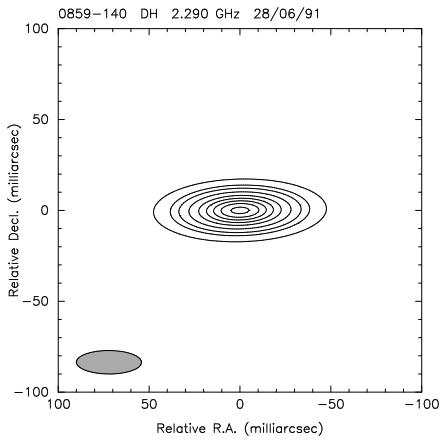

(u)

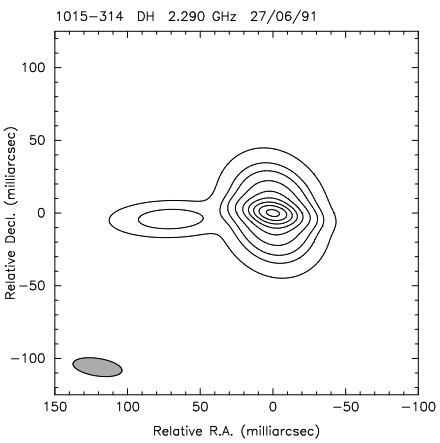

(v)

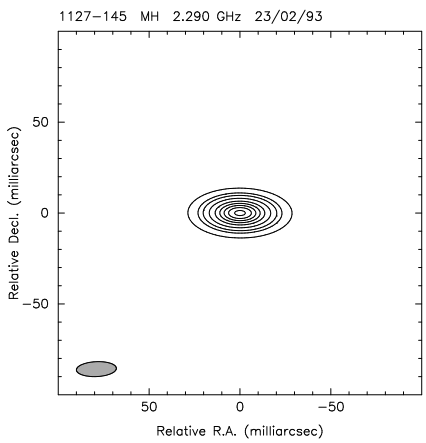

Source model contour plots continued...

(w)

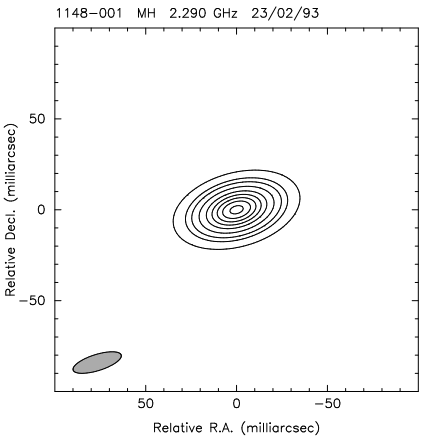

Maximum: 1.682 JY/BEAM
Beam: FWHM 27.70 × 8.90 (milliarcsec), p.a. −72.6°

(x)

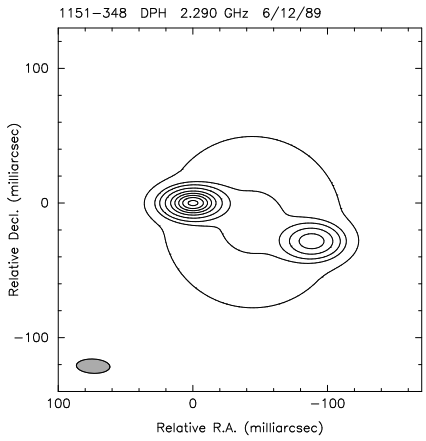

Maximum: 1.322 JY/BEAM
Beam: FWHM 24.90 × 10.60 (milliarcsec), p.a. 87.5°

(y)

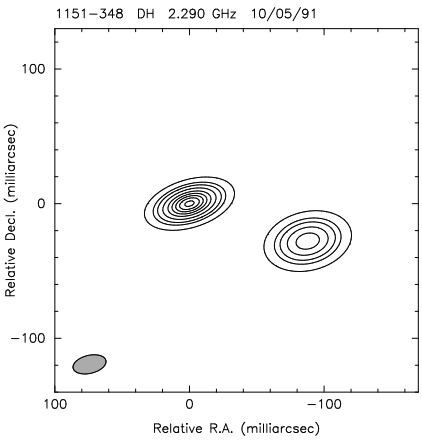

Maximum: 1.491 JY/BEAM
Beam: FWHM 25.00 × 13.40 (milliarcsec), p.a. −76.5°

(z)

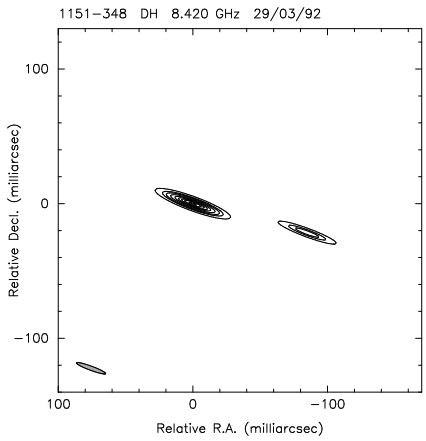

Maximum: 0.1913 JY/BEAM
Beam: FWHM 23.10 × 3.10 (milliarcsec), p.a. 69.7°

(aa)

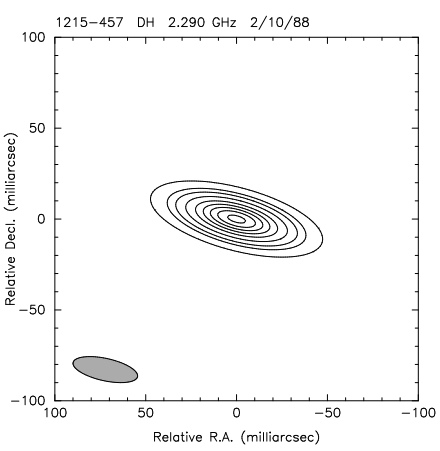

Maximum: 1.299 JY/BEAM
Beam: FWHM 36.30 × 12.30 (milliarcsec), p.a. 77.6°

(ab)

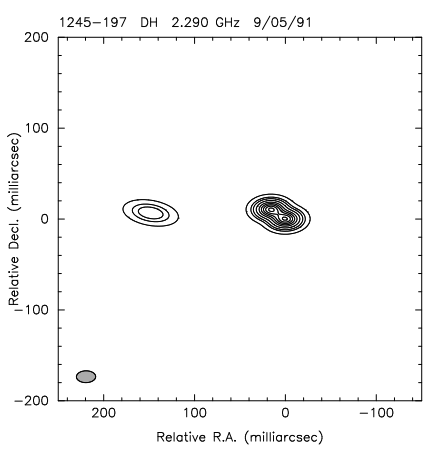

Maximum: 1.213 JY/BEAM
Beam: FWHM 21.20 × 13.00 (milliarcsec), p.a. −89.3°

Source model contour plots continued...

(ac)

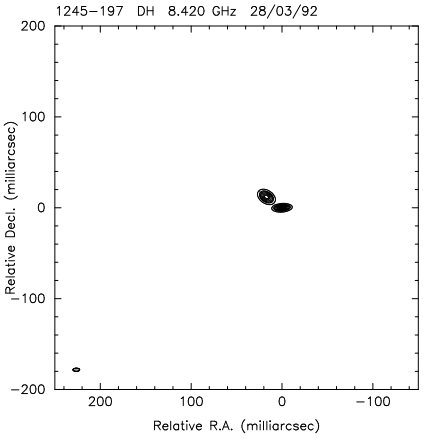

Maximum: 0.2893 JY/BEAM
Beam: FWHM 7.30 × 3.50 (milliarcsec), p.a. −90.0°

(ad)

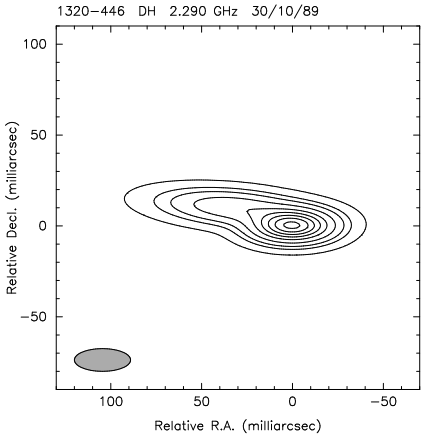

Maximum: 0.8069 JY/BEAM
Beam: FWHM 30.90 × 12.50 (milliarcsec), p.a. 90.0°

(ae)

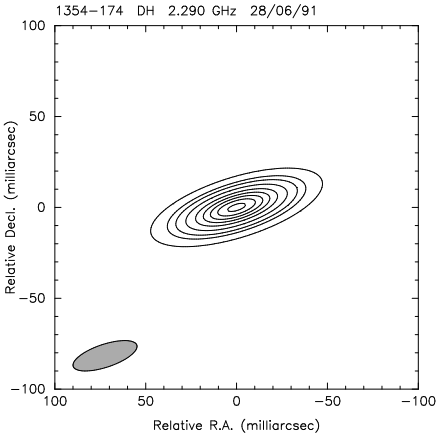

Maximum: 1.031 JY/BEAM
Beam: FWHM 36.90 × 12.60 (milliarcsec), p.a. −71.5°

(af)

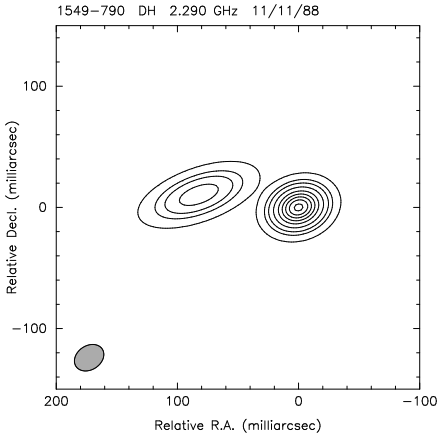

Maximum: 2.716 JY/BEAM
Beam: FWHM 26.00 × 19.80 (milliarcsec), p.a. −56.4°

(ag)

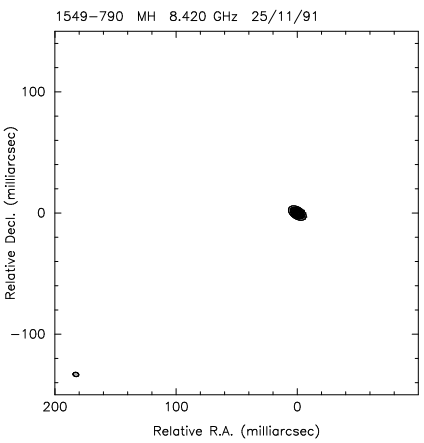

Maximum: 2.096 JY/BEAM
Beam: FWHM 4.80 × 3.50 (milliarcsec), p.a. 78.6°

(ah)

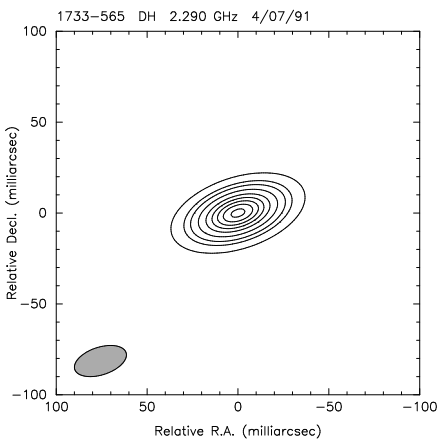

Maximum: 0.4394 JY/BEAM
Beam: FWHM 29.70 × 15.20 (milliarcsec), p.a. −71.9°

Source model contour plots continued...

(ai)

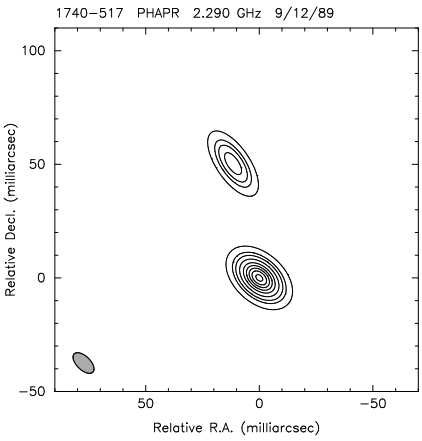

Maximum: 2.672 JY/BEAM
Beam: FWHM 11.50 × 6.00 (milliarcsec), p.a. 45.9°

(aj)

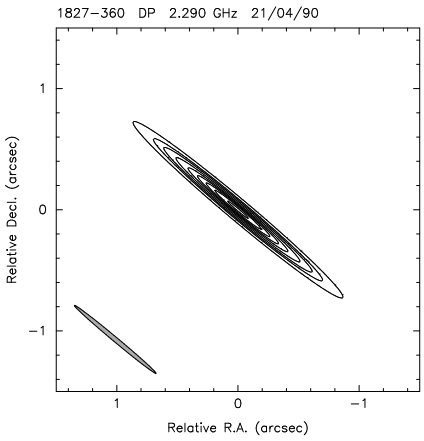

Maximum: 0.3837 JY/BEAM
Beam: FWHM 0.88 × 0.04 (arcsec), p.a. 50.2°

(ak)

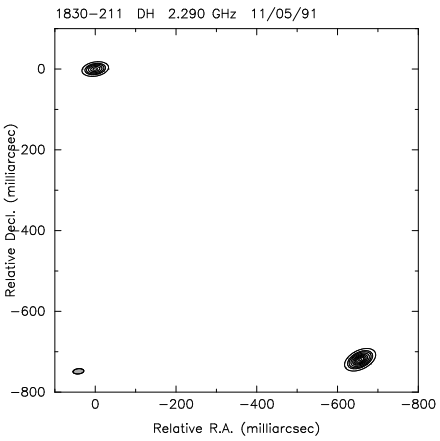

Maximum: 0.6871 JY/BEAM
Beam: FWHM 26.80 × 13.00 (milliarcsec), p.a. −84.4°

(al)

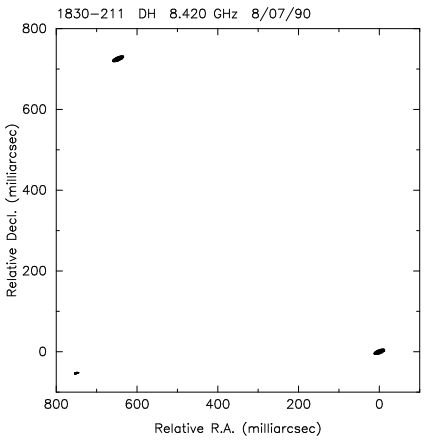

Maximum: 0.6442 JY/BEAM
Beam: FWHM 8.80 × 3.40 (milliarcsec), p.a. −74.4°

(am)

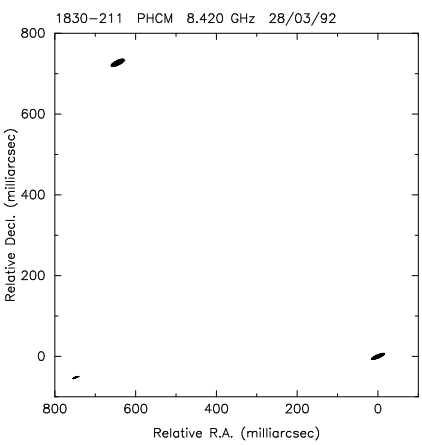

Maximum: 2.624 JY/BEAM
Beam: FWHM 13.20 × 2.30 (milliarcsec), p.a. −67.5°

(an)

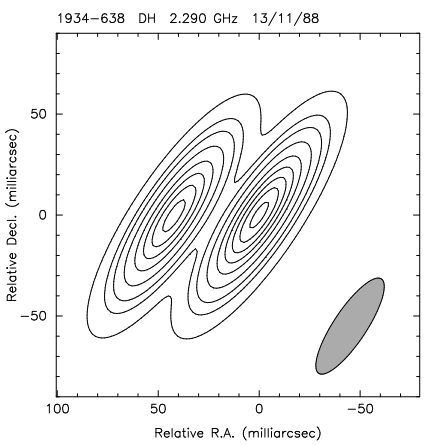

Maximum: 5.844 JY/BEAM
Beam: FWHM 56.10 × 16.30 (milliarcsec), p.a. −33.6°

Source model contour plots continued...

(ao)

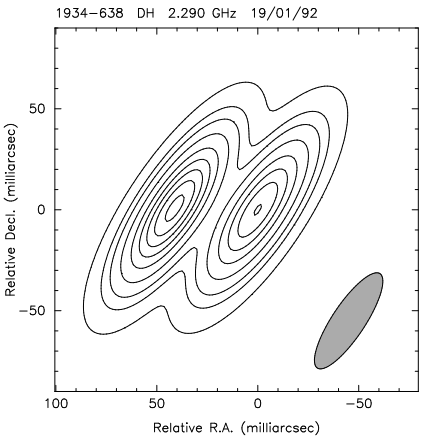

Maximum: 5.925 JY/BEAM
Beam: FWHM 56.10 × 16.30 (milliarcsec), p.a. −33.6°

(ap)

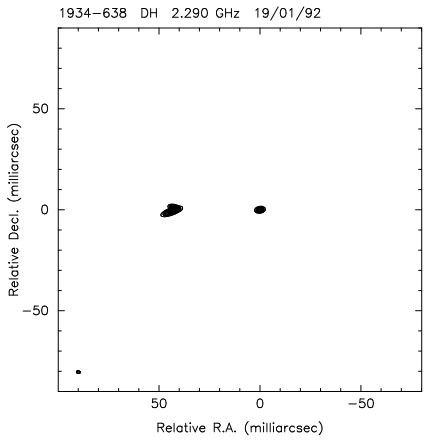

Maximum: 0.3267 JY/BEAM
Beam: FWHM 1.90 × 1.20 (milliarcsec), p.a. 83.0°

(aq)

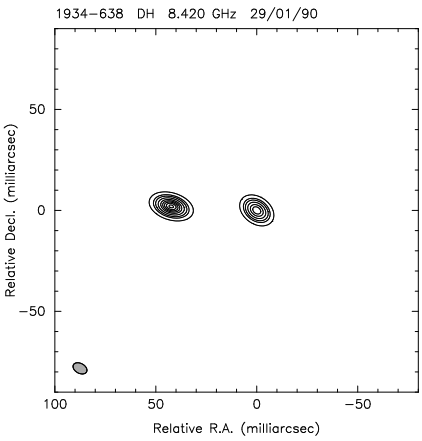

Maximum: 1.068 JY/BEAM
Beam: FWHM 7.40 × 4.90 (milliarcsec), p.a. 61.5°

(ar)

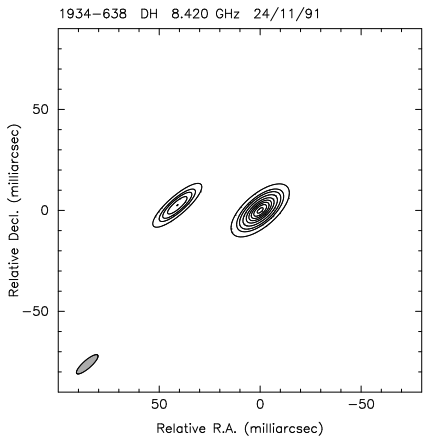

Maximum: 1.157 JY/BEAM
Beam: FWHM 13.80 × 4.00 (milliarcsec), p.a. −48.8°

(as)

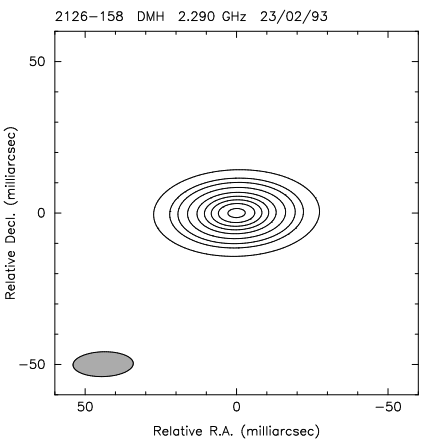

Maximum: 0.8325 JY/BEAM
Beam: FWHM 19.90 × 8.20 (milliarcsec), p.a. −88.4°

(at)

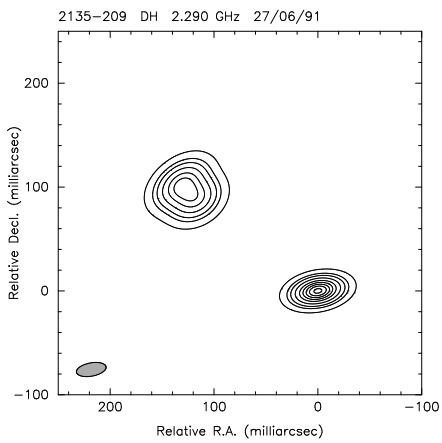

Maximum: 0.7134 JY/BEAM
Beam: FWHM 29.00 × 12.80 (milliarcsec), p.a. −79.4°

Source model contour plots continued...

(au)

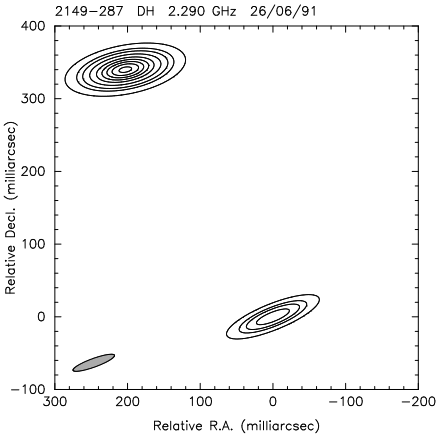

Maximum: 0.1700 JY/BEAM
Beam: FWHM 60.60 × 11.80 (milliarcsec), p.a. −70.0°

(av)

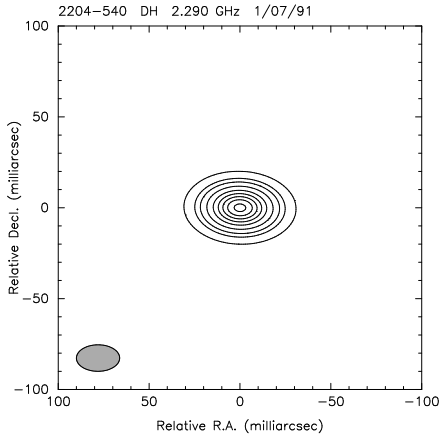

Maximum: 0.9770 JY/BEAM
Beam: FWHM 23.80 × 14.60 (milliarcsec), p.a. −89.8°

(aw)

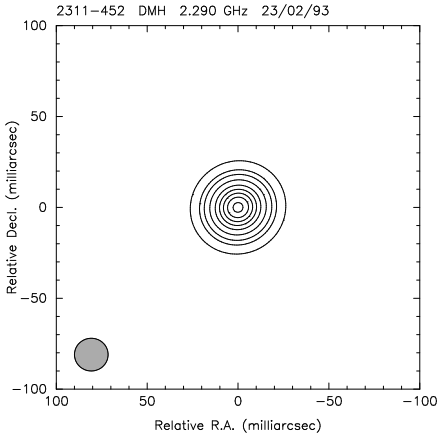

Maximum: 1.249 JY/BEAM
Beam: FWHM 18.50 × 18.00 (milliarcsec), p.a. −89.9°

Figure 6.5: Fits of the source models presented in Table 6.1 to the visibility amplitude and closure phase data.

(a)

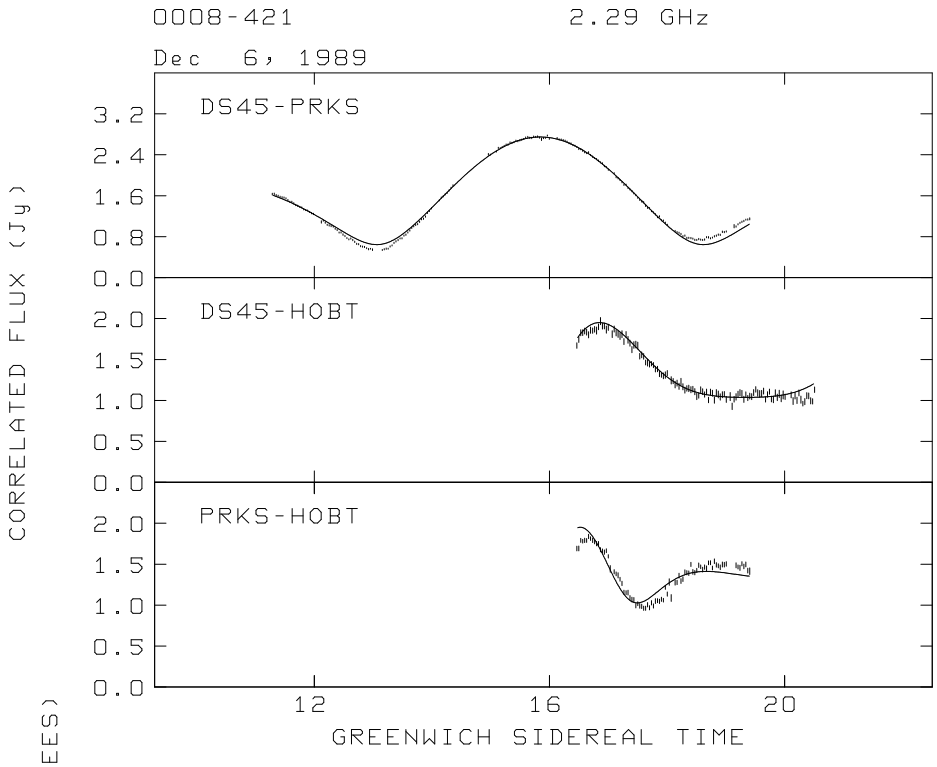

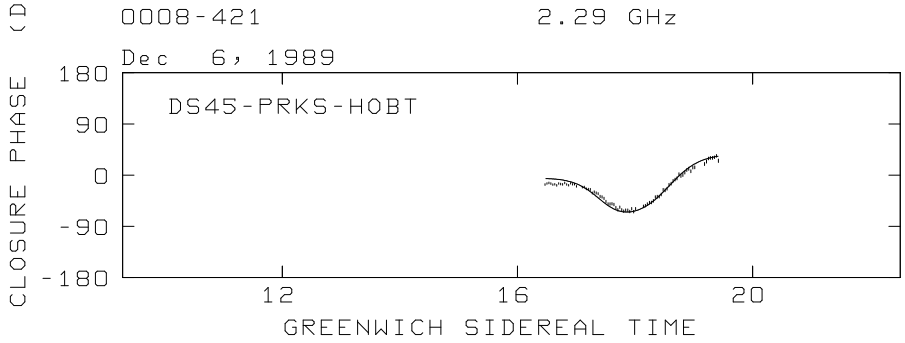

(b)

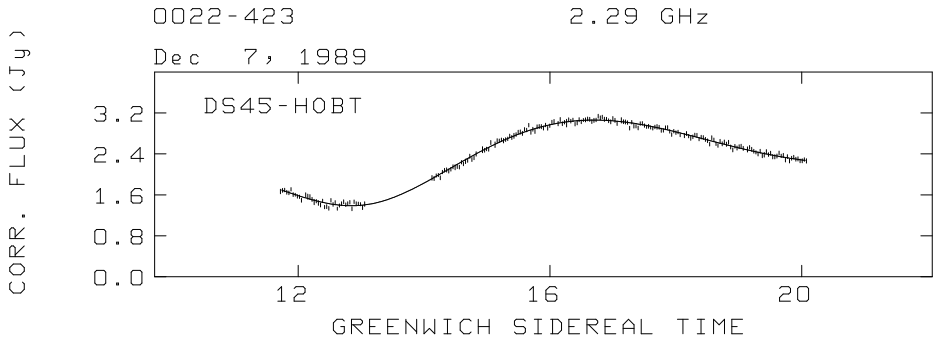

Source model visibility fits continued...

(c)

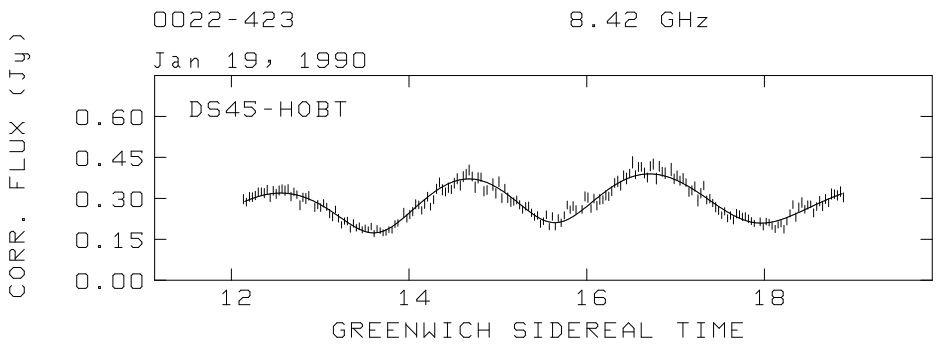

(d)

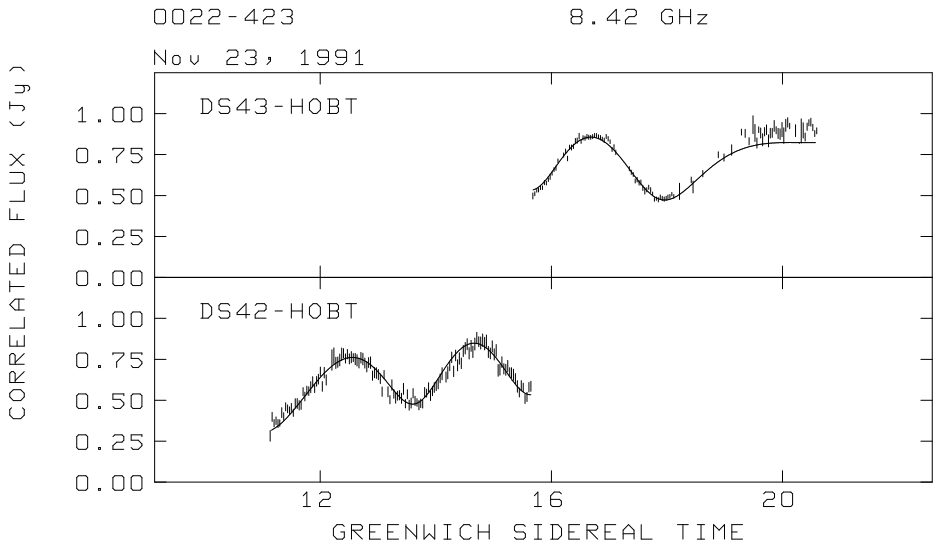

(e)

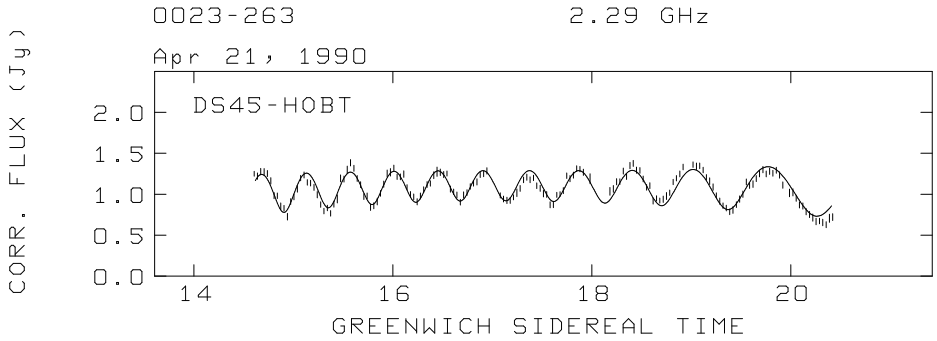

Source model visibility fits continued...

(f)

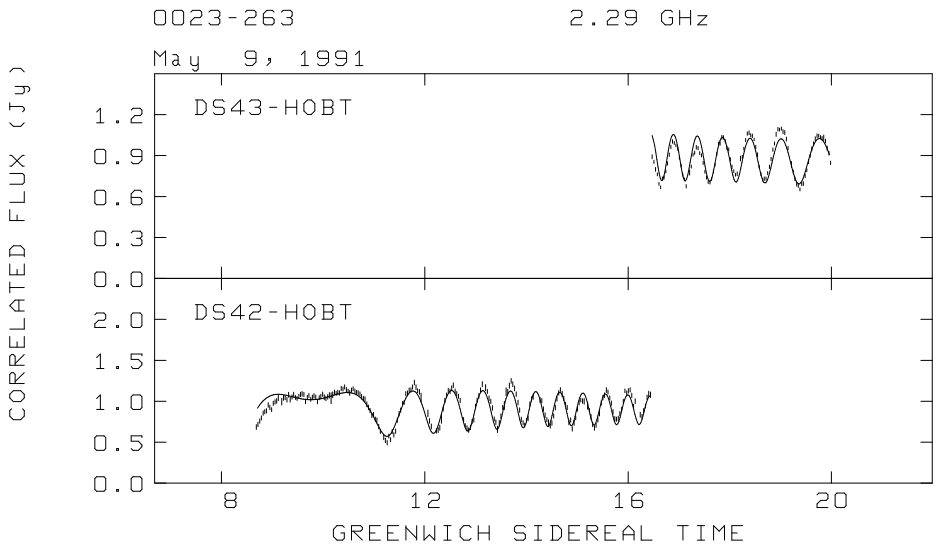

(g)

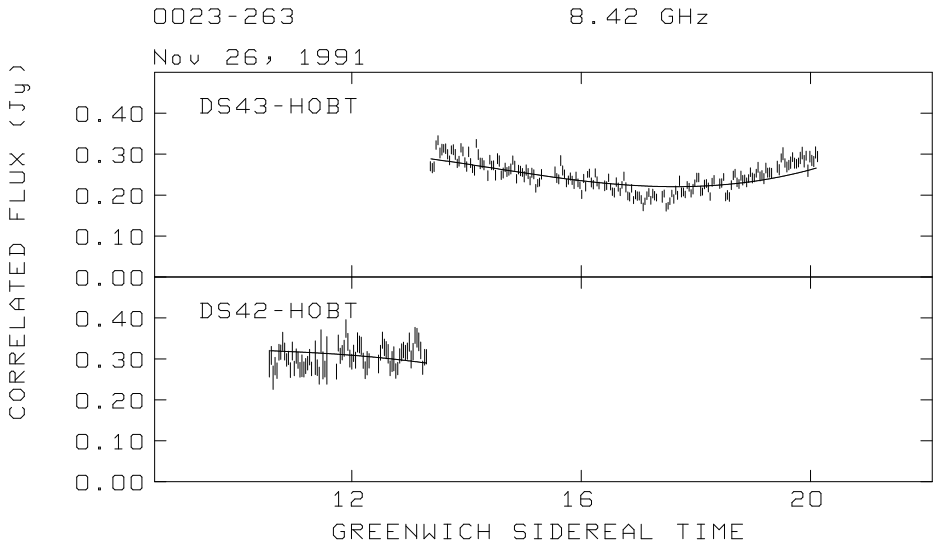

(h)

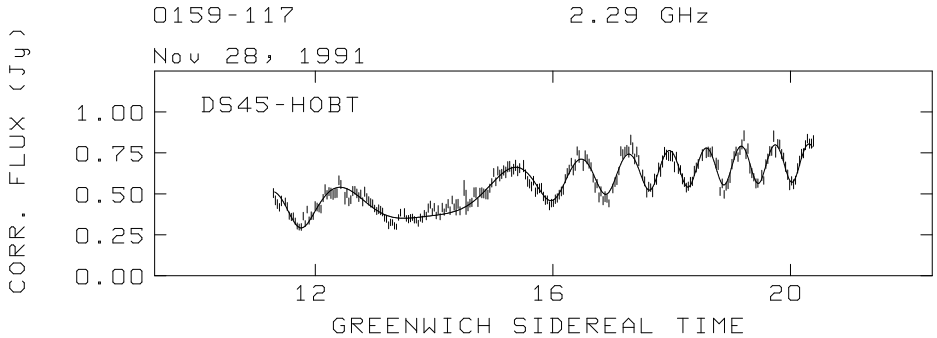

Source model visibility fits continued...

(i)

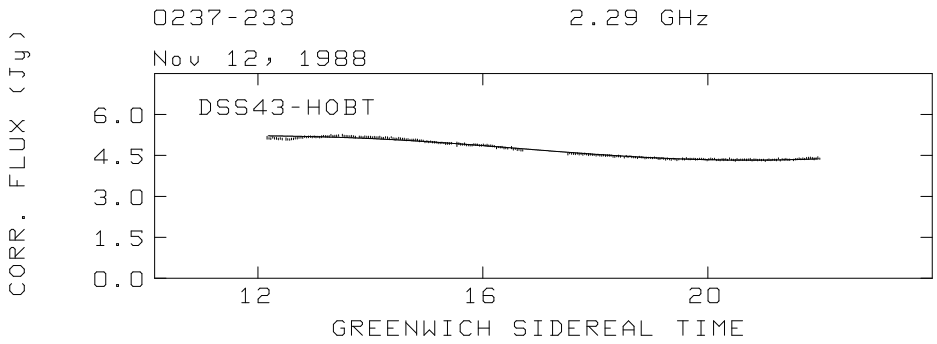

(j)

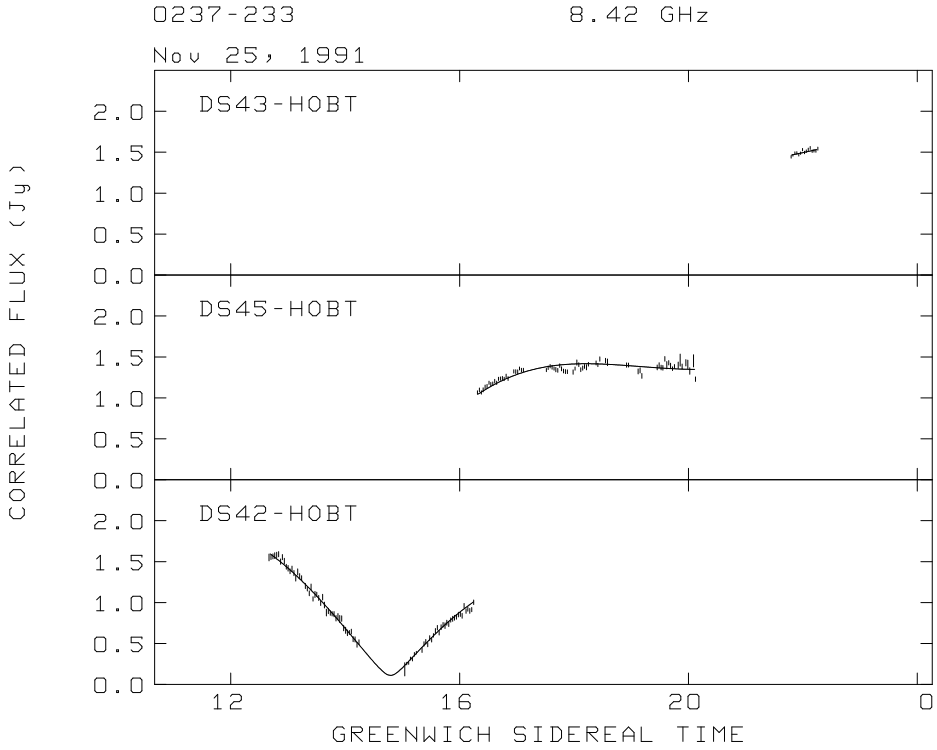

(k)

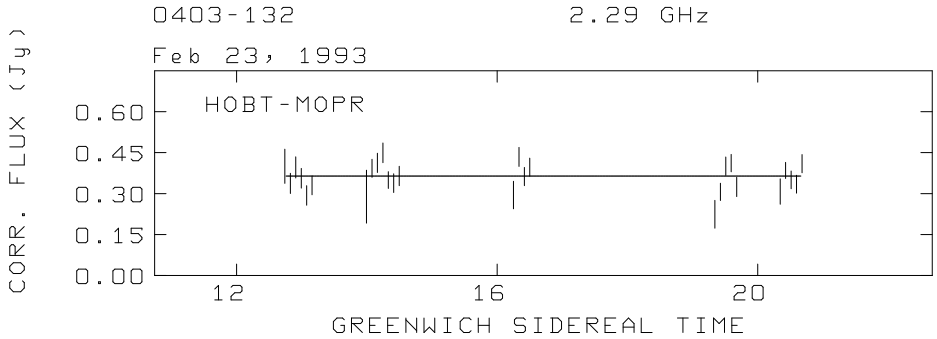

Source model visibility fits continued...

(l)

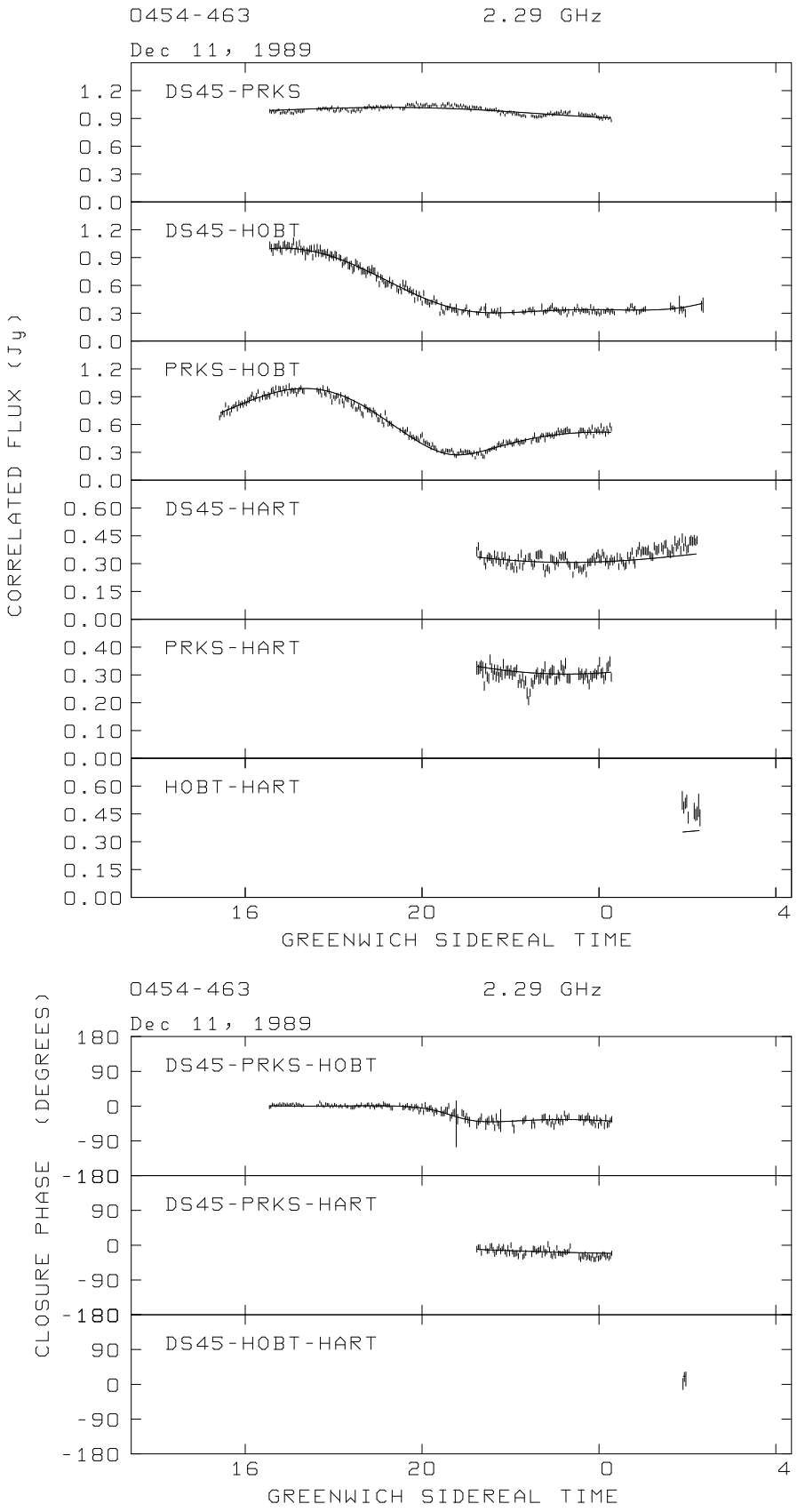

Source model visibility fits continued...

(m)

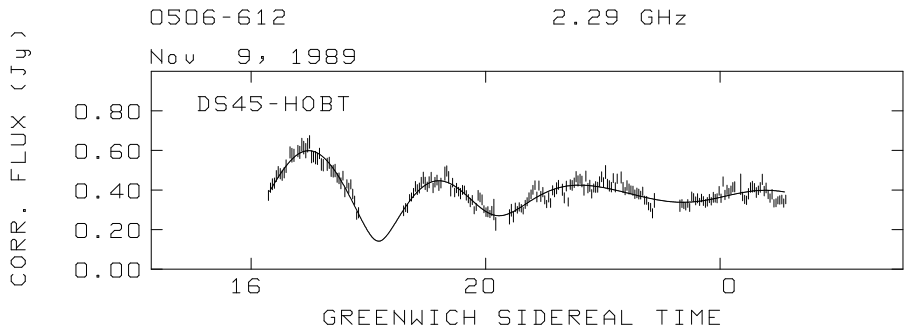

(n)

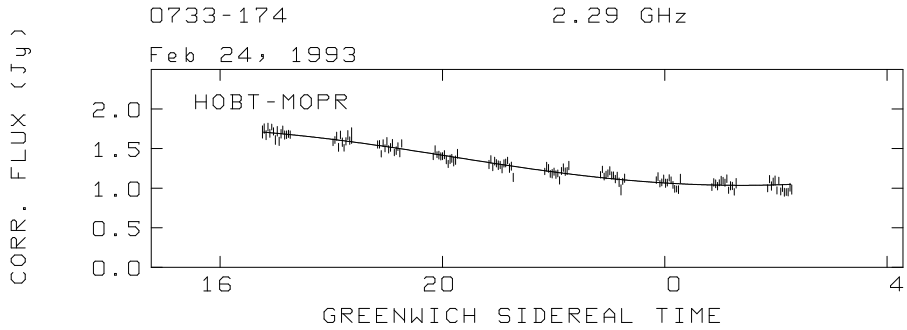

(o)

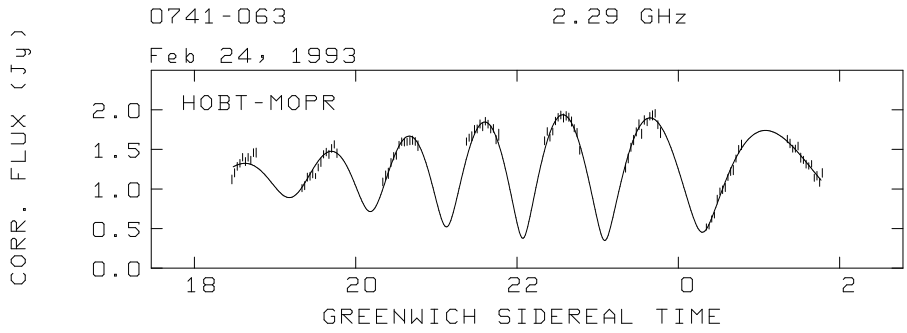

(p)

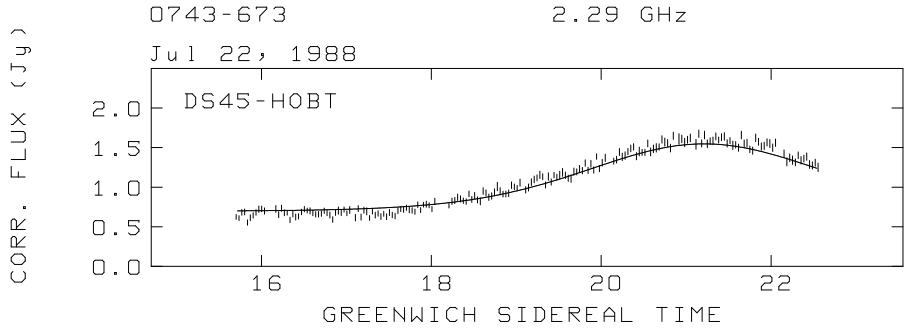

(p)

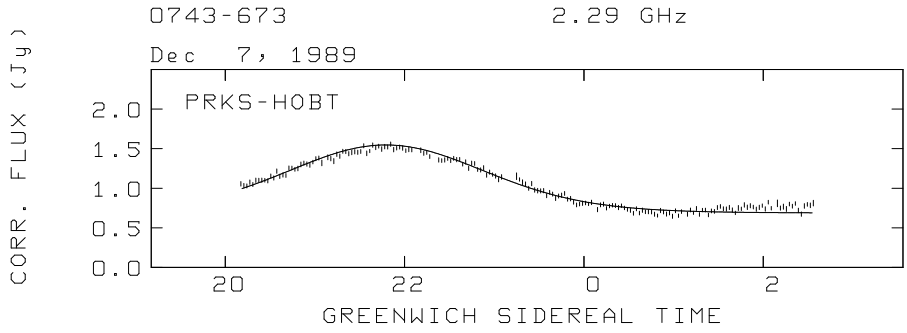

Source model visibility fits continued...

(q)

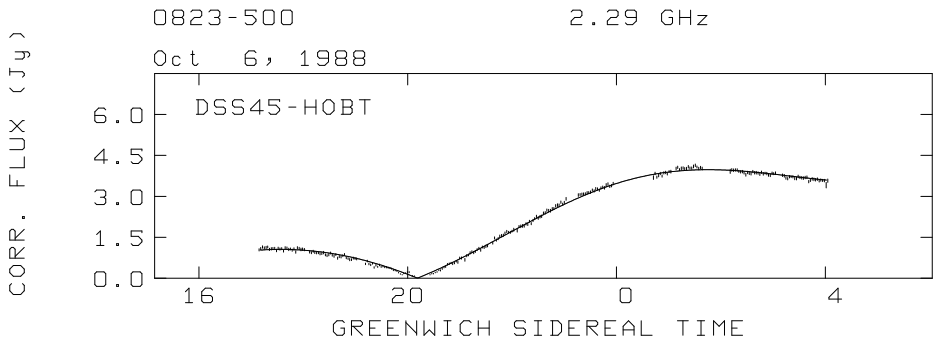

(r)

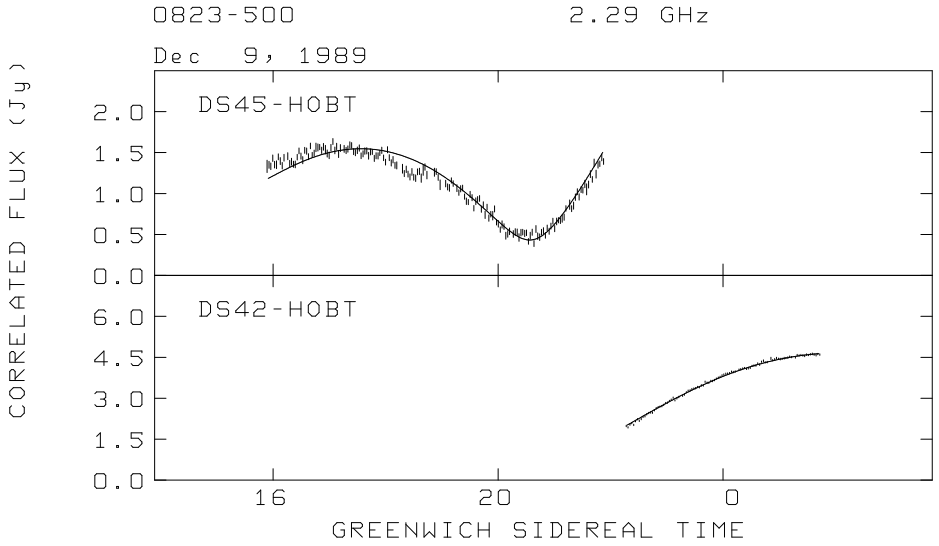

(s)

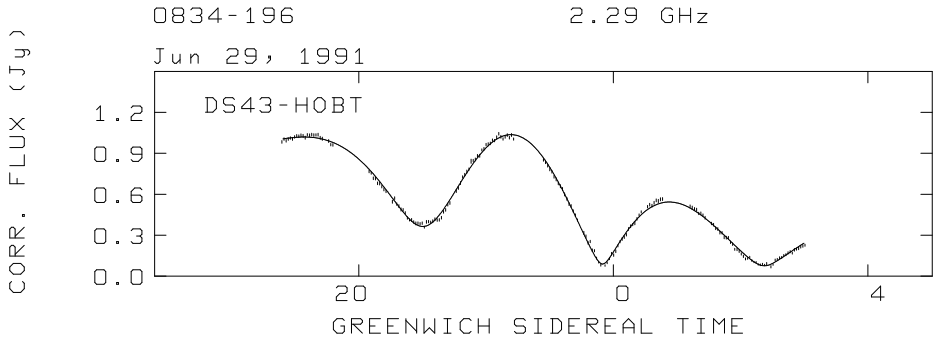

(t)

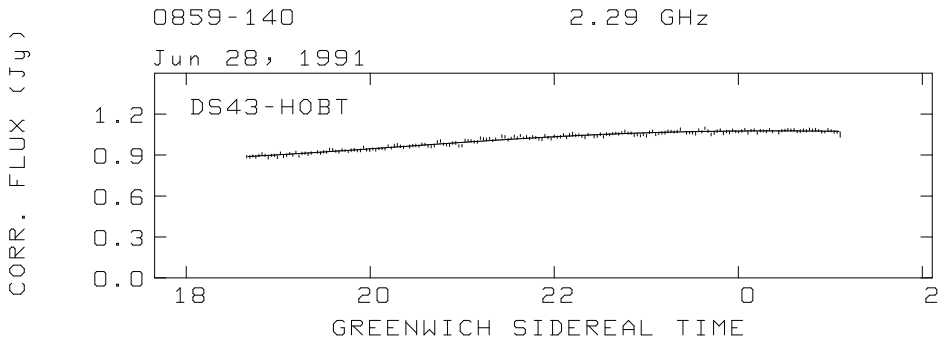

Source model visibility fits continued...

(u)

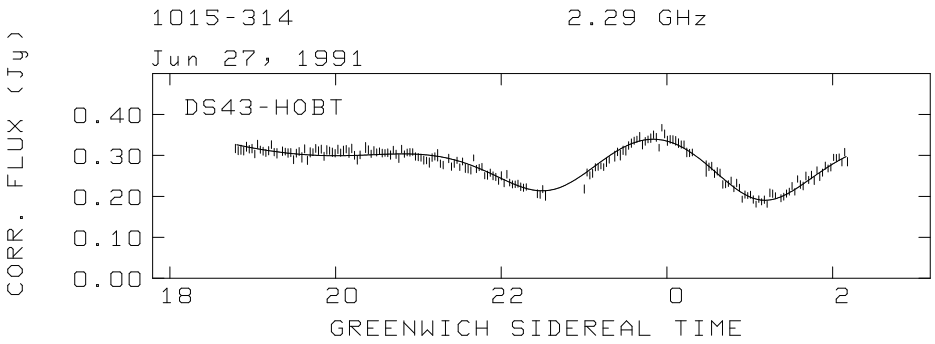

(v)

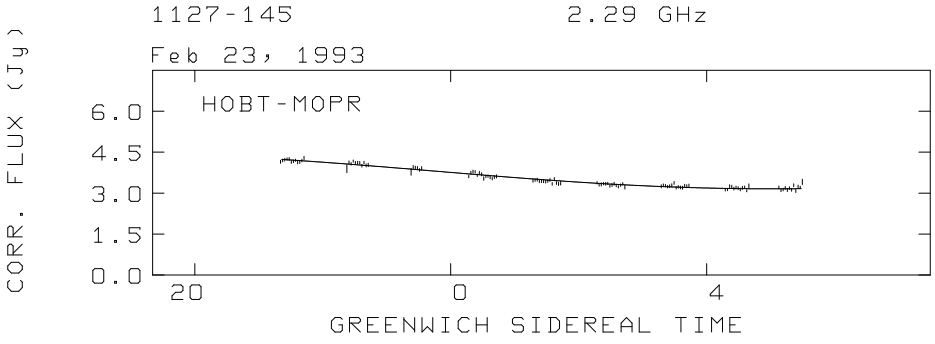

(w)

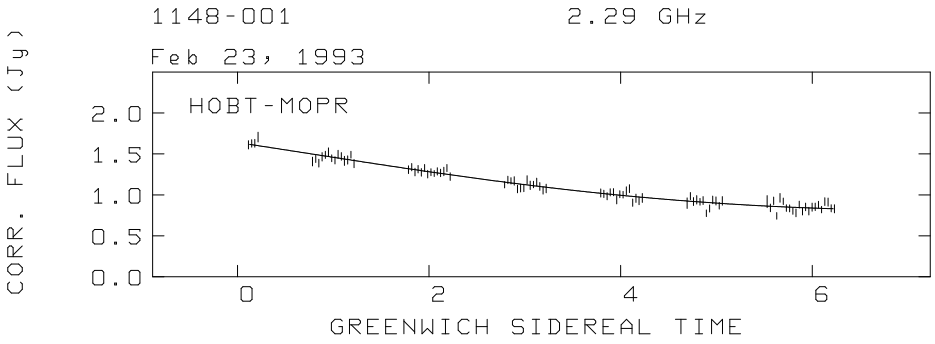

Source model visibility fits continued...

(x)

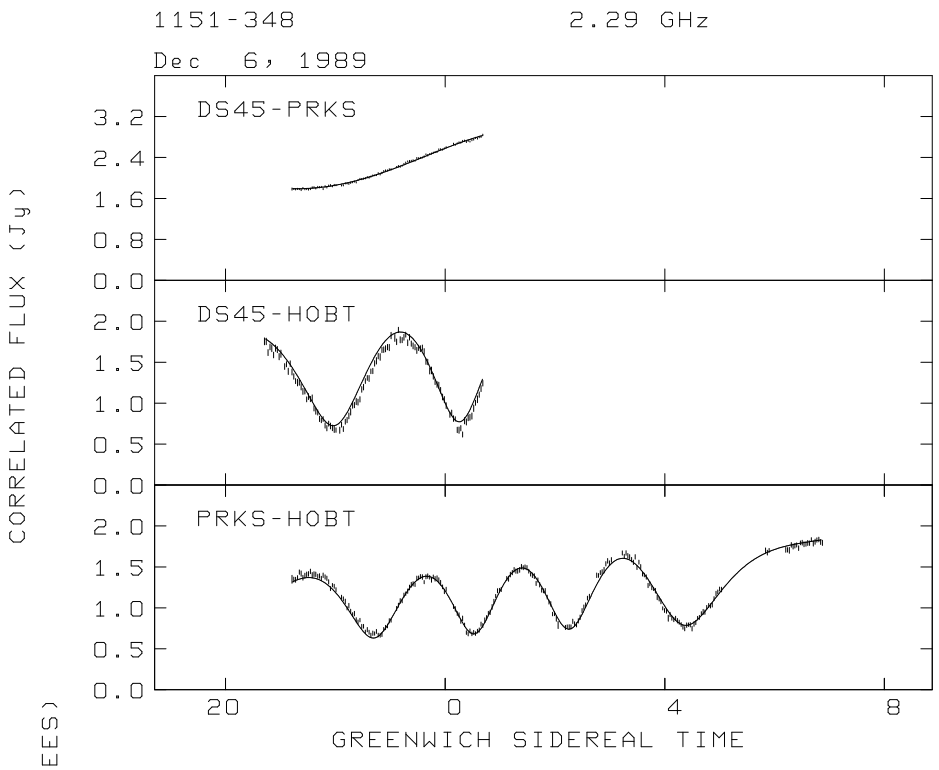

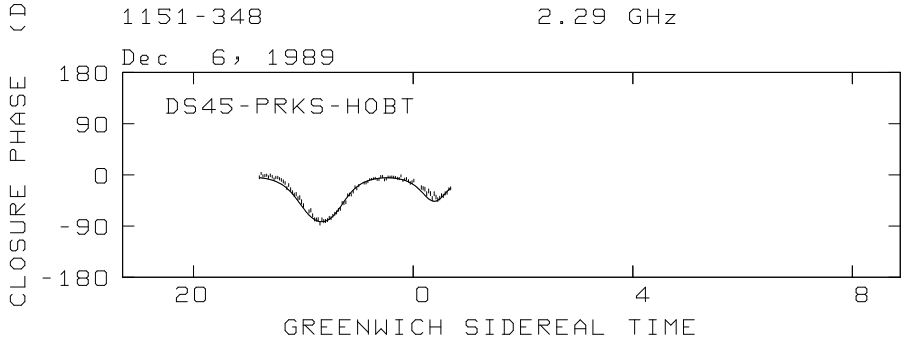

(y)

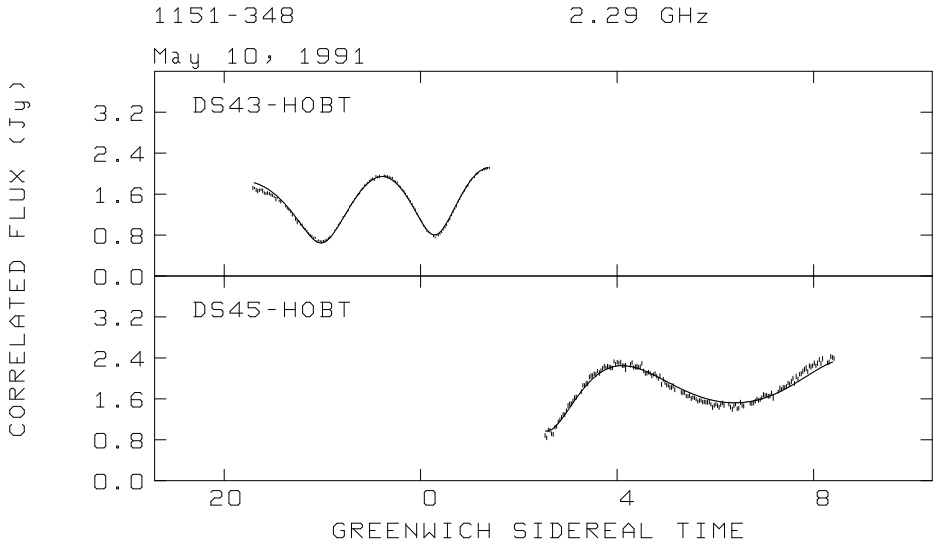

Source model visibility fits continued...

(z)

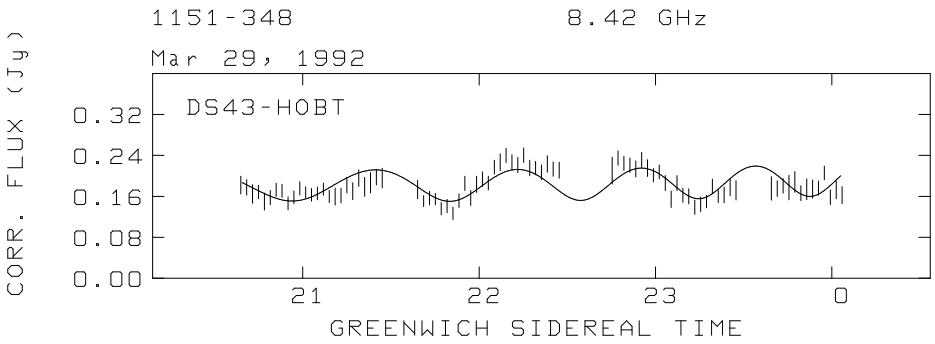

(aa)

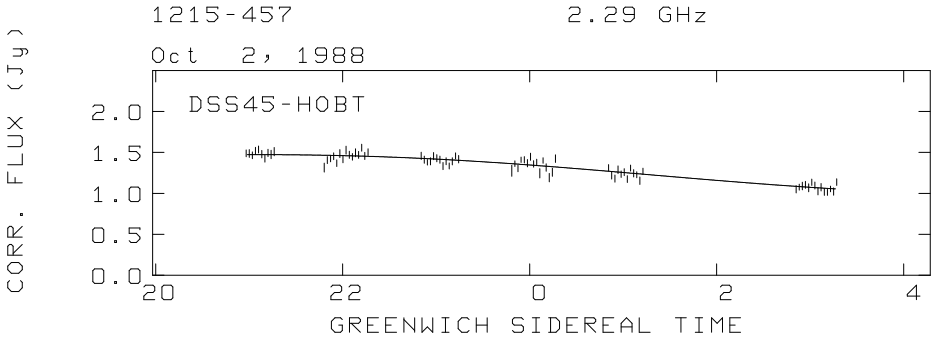

(ab)

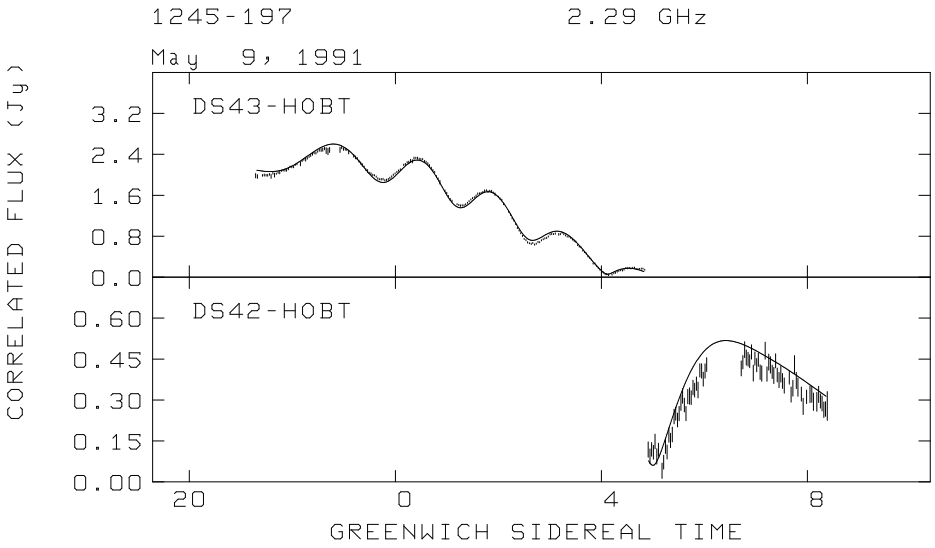

Source model visibility fits continued...

(ac)

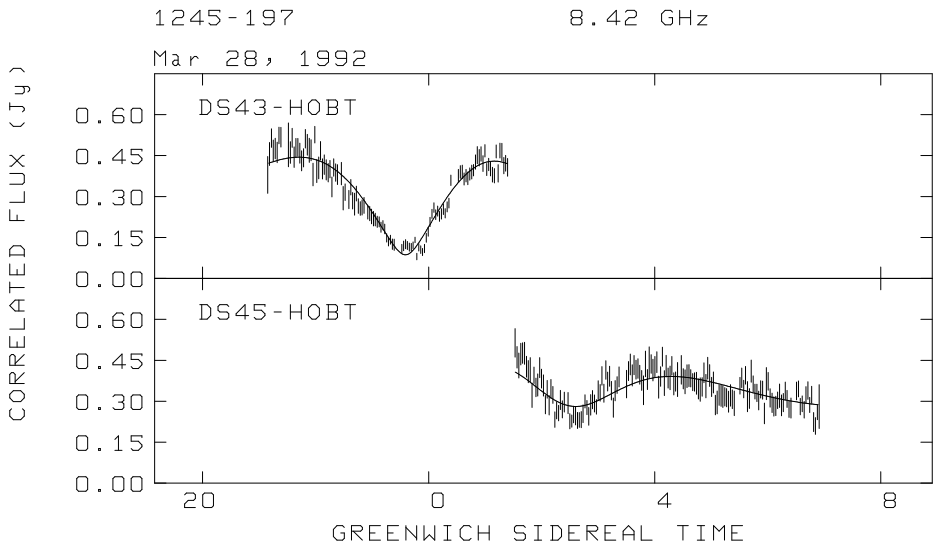

(ad)

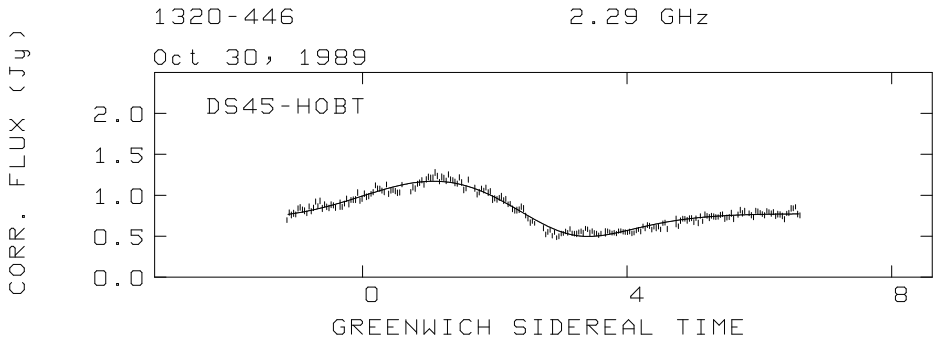

(ae)

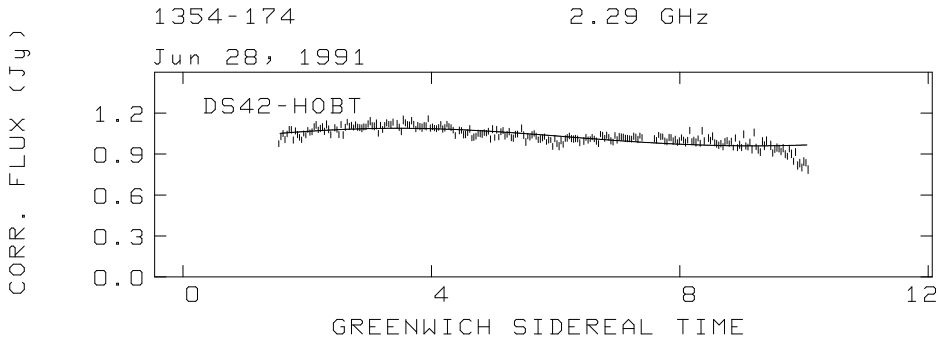

(af)

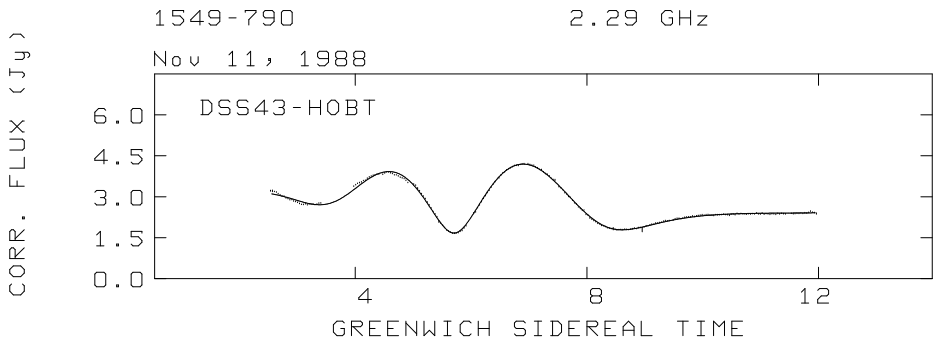

Source model visibility fits continued...

(ag)

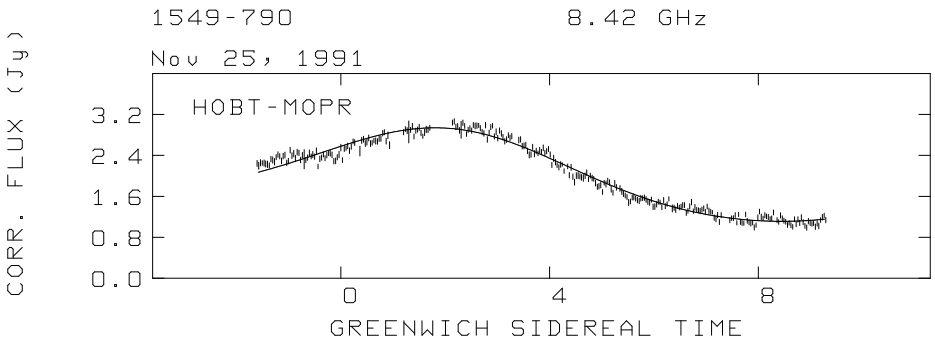

(ah)

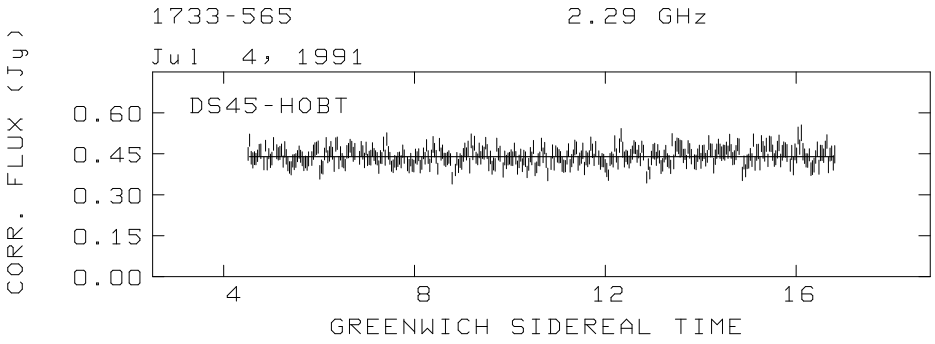

(ai)

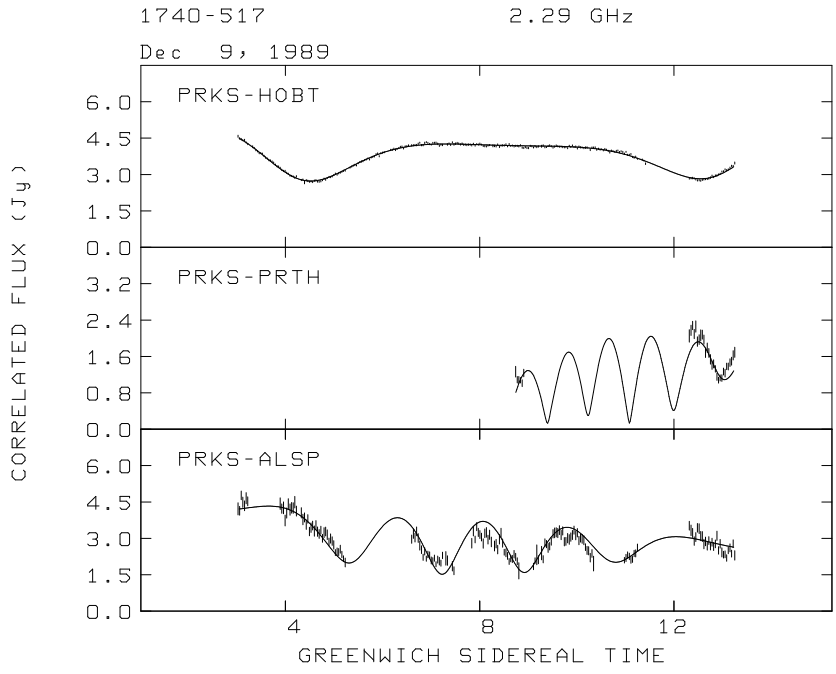

(aj)

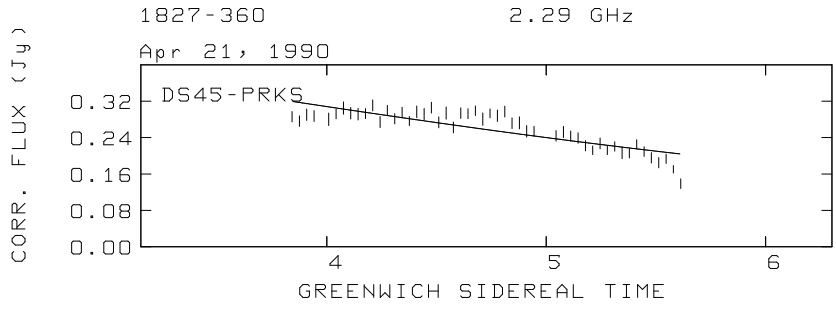

Source model visibility fits continued...

(ak)

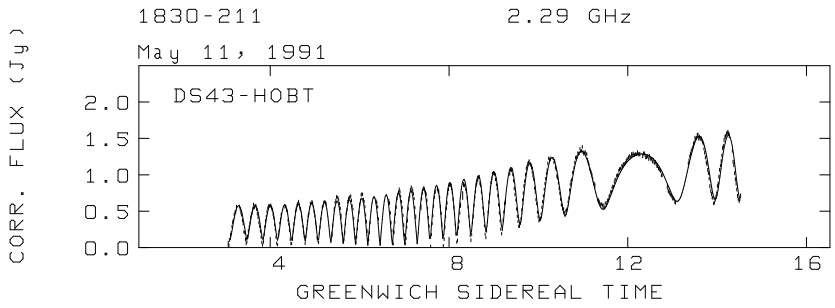

(al)

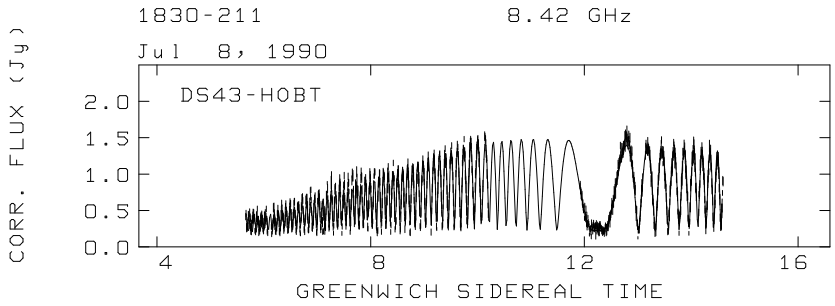

Source model visibility fits continued...

(am)

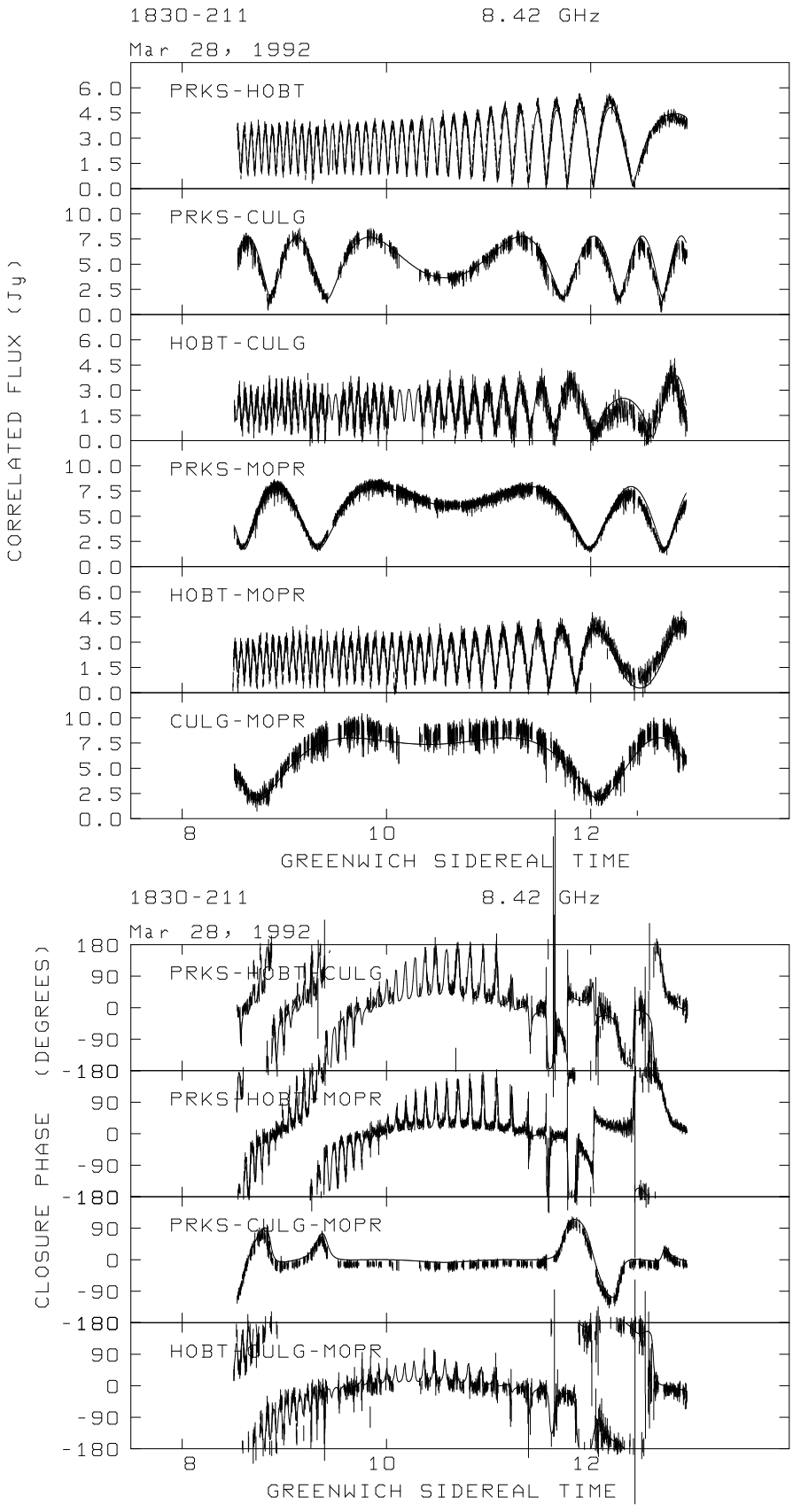

Source model visibility fits continued...

(an)

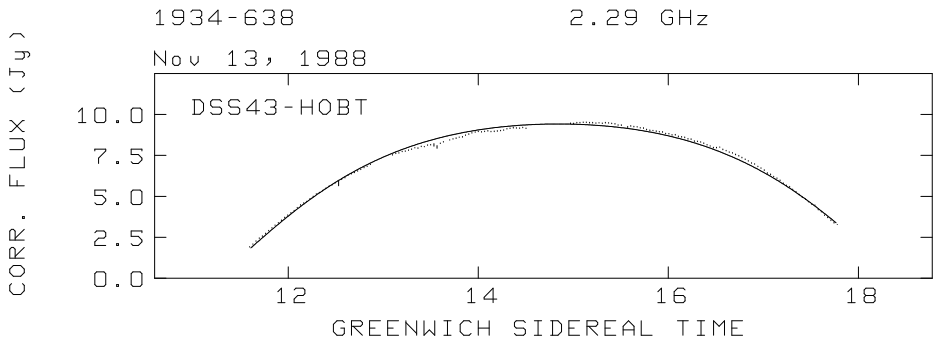

(ao)

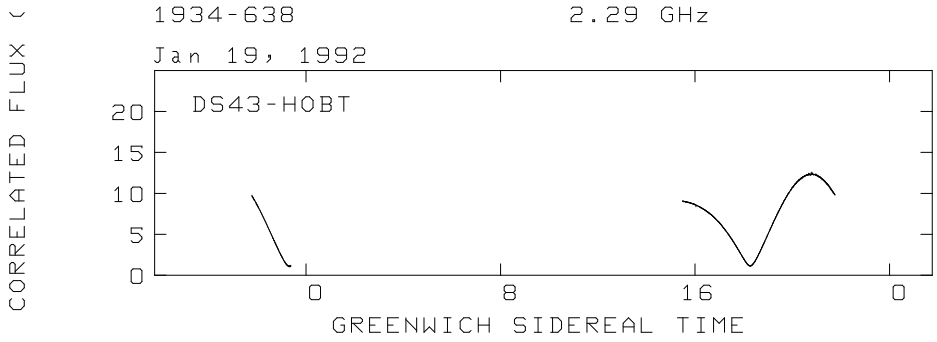

(ap)

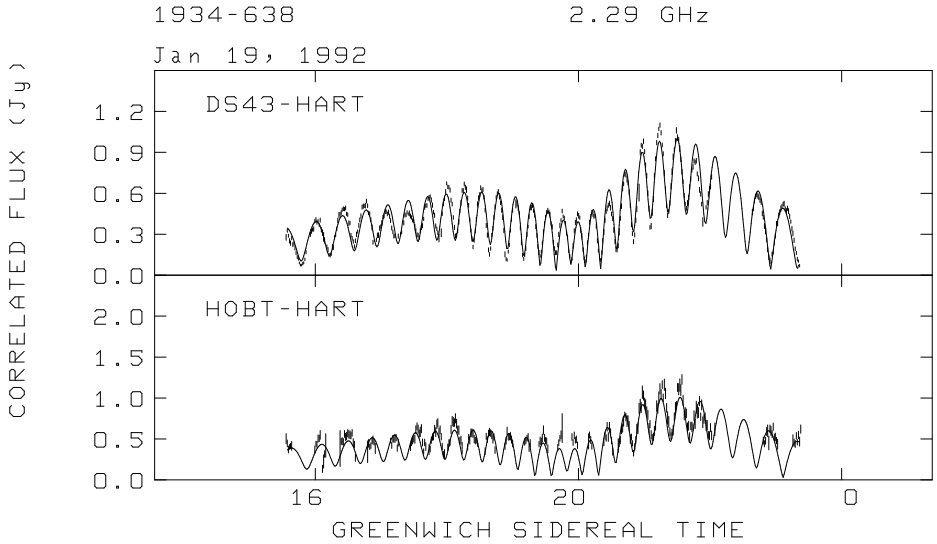

(aq)

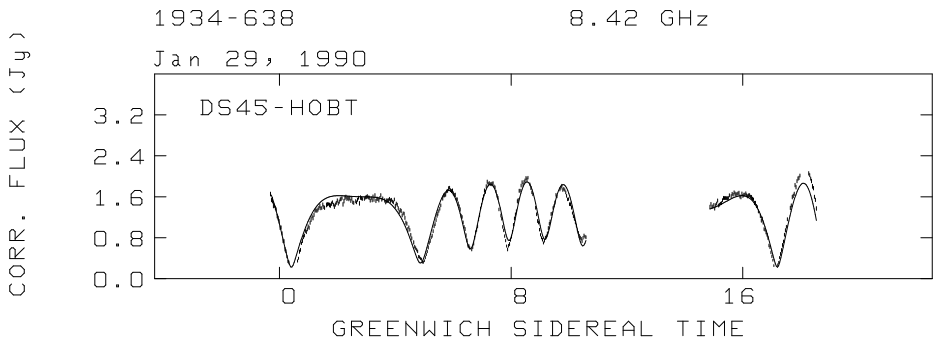

Source model visibility fits continued...

(ar)

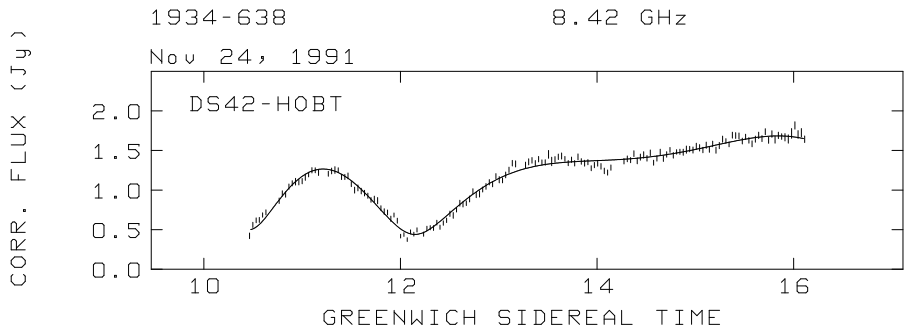

(as)

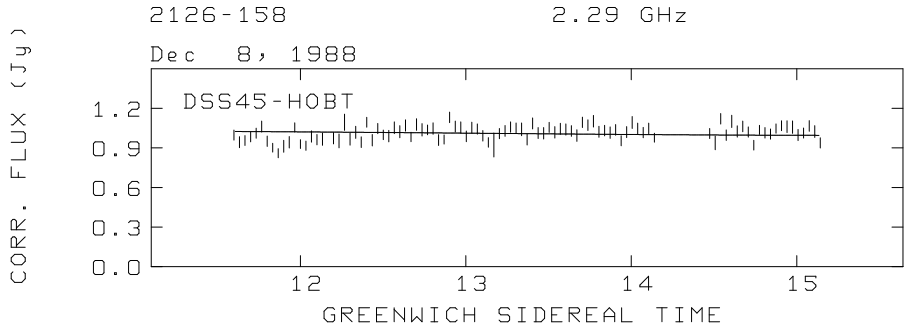

(as)

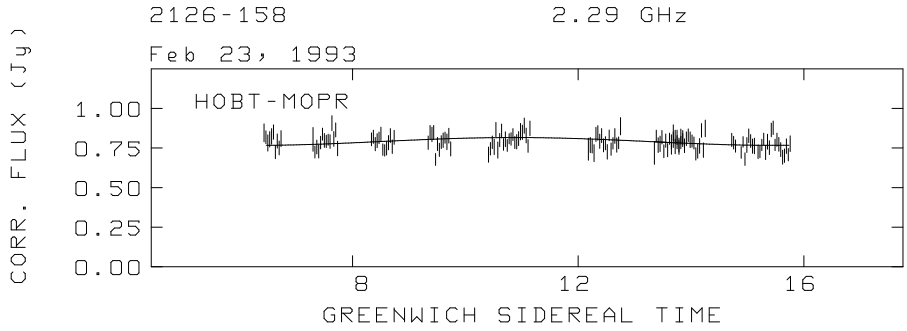

(at)

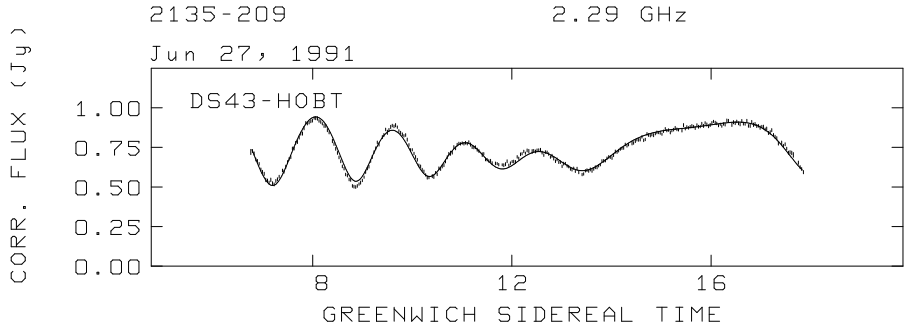

(au)

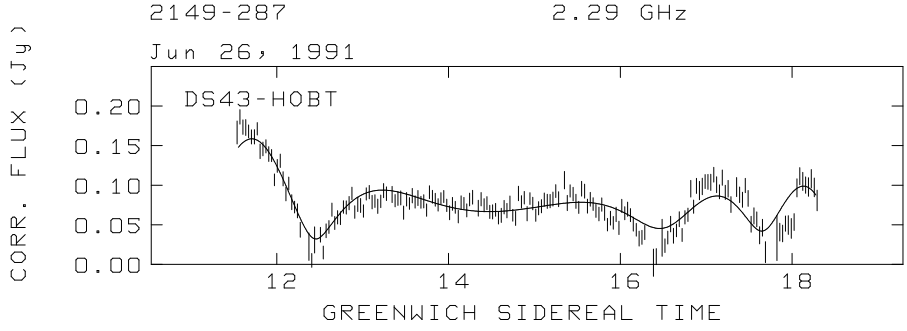

Source model visibility fits continued...

(av)

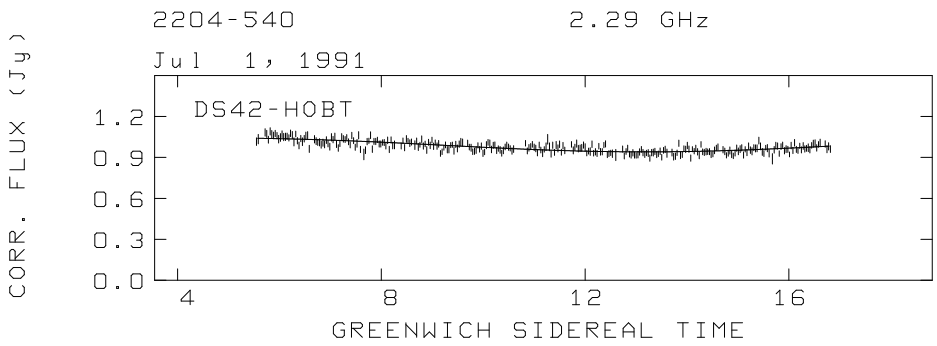

(aw)

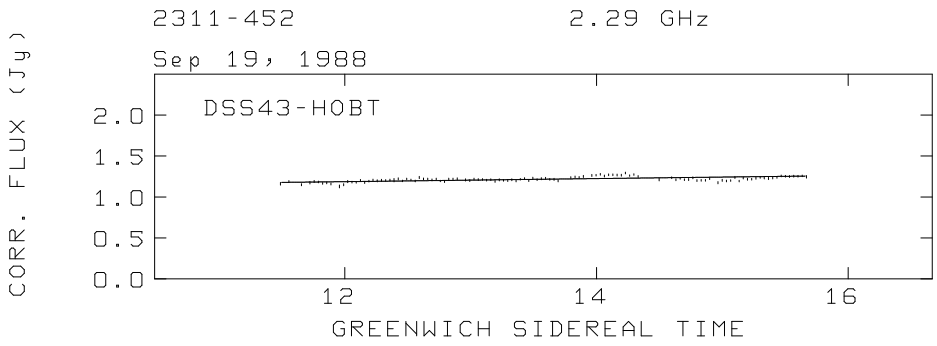

(aw)

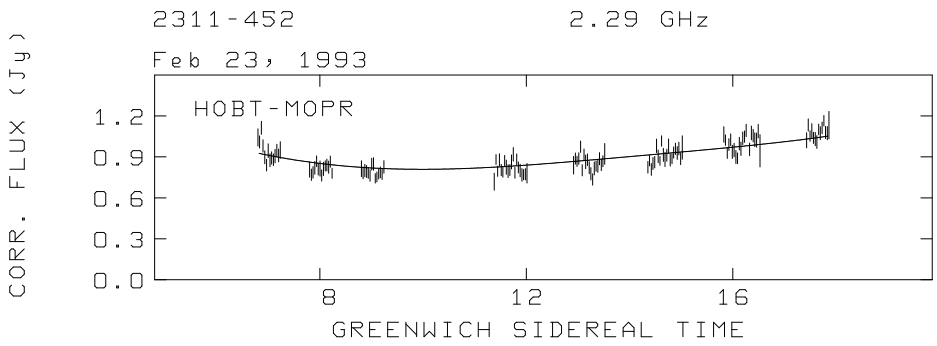

6.6 Notes on Individual Source Models

Features of particular models are discussed below on a source by source basis. The discussion includes only the details relevant to the formulation of the models, together with conclusions regarding source structure that can readily be deduced from the model fitting results. Discussion of the physical parameters determined by the model fitting process will appear in subsequent chapters concerning the properties of the source sample. Calculation of spectral indices for double sources is complicated by the 180° orientation ambiguity arising from the absence of phase information inherent in single baseline observations.

0008-421 (a): These data from an 2.3 GHz imaging experiment in November 1989 are well described by a model comprising two aligned linear components. Allowing the components to become elliptical only resulted in a few percent improvement in the agreement factor.

0022-423 (b,c,d): These three models both fit the data well and the separation and relative orientation of the components agree well at all three epochs and both

frequencies. At 8.4 GHz the stronger component has the same size and orientation within 8°. Unfortunately the calibration of the January 1990 data (c) is very uncertain and it is not possible to comment on changes in the flux density of the components. However the range of parameters method was used to set limits on the change in separation of the components; these limits are $28.11^{+0.75}_{-1.00}$ mas (c) and $28.51^{+0.65}_{-0.75}$ mas (d), or $0.22 masyr^{-1}$, consistent within the errors with with no significant relative motion in the 1.85 years between the two observations. If the two models (b) and (d) have the same relative orientation, so that the strongest component in (b) is correctly identified with the strongest component in (d), then both components have spectral indices of -0.9. Otherwise they are -1.6 and -0.2.

0023-263 (e,f,g): All of these models contain substantially less than the total flux of the source indicating the presence of much extended structure. Only one component was detected at 8.4 GHz (g) and though the simple elliptical Gaussian model does not fit these data completely, there is no evidence for a second component. The 2.3 GHz models have very similar component orientations and *relative* sizes. The separations of the components in these two models are 657.1^{+5}_{-6} mas (e) and $653.6^{+1.5}_{-1.0}$ mas (f), corresponding to a decrease in separation of $-3.4 masyr^{-1}$, which in not significant given the estimated uncertainties. Identifying the solitary component in (g) with the stronger more compact component in (f) yields a spectral index for this component of -0.17.

0159-117 (h): This simple model composed of a line and a point fits the data very well but contains only 40 percent of the total flux of the source. With a component separation of 1.59 arcseconds, this model has the largest angular component separation of any object in the survey.

0237-233 (i,j): Both of these models, at 2.3 GHz and 8.4 GHz, contain the total flux of the source, demonstrating that any extended structure is either exceedingly weak or absent. The 2.3 GHz model (i) does not have sufficient resolution to distinguish two separate components. If the flux densities of both components of model (j) are combined, the spectral index is -0.6. If the spectral indices of one of the components is flatter, then the other is steeper than -0.6.

0403-132 (k): Very little data was obtained for this source (owing to difficulties with equipment at Mopra). The low correlated flux density is barely ten percent of the total.

0454-463 (l): The simple model for this source fits both the trans-oceanic baselines and the shorter Australian baselines very well, suggesting that there is no very compact structure in the weaker component which is resolved to Hartebeesthoek.

0506-612 (m): Considerable effort was expended in trying to fit this source with only two components however no satisfactory model was found. The final model, with three components comprising nearly half the total flux density, is more acceptable and indicates that there are basically two separate components,

one of which is complex.

0733-174 (n): A circular Gaussian component was not sufficient to represent these data. The source is slightly elongated and the peak correlated flux density of 1.7 Jy suggests that 0733-174 is partially resolved at this resolution.

0741-063 (o): These data are well fit by two components that together contain only 35 percent of the total flux density.

0743-673 (p): Two different baselines separated by sixteen months in time, and both from unsuccessful imaging experiments, are available for this source. Both data sets are fit well by two similar but independent models. Model (p), plotted in the figures, was derived by merging the two data sets and fitting both simultaneously. It is very similar to the individual models and contains about half the total flux density.

0823-500 (q,r): Both these observations are adequately fit by models consisting of a point and a circular Gaussian. The source has clearly changed significantly in the fourteen months between the two observations. The minimum correlated flux density in the 1989 data is 0.5 Jy compared with 0.0 Jy in the earlier observation. The 1988 data demonstrates the importance of the amplitude bias correction discussed in Section 6.4. Examination of the *unaveraged* amplitudes and phases in the vicinity of the minimum indicate that the earlier correlated flux density is indeed zero. It is worth noting that even coherent averaging does not produce the correct result for these data. In principle, coherent averaging should yield a zero flux density because of the random phase distribution in zero signal to noise ratio data (Moran, 1976). However this relies on a sufficiently large number of points being averaged; for these data a two minute coherent average yielded a minimum flux density of 0.14 Jy.

No total flux density measurement is available for the 1988 observation, however the 4.5 Jy in the model is significantly less than the mean of 5.5 Jy observed during the subsequent flux monitoring survey (Chapter 3). Unfortunately the 6.2 Jy in model (r) is nearly nine percent in excess of the total flux density measured during the experiment (5.7 Jy) and the discrepancy is larger than can be accomodated by reasonable estimates of the calibration uncertainties. This problem most likely arises because the size of the circular Gaussian component is not well constrained by the data which cover only a very narrow range of spacings in the *uv*-plane between 4.8 and 6.2 Mλ. However the only simpler model, two point sources, is a much poorer fit to the data and therefore makes it much more difficult to set limits on the acceptable parameter ranges. The underlying cause of the problem is probably that the circular Gaussian component is not the ideal object with which to represent the the source, though these data neither require nor constrain more complicated components.

Table 6.2 gives the parameters and limits on the flux densities and component separations of the models fit to each of the two data sets. The measurements show that there is no significant change in the spacing of the two components and that

the flux density of the unresolved component has remained constant. However, although the quoted limits can just accomodate no change in the extended component, it appears to have undergone an increase in flux density of approximately seventy percent. If the constraint that the flux density in the model is not permitted to exceed the 5.7 Jy measured total flux density is applied, then this estimate is closer to fifty percent.

Despite the difficulties involved in quantifying the exact magnitude of the changes in this source, a straightforward visual inspection of the two sets of visibilities makes it quite clear that there has been a change of at least 0.5 Jy in the relative flux densities of the two components.

Epoch	Flux Density (Jy)	Radius (mas)	Angle (°)	Size (mas)	Agreement Factor
88.77	$1.96^{+0.13}_{-0.12}$	0	0	0	1.99
	$2.5^{+1.2}_{-1.0}$	$21.3^{+0.6}_{-0.4}$	127	8.5	
89.93	$2.02^{+0.06}_{-0.07}$	0	0	0	1.92
	$4.2^{+2.0}_{-0.8}$	$21.7^{+0.4}_{-0.6}$	130	12.7	

Table 6.2: Model parameters and limits for 0823-500.

0834-196 (s): The changing spacing of the amplitude maxima and minima in the *uv*-plane for this source signify that more than two components are required to fit these data. The final model, consisting of a point source and two partially resolved components that appear to both be part of the same structure, fits the data very well and accounts for 85 percent of the total flux density.

0859-140 (t): The slow change in visibility amplitude for this object indicates that it is only slightly resolved. However, the component giving rise to the correlated flux density on this baseline contains less than half the total flux of the source.

1015-314 (u): This three component model consists essentially of two distinct components, one of which has additional complexity. Before GST 21:00 the model only just fits the data, within the error bars, and it is likely that more data at different spacings would lead to a somewhat different model. There is certain to be other structure since the model accounts for less than half the total flux density.

1127-145 (v): 1127-145 is only slightly resolved between Hobart and Mopra. Almost the total flux density is present on this baseline, indicating minimal extended emission.

1148-001 (w): The thirty percent drop in correlated flux over the duration of this observation strongly suggests that this source is partially resolved. However the single component model has a flux density of 3.0 Jy, considerably in excess of

the 2.6 Jy computed by interpolation from the Parkes Catalogue values. Unfortunately this object was not included in the flux monitoring survey and there is no independent measurement of the total flux so it is not possible to gauge whether this discrepancy arises from variability or calibration errors.

1151-348 (x,y,z): The 2.3 GHz data from 1989 (x) require an extended third component to fit the short baselines. This component does not appear in the other two models since they are based only on the longer baseline or higher frequency data. The three component model has slightly more than the total flux density of this source so there is unlikely to be very much emission from any other extended components. The evidence for the second component at 8.4 GHz (z) is not strong and the data do not constrain its location very tightly. The source is well resolved with the model containing only fifteen percent of the total 8.4 GHz flux density. The separations of the two compact components in models (x) and (y) are $93.0^{+1.2}_{-0.5}$ mas and $92.1^{+1.0}_{-0.8}$ mas respectively ($-0.6 masyr^{-1}$), consistent with no significant change over a period of 1.4 years. Identifying the two strongest components in (y) and (z) with one another yields a spectral index of -1.4. The flux density of the weak third component in (z) is poorly determined, simply because of the low signal to noise ratio, but it appears to posses an even steeper index of -2.8.

1215-457 (aa): A single linear component model fits these data well but provides less than half the total flux density.

1245-197 (ab,ac): The three components in the 2.3 GHz model posses almost sixty percent of the total flux density of the source. The short segment of data from the DSS 42 baseline is crucial in the determination of the double structure of the strong compact component. The single beat on this baseline can not be fit by a two component model, although a moderately good fit can be achieved for the DSS 43 baseline with only two components. The 8.4 GHz model clearly resolves the strong component to reveal the two compact 'cores' which account for nearly half the flux density at this frequency. Both have spectral index -0.9, with only slight variation (2%) if the orientation is in error by 180°. Evidence of the weaker component seen at 2.3 GHz is absent in the 8.4 GHz data.

1320-446 (ad): The model of this object fits the data well but approximately a third of the total flux density is missing in the model, probably owing to substantial resolution of the an extended elongated component.

1354-174 (ae): The detection of slight elongation in 1354-174 depends rather tenuously upon accurate calibration of the data. While the model fits better than would a point source, the agreement between the model and measured visibilities is not entirely convincing. This is particularly so near the end of the observation where the most substantial discrepancy occurs, possibly due to poor calibration as the source set.

1549-790 (af,ag): The 2.3 GHz model (af) is an exceptionally good fit to

the data and contains more than ninety percent of the total flux density. The 8.4 GHz data is taken from an imaging experiment in November 1991 for which the Tidbinbilla–Hobart baseline observed for only two hours. The Hobart–Mopra baseline, with more than ten hours of data, was selected for model fitting instead. Since several of the single baseline survey sources have been observed on this baseline these data can provide a check of the success of the model fitting (compared to the images) on the longer baseline. The single component accounts for eighty percent of the total flux density and has a spectral index of -0.05.

1733-565 (ah): There is no evidence for any milli-arcsecond scale structure in these data which are well fit by a point source. The model has only eight percent of the total flux density so there is clearly much extended emission.

1740-517 (ai): These data come from an imaging experiment in December 1989. No correlations were detected between Hobart, Perth and Alice Springs for this source. The model is good fit to the shortest baseline but does not account for the longer baselines so well, indicating either the presence of more complicated complex compact structure or else poorer calibration of the less sensitive stations. The total flux density of 5.2 Jy is slightly less than the 5.4 Jy of the model. Thus all the emission is concentrated in the modelled compact components.

1827-360 (aj): Very few conclusions can be drawn from this short data set which demonstrates only that a weak compact component is present in this source.

1830-211 (ak,al,am): Both the 2.3 GHz and 8.4 GHz models of the single baseline data (ak,al) fit the observations well. However neither accounts for more than 25 percent of the total flux density so there is clearly substantial emission from structures with larger angular sizes to which these observations are insensitive. The orientations of both the components in all the models derived from the three independent data sets are *all* consistent within 35° so the data do constrain these parameters for this source.

The extensive data set on which model (am) is based comes from an imaging experiment in 1992. The data were not amenable to imaging because the uv-coverage was too limited. Only four hours of data were available and no Tidbinbilla antenna participated resulting in a very large gap in the uv-plane between the baselines between the three ATNF antennas and the baselines to Hobart. However the model, composed only of two elliptical Gaussians, fits the data very well. The severest discrepancy is on the shortest baseline (Culgoora–Mopra) indicating the presence of emission from components with an angular size of several hundred milli-arcseconds.

The difference between the model and total flux density for model (al) is 4.3 Jy, whereas for the 1992 data set, taken only a few weeks after the peak in the 8.4 GHz light curve (Chapter 3), the difference is 2.7 Jy. This corresponds to an apparent decrease of, at most, 1.6 Jy (37%) in the extended structure compared with a 6.6 Jy (450%) increase in the compact components. Clearly the flux density outburst observed in this source is concentrated in the compact structure, and it is not

confined to just one of the compact components, *both* have increased greatly in flux density. The apparent decrease in the flux density of the extended structure may not be real, reflecting rather the limitations of the modelling procedures when confronted with a very complicated source. The substantial flux density variations seen in this object mean that spectral index measurements must be based on observations close, if not coincident, in time.

While there is still missing extended flux in the model derived from the 1992 data set, the observation is still sensitive to some of the extended structure. This makes it very difficult to test for changes in the separation of the compact components since the previous 8.4 GHz observation (model al) because the large scale emission has the potential to interfere with, and bias the separation measurement. To test whether this effect is important the three baselines to Hobart, which are sensitive to only the most compact components, were selected and the model was refit using these alone. The procedure was repeated also for just the Parkes–Hobart baseline which, as well as being the most sensitive, is the closest in the uv-plane to the Tidbinbilla–Hobart baseline in the 1990 observation. The separations determined from these different data groups proved to be very similar and the limits on these values were also in good agreement; each of the three measurements accommodating the others within the error estimates. The mean value is $971.46^{+0.15}_{-0.45}$ mas. This is 0.44 mas smaller than the $971.90^{+0.25}_{-0.15}$ mas separation obtained from the 1990 data, corresponding to a rate of change of $-0.25 masyr^{-1}$. It is not certain that this measurement of a decreased separation is accurate since the baselines are different and, given the apparent complexity of the source, the two observations may well be sensitive to different structures. However, it would perhaps not be surprising if such a marked change in the total flux density were not accompanied by some structural changes.

1934-638 (an,ao,ap,aq,ar): The very high signal to noise ratio achieved on the Tidbinbilla–Hobart baseline leads to a large agreement factor of 7.3 for model (an). Whilst this could reflect the presence of genuine source structure it is more probable that the error bars fail to adequately describe the fluctuations in visibility amplitude that occur on timescales greater than the averaging time and are not accounted for by the calibration procedures. The range of parameters method for determining the limits on the component separation worked well for these data, depending as it does on the visual fit rather than the χ^2 which changes extremely rapidly when the error bars are so small. The spacing found for the two components is $42.2^{+1.1}_{-1.6}$ mas.

The data sets (ao) and (ap) both come from the same three station experiment in January 1992. However the Australian baseline is sensitive to a very different scale of structure to the Hartebeesthoek baselines so these were modelled separately. No model with less than five separate components was found that satisfactorily fit all three baselines simultaneously. The well calibrated Tidbinbilla–Hobart baseline (ao) is very sensitive to changes in the component separations and the value obtained is $41.2^{+0.5}_{-0.6}$ mas, which taken with the 1988 measurement, yields a rate of $-0.31 masyr^{-1}$ that, within the errors, is consistent with no relative motion. The sum of the flux densities of the two components exceeds by 0.3 Jy

the total flux density of 12.2 Jy, probably because the component sizes are not well constrained by the *uv*-coverage, but do indicate that there is no significant flux density in extended structure. The trans-oceanic baselines (ap) resolve the two main components and reveal complicated milli-arcsecond scale structure. The three component model reproduces all the beats in the data very well but does not fit all the peaks and troughs perfectly. These three components account for only 1.5 Jy of the total flux density of 12.2 Jy and are separated by approximately 1.5 mas more than the centroids of the two components seen on the Australian baselines.

The resolution on the Tidbinbilla–Hobart baseline at 8.4 GHz is nearly 8 mas, and is approaching that achieved by the Australia–Hartebeesthoek baselines at 2.3 GHz. Unfortunately the two 8.4 GHz observations (aq,ar) cover almost mutually exclusive hour angle ranges and the 1991 measurement does not constrain the component positions well. The 1990 model (aq) does not account for all the structure detected in the observation and the two components posses two thirds of the total flux density. The ranges of component separations for the two models are $42.40^{+0.25}_{-0.2}$ mas and $41.1^{+1.0}_{-1.5}$ mas in 1990 and 1991 respectively.

While the 2.3 GHz data are consistent with no separation change over 3.2 years the 8.4 GHz data, taken at face value, indicate that a significant *decrease* in separation has occured during the intervening 1.82 years. This result is however equivocal because of a number of 'systematic' effects not accounted for by the quoted errors. Firstly, the two models do not have identical component types, so there is scope for variation in component separation as the two models accomodate the data in different ways. Secondly, model (aq) is not a perfect fit to the data and it is difficult to know how to quantify the extent to which this affects the final separation measurement, or even how to judge an already askew model as being 'significantly worse', as required in the range of parameters limit-setting method. Attempts to find a slightly more complicated model that fit the data significantly better were unsuccessful. A much more reliable test of source changes would be possible if another data set that substantially overlapped one of the others were available.

There are several possible combinations of flux densities that can be used to calculate the spectral indices for this source. The simplest approach is to assume that the strong components ($\sim$ 6 Jy) seen at lower resolution at 2.3 GHz(an,ao) are identified with the 8.4 GHz components, in which case the spectral indices lie between -1 and -2.5. Alternatively, if it is argued that the bulk of the 2.3 GHz emission arises from extended (10 mas) structure with a steep spectral index which is not detected on the Hartebeesthoek baselines (ap) or at 8.4 GHz, then the indices of the residual compact structures are much flatter and possible values lie in the range -0.9 to 1.45. Treating the two nearby components in (ap) as one, and then associating the components with the largest flux densities at 2.3 GHz and 8.4 GHz with one another, the range of spectral index for the compact components is 0.14 to 0.5.

2126-158 (as): Two different observations of this source were made using first

the Tidbinbilla–Hobart baseline, and then the longer Mopra–Hobart baseline. Although these two data sets were taken 4.2 years apart, a single circular Gaussian component model fits both well and accounts for the whole of the flux density of this source. The parameters of point source models fit separately to each data set separately also appear in Table 6.1, though only the joint model is plotted in Figures 6.4 and 6.5.

2135-209 (at): Although this model has three components, two are separated by only eighteen mas and reflect the presence of detail within a single structure which is approximately 150 mas from the third component. The model accounts for 85 percent of the total flux density and fits the data well so there is little emission arising from extended structure.

2149-287 (au): The compact structure in this source is so weak ($S_{model} < 0.03 S_{total}$) that the bulk of the data lies very close to the asymptote ($Z/\sigma \sim \sqrt{\frac{\pi}{2}}$) in the bias correction function discussed in Section 6.4 (Figure 6.1). Consequently small variations in the noise dramatically affected the corrections, despite the smoothing applied to to stabilise the correction. In view of the serious potential this had for the introduction of false structure, it was decided to integrate these data coherently. The resulting data are much smoother and are reasonably well fit by the model. The data were extremely difficult to fit because the large beat at the start of the observation dominated the χ^2 calculation and the small beats near the end, which clearly contain useful structural information, were largely ignored by the fitting program. The model presented was obtained by repeated careful adjustment, by hand, of the trial model until it was in very close agreement with the data. The model fitting program was then used to refine each parameter in turn before being allowed to search for the global minimum by varying all the (fitted for) parameters simultaneously.

2204-540 (av): The detection of elongation in this object depends crucially upon the accuracy of the calibration. However the single linear component model reflects the trend in the data well and fits with a significantly better agreement factor than a point model (AF=1.1 rather than 1.6 for a point source). The model accounts for two thirds of the total flux.

2311-452 (aw): The two observations of this source, separated by 4.4 years, and using different baselines are both well fit by a single elliptical Gaussian model component. The single component models fit to each data set separately are shown in Table tab:srcmod but only the joint model is plotted.

Undetected or Unobserved Sources

Five sources were observed with either the Tidbinbilla–Hobart or Mopra–Hobart interferometer but no fringes were detected. In all cases these observations were bracketed by, or interleaved with, successful observations of other sources so it is improbable that the detection failure results from equipment malfunctions such

as clock errors. The sources are 0624-058 (0.07), 0704-231 (0.11), 1221-423 (0.09), 1302-492 (0.11) and 1323-611 (0.11). The quantity in braces is the upper limit on the possible correlated flux density (Jy) assuming the non-detection resulted from the source being totally resolved.

Five objects, 0405-132, 1306-095, 1514-241, 1937-101 and 2052-474, were not observed during the survey.

6.7 Comparison with Imaging Data

The source models constructed and described above are based on a very limited, usually one, number of baselines and have been formulated according to a strict set of rules designed to prevent the introduction of false structure. However, before proceeding to use or interpret the information contained within these models, it is appropriate (and prudent) to test the success of the procedure and establish the reliability of the one baseline model parameters. To this end, a single baseline from each of the imaging data sets presented in Chapter 5, has been taken and subjected to the same modelling procedures and rules as the single baseline survey data. The Tidbinbilla–Hobart baseline was chosen in each case, except for 1549−790 at 8.4 GHz where the Tidbinbilla–Hobart baseline comprised only two hours of data and the Mopra–Hobart baseline was used instead. The models derived from these data have already been presented but are summarised here in Table 6.3.

Source parameters, including component flux densities, angular sizes and separations, have been measured from the images created using the complete data sets (Chapter 5). These values can be used to assemble simple models representing structure observed in the images and so permit a direct numerical comparison with the corresponding single baseline data models. These "image models" are also listed in Table 6.3.

A general comparison of imaging and model fitting for the array data can be made simply through examination of the images (Chapter 5) and the contour plots of the single baseline models (Figure 6.4). The references to the relevant contour plots are given, together with the image figure references, in Table 6.3.

The result of this comparison is that the number of model components and their relative positions agree well with the images. Even for 1151−348 at 8.4 GHz (model-z), where the evidence for the secondary is very weak, the model fitting has located the component with remarkable accuracy. In only three cases, all at 8.4 GHz (0023−263, 1245−197 and 1549−790), the single baseline models do not recognise a weak and extended secondary component that is visible in the corresponding images. This is because the Tidbinbilla–Hobart baseline (or in the case of 1549−790, the Mopra–Hobart baseline) has insufficient surface brightness sensitivity to reveal the presence of these components. The model of 1934−638 made from the baselines to South Africa (model-ap) does not reproduce the detailed structure in the resolved component very accurately (*cf* Figure 5.19), but it is readily apparent from the fit of the model to the data that this model is not completely adequate. In *no* cases do the models contain *more* components than are seen in the images, indicating that the restrictive model fitting rules have

Fig. ref.	Source name	Obs. freq. (GHz)	Cpt. f.d. (Jy)	Centroid Radius (mas)	Centroid Angle (°)	Major axis (mas)	Axial ratio	Posn. angle (°)
(b)	0022-423	2.3	2.22	0	0	0	1	0
			0.84	28	119	0	1	0
5.1	0022-423	2.3	2.20	0	0	3.8	0.2	113
			0.76	28	118	5.4	0.2	126
(d)	0022-423	8.4	0.69	0	0	4.0	0	110
			0.26	28	119	3.2	0	15
5.1	0022-423	8.4	0.73	0	0	3.5	0.2	117
			0.23	28	119	2.9	0.6	151
(f)	0023-263	2.3	0.90	0	0	8.0	0	102
			0.29	654	145.9	13.6	0	53
5.4	0023-263	2.3	1.6	0	0	12.1	0.9	134
			1.2	645	146	33	0.7	143
(g)	0023-263	8.4	0.72	0	0	5.1	0.8	46
5.5	0023-263	8.4	0.64	0	0	5.3	0.8	45
			0.25	646	146	31	0.5	128
(i)	0237-233	2.3	5.2	0	0	7.8	0	53
5.7	0237-233	2.3	4.9	0	0	6.7	0.4	48
(j)	0237-233	8.4	1.61	0	0	4.5	0	21
			0.75	10	-127	0	1	0
5.8	0237-233	8.4	1.52	0	0	5.5	0.5	66
			1.07	9.9	-127	0	1	0
(r)	0823-500	2.3	2.0	0	0	0.0	1	0
			4.2	22	130	12.7	1	0
5.9	0823-500	2.3	3.6	0	0	17.5	0.6	-72
			2.2	24	124	10.7	0.7	-69
(y)	1151-348	2.3	1.6	0	0	10.1	0	123
			1.1	92	-108	12.8	1	0
5.10	1151-348	2.3	2.2	0	0	14.1	0.7	110
			1.3	91	-108	17.2	0.8	101
(z)	1151-348	8.4	0.248	0	0	2.7	0	-37
			0.030	88	-104	0	1	0
5.11	1151-348	8.4	0.9	0	0	9.1	0.7	-27
			0.3	91	-108	12.5	0.7	40
(ab)	1245-197	2.3	1.16	0	0	0	1	0
			1.18	19	56	0	1	0
			0.32	148	87	22.0	0	74
5.12	1245-197	2.3	1.31	0	0	12.5	0.5	81
			1.73	19	55	19.9	0.4	82
			0.36	130	88	20.4	0.4	76
(ac)	1245-197	8.4	0.36	0	0	4.9	0	102
			0.37	21	55	6.8	0	29
5.13	1245-197	8.4	0.60	0	0	5.2	0.7	67
			0.53	17	55	16.8	0.3	70
(af)	1549-790	2.3	3.1	0	0	12.3	0	76
			1.5	83	83	41	0	107
5.15	1549-790	2.3	3.1	0	0	7.7	0.3	64
			1.4	86	80	45	0	107
(ag)	1549-790	8.4	2.9	0	0	4.2	0	46
5.16	1549-790	8.4	3.1	0	0	4.7	0.2	46
(ak)	1830-211	2.3	0.44	0	0	8.8	0	143
			1.14	974	-137.7	21.6	0	142
5.18	1830-211	2.3	1.68	0	0	37	0.4	125
			0.99	973	-137.8	25	0.7	109
(an)	1934-638	2.3	5.8	0	0	0	1	0
			5.1	42.2	91	0	1	0
5.20	1934-638	2.3	5.4	0	0	6.8	0.5	94
			6.9	41.3	89	7.9	0.8	11
(ar)	1934-638	8.4	1.80	0	0	4.7	0	43
			0.41	41.1	86	0	1	0
5.21	1934-638	8.4	1.41	0	0	4.8	0.5	85
			1.32	42.3	88	5.2	0.8	32

Table 6.3: Models derived from single-baseline subsets and images. The first column gives the reference to either Table 6.1 (for the single baseline models) or the relevant figure in Chapter 5 (for the models from the images).

successfully prevented the introduction of spurious components.

Having thus established the general validity of the model fitting procedures, a value by value comparison of the two sets of models (derived independently from the single baseline data and the images) can be undertaken. Flux density ratios of corresponding components, relative angular separations, orientation differences, component size ratios and position angle differences are listed in Table 6.4. Although the relative orientations of the single baseline model components may be fixed, it is possible to rotate the entire model through 180° on the sky without affecting the fit because of the orientation ambiguity arising from the absence of phase measurements with single baseline data. This has been done for several of the models here when comparison indicated an inconsistency between the relative flux densities of double source components (*e.g.* the models of 1934−638 at 2.3 GHz).

Source name	Obs. freq. (GHz)	S_{mod}/S_{im}	Centroid		r_{mod}/r_{im}	AR_{mod}/AR_{im}	$\lvert\phi_{mod}-\phi_{im}\rvert$ (°)
			R_{mod}/R_{im}	$\lvert\theta_{mod}-\theta_{im}\rvert$ (°)			
0022-423	2.3	1.01	–	–	0/3.8	1/0.2	–
		1.11	1.00	1	0/5.4	1/0.2	–
0022-423	8.4	0.95	–	–	1.14	0/0.2	7
		1.13	1.00	0	1.10	0/0.6	44
0023-263	2.3	0.56	–	–	0.66	0/0.9	32
		0.24	1.01	0.1	0.41	0/0.7	90
0023-263	8.4	1.13	–	–	0.96	1.0	1
0237-233	2.3	1.06	–	–	1.16	0/0.4	5
0237-233	8.4	1.06	–	–	0.82	0/0.5	45
		0.70	1.01	0	0/0	1/1	–
0823-500	2.3	1.16	–	–	0.72	1/0.6	–
		0.91	0.91	6	0/10.7	1/0.7	–
1151-348	2.3	0.72	–	–	0.72	0/0.7	13
		0.84	1.01	0	0.74	1/0.8	–
1151-348	8.4	0.28	–	–	0.3	0/0.7	10
		0.01	0.97	4	0/12.5	1/0.7	–
1245-197	2.3	0.89	–	–	0/12.5	1/0.5	–
		0.68	1.00	1	0/19.9	1/0.4	–
		0.89	1.13	1	1.08	0/0.4	2
1245-197	8.4	0.60	–	–	0.94	0/0.7	35
		0.70	1.24	0	0.40	0/0.3	41
1549-790	2.3	1.00	–	–	1.60	0/0.3	12
		1.07	0.96	3	0.91	0/0	0
1549-790	8.4	0.94	–	–	0.89	0/0.2	0
1830-211	2.3	0.67	–	–	0.58	0/0.4	17
		0.44	1.00	0.1	0.35	0/0.7	34
1934-638	2.3	0.94	–	–	0/6.8	1/0.5	–
		0.84	1.02	2	0/7.9	1/0.8	–
1934-638	8.4	1.28	–	–	0.98	0/0.5	42
		0.31	0.97	2	0/5.2	1/0.8	–

Table 6.4: Comparison of source parameters obtained from model fitting and imaging.

The data in Table 6.4 show very clearly the excellent correspondence achieved for the component separations and relative positions between the single baseline models and the models based on the images. Excluding the results for 1245−197, the separations are all consistent to within four percent, and the relative position angles differ by less than 6°. The differences between the position angles of individual components are also relatively small, exceeding 45° in only one

case, for 0023−263 where substantial extended structure is not detected on the Tidbinbilla−Hobart baseline. The flux densities are not so well determined, particularly for sources with extended structure. The effect of the preference for point and line components during the model fitting is apparent with model flux densities more than ten percent greater than those in the images occuring in only five of the thirty comparisons. Generally the model flux densities lie between 60 and 110 percent of the image values with the best agreement achieved for sources with the least extended structure. The component size measurements from the model fitting are least reliable. Even so, a third of the size estimates differ by less than twenty percent. This does not seem to depend on either the source declination (uv-coverage), component size to separation ratio, or the presence of extended structure. In many cases a direct comparison is not possible because the model components are often only lines or points as a consequence of the choices made in the fitting process. If this restriction were relaxed then the component flux densities would be much less constrained, and hence, unreliable.

Note that comparison with images is a very strong test of model reliability. The confidence with which model fits are normally regarded, usually comes from several workers independently deriving the same, or similar, models. It is important to recognise that this provides no guarantee that each will not make the same errors, leading to a popular, but misleading, model. However, although the level of detail can most certainly increase, the *overall* characteristics of sources derived from images do not generally change with increasing numbers of antennas, resolution, or sensitivity. Moreover, despite their dependence on various assumptions about confining cleaning to particular windows etc., images are the "state of the art" when it comes to investigating source structure; they provide literally the best representation of what a source actually looks like[2]. Images can therefore be regarded as a very stringent benchmark by which to measure the success of a model fitting approach. The comparison above vindicates the choice of rules made prior to embarking on the analysis by showing that the models do not mislead as regards the overall source structure, and that some parameters are actually very well determined by this method. Where the models do not show all the components seen in the images, the reason is more to do with the limitations of the one baseline data than in the model fitting procedure itself.

6.8 Summary

This chapter has described the model fitting approach to VLBI data analysis and presented the results of its application to a substantial volume of data with a limited number of baselines. Through a comparison with images made from more complete data sets, the overall reliability of the model fitting technique has been demonstrated convincingly. The accuracy of the fits of the models to the visibility data shows that the assumptions regarding the suitability of the types of basic components from which the models are constructed are well founded.

[2]This does not necessarily make them right

Particularly noteworthy is the demonstration that useful and reliable information about the structure of radio sources, albeit with some well determined limitations, can be obtained using only a one baseline interferometer. Multi-station VLBI experiments in Australia are more difficult to organise and require a very large investment of personnel and resources. In the south, where resources are particularly scarce, the Tidbinbilla–Hobart interferometer has been shown here to be an efficient and effective means of gathering a great deal of information about basic source structures where none previously existed. The data obtained with this instrument and presented above, will be used in subsequent chapters of this thesis.

Chapter 7

Results and Source Parameters

This chapter draws together and summarises the data obtained for the survey sources from the investigations in the preceding chapters. In addition, extensive literature searches have been used to assemble a database of other source properties, including optical identifications, magnitudes, redshifts and radio polarisation. Brightness temperatures, or limits, are calculated for all source components. Optical and radio luminosities are computed for sources having a known redshift. Component sizes and separations are also evaluated using the angular sizes of these objects. The sizes of the components measured in the images are more reliably determined than those found by model-fitting and are used to tabulate estimates of magnetic field strengths and energy densities prevailing within the sources.

7.1 Calculation of Source Properties

Linear Dimensions

If a radio source has an identified optical counterpart with a measured redshift it is possible, given assumptions about an appropriate cosmological model, to compute a conversion between angular and linear size. Following Lang (1980), the luminosity distance (for which the apparent radiation intensity falls off as the square of the distance) is

$$D_L = \frac{zc}{H_0}$$

where z is the redshift, c the velocity of light ($km.s^{-1}$) and H_0 the Hubble Constant ($km.s^{-1}.Mpc^{-1}$). The form of this relation depends on the actual cosmological model chosen; for a standard Friedmann-Robertson-Walker model, parameterised by H_0 and a deceleration parameter q_0, the appropriate expression is

$$D_L = \frac{c}{H_0 q_0^2}\left[q_0 z + (q_0 - 1)(\sqrt{1 + 2q_0 z} - 1)\right]$$

The angular size distance $D_\theta = D_L(1+z)^{-2}$ can be used to calculate a linear size (projected onto the plane of the sky) of

$$l = D_\theta \theta = \frac{c\theta}{H_0 q_0^2 (1+z)^2}\left[q_0 z + (q_0 - 1)(\sqrt{1 + 2q_0 z} - 1)\right].$$

For calculations in this section, a value of $q_0 = 0.5$, corresponding to a "critical" universe, neither open nor closed, will be assumed. The prevailing uncertainty associated with the value of the Hubble Constant will be expressed by the inclusion of a dimensionless scaling parameter h and adopting a value of

$$H_0 = 100h\ km.s^{-1}.Mpc^{-1}.$$

With these assumptions, the linear size relation reduces to

$$1mas = 29.1\frac{1+z-\sqrt{1+z}}{(1+z)^2}h^{-1}\ pc.$$

Luminosities

The luminosity of an object at a distance D metres and with redshift z is

$$P_\nu = S_\nu D_L^2(1+z)^{1-\alpha}\ W.Hz^{-1}.sr^{-1}.$$

α is the spectral index at frequency ν where the flux density is $S_\nu\ W.m^{-2}.Hz^{-1}$ and D_L is the luminosity distance (m). This expression is equally applicable for both radio and optical luminosities, though for optical measurements it is first necessary to convert magnitudes to flux densities using

$$S = S_0 \times 10^{-\frac{m}{2.5}}\ W.m^{-2}.Hz^{-1}.$$

The value of S_0 depends on the magnitude system being used. Johnson (1966) gives $S_0 = 1.77{\times}10^{-23}\ W.m^{-2}.Hz^{-1}$ for J-magnitudes and $S_0 = 3.81{\times}10^{-23} W.m^{-2}.Hz^{-1}$ for V-magnitudes.

Brightness Temperatures

For blackbody radiators at radio frequencies, the brightness (flux density per steradian) is given by the Rayleigh-Jeans law,

$$B = \frac{S}{\Omega} = \frac{2\nu^2 kT_B}{c^2}$$

where S is the flux density of the source which subtends solid angle Ω (sr), ν is the frequency (Hz), k is Boltzmanns constant, c the velocity of light, and T_B the equivalent blackbody temperature of the source, known as the brightness temperature. The brightness temperature then is

$$T_B = \frac{c^2 S}{2k\nu^2\Omega}.$$

For an elliptical source with major and minor axes A and B (radians), the effective solid angle is

$$\Omega = \frac{\pi AB}{4\ln 2}.$$

For source components with measured sizes and flux densities, the brightness temperature is readily calculable. However, if a component is unresolved, then only a lower limit can be placed on the brightness temperature.

Equipartition Magnetic Fields

Miley (1980) gives expressions for calculating the magnetic field strength (B_{me}) and minimum energy density (u_{me}) corresponding (almost) to equipartition of energy between the magnetic field and the relativistic particles in a synchrotron radio source. Provided the source redshift is known, only the flux density, S, and angular size (θ_x, θ_y) of the source are required:

$$B_{me} = 1.51 \times 10^{-4}(1+z)^{1.1}\nu^{0.22}\left[\frac{S}{\theta_x\theta_y l}\right]^{\frac{2}{7}}$$

$$u_{me} = \frac{7}{3}\frac{B_{me}^2}{8\pi}.$$

Here the angular sizes are in *arcseconds*, the flux density in Jy, the frequency ν in GHz, and B_{me} and u_{me} are in Gauss and $erg.cm^{-3}$ respectively. The quantity l is the path length through the source in kiloparsec, and is usually taken as the largest angular dimension (converted to a projected linear size). Numerous assumptions are made in deriving these expressions, including that the ratio of energy in the heavy particles to the electrons is unity, and that the radiation is emitted uniformly from a component, not from unresolved filaments. Miley describes the assumptions in considerable detail.

Magnetic Fields from Synchrotron Self Absorption

For self absorbed synchrotron radio sources, the presence of the peak in the radio spectrum can be used to calculate the magnetic field strength in the emitting regions. Kellermann (1974) gives the appropriate relation:

$$B \sim 2.3 \times 10^{-5}\left(\frac{S_m}{\theta^2}\right)^{-2}\nu_m^5(1+z)^{-1}Gauss.$$

Here S_m is the peak flux density (Jy) occuring at frequency ν_m (GHz), and θ is the source size in milli-arcseconds. The strong dependence on angular size and frequency of the peak means that the uncertainty in the result can be large; errors of about eighty percent in source size, or sixty percent in the frequency of the peak correspond to an order of magnitude change in the magnetic field.

7.2 Optical Properties and Luminosities

Optical counterparts for 34 sources in the survey sample were found via a search of the published literature. Two more objects were tentatively identified by querying the COSMOS/UKST database of digitised Schmidt J-plates (Yentis *et al.*, 1992). Of the remaining seven sources without any optical ID, all have $|b| < 12°$, and are either not covered by the COSMOS database, or the digitised plates show no objects within several arcseconds of the best radio positions (see Table 2.1).

The identifications, magnitudes and redshifts for all sources are listed in Table 7.1, together with their references; the key to the references is in Table 7.2. The

classifications given in Table 7.1 are: G=Galaxy, G?=probable galaxy, Q=quasar, Q?=probable quasar. The two sources listed as probable quasars (1320−446 and 2149−287) were identified via the COSMOS search. The digitised fields show a stellar object within an arcsecond of the radio position for 2149−287, and two stellar objects within three arcseconds for 1320−446. However spectroscopy is required before these identifications can be considered secure.

The redshifts of most sources were found in the literature, mostly via the compilation of Hewitt and Burbidge (1993) for the quasars, and through Wall and Peacock (1985) and Tadhunter *et al.* (1993) for the galaxies. References for objects with redshifts not given by these authors were generally found through a search of the NASA/IPAC Extragalactic Database, NED. All the references are listed in Tables 7.1 and 7.2. Five of the galaxy and probable galaxy redshifts are estimates given by Wall and Peacock, who estimated the redshifts of these galaxies, which are indicated in the table, using a Hubble diagram comprising ninety galaxies. Four other sources in the survey sample had redshifts estimated in this manner by Wall and Peacock but have since had values measured and all but one show the estimated values to be accurate to better than thirty percent. It is inappropriate to conduct a similar estimation for the two potential quasars since (a): the Hubble relation is much less well defined for quasars (*e.g.* Wall and Peacock, 1985) and (b): redshifts are needed to confirm that these objects are indeed quasars and not stars. Column five of Table 7.1 gives the luminosity distances for the objects with redshifts (either measured or estimated).

The COSMOS fields were checked for all sources with optical identifications in an attempt to obtain a homogeneous set of magnitude measurements. Wherever possible, the J-magnitudes from the COSMOS fields are given in Table 7.1. J-magnitudes quoted in the table not from COSMOS often come from literature sources that have used the original UK IIIaJ Schmidt plates. The other magnitudes listed are generally V-magnitudes, or magnitudes converted by authors to the V scale. Optical luminosities have been calculated for all sources using the expressions given in the previous section assuming an optical spectral index of unity, a value typical of the indices calculated for the sources for which both V and J-magnitudes were found in the literature[1]. The optical luminosities, together with the radio luminosities at 2.3 GHz, are listed in Table 7.1. The radio spectral index used in the calculation was estimated from the slope of a line drawn tangent to the radio spectra (Figure 2.1) at 2.3 GHz, the main frequency of the present survey.

7.3 Radio Spectra

Complete radio spectra for the sources in the survey sample were presented in Section 2.3 and the origin of the flux density measurements plotted were also given. Examination of those spectra show that while there are mostly peaked spectrum sources in the sample, some objects do not fully satisfy this criterion,

[1]This may reflect an intrinsic source property or, alternatively, a common choice of method by authors when converting their observations to visual magnitudes.

Source name	ID	m_J	z	D_L (Gpc)	$\log_{10} P_{opt}$ (W.Hz^{-1}.sr^{-1})	$\log_{10} P_{2.3}$	Refs. ID,m,z
0008-421	G?	22.0	(1.600)	5.9	21.4	27.7	1,1,2
0022-423	G?	(20.6)	(0.661)	2.2	21.2	26.4	2,2,2
0023-263	G	20.22	0.322	1.0	20.3	26.0	3,4,3
0159-117	Q	16.3	0.669	2.3	22.6	26.3	3,4,3
0237-233	Q	16.4	2.223	8.6	24.0	28.3	8,4,7
0403-132	Q	16.78	0.571	1.9	22.3	26.4	8,4,8
0405-123	Q	14.45	0.574	1.9	23.2	26.1	8,4,8
0454-463	Q	18.1	0.858	3.0	22.2	26.5	8,9,9
0506-612	Q	(16.85)	1.093	3.9	23.3	26.7	8,8,8
0624-058	G?	(21)					10,10,–
0704-231							–
0733-174	EF						5,–,–
0741-063	EF						5,–,–
0743-673	Q	16.17	1.511	5.6	23.6	27.7	8,4,8
0823-500							–
0834-196	G?	22.7	(0.692)	2.3	20.1	26.6	1,4,2
0859-140	Q	(16.59)	1.339	4.9	23.7	27.2	8,8,8
1015-314	G?	21.2	(0.550)	1.8	20.5	26.2	1,1,2
1127-145	Q	16.95	1.187	4.2	23.0	27.3	8,4,8
1148-001	Q	17.13	1.980	7.5	23.6	27.8	8,4,8
1151-348	Q	(17.84)	0.258	0.82	21.3	25.6	3,8,3
1215-457	Q	18.96	0.529	1.8	21.3	26.3	8,4,8
1221-423	G	(18)	0.171	0.53	20.9	24.8	11,15,14
1245-197	G	21.57	1.275	4.6	21.3	27.4	16,4,16
1302-492	G	9.41	0.002	0.006	20.0	21.3	6,4,6
1306-095	G?	24.25	0.464	1.5	19.1	26.1	3,4,3
1320-446	Q?	17.7					4,4,–
1323-611							–
1354-174	Q		3.147	13		28.1	18,–,18
1514-241	Q	16.4	0.049	0.15	20.0	23.6	8,4,19
1549-790	G	19.4	0.150	0.47	19.9	25.1	3,4,3
1733-565	G	17.23	0.098	0.30	20.3	24.8	3,4,3
1740-517	G	20.2	(0.347)	1.1	20.4	26.0	1,1,2
1827-360							–
1830-211							–
1934-638	G	(18.9)	0.183	0.57	20.6	25.7	17,13,13
1937-101	Q	18.27	3.787	16	24.0	28.2	12,4,12
2052-474	Q	(19.1)	1.489	5.5	22.8	27.1	8,8,8
2126-158	Q	16.60	3.266	13	24.5	27.7	8,4,8
2135-209	G	20.4	0.639	2.2	20.9	26.4	3,1,3
2149-287	Q?	21.40					4,4,–
2204-540	Q	17.92	1.206	4.3	22.7	26.8	8,4,8
2311-452	Q	19.09	2.883	11	23.3	28.2	19,4,26

Table 7.1: Optical identifications and luminosities of sources in the survey sample. The references given in the last column are listed in Table 7.2. Entries with brackets are V magnitudes and redshifts estimated by Wall and Peacock.

1.	Prestage and Peacock, 1983	11.	Ulvestad *et al.*, 1981
2.	Wall and Peacock, 1985	12.	Lanzetta *et al.*, 1991
3.	Tadhunter *et al.*, 1993	13.	Penston and Fosbury, 1978
4.	COSMOS Database	14.	Simpson *et al.*, 1993
5.	Saika *et al.*, 1987	15.	Bolton *et al.*, 1965
6.	Burbidge and Burbidge, 1972	16.	Mantovani *et al.*, 1992
7.	Burbidge and Burbidge, 1969	17.	Kellerman, 1966
8.	Hewitt and Burbidge, 1993	18.	Savage *et al.*, 1990
9.	Jauncey *et al.*, 1989a	19.	White, 1992
10.	Perley, 1982		

Table 7.2: References for optical properties in Table 7.1.

Source name	S_{max} (Jy)	ν_{max} (GHz)	Source Frame (GHz)	Spectral Index
0008-421	6.8	0.58	1.51	-1.1
0022-423	3.1	1.80	2.99	-0.8
0023-263	22.0	0.16	0.21	-0.6
0159-117	10.0	<0.10	<0.17	-0.6
0237-233	7.7	1.00	3.22	-0.9
0704-231	11.0	<0.10		-0.6
0741-063	11.0	0.50		-0.8
0823-500	5.3	2.10		-1.1
0834-196	10.5	0.34	0.58	-0.9
1015-314	19.0	0.11	0.17	-0.7
1127-145	7.0	1.05	2.30	-0.5
1151-348	10.5	0.21	0.26	-0.6
1215-457	14.0	<0.07	<0.11	-0.7
1221-423	7.0	<0.08	<0.09	-0.7
1245-197	8.1	0.40	0.91	-0.8
1354-174	1.8	1.30	5.39	-0.6
1733-565	13.0	0.60	0.66	-0.8
1740-517	7.1	0.89	1.20	-0.5
1827-360	24.0	0.31		-1.15
1934-638	15.0	1.40	1.66	-1.0
2052-474	2.2	3.20	7.96	-0.6
2126-158	1.2	4.00	17.06	-0.6
2135-209	11.0	0.20	0.33	-0.6
2311-452	3.8	<0.18	<0.70	-0.5

Table 7.3: Maximum flux density and frequency of maximum for sources in the sample with peaked spectra. The frequency of the peak in the source frame and the high frequency spectral index are also shown.

and are either steep spectrum sources that do not have a spectral turnover at low frequencies, flat spectrum objects that have been incorrectly classified because of variability or insufficient data, or else flat spectrum objects with optically thin low frequency components. It should be remembered that the initial source selection was not made on the basis of spectra with as many points as those shown, and that the scarcity of low frequency data meant that an otherwise straight spectrum could appear convex depending upon which points were available at the time of selection and their relative flux density scales.

Table 7.3 lists sources in the sample that are judged to be genuine peaked spectrum objects from inspection of the spectra in Figure 2.1. The peak flux density, and the frequency at which the peak occurs are also listed. For sources with measured redshifts, the frequency of the peak in the source frame has been calculated ($\nu_{source} = (1+z)\nu_{observer}$). The spectral index at high frequencies, measured from the plotted spectra, is given for each source, and is never greater than -0.5. Attempts were made to decompose the spectra of 0733−174 and 2052−474 into steep and peaked components, however in each case there were insufficient reliable data near the ends of the spectra to enable the procedure to be performed with any confidence.

Although Table 7.3 lists only 24 sources, there are several others in the sample (*e.g.* 0624−058, 1320−446 and 2149−287) which have convex spectra that are certainly bending downwards at lower frequencies but do not flatten out completely. These objects may be exhibiting the same self absorption processes as are believed to operate in the objects having distinct peaks in their spectra.

7.4 Radio Polarisation

Linear polarisation measurements for 41 of the 43 sources in the survey sample have been made either by Gardner *et al.* (1975) or Perley (1982). The observations by Perley with the VLA at 1465 MHz and 4885 MHz include nineteen of the sources. The survey by Gardner *et al.* at Parkes, undertaken at frequencies of 1.42, 1.6, 2.7 and 5 GHz, includes a total of 36 objects from the sample. A study of polarisation variations at 5 GHz by Komesaroff *et al.* (1984), also using Parkes, includes five of the sample sources (0237−233, 0624−058, 1127−145, 1306−095 and 1934−638), none of which were found to be variable. Polarisation maps from Parkes at 4.75 and 8.55 GHz with arcminute resolution have been presented by Harnett *et al.* (1989; 1990; 1991) for one of the survey sources, 1302-492 (NGC4945).

Measurements of the percentage of linear polarised flux density and the position angle of the polarised component are compiled for reference in Table 7.4. The values for 5 GHz and 1.4 GHz quoted without error all come from the VLA. Perley provides a generic error estimate for the two frequencies of 0.20% and 0.25% respectively. The remainder of the measurements in the table are from Parkes, and with the exception of the 5 GHz values for 1306−095 and 1934−638, which are from Komesaroff *et al.*, all are taken from Gardner *et al.*. The source 0624−058 was almost completely resolved at the VLA at 5 GHz and no measurement is

Source	5 GHz		2.7 GHz		1.66 GHz		1.4 GHz	
name	%	(PA°)	%	(PA°)	%	PA(°)	%	PA(°)
0008−421	0.1	-33	0.6±0.6	89			0.3	-27
0022−423	0.3	-1	0.4±0.2	180±3			0.1	13
0023−263	0.1	–	<1.0		0.7±0.2	96±4	0.1	9
0159−117	2.1±0.4	21±4	2.0±0.7	40±8	1.5±1.0	60±25	2.9±1.0	40±8
0237−233	4.2	-37	3.4±0.5	143±4	1.7±0.4	167±4	1.2	12
0403−132	2.6±0.3	177±3	2.8±0.3	1±3	2.2±0.2	24±5	1.8±0.6	19±7
0405−123	0.7±0.3	84±13	1.2±0.6	155±10			<1.5	
0454−463	2.8±0.3	14±2	3.5±0.8	30±10	5.4±1.0	38±9	5.6±0.8	45±3
0506−612	2.2±0.4	168±5	4.6±1.3	59±5	1.6±0.4	46±7	1.8±0.8	50±10
0624−058	4.9±0.3	-58	10.1±0.2	173±2	9.5±0.2	133±2	9.6	12
0704−231	5.0±0.4	16±2	1.7±0.9	137±10			<1.1	
0733−174	0.1	38	0.3±0.2				0.2	1
0741−063	0.1	53	0.4±1.0	156			0.1	58
0743−673	1.4±0.3	25±5	1.7±0.6	97±15	2.8±0.8	86±12	5.5±1.0	57±3
0823−500								
0834−196	0.5±0.4	5±13	1.8±1.8	95±25			1.5±0.2	0±7
0859−140	2.0	77	2.9±1.0	88±10	2.1±0.2	96±4	3.2	-72
1015−314	0.1	10	<0.7				0.1	16
1127−145	4.9	-30	1.9±0.7	4±10	3.6±0.3	46±3	4.9	75
1148−001	4.1	-37	3.6±0.7	159±8	3.2±0.3	151±4	4.5	-27
1151−348	0.5	20	1.6±0.8	165±10			0.2	-14
1215−457	1.7±0.3	95±4	1.6±0.7	14±12			0.9±0.8	153
1221−423	2.4±0.5	6±8	1.9±0.4	145±13			2.0±0.5	72±9
1245−197	0.1	16	0.7±0.8	101			–	–
1302−492	0.5±0.2	145±12	0.1±0.5				<0.4	
1306−095	0.8±0.2	29±7	0.8±0.6	159±25			0.7±0.8	83
1320−446	0.8	72					0.4	-25
1323−611	6.8±0.2	48±1	6.9±0.7	150±4	4.0±0.3	1±2	3.6±0.5	119±5
1354−174	4.4±0.5	20±3	4.0±1.2	3±8			0.7±1.2	131
1514−241	7.4	50	4.4±1.0	37±4	4.9±0.3	9±3	6.0	37
1549−790	1.0±0.3	41±10	1.1±0.4	155±7			0.5±0.5	109
1733−565	1.5±0.8	30±12	0.5±0.5	30			1.9±0.5	169±5
1740−517								
1827−360	0.2	56	0.5±0.5	88±25			0.1	23
1830−211	0.4±0.2	129	0.5±0.2	136±20			1.0±0.5	137±10
1934−638	<0.1		<0.3				<0.2	
1937−101	2.1	-88					–	–
2052−474	5.1±0.3	176±2	3.6±0.8	22±5	3.7±0.7	71±10	4.4±0.8	86±7
2126−158	0.4	25					0.3	25
2135−209	0.3	-16					0.2	-25
2149−287	3.4±0.5	133±4	5.5±0.8	103±5	5.0±1.1	55±12	4.4±0.8	30±6
2204−540	1.1±0.2	144±7	2.9±0.2	149±3			3.5±0.4	10±5
2311−452	2.5±0.3	10±4	1.6±0.2	16±7				

Table 7.4: Source polarisation at 5, 2.7, 1.66 and 1.4 GHz.

available. However the lower resolution of Parkes enabled Komesaroff *et al.* to obtain the value given here.

7.5 Compact Structure and Variability

The two and a half year duration flux density monitoring survey of the sample objects was described in Chapter 3 and demonstrated the overall lack of variability among these objects. Flux density variability is normally associated with the most compact structure in extragalactic sources. Table 7.5 lists the fraction of the total flux density for each source contributed by the structure seen in the VLBI observations described in Chapters 5 and 6. Measurements are available for all but six objects at 2.3 GHz. Sources that were observed but not detected are listed as 0.0. A few of the ratios exceed unity either because the source models included a component that had a poorly constrained size, or because of calibration uncertainties. The ratio of VLBI flux density to total flux density is also given in Table 7.5 for objects that were imaged at 8.4 GHz.

The fractional variability of a radio source is defined as the magnitude of the fluctuations divided by the mean flux density. However, quantifying the variations simply by taking the difference of the maximum and minimum flux densities is not a robust approach since it can be very sensitive to noise in the measurements. A more reliable alternative method which uses all the data, and not just the extrema, comes from recognising that the root mean square (RMS) variation of the flux density measurements is (approximately) the quadrature sum of contributions due to the intrinsic variability and the measurement errors (Fanti *et al.*, 1978). The range of the variability then can be calculated as

$$\Delta S = 3\sqrt{RMS^2 - \sigma^2}$$

where σ is the mean measurement error. The factor of three conservatively accounts for the property of Gaussian noise of having an RMS typically between a third and a fifth of the peak to peak variation. The fractional variability ($\Delta S/\overline{S}$) of objects listed as either variable or possibly variable in Table 3.3 is also given in Table 7.5.

7.6 Component Motion

Table 7.6 summarises the measurements of relative motion described in Chapter 6. The velocities are given in units of the velocity of light. For 0823−500 and 1830−211 which have no measured redshift, the conversion from milli-arcseconds to linear scales (pc) has been accomplished by assuming a redshift of z=1.2 which corresponds to the maximum linear scale ($4.3 pc.mas^{-1}$) achievable with the adopted metric ($q_0 = 0.5, H_0 = 100h$). Note that all velocities in Table 7.6 scale as h^{-1}.

With the exception of 1830−211, and 1934−638 at 8.4 GHz, all the measured velocities are consistent with no motion. As was explained in Chapter 6 these

Source name	ID	2.3 GHz $\frac{S_{vlbi}}{S_{total}}$	2.3 GHz Frac. Var.	8.4 GHz $\frac{S_{vlbi}}{S_{total}}$	8.4 GHz Frac. Var.
0008-421	G?	0.97			
0022-423	G?	0.97		0.95	
0023-263	G	0.40	0.09	0.41	
0159-117	Q	0.39			
0237-233	Q	0.99		0.98	
0403-132	Q	0.10	0.10		
0405-123	Q				
0454-463	Q	0.60			
0506-612	Q	0.49			
0624-058	G?	0.0			
0704-231		0.0			
0733-174	EF				
0741-063	EF	0.35			
0743-673	Q	0.50	0.18		
0823-500		1.01			
0834-196	G?	0.85			
0859-140	Q	0.42			
1015-314	G?	0.50			
1127-145	Q	0.96	0.09		0.15
1148-001	Q	1.15			
1151-348	Q	0.76		0.68	
1215-457	Q	0.42			
1221-423	G	0.0			
1245-197	G	0.86		0.72	
1302-492	G	0.0			
1306-095	G?				
1320-446	Q?	0.59			
1323-611		0.0	0.07		
1354-174	Q	0.65			
1514-241	Q				0.37
1549-790	G	0.96	0.11	0.93	
1733-565	G	0.08			
1740-517	G	1.04	0.15		
1827-360		0.19			
1830-211		0.29	0.13	0.26–0.75	0.80
1934-638	G	1.00	0.05	0.90	
1937-101	Q				
2052-474	Q				
2126-158	Q	1.09			
2135-209	G	0.87	0.23		
2149-287		0.18			
2204-540	Q	0.67	0.44		
2311-452	Q	0.79	0.24		

Table 7.5: Ratios of VLBI component flux densities to total flux densities and fractional variability (see text) at 2.3 and 8.4 GHz.

two measurements that, taken at face value, are suggestive of real motion are best treated with some caution. Both are based on observations at either different hour angles or with different baselines. Since both objects are known to have complex structure, the likelihood is that the apparent motions are a consequence of measurements of different component centroids and as such ought not be regarded (yet) as true detections of relative component motion. Further observations on a common baseline or at the same hour angles are needed to confirm or disprove these results. Note also for 1830−211, Jones *et al.* (1993) have found significant structural changes at 5 GHz from observations before and during the flux density outburst seen in the data presented in Chapter 3. Such structure changes may be the cause of the apparent changes in separation, since the two 8.4 GHz occured before and during the outburst.

Source name	Freq. (GHz)	$\dot{\theta}$	Maximum ($mas.yr^{-1}$)	Minimum	Velocity (c)	Δt (years)
0022-423	8.4	0.22	1.11	-0.60	2.8	1.85
0023-263	2.3	-3.4	3.8	-9.1	-31.	1.04
0823-500	2.3	4.91	14.44	-9.67	(4.8)	1.16
1151-348	2.3	-0.64	0.43	-2.06	-5.2	1.41
1830-211	8.4	-0.254	-0.081	-0.659	(-3.56)	1.73
1934-638	2.3	-0.31	0.35	-0.85	-2.0	3.19
1934-638	8.4	-0.71	-0.06	-1.68	-4.6	1.82

Table 7.6: Summary of component relative velocity measurements. Values in braces are upper limits (see text).

7.7 Source Sizes and Brightness Temperatures

Projected linear sizes can be calculated from angular sizes for all sources with a known redshift. This has been done for each of the source models constructed in Chapter 6 and presented in Table 6.1. The results are shown in Table 7.7. For components with measured angular sizes the calculation is straightforward. However many of the model components are either point sources or lines of zero width. For such components, only an upper limit, depending on the resolution, can be placed on the angular sizes. It is usually possible to detect sizes between a third and half the angular resolution, so a reasonable upper limit to the size is a third of the beam width. For point model components, the angular size limits then are just one third the dimensions of the effective synthesised beam. For line components, the length of the projection of a normal to the component onto the synthesised beam has been calculated and one third of this value is used as the size limit.

Brightness temperatures for all model components are also given in Table 7.7. The upper limits for the angular sizes of components translate into lower limits

on the brightness temperatures. The only components for which brightness temperature lower limits $\sim 10^{11}K$ are detected are the cores in 1934−638. However measured values and lower limits of $\sim 10^{10}K$ are not uncommon.

Similar calculations of brightness temperatures have been made for the components seen in the images of Chapter 5. These values are given in Table 7.8 and overall, are similar to those found from the model fitting. For 0237−233 at 8.4 GHz, the model fit to the image indicated that component B was a point source (Table 5.4). In Table 7.8, limits have been set on the size of this component by considering the synthesised beam in a similar manner to that for the source models, as discussed above. All measured spectral indices are also summarised in the table. Three objects have brightness temperatures $>\sim 10^{11}K$.

Table 7.7: Projected linear sizes, separations, and brightness temperatures for components of VLBI source models. Note that all sizes and separations scale as h^{-1}. The first four columns correspond to those in Table 6.1.

Model ref.	Source name	Freq. (GHz)	Epoch	Separation (pc)	Extent (pc)	T_B (K)
(a)	0008-421	2.3	89.93		53×<21	>6.2×10^9
				527	124×<21	>1.7×10^9
(b)	0022-423	2.3	89.93		<43×<17	>1.1×10^{10}
				109	<43×<17	>4.2×10^9
(c)	0022-423	8.4	90.05		15×<4.4	>1.2×10^9
				109	<14×<4.3	>3.8×10^8
(d)	0022-423	8.4	91.90		16×<4.5	>2.6×10^9
				109	13×<11	>4.9×10^8
(e)	0023-263	2.3	90.30		49×<11	>3.8×10^9
				1883	73×<48	>8.9×10^8
(f)	0023-263	2.3	91.34		23×<12	>6.0×10^9
				1875	39×<15	>9.3×10^8
(g)	0023-263	8.4	91.90		15×12	6.0×10^8
(h)	0159-117	2.3	91.91		52×<18	>2.7×10^9
				6279	<39×<13	>8.3×10^8
(i)	0237-233	2.3	88.86		31×<21	>2.9×10^{10}
(j)	0237-233	8.4	91.90		18×<10	>2.4×10^9
				40	<12×<4.5	>3.8×10^9
(k)	0403-132	2.3	93.15		<23×<10	>4.9×10^9
(l)	0454-463	2.3	89.93		5.0×5.0	9.8×10^{10}
				91	73×<4.5	>5.1×10^9
(m)	0506-612	2.3	89.86		<44×<20	>1.8×10^9
				459	218×<22	>2.1×10^8
				618	256×<21	>1.4×10^8
(n)	0733-174	2.3	93.15			>1.2×10^{10}
(o)	0741-063	2.3	93.15			>1.1×10^{10}
						>2.8×10^9
(p)	0743-673	2.3	89.93		224×<16	>1.0×10^9
					<42×<16	>4.4×10^9
(q)	0823-500	2.3	88.77			>1.2×10^{10}
						8.0×10^9
(r)	0823-500	2.3	89.93			>1.1×10^{10}
						6.0×10^9
(s)	0834-196	2.3	91.48		55×55	7.7×10^8
				413	235×<19	>4.7×10^8
				413	60×60	1.4×10^9

Model ref.	Source name	Freq. (GHz)	Epoch	Separation (pc)	Extent (pc)	T_B (K)
(t)	0859-140	2.3	91.48		41×<20	$>5.8\times10^{9}$
(u)	1015-314	2.3	91.48		<42×<15	$>1.3\times10^{9}$
					130×<38	$>5.6\times10^{8}$
				262	123×<16	$>1.3\times10^{8}$
(v)	1127-145	2.3	93.15		32×<22	$>2.9\times10^{10}$
(w)	1148-001	2.3	93.15		54×<36	$>6.0\times10^{9}$
(x)	1151-348	2.3	89.93		27×20	4.8×10^{9}
				233	34×29	1.5×10^{9}
				116	193×193	7.8×10^{7}
(y)	1151-348	2.3	91.34		25×<12	$>7.9\times10^{9}$
				231	32×32	1.6×10^{9}
(z)	1151-348	8.4	92.24		6.8×<8.2	$>4.9\times10^{8}$
				221	<19×<2.6	$>6.5\times10^{7}$
(aa)	1215-457	2.3	88.75		43×<17	$>6.3\times10^{9}$
(ab)	1245-197	2.3	91.34		<30×<19	$>8.8\times10^{9}$
				82	<30×<19	$>8.9\times10^{9}$
				638	95×<19	$>7.6\times10^{8}$
(ac)	1245-197	8.4	92.24		21×<5.1	$>1.1\times10^{9}$
				91	29×<7.9	$>5.2\times10^{8}$
(ad)	1320-446	2.3	89.83			$>4.2\times10^{9}$
						$>5.8\times10^{8}$
(ae)	1354-174	2.3	91.48		37×<15	$>5.7\times10^{9}$
(af)	1549-790	2.3	88.86		21×<12	$>8.1\times10^{9}$
				142	70×<11	$>1.3\times10^{9}$
(ag)	1549-790	8.4	91.90		7.2×<2.1	$>9.5\times10^{9}$
(ah)	1733-565	2.3	91.51		<12×<6.1	$>2.0\times10^{9}$
(ai)	1740-517	2.3	89.93		20×17.2	2.6×10^{10}
				155	30×<6.3	$>1.2\times10^{10}$
(aj)	1827-360	2.3	90.30			$>1.0\times10^{8}$
(ak)	1830-211	2.3	91.34			$>2.0\times10^{9}$
						$>2.2\times10^{9}$
(al)	1830-211	8.4	90.51			$>1.9\times10^{9}$
						$>1.1\times10^{9}$
(am)	1830-211	8.4	92.24			7.1×10^{9}
						1.1×10^{10}
(an)	1934-638	2.3	88.86		<37×<11	$>1.3\times10^{10}$
				84	<37×<11	$>1.2\times10^{10}$
(ao)	1934-638	2.3	92.05		20×20	1.3×10^{10}
				82	17×17	2.0×10^{10}
(ap)	1934-638	2.3	92.05		2.6×<0.91	$>1.0\times10^{11}$
				87	8.1×<0.86	$>1.0\times10^{11}$
				84	3.8×<0.81	$>1.3\times10^{11}$
(aq)	1934-638	8.4	90.08		5.8×<4.2	$>2.2\times10^{9}$
				84	9.7×<3.4	$>2.7\times10^{9}$
(ar)	1934-638	8.4	91.90		9.3×<9.1	$>1.5\times10^{9}$
				81	<9.1×<2.6	$>1.2\times10^{9}$
(as)	2126-158	2.3	93.15		26×26	5.1×10^{9}
(at)	2135-209	2.3	91.48		36×<38	$>2.3\times10^{9}$
				649	96×<26	$>1.0\times10^{9}$
				579	85×<32	$>8.0\times10^{8}$
(au)	2149-287	2.3	91.48			$>1.9\times10^{8}$
						$>4.8\times10^{8}$
(av)	2204-540	2.3	91.50		25×<30	$>5.7\times10^{9}$
(aw)	2311-452	2.3	93.15		34×27	5.0×10^{9}

Source name	Cpt.	Freq. (GHz)	S_{cpt} (Jy)	$\alpha_{2.3}^{8.4}$	Maj (pc)	Min (pc)	T_B (K)
0022-423	A	2.3	2.21	-0.86	14.78	2.67	2.0×10^{11}
	A	8.4	0.73		13.72	3.34	4.2×10^{9}
	B	2.3	0.76	-0.93	21.22	4.48	2.9×10^{10}
	B	8.4	0.23		11.55	6.80	7.8×10^{8}
0023-263	A	2.3	1.35	-0.58	34.73	29.85	2.5×10^{9}
	A	8.4	0.64		15.12	12.69	4.8×10^{8}
	B1	2.3	0.35	-0.52	53.67	14.58	8.6×10^{8}
	B1	8.4	0.18		49.65	28.56	1.8×10^{7}
	B2	2.3	1.13	-2.11	108.49	65.44	3.0×10^{8}
	B2	8.4	0.07		Component is too weak		
0237-233	A	2.3	3.76	-0.70	16.60	7.72	1.1×10^{11}
	A	8.4	1.52		21.80	11.84	1.6×10^{9}
	B	2.3	0.49	0.60	24.56	5.20	1.4×10^{10}
	B	8.4	1.07		<10.44	<3.96	$>7.2\times10^{9}$
0823-500	A	2.3	3.56		(17.50)	(10.60)	4.4×10^{9}
	B	2.3	2.23		(10.70)	(7.50)	6.4×10^{9}
1151-348	A	2.3	2.20	-0.68	35.29	23.54	3.9×10^{9}
	A	8.4	0.91		22.77	16.01	2.7×10^{8}
	B	2.3	1.32	-1.12	43.17	35.14	1.3×10^{9}
	B	8.4	0.31		31.38	22.34	4.8×10^{7}
1245-197	A1	2.3	1.31	-0.60	53.88	25.00	4.2×10^{9}
	A1	8.4	0.60		22.28	15.30	5.7×10^{8}
	A2	2.3	1.73	-0.91	85.77	38.36	2.3×10^{9}
	A2	8.4	0.53		72.19	19.01	1.2×10^{8}
	B	2.3	0.36	-1.44	87.92	36.46	4.9×10^{8}
	B	8.4	0.06		Component is too weak		
1549-790	A1	2.3	3.10	0.00	13.12	4.04	4.0×10^{10}
	A1	8.4	3.13		8.09	1.86	1.1×10^{10}
	A1′	2.3	2.16		6.17	1.25	1.9×10^{11}
1830-211	A	2.3	1.68		(34.72)	(12.76)	8.8×10^{8}
	B	2.3	0.99		(24.54)	(16.50)	5.6×10^{8}
1934-638	A	2.3	5.43	-1.04	13.38	6.57	5.6×10^{10}
	A	8.4	1.41		9.56	4.75	2.1×10^{9}
	B	2.3	6.90	-1.28	15.70	11.80	3.4×10^{10}
	B	8.4	1.32		10.38	7.80	1.1×10^{9}
	A′	2.3	5.30		12.14	6.22	6.4×10^{10}
	B1	2.3	1.82		9.64	3.15	5.4×10^{10}
	B2	2.3	3.41		15.84	6.59	3.0×10^{10}
	B3	2.3	1.09		6.79	4.10	3.5×10^{10}

Table 7.8: Intrinsic properties of components seen in images. Component sizes for sources without redshifts are given as milli-arcseconds and are indicated by braces. The component labelling is the same as that used in the individual tables of Chapter 5.

7.8 Magnetic Fields

For sources with known redshifts, equipartition magnetic fields and minimum energy densities have been calculated for the components measured by fitting Gaussian models to the SHEVE images (Chapter 5). The values obtained are listed in Table 7.9. Typical field strengths are $\sim 10^{-2}$ Gauss, very similar to the values found in other compact radio cores (*e.g.* Conway *et al.*, 1992, Miley, 1980).

The task of accurately calculating the magnetic fields from synchrotron self absorption is a more formidable task. The calculation must be performed using the angular size and flux density of the components at the frequency of the peak in the spectrum. For none of the images of sources with distinct peaks, do the peaks lie at a frequency close to that of the observations. Therefore the component sizes and flux densities must be calculated by extrapolation or interpolation of the measurements at other frequencies. Every source for which images were obtained has at least two components so it is further necessary to try and decompose the total spectrum into the spectra of the individual components to calculate the relevant flux densities. This can be a very uncertain procedure if component flux densities are measured at only two frequencies, as they are here, since the spectral turnovers for the various components may occur at different frequencies. Moreover, flux density arising in unmodelled extended structure can further complicate this process.

Nevertheless, it is possible to attempt the calculation for some sources by making some straightforward assumptions. Selecting the objects for which the VLBI structure accounts for essentially the whole of the total flux density removes the uncertainty associated with the contribution due to extended structure. Four of the objects imaged satisfy this criterion, 0022−423, 0237−233, 0823−500 and 1934−638. Unfortunately no redshift is known for 0823−500. The three remaining sources are basically doubles with measured spectral indices between 2.3 and 8.4 GHz.

For 0022−423 and 1934−638, the ratio of the component flux densities at the peak can be calculated by assuming that the individual component spectral indices are constant at frequencies above the peak and that they both turn over at the same frequency. In practice this procedure yields total flux densities in excess of those measured, but it does allow the relative proportions of the total flux density contributed by the individual components to be estimated in a manner that gives regard to the different spectral indices. For two components with a flux density ratio estimated thus, the total flux density at the peak can be used to solve for the individual component flux densities.

For 0237−233, if it is assumed that the inverted spectrum component has a constant spectral index below 8.4 GHz, so that the peak in the total flux density spectrum is due entirely to the component with the steep high frequency spectrum, then provided these two components still contribute the whole of the flux density at frequencies in the vicinity of the peak, the flux density of the peaked component at the frequency of the peak can be calculated by subtraction. Since the non-peaked spectrum component does not have a flat spectrum, the frequency of the peak in the other component will differ from that of the peak in the total flux density

Source name	Cpt.	Freq. (GHz)	S_{cpt} (Jy)	B_{me} (Gauss)	u_{me} (erg/cc)
0022-423	A	2.3	2.21	5.3×10^{-2}	2.6×10^{-4}
	A	8.4	0.73	5.0×10^{-2}	2.3×10^{-4}
	B	2.3	0.76	2.7×10^{-2}	6.9×10^{-5}
	B	8.4	0.23	3.2×10^{-2}	9.6×10^{-5}
0023-263	A	2.3	1.35	9.1×10^{-3}	7.8×10^{-6}
	A	8.4	0.64	2.0×10^{-2}	3.8×10^{-5}
	B1	2.3	0.35	6.0×10^{-3}	3.3×10^{-6}
	B1	8.4	0.18	5.6×10^{-3}	3.0×10^{-6}
	B2	2.3	1.13	3.6×10^{-3}	1.2×10^{-6}
	B2	8.4	Component is too weak		
0237-233	A	2.3	3.76	8.9×10^{-2}	7.3×10^{-4}
	A	8.4	1.52	6.9×10^{-2}	4.4×10^{-4}
	B	2.3	0.49	4.4×10^{-2}	1.8×10^{-4}
	B	8.4	1.07	$>1.3\times10^{-1}$	$>1.6\times10^{-3}$
1151-348	A	2.3	2.20	9.8×10^{-3}	8.9×10^{-6}
	A	8.4	0.91	1.4×10^{-2}	1.9×10^{-5}
	B	2.3	1.32	6.7×10^{-3}	4.2×10^{-6}
	B	8.4	0.31	8.1×10^{-3}	6.0×10^{-6}
1245-197	A1	2.3	1.31	1.7×10^{-2}	2.7×10^{-5}
	A1	8.4	0.60	3.4×10^{-2}	1.1×10^{-4}
	A2	2.3	1.73	1.2×10^{-2}	1.4×10^{-5}
	A2	8.4	0.53	1.6×10^{-2}	2.4×10^{-5}
	B	2.3	0.36	8.0×10^{-3}	5.9×10^{-6}
	B	8.4	Component is too weak		
1549-790	A1	2.3	3.10	2.3×10^{-2}	4.9×10^{-5}
	A1	8.4	3.13	5.0×10^{-2}	2.3×10^{-4}
	A1′	2.3	2.16	4.4×10^{-2}	1.8×10^{-4}
1934-638	A	2.3	5.43	2.6×10^{-2}	6.2×10^{-5}
	A	8.4	1.41	3.1×10^{-2}	9.0×10^{-5}
	B	2.3	6.90	2.1×10^{-2}	4.2×10^{-5}
	B	8.4	1.32	2.5×10^{-2}	5.9×10^{-5}
	A′	2.3	5.30	2.8×10^{-2}	7.1×10^{-5}
	B1	2.3	1.82	2.8×10^{-2}	7.4×10^{-5}
	B2	2.3	3.41	2.1×10^{-2}	3.9×10^{-5}
	B3	2.3	1.09	2.8×10^{-2}	7.1×10^{-5}

Table 7.9: Magnetic field estimates calculated assuming energy equipartition for the components measured in the images. The calculation can not be performed for the two sources without redshifts.

spectrum. However, in this case, when the subtraction is performed the effect is found to be insignificant.

The component sizes at the frequency of the peaks are difficult to estimate as there is no obvious systematic relationship between the component sizes at different frequencies for all the three sources and the measurements do not bracket the frequencies of the peaks. In view of the uncertainties inherent in attempting to estimate the component sizes under such circumstances, the values measured from the 2.3 GHz images were adopted for the calculations. All the the parameters used in these calculations, and the results, are given in Table 7.10. The corresponding equipartition field strengths are calculated for comparison. Brightness temperatures are also shown. The SSA magnetic fields are typically smaller than the equipartition fields, suggesting that the equipartition condition holds in very few of the components. For the sources in which the SSA fields are smaller, the majority of the energy must be carried by the particles and not the field. All components have very high brightness temperatures at the frequency of the peak.

Source name	Cpt.	Freq. (GHz)	S_{cpt} (Jy)	Maj (mas)	Min (mas)	B_{ssa} (Gauss)	B_{me} (Gauss)	T_B (K)
0022-423	A	1.80	2.30	3.76	0.68	3×10^{-4}	1×10^{-2}	3×10^{11}
	B	1.80	0.80	5.40	1.14	2×10^{-2}	6×10^{-3}	5×10^{10}
0237-233	A	1.00	7.40	4.15	1.93	8×10^{-6}	2×10^{-2}	1×10^{12}
1934-638	A	1.40	6.10	6.76	3.32	1×10^{-3}	5×10^{-3}	2×10^{11}
	B	1.40	8.90	7.93	5.96	3×10^{-3}	5×10^{-3}	1×10^{11}

Table 7.10: Magnetic field strengths from synchrotron self absorption (SSA). The choice of parameters is discussed in the text.

7.9 Summary

This chapter has assembled an extensive database of the properties of all the sources in the survey sample, drawn both from the literature and the observations presented in earlier chapters. The single dish and VLBI flux density measurements were already incorporated into the source radio spectra presented in Chapter 2. The spectral properties of the sources showing distinct peaks have been summarised and radio polarisation measurements from the literature presented. All known optical identifications found in the literature were compiled, and the measured redshifts used to calculate luminosities, distances, component sizes, separations, and relative motion, all based on the data from the VLBI and single dish observations. The fraction of the total flux density contributed by the compact structure was calculated for all sources observed with VLBI. Brightness temperatures, or limits, have been tabulated for all VLBI structures. Calculations of magnetic field strengths in the components of the imaged souces were calculated assuming equipartition of energy between the particles and fields. Magnetic fields in three sources were estimated from synchrotron self absorption theory.

Chapter 8

Conclusions

This thesis has presented an extensive collection of new data for a sample of Southern radio sources with spectra dominated by components that are steep at high frequencies and that flatten or peak at frequencies below 2–3 GHz. The sample includes a small number of additional objects with spectra which were subsequently found to have been incorrectly identified as members of this class on the basis of insufficient data. However for almost all of these objects, the data presented are the first at high angular resolution at radio wavelengths. The observations of these sources encompass investigations of the emission in the spatial, spectral and temporal dimensions and have used single dish antennas, single baseline interferometers and a multi-station VLBI array.

Astrophysical Implications

The primary thrust of the investigation has been directed towards an examination of the properties of the compact structure in these peaked spectrum sources. A dual frequency flux density monitoring program using a 26 m antenna revealed that strong flux density variability, most frequently observed in flat spectrum compact sources, is virtually absent in the surveyed objects. This result points strongly to the conclusion that the types of active flat spectrum cores seen in many extragalactic objects do not make a large contribution to the totality of the emission from peaked spectrum sources. It does not however preclude the possibility that compact structures exist in such objects.

A measure of the contribution made by compact structure was obtained through VLBI observations. Twenty two of the 37 objects (∼sixty percent) observed at 2.3 GHz have more than fifty percent of their flux density in components with sizes of the order of tens of milli-arcseconds. Considering only the sources with peaked spectra (see Table 7.3), the proportion is somewhat higher at sixty five percent (15 out of 23 objects). At 8.4 GHz the emission of five of the six peaked spectrum objects is dominated by the VLBI structure. It is therefore clear that these objects do include strong, bright compact components (cores). Coupling this observation with the low incidence of variability, it is not unreasonable to suggest that since these core-like components do make a substantial contribution to the total flux density for many sources, they are intrinsically stable components and, as such, are distinct from other compact cores. This particular feature of peaked

spectrum sources (the presence of stable milli-arcsecond structure) makes them good candidate flux density calibrators for arcsecond-scale synthesis arrays.

A total of thirty eight objects in the sample were observed at 2.3 GHz with at least a single baseline interferometer having a resolution of between twenty and thirty milli-arcseconds. All but five of the sources were detected. Of the thirty three detections, only thirteen could be adequately modelled with a single component at this resolution. This proportion is approximately the same if only the peaked spectrum sources are considered, so complex structure is evidently not unusual in these objects. When multiple components are found in sources, it is natural to question what their relationship to one another is. For the sources with two or more components, there is often a more compact component accompanied by a larger partially resolved elongated structure similar to core-jet type sources. In at least one case (0023−263) it appears that the two bright components are hotspots at the terminations of weak jets. Whatever the mechanism responsible for the transport of energy between the strong components, it is either episodic (and turned off), extinct, or is undetectable for some other reason. However it might be expected that some mechanism must exist in order to sustain the highly luminous VLBI components.

Two objects which are particularly puzzling are 0022−423 and 1934−638, which both comprise compact, widely separated components possessing high brightness temperatures that contribute virtually the whole of the total flux density. Moreover, the spectral indices of the two components are very similar. These observations cannot easily accommodate models involving jets as there is very little space in the flux density budget for any other emission. A possibility is that one component has been ejected from the other and is moving away independently. However, considering the strong flux density variability often associated with ejecta in flat spectrum objects, this type of behaviour is at clearly odds with low incidence of variability in these sources. Furthermore, arguments based on angular size to angular separation ratios and physical limits to expansion rates (see for example Mutel *et al.*, 1985) indicate that confinement of the ejecta is taking place. However if this confinement is due to pressure from the external medium then it might be expected that a component moving with some bulk velocity through it would show considerable distortion; clearly for these sources this is not seen. An alternative interpretation of these double sources is that they may be a consequence of gravitational lensing. This explanation has the benefit that no bridges, jets or relative motion are required since only one luminous component is involved. Detailed measurements of the spectra of the two components will help to show whether or not this mechanism is applicable for these objects.

VLBI imaging of several sources has permitted reliable measurement of component sizes and flux densities, and in turn, calculation of magnetic field strengths and energy densities. The typical field strengths computed are generally of the order $\sim 10^{-2}$ G, assuming that energy in these sources is shared equally between the field and the particles. For three sources with peaked spectra, the magnetic field strengths have been computed by assuming that synchrotron self absorption causes the peak. In all cases the magnetic field estimates so computed are 100–1000 times less than those expected from equipartition, leading to the conclusion

that particles are the dominant energy carriers in these components. The lesser importance of the magnetic fields accords with the incidence of low polarisation in most of the sources.

A small number of sources have been observed at more than one epoch allowing limits to be set on relative motion between the components. However the measurements are generally not well constrained and most of the time baselines are only of one to two years duration so the limits are not very stringent. For most sources, the relative positions of the components measured at two epochs are consistent with no relative motion.

The brief discussion above shows that there is clearly a very great deal of astrophysics still to be extracted from the data presented here. The dataset is large and contains the first detailed information for many of these sources. With regard to the VLBI data presented, a great deal of effort has been expended in developing correct procedures and establishing the integrity of the data produced by the new SHEVE array. As such, this thesis represents only the first step in the investigation of Southern peaked spectrum objects. Now that the instrument (SHEVE) has been created and understood (in terms of its practical limitations and capabilities) the focus of the investigation will inevitably turn more towards the astrophysics. Many of the sources could profitably be imaged with VLBI at lower frequencies to further constrain the individual component sizes and flux densities in the vicinity of the spectral peaks. Of the peaked spectrum sources with optical identifications, the division between quasars and galaxies is about equal. Several sources remain unidentified however and more work is needed to find their optical counterparts and measure the redshifts. It is also necessary to obtain reliable redshifts for those sources for which only estimates are presently available. VLBI astrometry programs, such as that already undertaken by members of the SHEVE team between Tidbinbilla and Hobart (Reynolds *et al.*, 1994), will continue to be necessary to provide the accurate radio source positions essential to the identification process.

Observational Consequences

From an observational standpoint, the data presented in the foregoing chapters have demonstrated the capability of the SHEVE array to produce high-resolution images of Southern radio sources. The work involved in the processing of both the single baseline survey and the imaging observations has required the solution of numerous problems associated with the establishment of a completely new VLBI network, including accurately locating new stations not previously used for VLBI, the characterisation of their operating parameters for the purposes of calibration, investigation of the properties and capabilities of a variety of available frequency standards, and the familiarisation of a large number of participants with new observing procedures and equipment.

The comparison of the single baseline model fitting results with the images showed the success that can be achieved with only a single baseline interferometer, provided some strict rules are adhered to when interpreting the data. The component separations, orientations, minimum flux densities, and often flux density ratios, are well determined by these types of observations. Considering the

small investment of effort and resources required to perform such a survey, the technique provides an exceptionally economic means of obtaining useful detail about sources at high resolution.

The SHEVE array is now well established as a unique tool for the investigation of Southern radio sources at high resolution. The future prospects for the array appear very good. The Mark-II VLBI recording system is presently being replaced with an S-2 system, and a correlator for this format is under construction at the ATNF headquarters in Sydney. This will permit more sensitive observations to be made more frequently and easily as the delay and expense associated with using an overseas correlator will be eliminated. Several antennas are being equipped for observations at 22 GHz, a step that will double the resolution achievable. The advent in the next few years of space VLBI, in which Australian observatories will actively participate, is going to permit Southern radio sources to be studied with unprecedented resolution. In particular, earth-space baselines will allow observations of peaked spectrum sources at frequencies at or below those of the peaks with a resolution comparable to the centimetre wavelength observations described here.

SHEVE observations have already incorporated antennas outside Australia and South Africa. Experiments involving Chinese, Japanese and Russian stations have been performed and correlated. More recently, joint observations with the VLBA have taken place. There is a prospect of a second-hand 30 m antenna becoming available within two years. This antenna is a decommissioned communications instrument located at Ceduna, near Adelaide, about halfway across the Australian continent. Should this antenna join the array, it will constitute a sensitive and versatile replacement for the Alice Springs antenna which is now rarely used. The east-west baselines between this antenna and the east coast stations will fill the gap in the uv-plane between Perth and the east coast leading to a substantial improvement in the dynamic range achievable in images. Furthermore, these new, and more sensitive, east west baselines will generate many more crossing points in the uv-plane, considerably easing the task of ensuring the correct internal calibration of the array.

Overall, the prospects for VLBI in the Southern Hemisphere are very good and will undoubtedly permit more detailed future investigations of peaked spectrum sources that will capitalise on the foundations laid by the observations presented in this thesis.

Appendix A

Flux Monitoring Receiver And Sampling

A.1 Introduction

This appendix elaborates upon the description given in Chapter 3 of the receiver and IF system used for the flux monitoring observations. The implementation of the noise-adding radiometer and issues relating to the signal digitisation are also discussed.

A.2 RF and IF Stages

A simplified schematic of the analogue hardware used for the flux monitoring observations is presented in Figure A.1. The choice of the precise observing frequencies was influenced by a variety of limitations imposed by the available equipment. The centres of the passbands entering the detectors corresponded to frequencies on the sky of 2302 MHz and 8436 MHz. The components labelled 'DC amplifiers and time constants' are included for the purpose of conditioning the detected signals so that they are suitable for input to the digitisers. They scale, offset and low-pass filter the detector output voltages so that they fall within the operating range of the digitisers and ensure that the sampling theorem is satisfied.

The observations are controlled via a PDP-11 computer which handles scheduling, interfaces with the antenna control computer, and switches the CAL signal while sampling the data which it stores on disk for off-line analysis.

A.3 Noise-adding Radiometer

System temperature fluctuations caused by receiver gain instabilities limit the accuracy with which flux intensity measurements can be obtained. One means of overcoming this difficulty is to calibrate the system gain by injecting a signal of known strength into the receiver input with sufficient frequency to characterise the gain variations over time. When this calibration is performed throughout an observation, the receiver configuration is known as a noise-adding radiometer

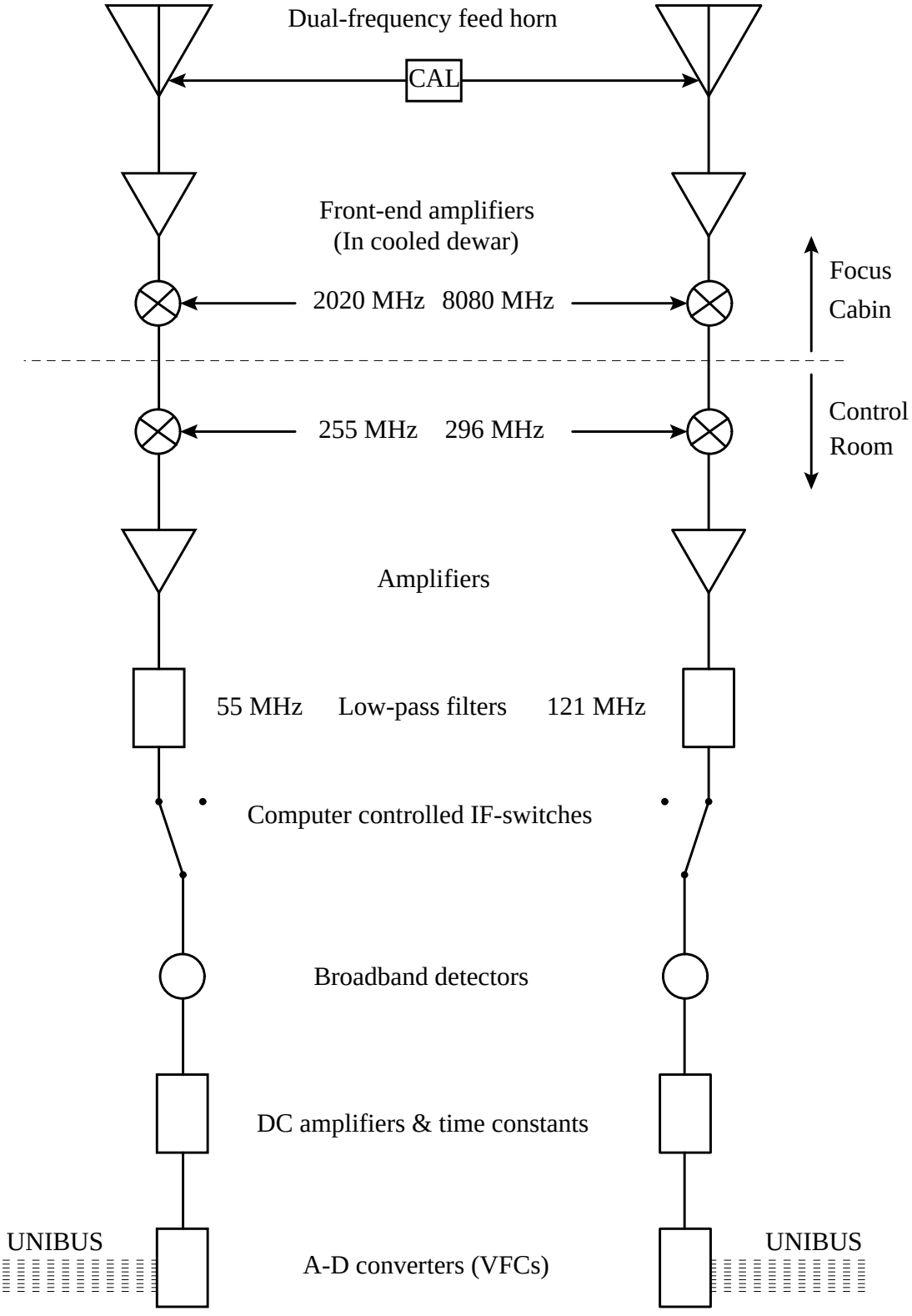

Figure A.1: Receiver and IF configuration used for the flux monitoring observations.

(NAR). Early implementations of NAR systems employed specialised analog electronic hardware to perform the gain calibration and apply appropriate corrections to the system temperature measurements (for example, Jelley and Cooper (1961), Batelaan *et al.* (1970) and Yerbury (1975)). However the complexity of such systems tended to compromise their flexibility and reliability. The NAR developed for the flux monitoring observations reported in Chapter 3 utilises a digital computer in place of the additional hardware and is decribed below.

Theory Of Operation

A NAR operates by switching a calibration signal (CAL) repeatedly throughout and observation and measuring the detector outputs for the CAL-off and CAL-on states separately, allowing continuous monitoring of the receiver gain. This is illustrated in Figure A.2. The voltage v_0 is due to offsets set in the DC amplifiers and is determined to establish the zero point for the measurements of the system temperature prior to each observation by opening the IF-switches (Figure A.1) so that there is no detector output signal. The voltages v_1' and v_2' then are

$$\left.\begin{array}{rcccl} v_1' & = & v_0 + v_1 & = & v_0 + GT_{sys} \\ v_2' & = & v_0 + v_2 & = & v_0 + G(T_{sys} + T_{cal}) \end{array}\right\} \tag{A.1}$$

where G is the system gain, T_{sys} and T_{cal} are the system and CAL temperatures, and v_1 and v_2 are the detector voltages when the CAL is off and on respectively. The system temperature is the sum of the receiver noise (T_{Rx}) and antenna temperatures (T_A). The quantity

$$v_R = \frac{v_1}{v_2 - v_1} = \frac{T_{sys}}{T_{cal}} \tag{A.2}$$

is then proportional to T_{sys} but independent of the gain G. In this manner, provided the CAL remains stable on timescales greater than the gain fluctuations and the system temperature does not change significantly between the measurement of v_1 and v_2, the system temperature can be determined reliably.

The primary disadvantages of this approach to the removal of gain fluctuations is that system sensitivity is reduced because time is spent measuring the contribution of the CAL, and any error in the determination of the denominator in Equation A.2 increases the uncertainty in the result. These two limitations oppose one another since any reduction in the duty cycle (d) of the CAL switching leads to a decrease in the accuracy of the CAL measurement itself. The determination of the CAL can be improved by making the CAL as large as possible compared with the system temperature. However the maximum size of the CAL is constrained by the need to operate the receiver system in the range of signal levels over which it is linear. An alternative method of improving the sensitivity of the system follows from the recognition that if the system gain is changing slowly compared with the CAL switching cycle, then many successive CAL measurements can be averaged to yield a more accurate result. This is true even if the system temperature is changing (when scanning across a strong source for example), since the CAL measurements are independent of T_{sys} provided the CAL is being switched sufficiently rapidly.

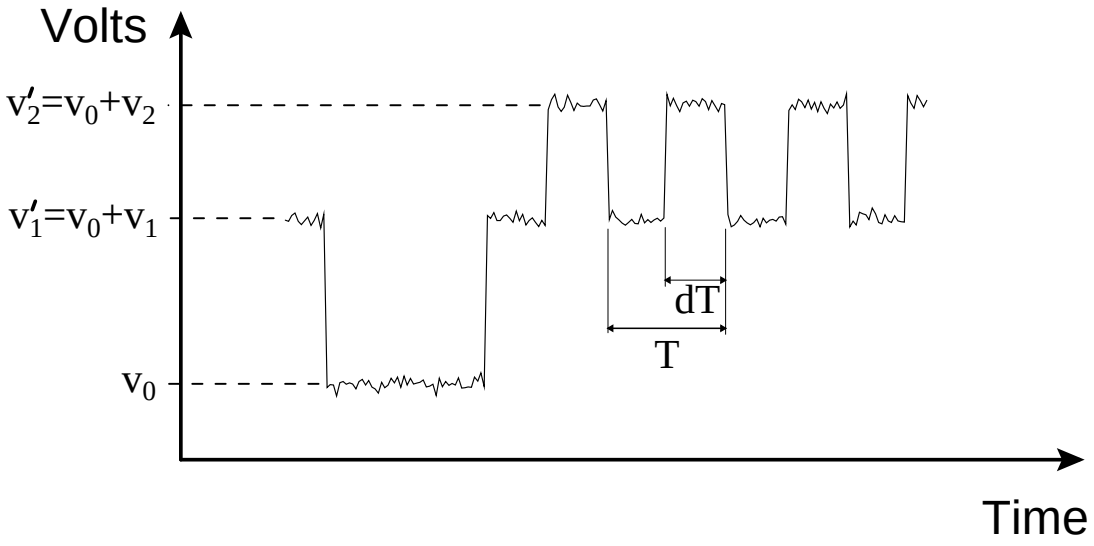

Figure A.2: The detector output voltage at the beginning of an observation with the NAR. The three voltages are explained in the text.

A derivation of the sensitivity of a NAR with CAL averaging is presented here. In what follows, the bar over a quantity $\overline{x}$ denotes an average of x over N samples. The mean value of the CAL is thus

$$\overline{C} = \frac{1}{N}\sum_{i=1}^{N}(v_{2_i} - v_{1_i}) = \overline{v_2} - \overline{v_1}$$

Provided that the fractional change in v_1 and v_2 over the averaging interval is small, and since v_1 and v_2 are independent, the error in this value is

$$\Delta\overline{C}^2 = \Delta\overline{v_1}^2 + \Delta\overline{v_2}^2$$

where

$$\Delta\overline{v_1} = \frac{\overline{v_1}}{\sqrt{NB(1-d)T}} \quad and \quad \Delta\overline{v_2} = \frac{\overline{v_2}}{\sqrt{NBdT}}$$

Here B is the pre-detection bandwidth and T is the CAL switching period, so that $(1-d)T$ and dT are the integration times when the CAL is off and on respectively (Figure A.2). The uncertainty in the CAL average is thus

$$(\Delta\overline{C})^2 = \frac{1}{NBT}\left(\frac{\overline{v_1}^2}{1-d} + \frac{\overline{v_2}^2}{d}\right)$$

If Equation A.2 is now modified to take into account the averaged CAL, then the new value of v_R is

$$v_R = \frac{v_1}{\overline{C}} = \frac{T_{sys}}{\overline{T}_{cal}} \tag{A.3}$$

Although $\overline{C}$ depends on v_1, provided N is large enough the dependence is sufficiently weak that the uncertainty in v_R can be written

$$\Delta {v_R}^2 = \left(\frac{\partial v_R}{\partial v_1}\right)^2 (\Delta v_1)^2 + \left(\frac{\partial v_R}{\partial \overline{C}}\right)^2 (\Delta\overline{C})^2$$

which becomes

$$\Delta v_R = \frac{v_1}{\overline{C}} \frac{1}{\sqrt{BT}} \left\{ \frac{1}{1-d} + \frac{1}{N} \left[\frac{1}{1-d} \left(\frac{\overline{v_1}}{\overline{C}} \right)^2 + \frac{1}{d} \left(\frac{\overline{v_2}}{\overline{C}} \right)^2 \right] \right\}^{\frac{1}{2}} \tag{A.4}$$

If the minimum detectable temperature T_{min} is defined to be the temperature that causes v_R to change by Δv_R, then from Equation A.3

$$\Delta v_R = \frac{T_{sys} + T_{min}}{\overline{T}_{cal}} - \frac{T_{sys}}{\overline{T}_{cal}} = \frac{T_{min}}{\overline{T}_{cal}} \tag{A.5}$$

Combining this with Equation A.4 and substituting the averaged form of Equation A.1 yields the result

$$T_{min} = \frac{T_{sys}}{\sqrt{BT}} \left\{ \frac{1}{1-d} + \frac{1}{N} \left[\frac{1}{1-d} \left(\frac{\overline{T}_{sys}}{\overline{T}_{cal}} \right)^2 + \frac{1}{d} \left(\frac{\overline{T}_{sys}}{\overline{T}_{cal}} + 1 \right)^2 \right] \right\}^{\frac{1}{2}} \tag{A.6}$$

Recall that the switching period T is chosen so that the difference between v_1 and v_2 due to changing T_{sys} is negligible for each pair of CAL-on and CAL-off measurements. Then if the receiver gain is known to be stable over a timescale τ, the number of cycles N, over which the CAL can be averaged is given by $N = \tau/T$. Having so fixed T and N, the optimum value of the duty cycle d, to yield the smallest T_{min} can be found by differentiating Equation A.6 which gives

$$d = \frac{1}{1 + \sqrt{\frac{N + \left(\frac{\overline{T}_{sys}}{\overline{T}_{cal}} \right)^2}{\left(1 + \frac{\overline{T}_{sys}}{\overline{T}_{cal}} \right)^2}}} \tag{A.7}$$

Note that for the special case where $d = 0.5$ and $N = 1$, Equation A.6 reduces to

$$T_{min} = \frac{2T_{sys}}{\sqrt{BT}} \left[\left(1 + \frac{\overline{T}_{sys}}{\overline{T}_{cal}} \right)^2 - \frac{\overline{T}_{sys}}{\overline{T}_{cal}} \right]^{\frac{1}{2}}$$

in agreement with Yerbury (1975)(pp 177). Furthermore, in the absence of gain fluctuations, if $N \to \infty$, then Equation A.7 indicates $d \to 0$ and

$$T_{min} = \frac{T_{sys}}{\sqrt{BT}}$$

which is just the conventional expression describing an ideal radiometer.

The validity of Equation A.6 was tested by comparison with measurements obtained from the NAR applied to the 2.3 GHz receiver with a range of different duty cycles and averaging times for the CAL. Graphs showing the results of these tests as a function of CAL averaging time (upper 9 panels) and duty cycle (lower 9 panels) are presented in Figure A.3. The switching frequency of the CAL is 23 Hz and the ratio $\overline{T}_{sys}/\overline{T}_{cal} \simeq 6.6$. The ordinate in each graph represents the root mean square deviation of the CAL-off measurements from each CAL-cycle (no averaging of the output across cycles having been applied), calculated over an interval of

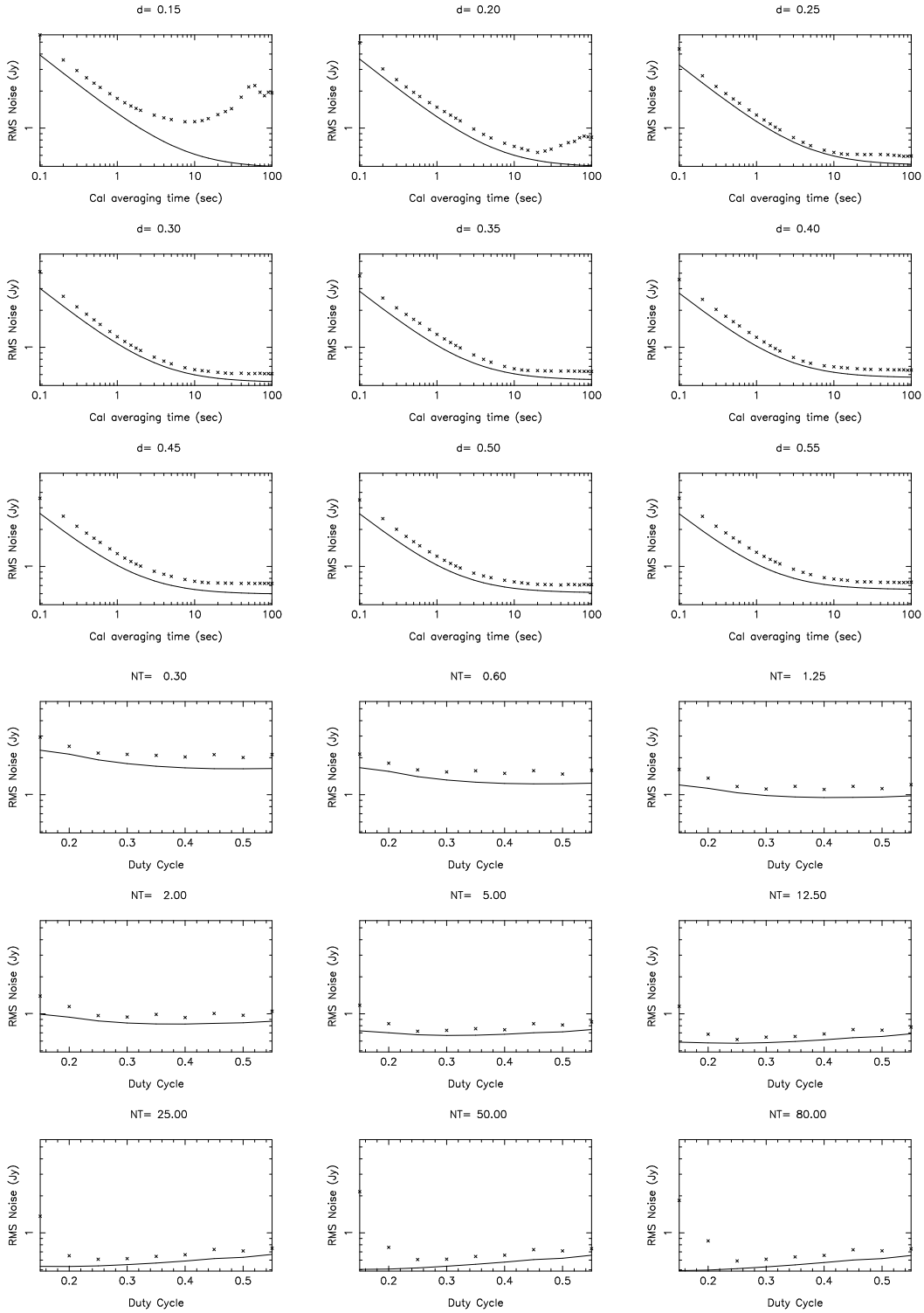

Figure A.3: Comparison of predicted (solid line) and actual (crosses) performance of the NAR. See text for details.

45 seconds. The predicted sensitivity of an ideal (gain-stable) radiometer operating under the same conditions (bandwidth, system temperature etc.) is approximately ~ 0.43 Jy. For CAL averaging times up to about 15 seconds Equation A.6 predicts the behaviour of the NAR very well. Beyond that time, receiver instabilities render further averaging ineffective. For an averaging time of 15 seconds, Equation A.7 indicates that the preferred duty cycle for this system is ~ 0.28 and it can be seen from the graphs that the performance of the NAR is indeed close to optimal for this value. The uniform offset between the predicted curves and the measured points indicates that the noise intrinsic to the receiver/sampling system has been underestimated by between 5 and 10 percent, possibly because of an incorrect estimate of the effective RF bandwidth or a contribution from quantization errors in the sampling process. The discrepancy could also arise, in part, from genuine variations in the antenna temperature during data acquisition. It is not feasible to remove these effects as part of the analysis process without compromising the sensitivity measurements themselves.

Implementation

The NAR, antenna control, and sampling are integrated within a single program that runs on a PDP-11 computer. The NAR program works by repeatedly sampling the detector output voltage and switching the CAL state after the appropriate number of samples to simulate the desired duty cycle (Figure A.4). All samples obtained in either the CAL-off or CAL-on state are averaged in real-time to yield measurements of v_1 and v_2 for each cycle which are buffered in memory before being periodically written directly to disk storage. Depending on the post-detector time constant, one or more of the samples immediately subsequent to a CAL state change are discarded so that no data is recorded whilst the detector voltage is in transition. This has the effect of marginally degrading the NAR performance since these data make no contribution to the output.

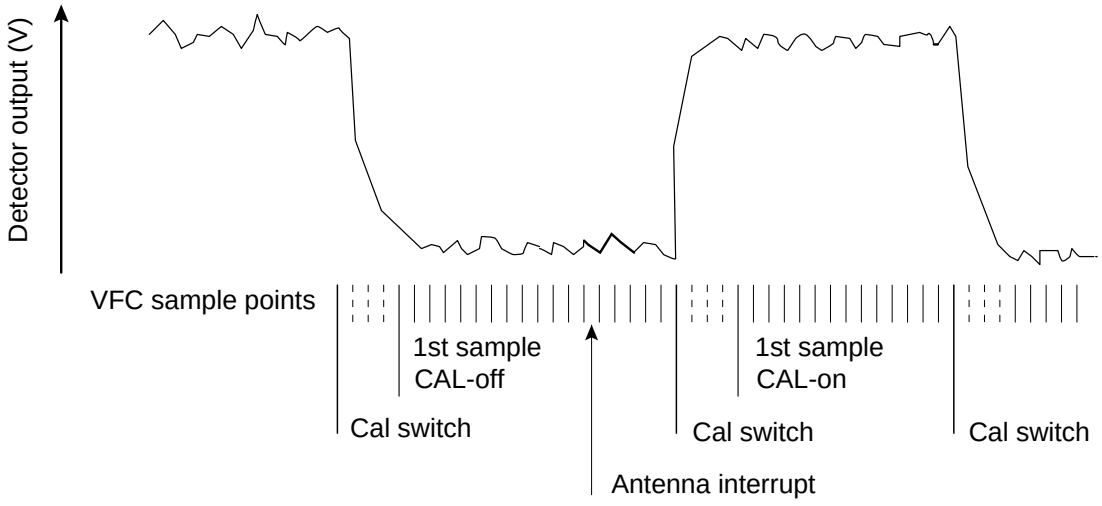

Figure A.4: The operation of the NAR over one CAL switching cycle showing the relationship between the VFC sampling, CAL state and antenna interrupts. The samples represented by dashed lines are rejected since they correspond to neither the CAL-off or CAL-on states.

Sampling of the detector voltage is achieved by means of analog to digital converters based on a voltage to frequency converter (VFC), a device which produces a periodic output signal with a frequency proportional to the input voltage. If the number of cycles of the output is counted for a fixed interval, the sum is a quantity proportional to the integrated input voltage. The sampling rate is determined by a programmable synthesiser which drives a Pulsar Timing Unit (PTU), a specialised pre-scaler that generates signals suitable for producing interrupts on the PDP-11 UNIBUS. These signals halt 12-bit counters in all the VFCs simultaneously. The control circuitry then automatically latches the counter contents into registers accessible from the UNIBUS before resetting and restarting the VFC counters. The same signal that triggers the VFCs is used to invoke an interrupt request on the PDP-11 (Figure A.5). The routine that services the interrupt is responsible for reading each VFC register and storing the data appropriately before the next interrupt is requested by the PTU.

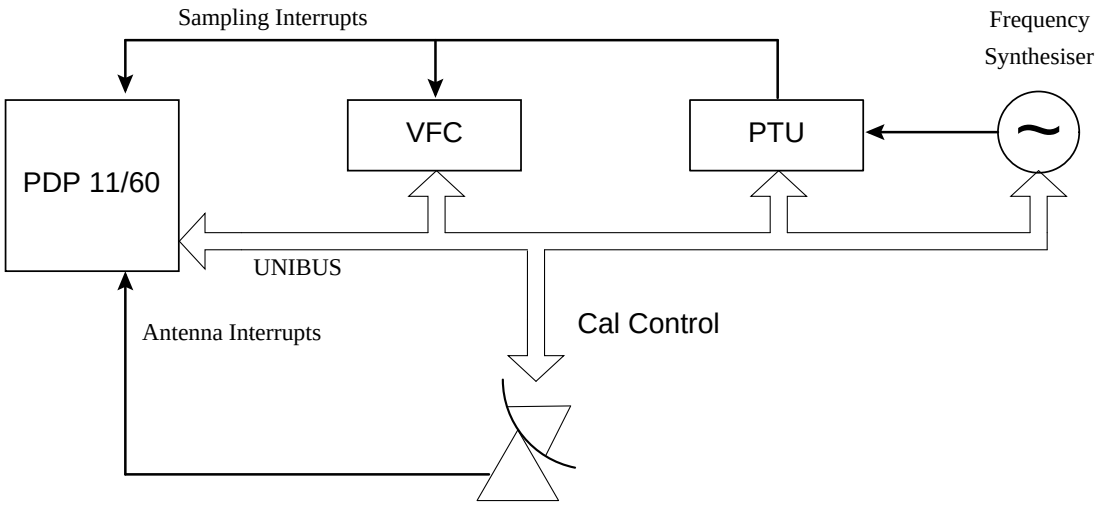

Figure A.5: Configuration of devices integral to the functioning of the NAR. The interrupt signals are actually delivered to the PDP-11 via the UNIBUS but are shown as separate signals for clarity.

Unless operated correctly, VFCs can be prone to severe quantization noise for very short sample intervals (or, equivalently, high sampling rates). The average quantization error in any digital sample is half the least-significant bit. For a sample-and-hold digitiser, this is not normally a problem since the input voltage can usually be scaled so that the least-significant bit is small compared with the digitizer output. However for a VFC, the output count is directly proportional to the sampling interval, so for high speed sampling half the least-significant bit can represent a substantial fraction of the total count. By averaging N samples together the effect of this sampling error can be reduced by a factor of approximately $1/\sqrt{N}$. However, if the sampling time is instead increased by a factor of N, then the sampling error will be reduced by $1/N$. This is an important consideration for the NAR since it is desirable to operate the VFCs at as high a rate as possible to achieve the maximum possible resolution for adjustment of the duty cycle and the interval over which samples are rejected following a change in the CAL

state. In practice it is usually possible to operate the system with a sufficiently low sample rate so that this effect is insignificant since the sensitivity of the NAR depends only weakly on the precise duty cycle used. The lowest sampling rate is determined by the rate at which the VFCs run (250kHz per volt input) and the number of bits available in the counters before overflow occurs. For the 12-bit counters the minimum sample rate for a 1 volt input signal is 61 Hz.

The VFC's have a linear operating range of 0.2−2.0 volts. The DC-amplifiers ensure that the input signals stay within this range, even when there is no input to the detectors. As described in the previous section, this is a condition established immediately before and after each observation when the IF-switches (Figure A.1) are opened to determine the zero level (v_0 in Figure A.2) for the system temperature measurement. The zero level measurements are made either side of each observation so that the effect of any drift in the DC amplifiers can be minimised by interpolation. This method of measuring the zero level (opening the IF-switches) depends critically on the linearity of the detectors and was chosen instead of the more common technique of insertion of a known attenuation into the IF-system primarily because of hardware availability. The linearity of the whole IF and sampling system was checked at intervals throughout the observing program and great care was taken to ensure that precisely the same components were used for all observations.

An interface to the antenna control computer permits the NAR control program running on the PDP-11 to request the antenna motions necessary to observe each source. It is important to be able to register the detector output samples with the antenna position so that pointing effects can be correctly quantified. The antenna control system can be requested to scan the antenna at a constant rate and to generate a signal at uniform angular increments. This signal is used to generate an interrupt on the PDP-11 which results in the recording of the number of VFC samples that have been taken. This list of sample numbers is used in subsequent processing to ascribe position information to the sampled data. There is no synchronization between the sampling and antenna interrupts so it is important that the sampling rate be large enough that the time when an antenna interrupt is delivered is well defined. The first interrupt generated by the antenna in each scan initiates the sampling process, ensuring that a common zero-point is established.

Appendix B

Imaging Visibilities

The visibilities from which the images in Chapter 5 were made are presented in Figure B.1. The visibility amplitudes and closure phases are shown, together with the model composed of the image clean components, plotted as a solid line. The data from the images of the three sources 0237−233, 1549−790 and 1934−638 that were made using only the Australian baselines are only subsets of the complete data sets and are not shown here separately.

Figure B.1: Complete visibility amplitudes and closure phases for the data used to produce the images in Chapter 5 appear on the following pages.

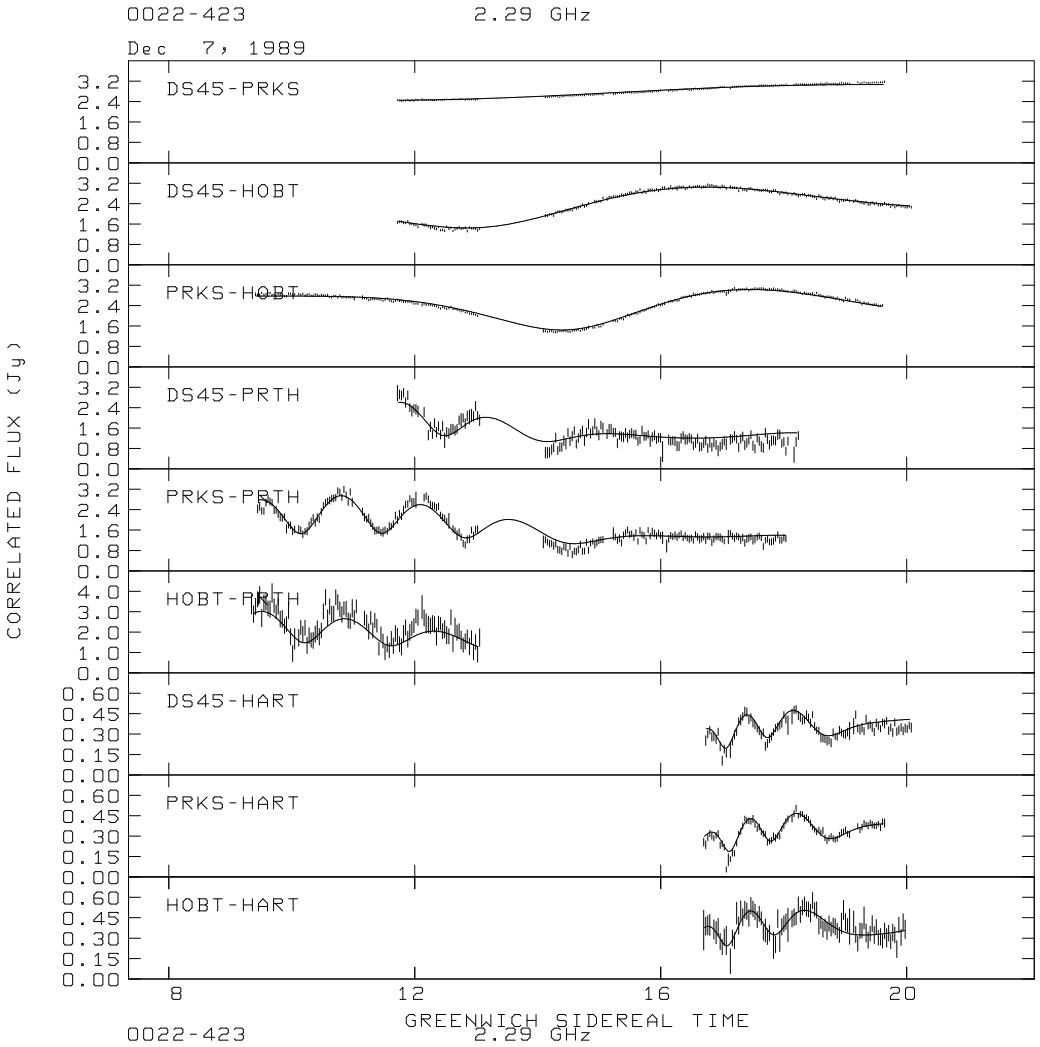
0022-423
2.29 GHz
Dec 7, 1989
DS45-PRKS
DS45-HOBT
PRKS-HOBT
DS45-PRTH
PRKS-PRTH
HOBT-PRTH
DS45-HART
PRKS-HART
HOBT-HART
CORRELATED FLUX (Jy)
GREENWICH SIDEREAL TIME

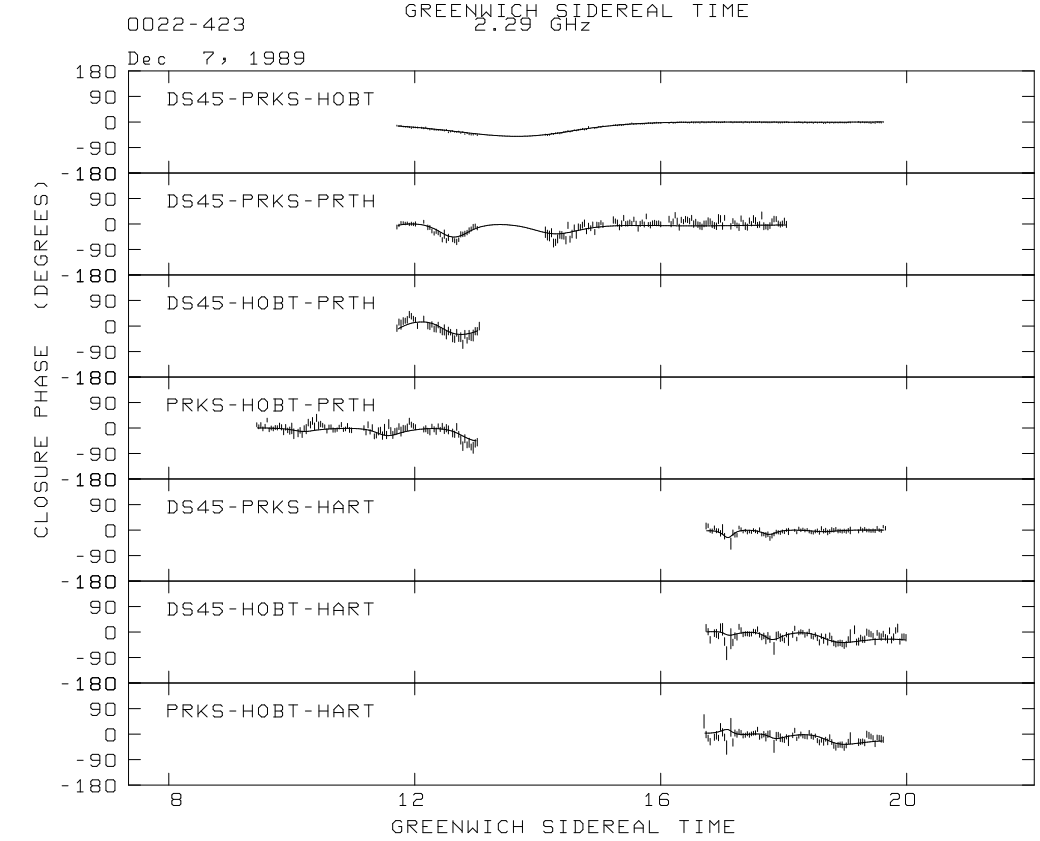
0022-423
2.29 GHz
Dec 7, 1989
DS45-PRKS-HOBT
DS45-PRKS-PRTH
DS45-HOBT-PRTH
PRKS-HOBT-PRTH
DS45-PRKS-HART
DS45-HOBT-HART
PRKS-HOBT-HART
CLOSURE PHASE (DEGREES)
GREENWICH SIDEREAL TIME

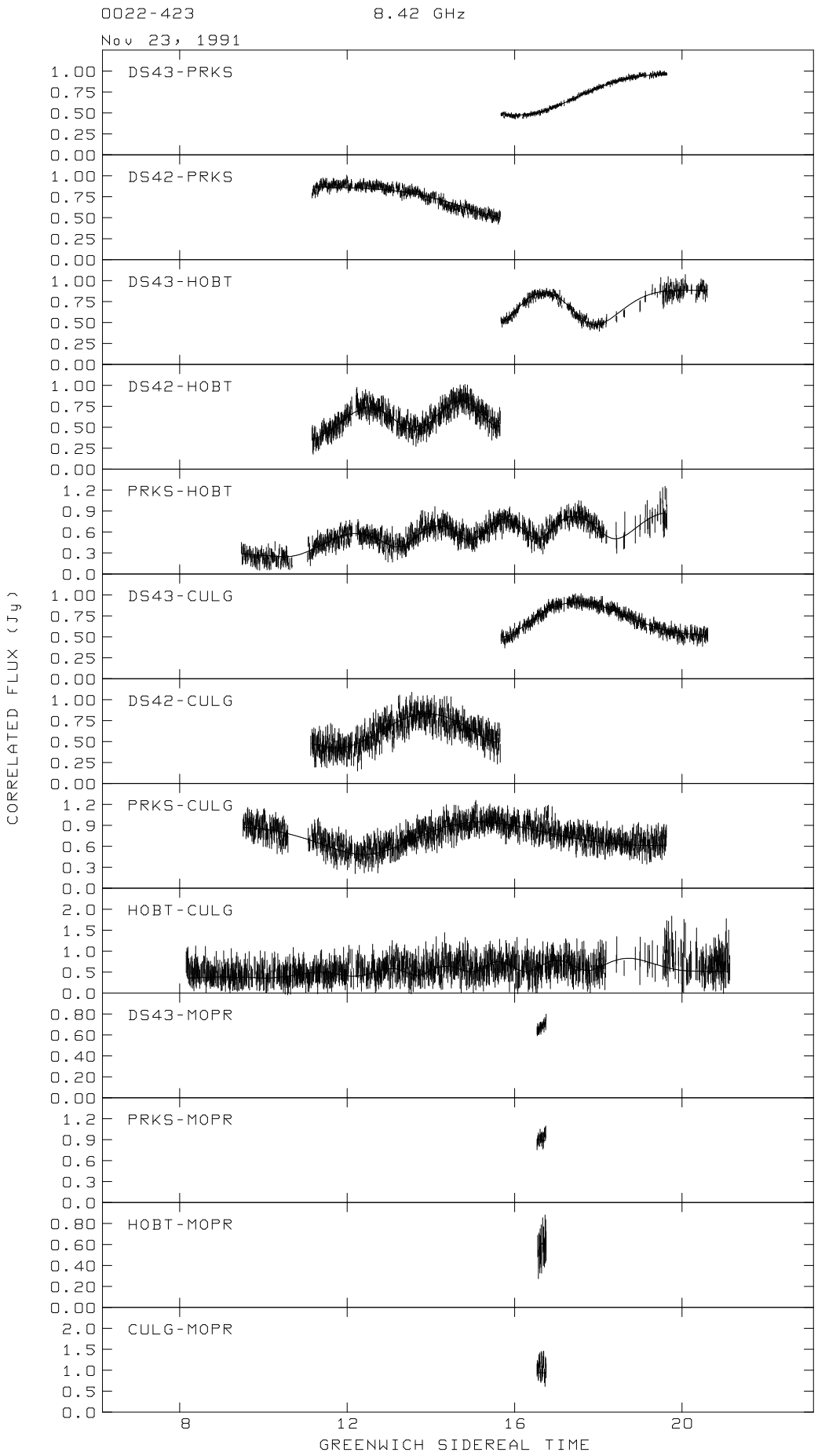
0022-423
8.42 GHz
Nov 23, 1991
DS43-PRKS
DS42-PRKS
DS43-HOBT
DS42-HOBT
PRKS-HOBT
DS43-CULG
DS42-CULG
PRKS-CULG
HOBT-CULG
DS43-MOPR
PRKS-MOPR
HOBT-MOPR
CULG-MOPR
CORRELATED FLUX (Jy)
GREENWICH SIDEREAL TIME
8
12
16
20

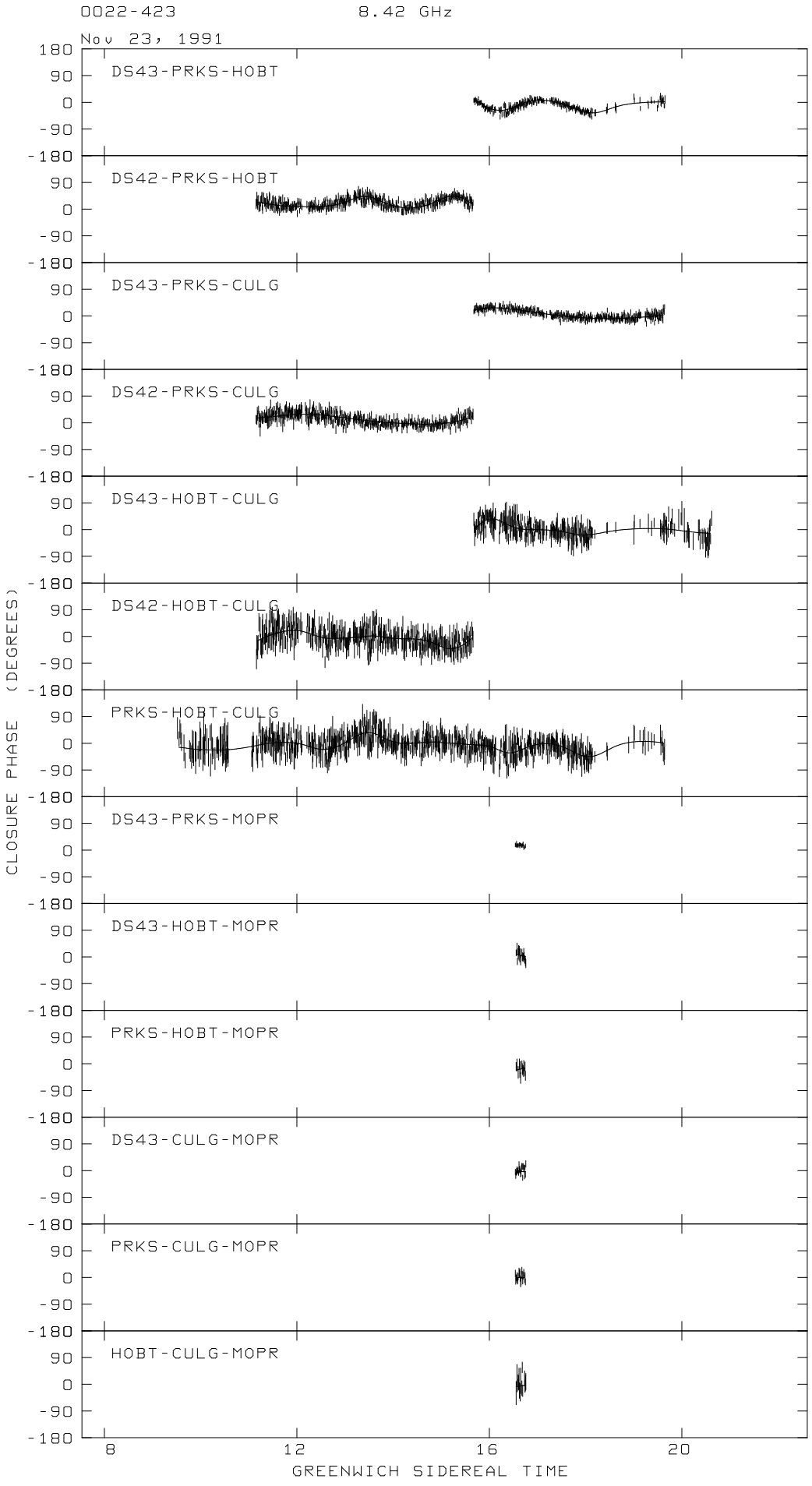
0022-423
8.42 GHz
Nov 23, 1991
DS43-PRKS-HOBT
DS42-PRKS-HOBT
DS43-PRKS-CULG
DS42-PRKS-CULG
DS43-HOBT-CULG
DS42-HOBT-CULG
PRKS-HOBT-CULG
DS43-PRKS-MOPR
DS43-HOBT-MOPR
PRKS-HOBT-MOPR
DS43-CULG-MOPR
PRKS-CULG-MOPR
HOBT-CULG-MOPR
180
90
0
-90
-180
CLOSURE PHASE (DEGREES)
8
12
16
20
GREENWICH SIDEREAL TIME

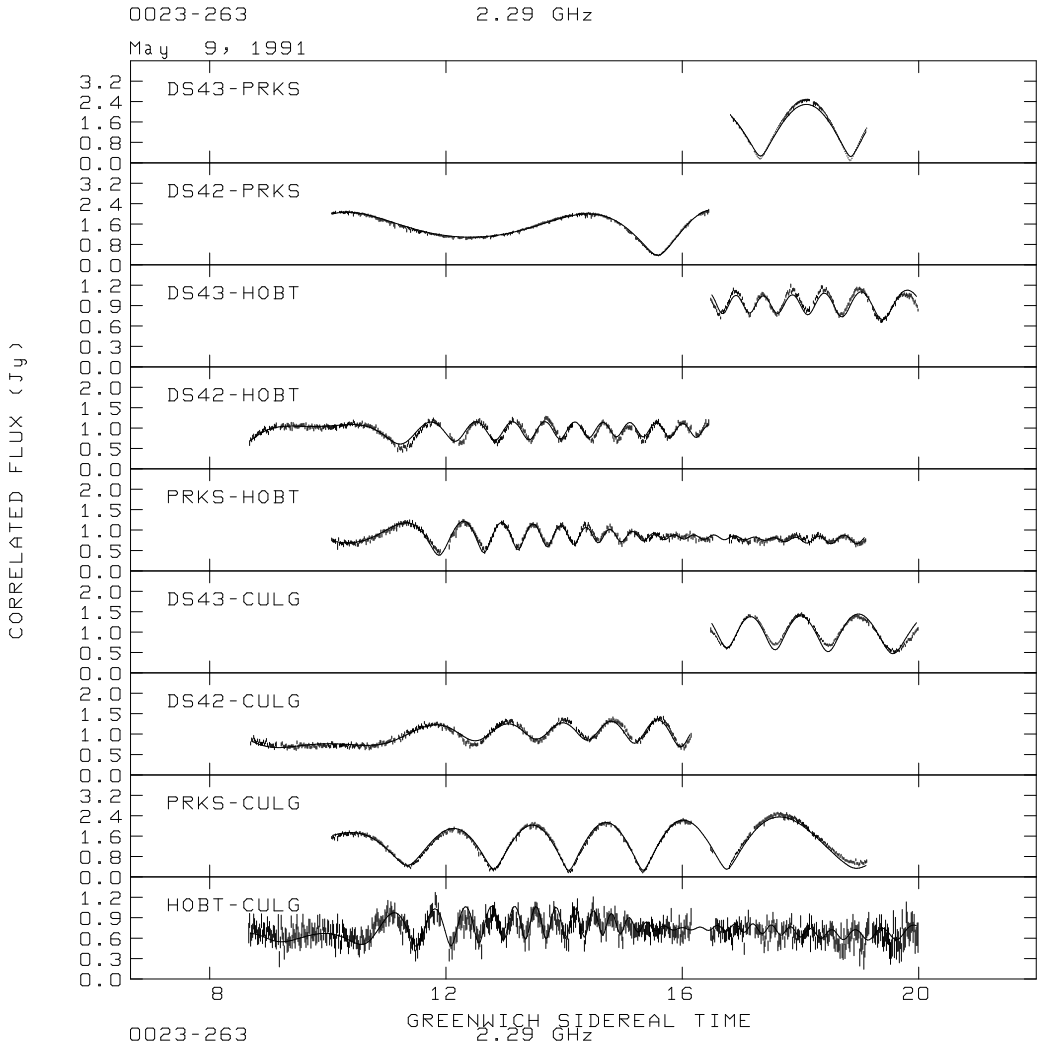
0023-263
2.29 GHz
May 9, 1991
DS43-PRKS
DS42-PRKS
DS43-HOBT
DS42-HOBT
PRKS-HOBT
DS43-CULG
DS42-CULG
PRKS-CULG
HOBT-CULG
CORRELATED FLUX (Jy)
GREENWICH SIDEREAL TIME

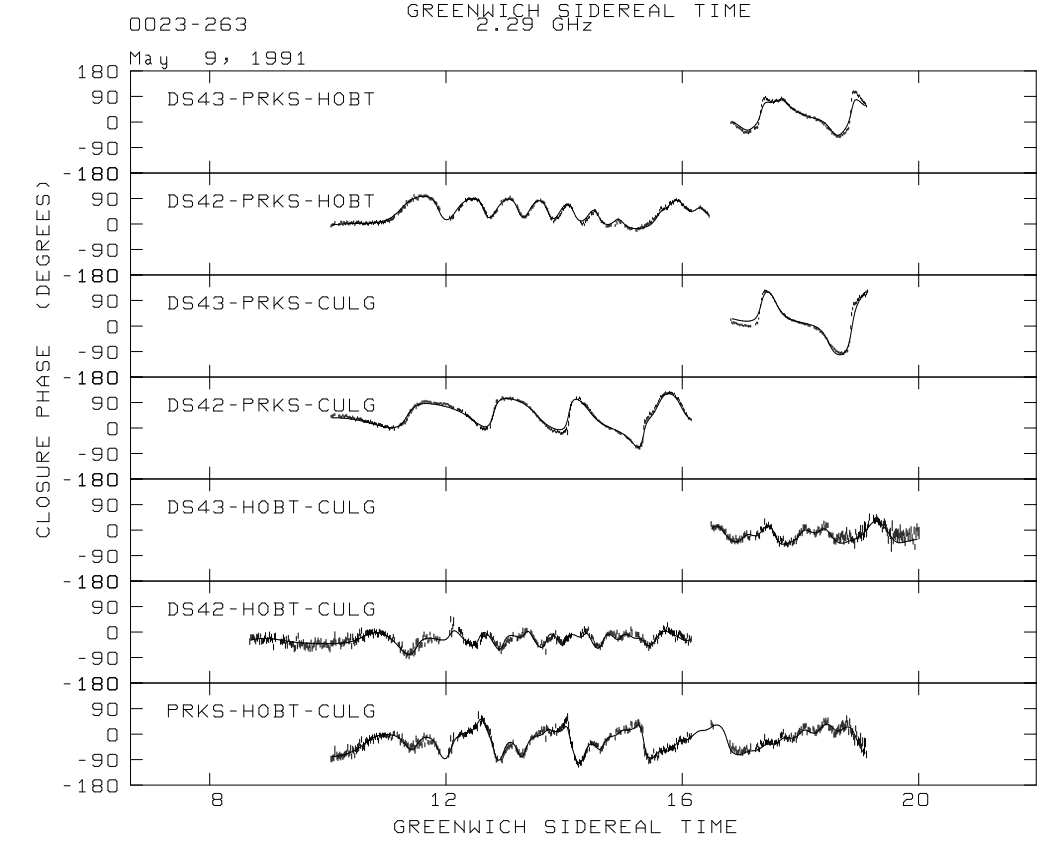
0023-263
2.29 GHz
May 9, 1991
DS43-PRKS-HOBT
DS42-PRKS-HOBT
DS43-PRKS-CULG
DS42-PRKS-CULG
DS43-HOBT-CULG
DS42-HOBT-CULG
PRKS-HOBT-CULG
CLOSURE PHASE (DEGREES)
GREENWICH SIDEREAL TIME

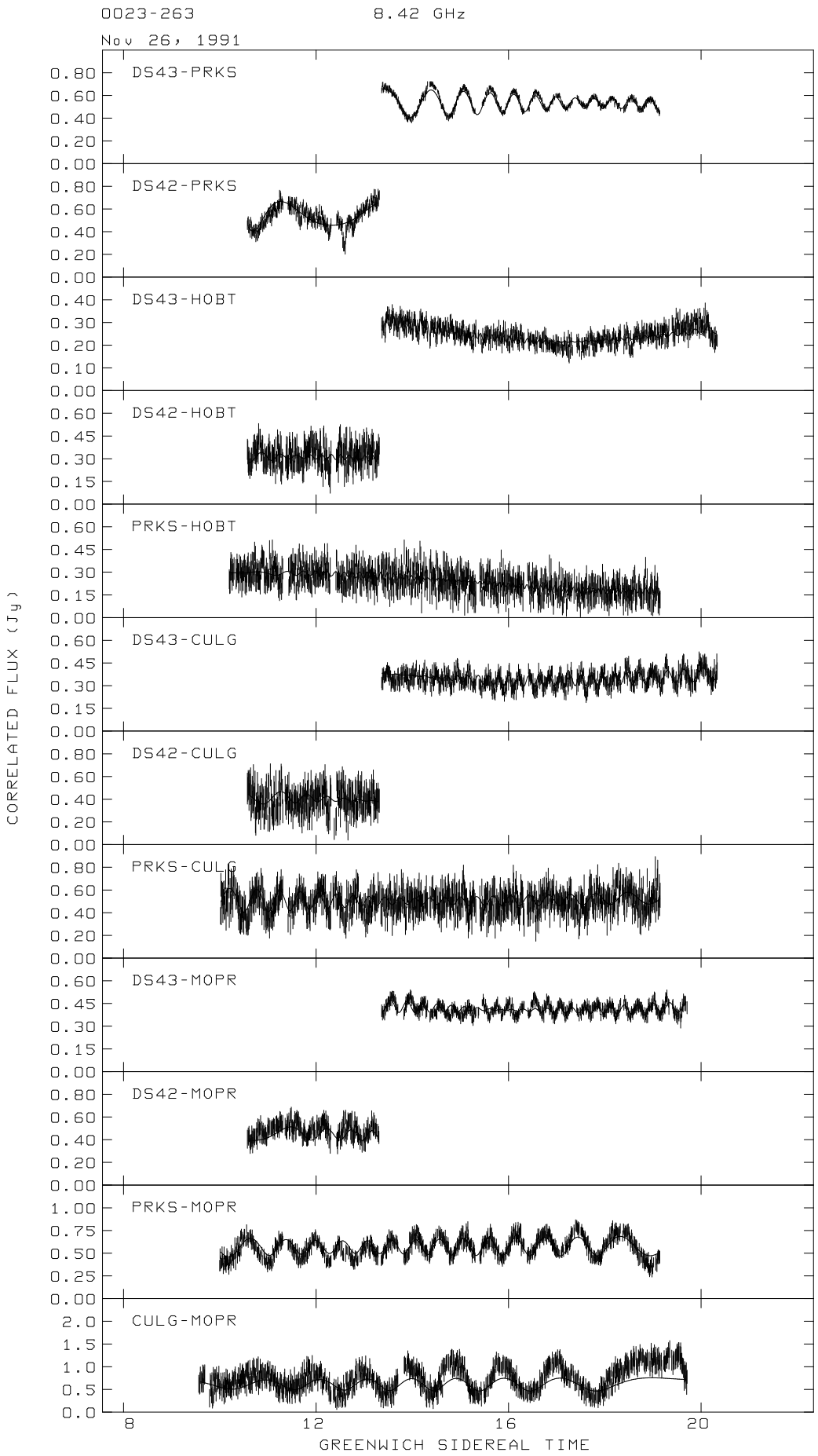
0023-263
8.42 GHz
Nov 26, 1991
DS43-PRKS
DS42-PRKS
DS43-HOBT
DS42-HOBT
PRKS-HOBT
DS43-CULG
DS42-CULG
PRKS-CULG
DS43-MOPR
DS42-MOPR
PRKS-MOPR
CULG-MOPR
CORRELATED FLUX (Jy)
GREENWICH SIDEREAL TIME
8
12
16
20

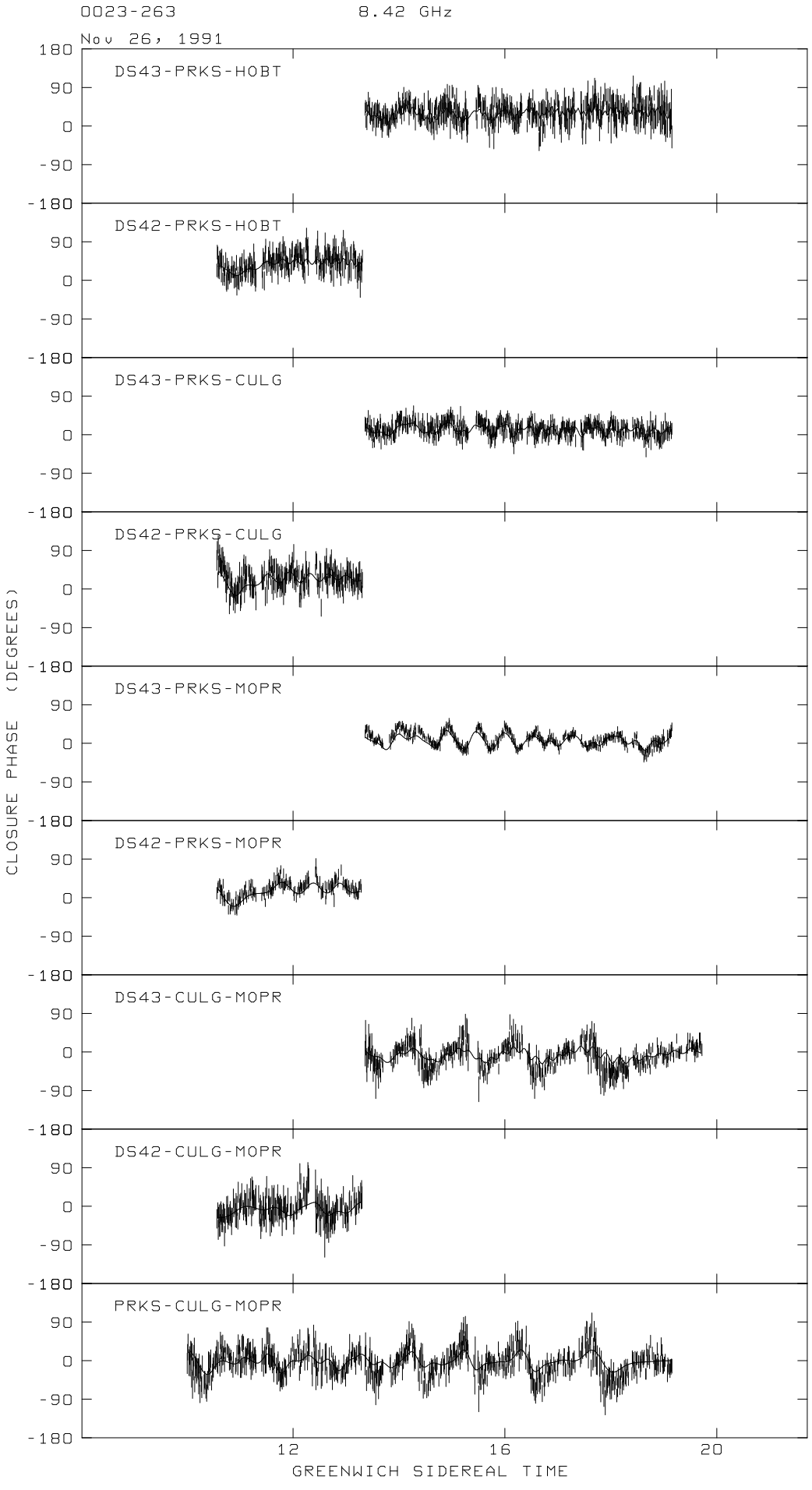
0023-263
8.42 GHz
Nov 26, 1991
DS43-PRKS-HOBT
DS42-PRKS-HOBT
DS43-PRKS-CULG
DS42-PRKS-CULG
DS43-PRKS-MOPR
DS42-PRKS-MOPR
DS43-CULG-MOPR
DS42-CULG-MOPR
PRKS-CULG-MOPR
180
90
0
-90
-180
CLOSURE PHASE (DEGREES)
12
16
20
GREENWICH SIDEREAL TIME

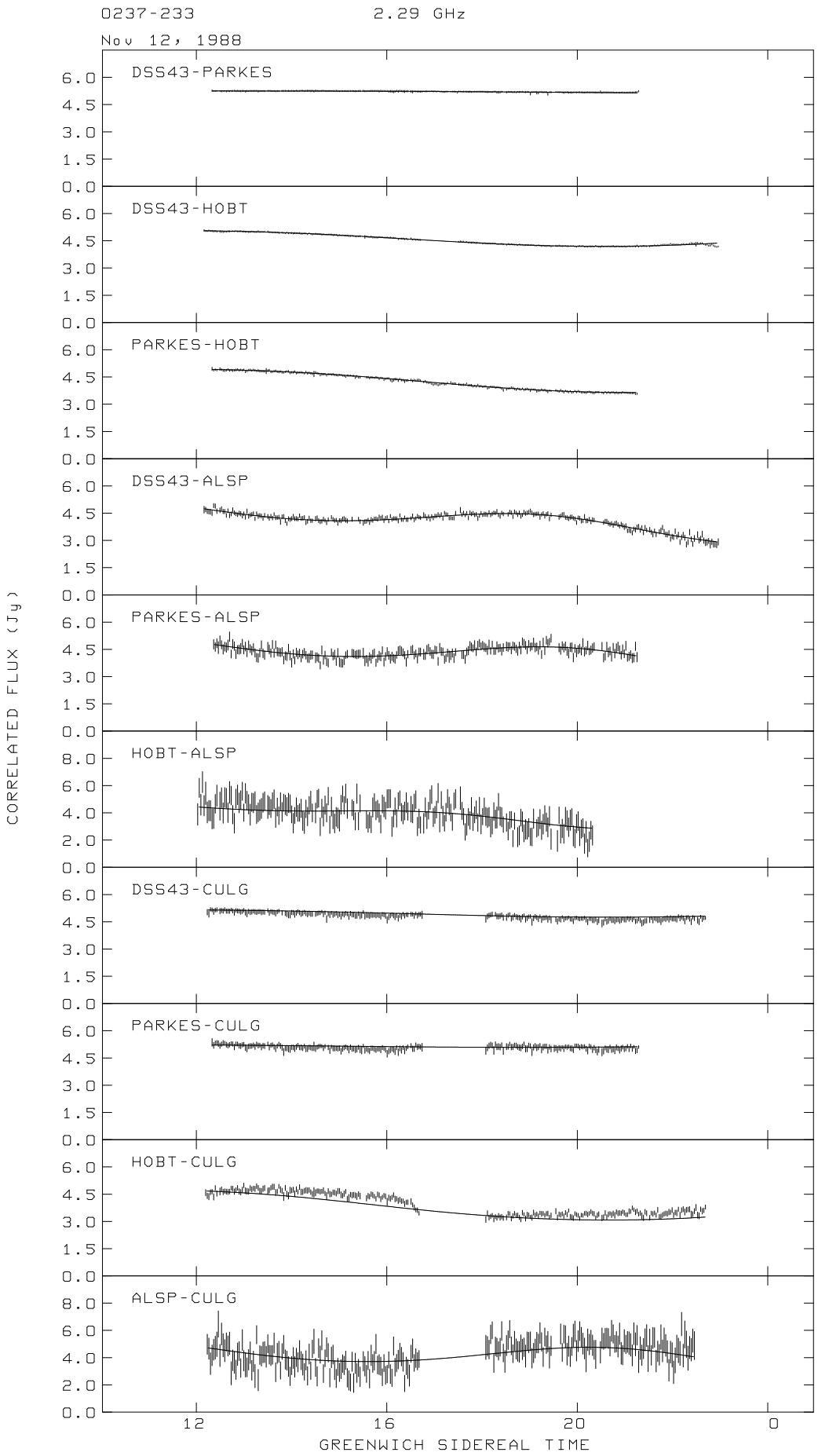
0237-233
2.29 GHz
Nov 12, 1988
DSS43-PARKES
DSS43-HOBT
PARKES-HOBT
DSS43-ALSP
PARKES-ALSP
HOBT-ALSP
DSS43-CULG
PARKES-CULG
HOBT-CULG
ALSP-CULG
CORRELATED FLUX (Jy)
GREENWICH SIDEREAL TIME
12
16
20
0

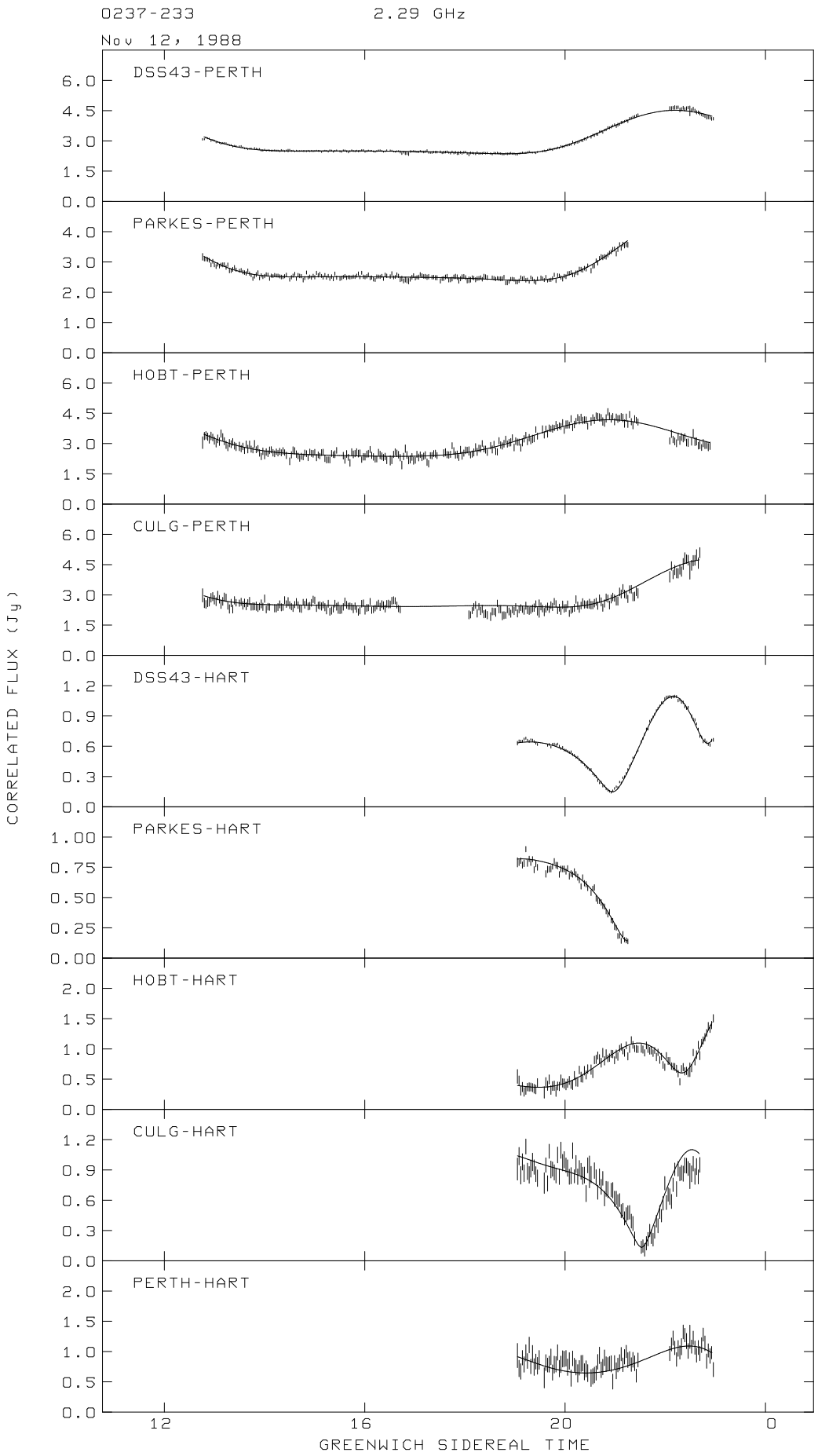
0237-233
2.29 GHz
Nov 12, 1988
DSS43-PERTH
PARKES-PERTH
HOBT-PERTH
CULG-PERTH
DSS43-HART
PARKES-HART
HOBT-HART
CULG-HART
PERTH-HART
CORRELATED FLUX (Jy)
GREENWICH SIDEREAL TIME
12
16
20
0

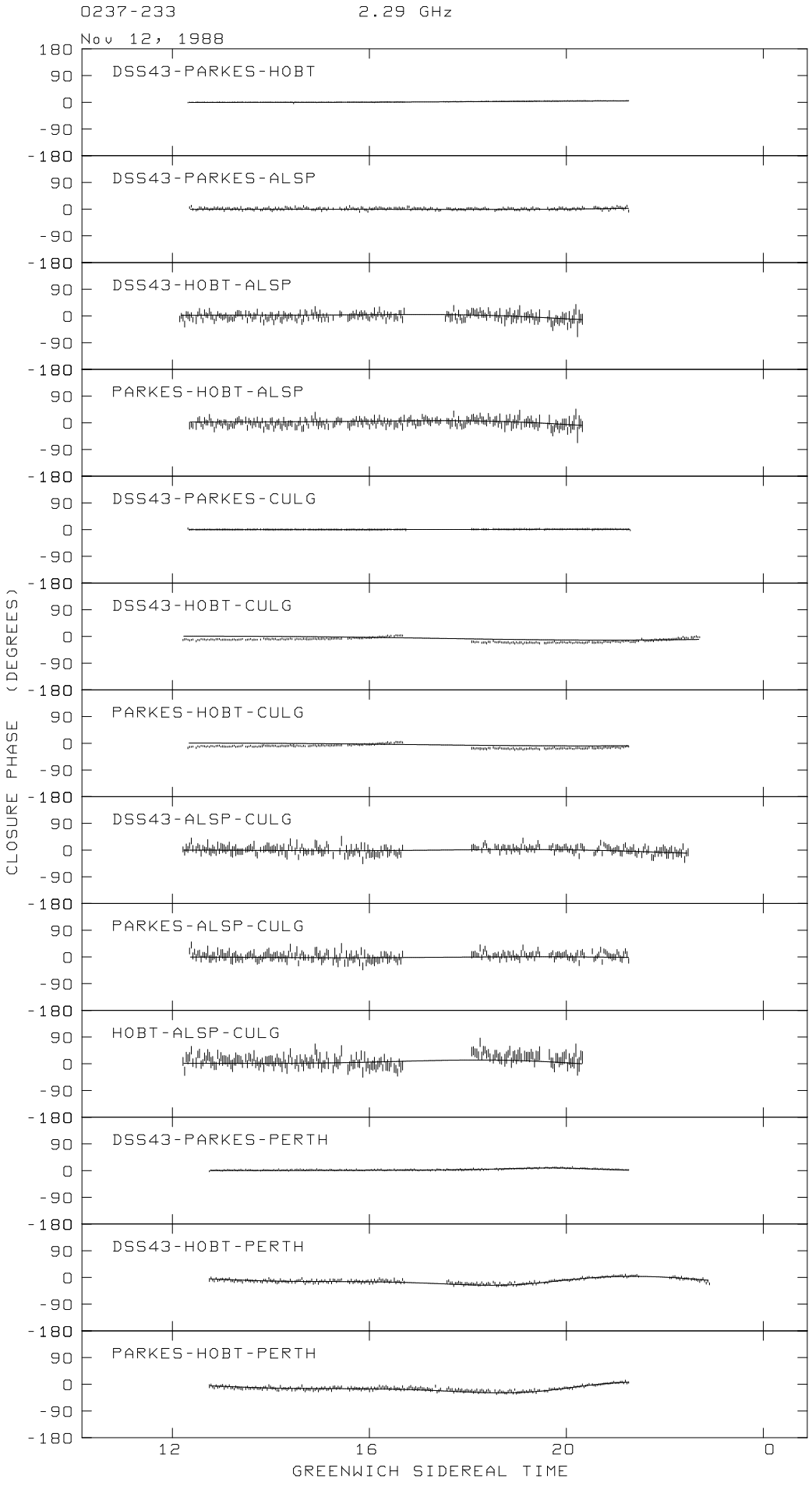
0237-233
2.29 GHz
Nov 12, 1988
DSS43-PARKES-HOBT
DSS43-PARKES-ALSP
DSS43-HOBT-ALSP
PARKES-HOBT-ALSP
DSS43-PARKES-CULG
DSS43-HOBT-CULG
PARKES-HOBT-CULG
DSS43-ALSP-CULG
PARKES-ALSP-CULG
HOBT-ALSP-CULG
DSS43-PARKES-PERTH
DSS43-HOBT-PERTH
PARKES-HOBT-PERTH
180
90
0
-90
-180
CLOSURE PHASE (DEGREES)
12
16
20
0
GREENWICH SIDEREAL TIME

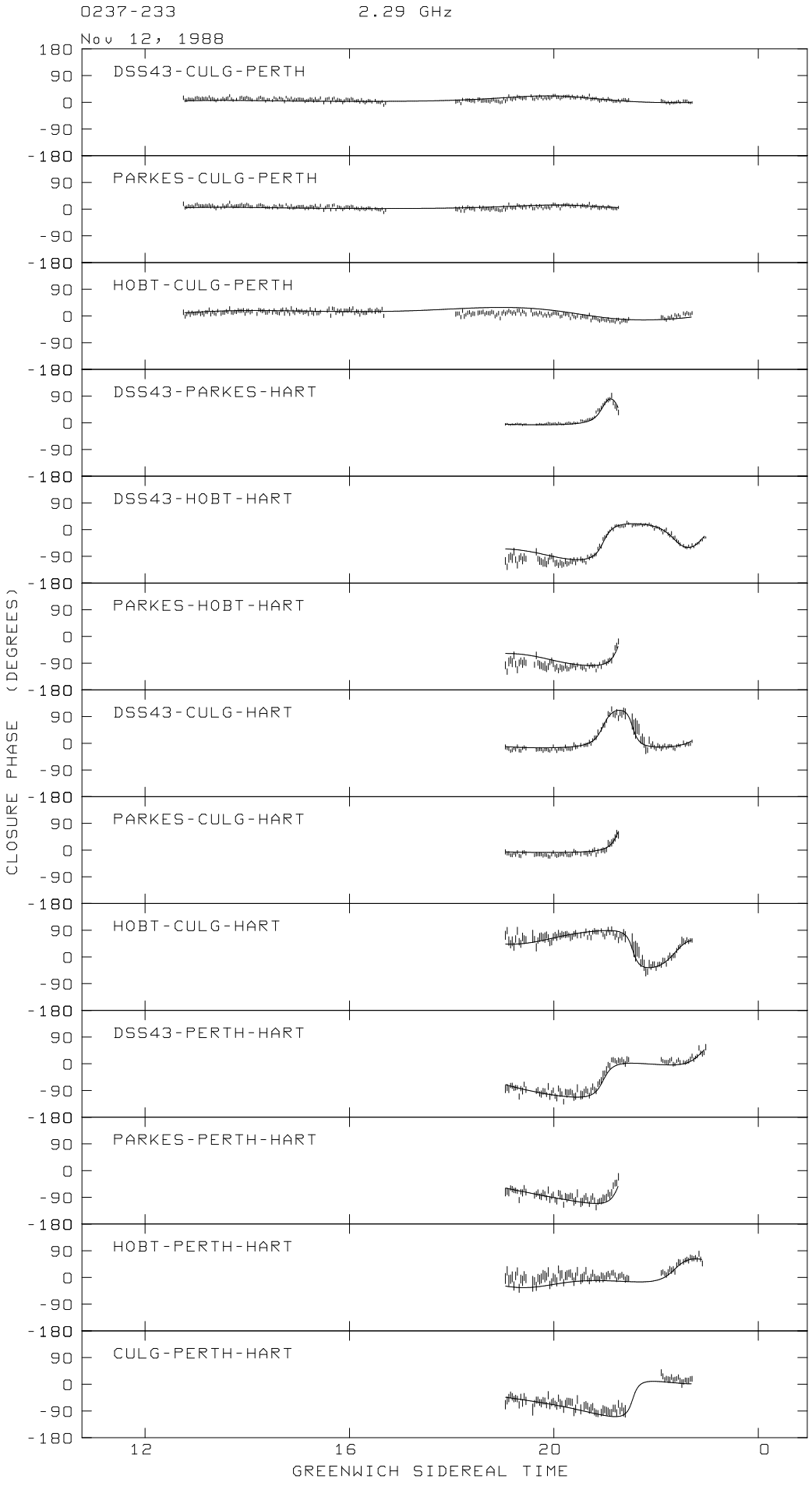
0237-233
2.29 GHz
Nov 12, 1988
DSS43-CULG-PERTH
PARKES-CULG-PERTH
HOBT-CULG-PERTH
DSS43-PARKES-HART
DSS43-HOBT-HART
PARKES-HOBT-HART
DSS43-CULG-HART
PARKES-CULG-HART
HOBT-CULG-HART
DSS43-PERTH-HART
PARKES-PERTH-HART
HOBT-PERTH-HART
CULG-PERTH-HART
180
90
0
-90
-180
CLOSURE PHASE (DEGREES)
12
16
20
0
GREENWICH SIDEREAL TIME

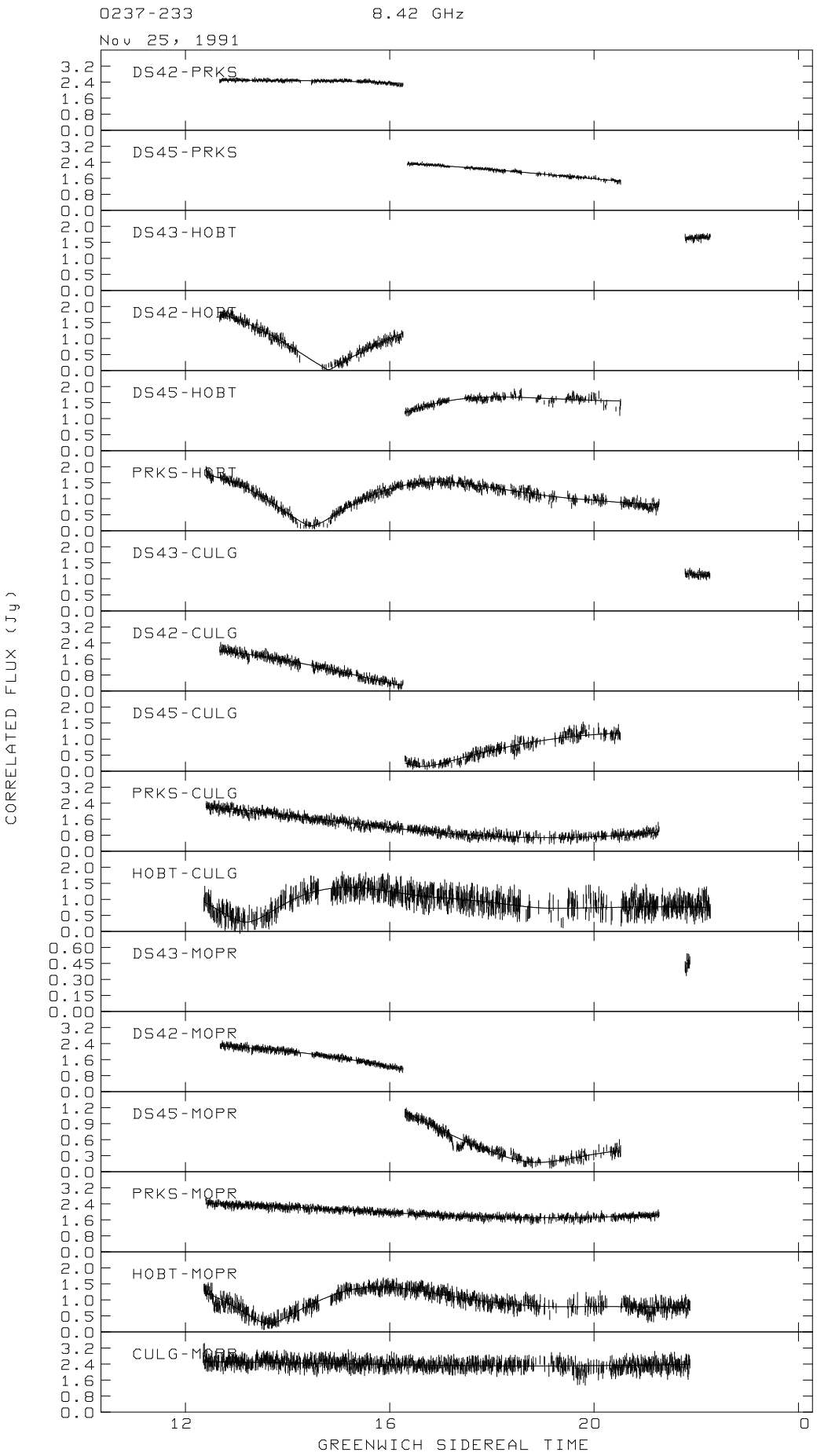
0237-233
8.42 GHz
Nov 25, 1991
DS42-PRKS
DS45-PRKS
DS43-HOBT
DS42-HOBT
DS45-HOBT
PRKS-HOBT
DS43-CULG
DS42-CULG
DS45-CULG
PRKS-CULG
HOBT-CULG
DS43-MOPR
DS42-MOPR
DS45-MOPR
PRKS-MOPR
HOBT-MOPR
CULG-MOPR
CORRELATED FLUX (Jy)
12
16
20
0
GREENWICH SIDEREAL TIME

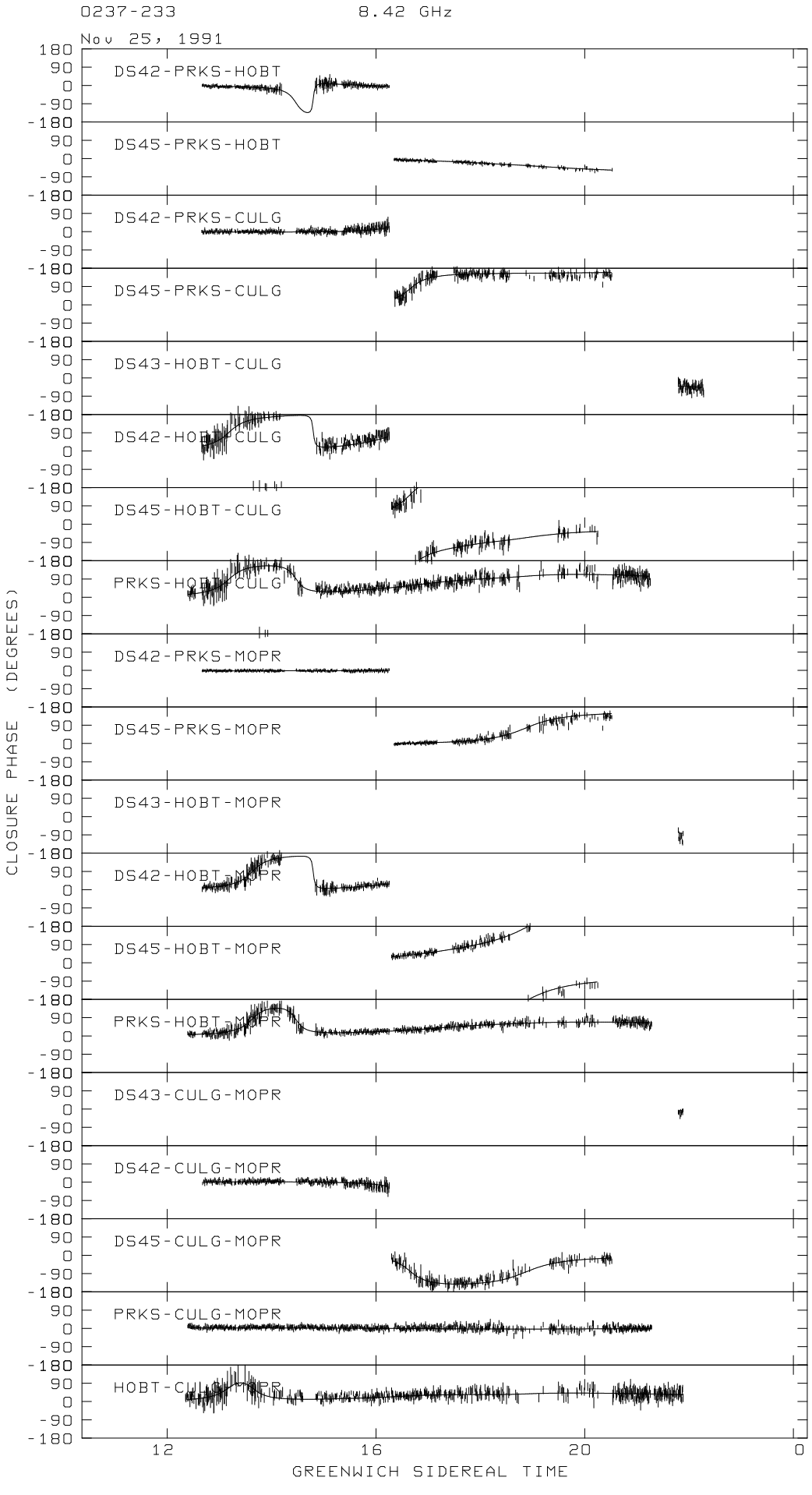
0237-233
8.42 GHz
Nov 25, 1991
DS42-PRKS-HOBT
DS45-PRKS-HOBT
DS42-PRKS-CULG
DS45-PRKS-CULG
DS43-HOBT-CULG
DS42-HOBT-CULG
DS45-HOBT-CULG
PRKS-HOBT-CULG
DS42-PRKS-MOPR
DS45-PRKS-MOPR
DS43-HOBT-MOPR
DS42-HOBT-MOPR
DS45-HOBT-MOPR
PRKS-HOBT-MOPR
DS43-CULG-MOPR
DS42-CULG-MOPR
DS45-CULG-MOPR
PRKS-CULG-MOPR
HOBT-CULG-MOPR
180
90
0
-90
-180
CLOSURE PHASE (DEGREES)
12
16
20
0
GREENWICH SIDEREAL TIME

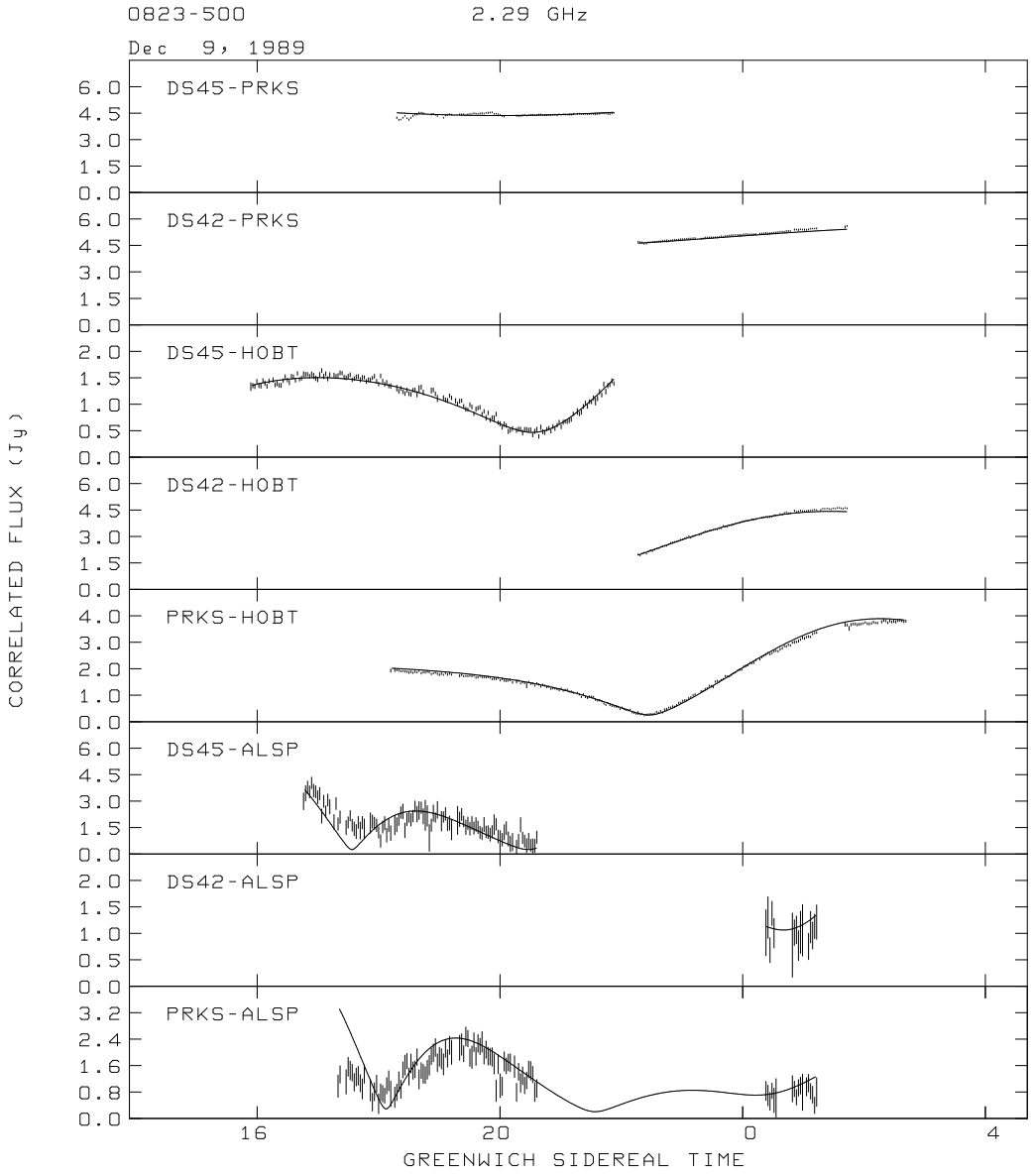
0823-500
2.29 GHz
Dec 9, 1989
DS45-PRKS
DS42-PRKS
DS45-HOBT
DS42-HOBT
PRKS-HOBT
DS45-ALSP
DS42-ALSP
PRKS-ALSP
CORRELATED FLUX (Jy)
16
20
0
4
GREENWICH SIDEREAL TIME

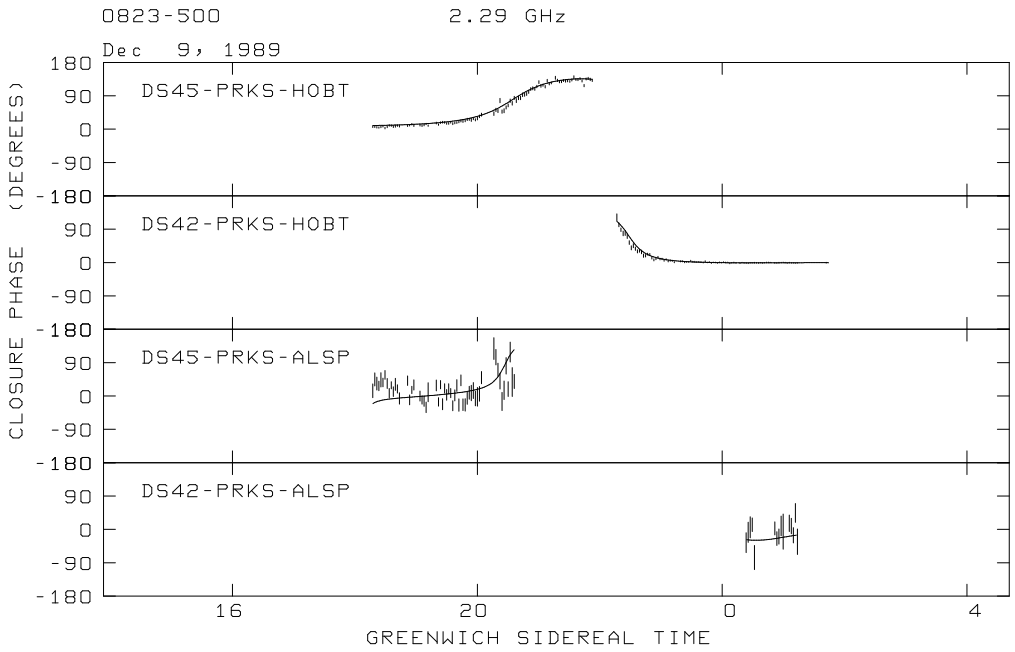
0823-500
2.29 GHz
Dec 9, 1989
DS45-PRKS-HOBT
DS42-PRKS-HOBT
DS45-PRKS-ALSP
DS42-PRKS-ALSP
CLOSURE PHASE (DEGREES)
16
20
0
4
GREENWICH SIDEREAL TIME

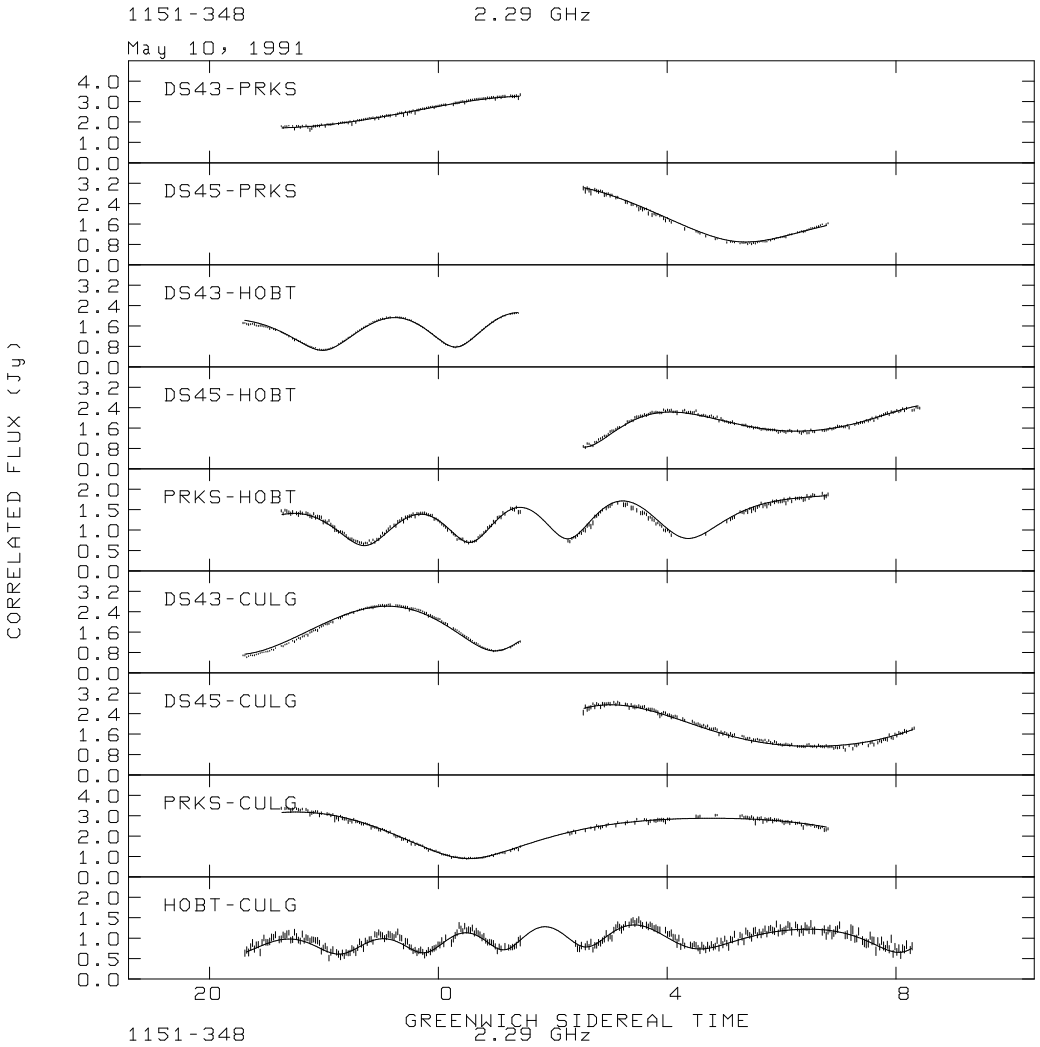
1151-348
2.29 GHz
May 10, 1991
DS43-PRKS
DS45-PRKS
DS43-HOBT
DS45-HOBT
PRKS-HOBT
DS43-CULG
DS45-CULG
PRKS-CULG
HOBT-CULG
CORRELATED FLUX (Jy)
GREENWICH SIDEREAL TIME

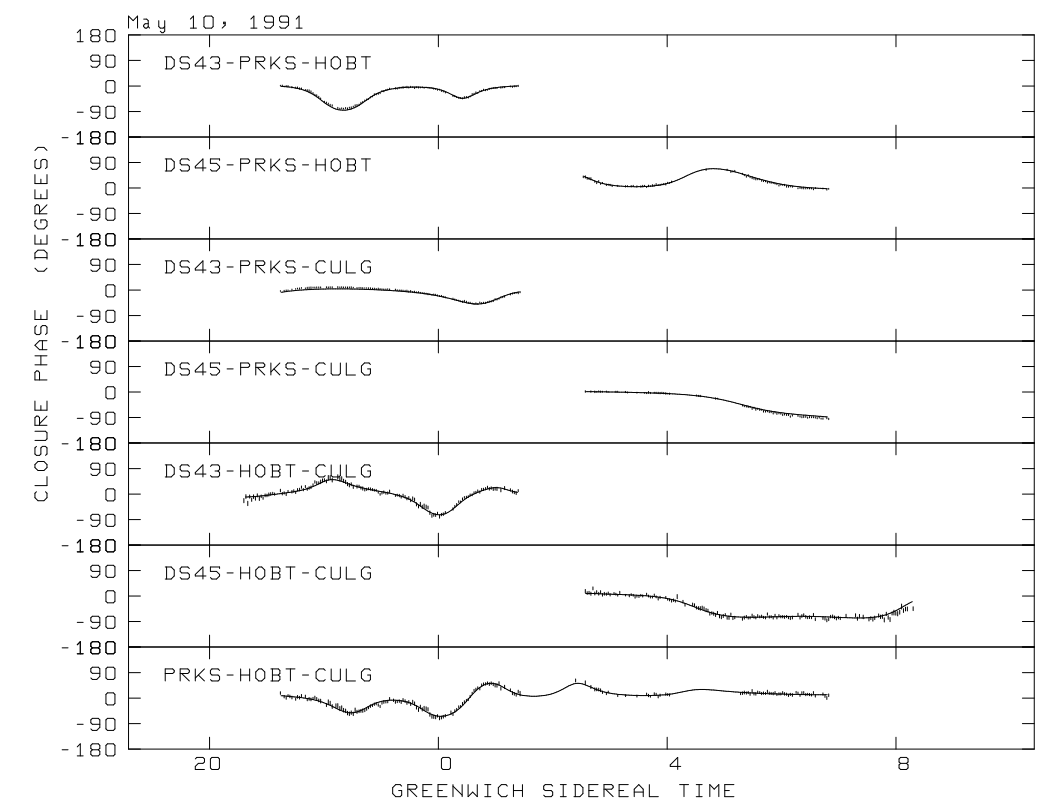
1151-348
2.29 GHz
May 10, 1991
DS43-PRKS-HOBT
DS45-PRKS-HOBT
DS43-PRKS-CULG
DS45-PRKS-CULG
DS43-HOBT-CULG
DS45-HOBT-CULG
PRKS-HOBT-CULG
CLOSURE PHASE (DEGREES)
GREENWICH SIDEREAL TIME

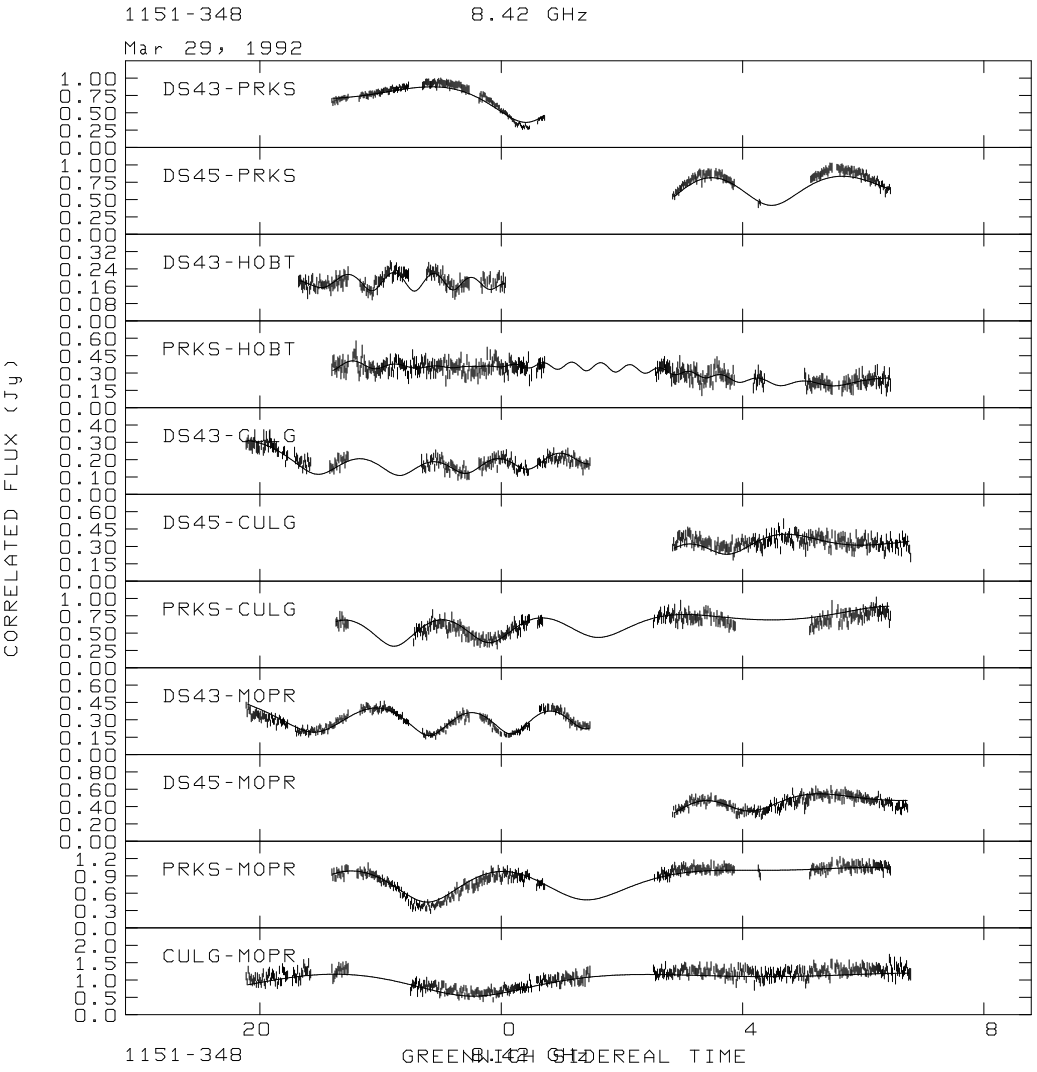
1151-348
8.42 GHz
Mar 29, 1992
DS43-PRKS
DS45-PRKS
DS43-HOBT
PRKS-HOBT
DS43-CULG
DS45-CULG
PRKS-CULG
DS43-MOPR
DS45-MOPR
PRKS-MOPR
CULG-MOPR
CORRELATED FLUX (Jy)
GREENWICH SIDEREAL TIME

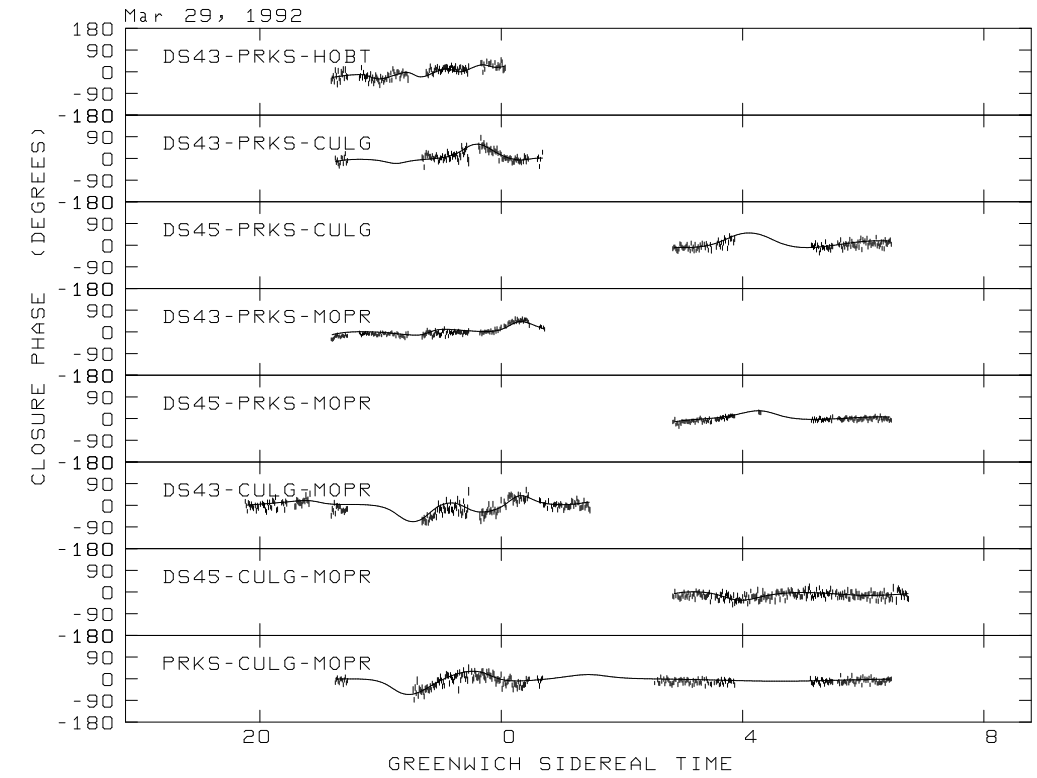
1151-348
8.42 GHz
Mar 29, 1992
DS43-PRKS-HOBT
DS43-PRKS-CULG
DS45-PRKS-CULG
DS43-PRKS-MOPR
DS45-PRKS-MOPR
DS43-CULG-MOPR
DS45-CULG-MOPR
PRKS-CULG-MOPR
CLOSURE PHASE (DEGREES)
GREENWICH SIDEREAL TIME

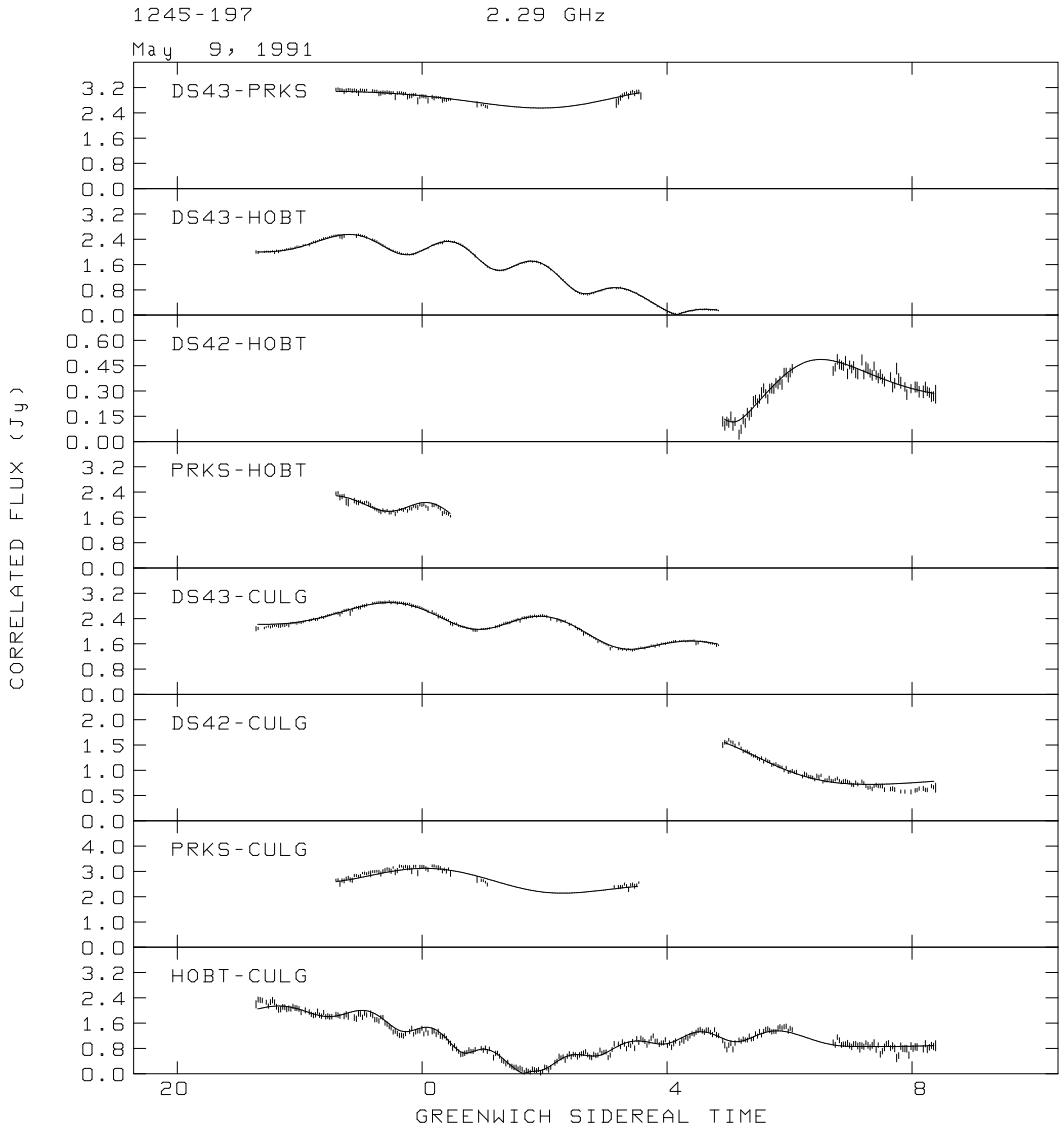
1245-197
2.29 GHz
May 9, 1991
DS43-PRKS
DS43-HOBT
DS42-HOBT
PRKS-HOBT
DS43-CULG
DS42-CULG
PRKS-CULG
HOBT-CULG
CORRELATED FLUX (Jy)
GREENWICH SIDEREAL TIME

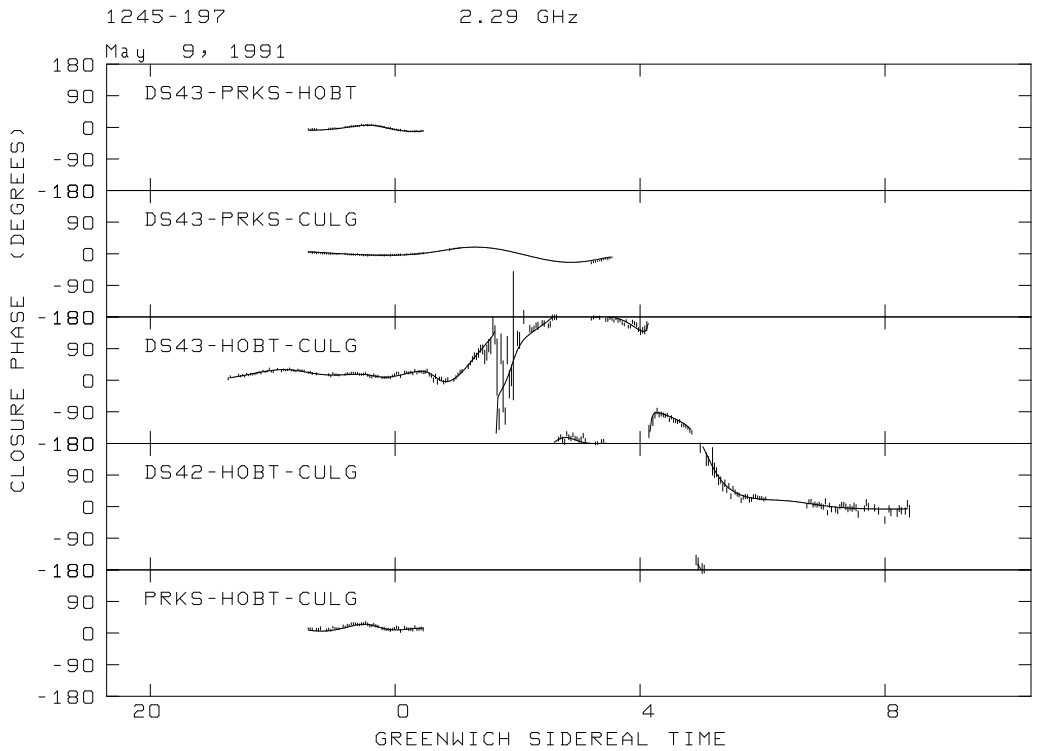
1245-197
2.29 GHz
May 9, 1991
DS43-PRKS-HOBT
DS43-PRKS-CULG
DS43-HOBT-CULG
DS42-HOBT-CULG
PRKS-HOBT-CULG
CLOSURE PHASE (DEGREES)
GREENWICH SIDEREAL TIME

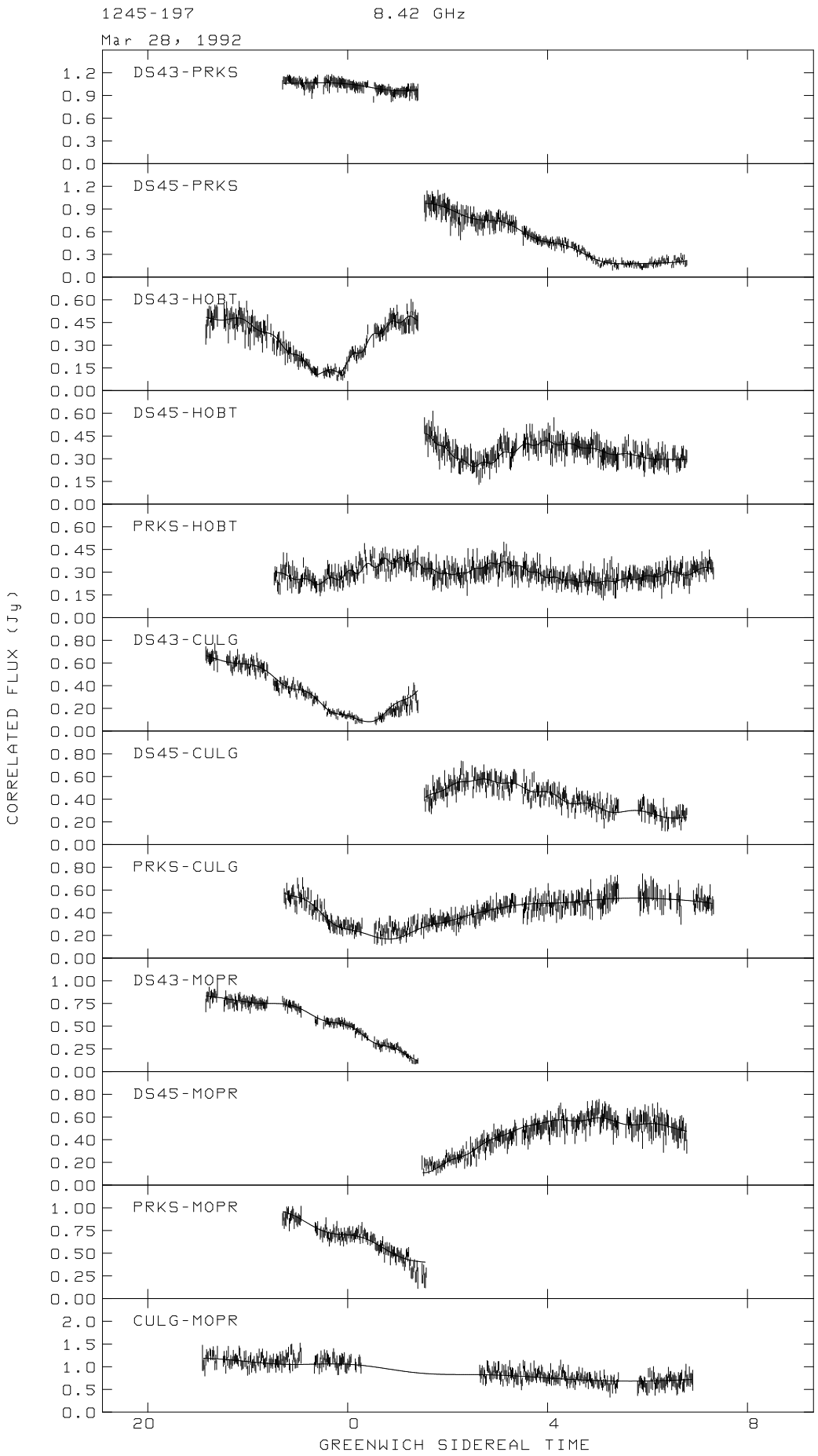
1245-197
8.42 GHz
Mar 28, 1992
DS43-PRKS
DS45-PRKS
DS43-HOBT
DS45-HOBT
PRKS-HOBT
DS43-CULG
DS45-CULG
PRKS-CULG
DS43-MOPR
DS45-MOPR
PRKS-MOPR
CULG-MOPR
CORRELATED FLUX (Jy)
GREENWICH SIDEREAL TIME
20
0
4
8

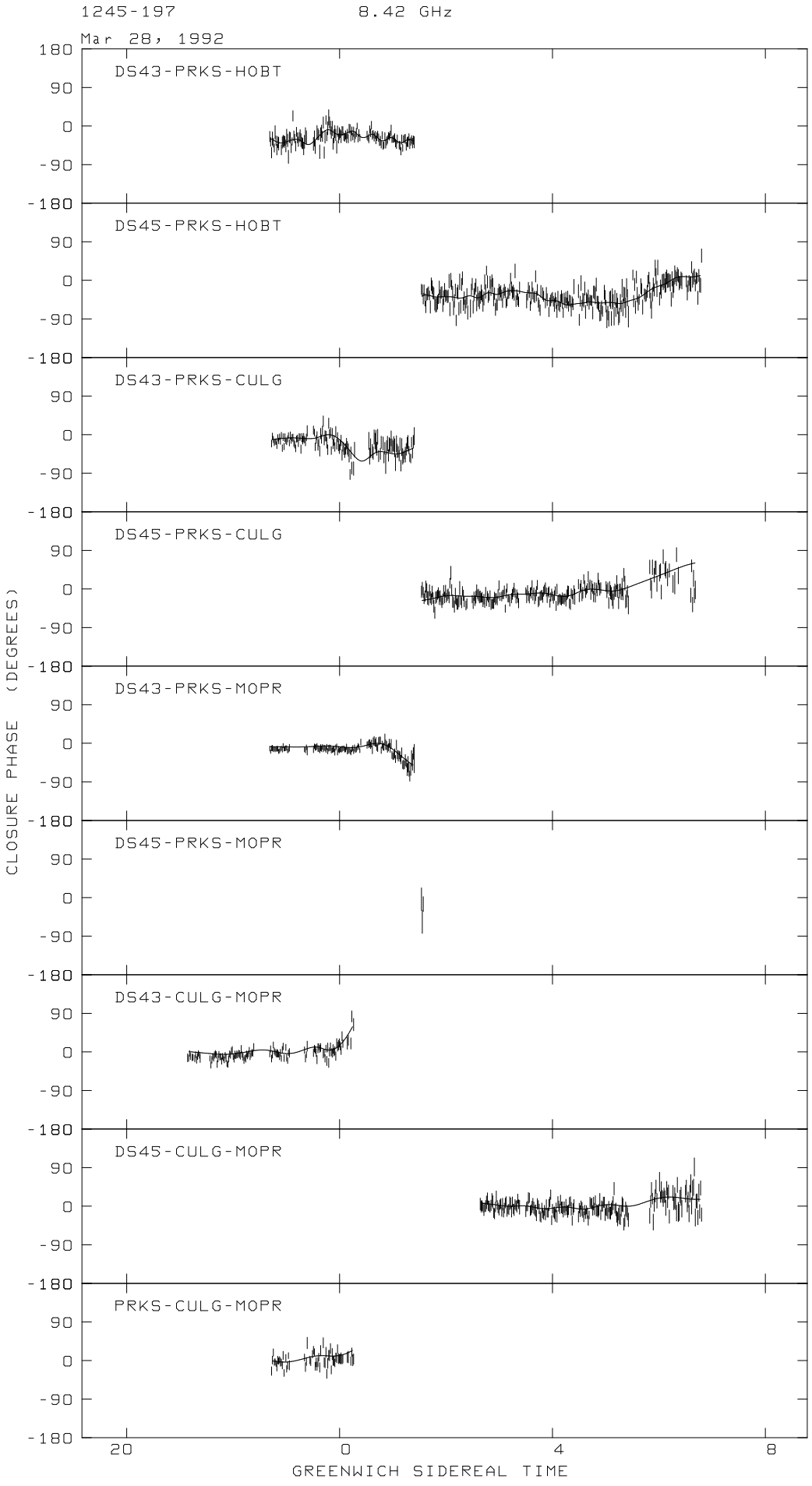
1245-197
8.42 GHz
Mar 28, 1992
DS43-PRKS-HOBT
DS45-PRKS-HOBT
DS43-PRKS-CULG
DS45-PRKS-CULG
DS43-PRKS-MOPR
DS45-PRKS-MOPR
DS43-CULG-MOPR
DS45-CULG-MOPR
PRKS-CULG-MOPR
180
90
0
-90
-180
CLOSURE PHASE (DEGREES)
20
0
4
8
GREENWICH SIDEREAL TIME

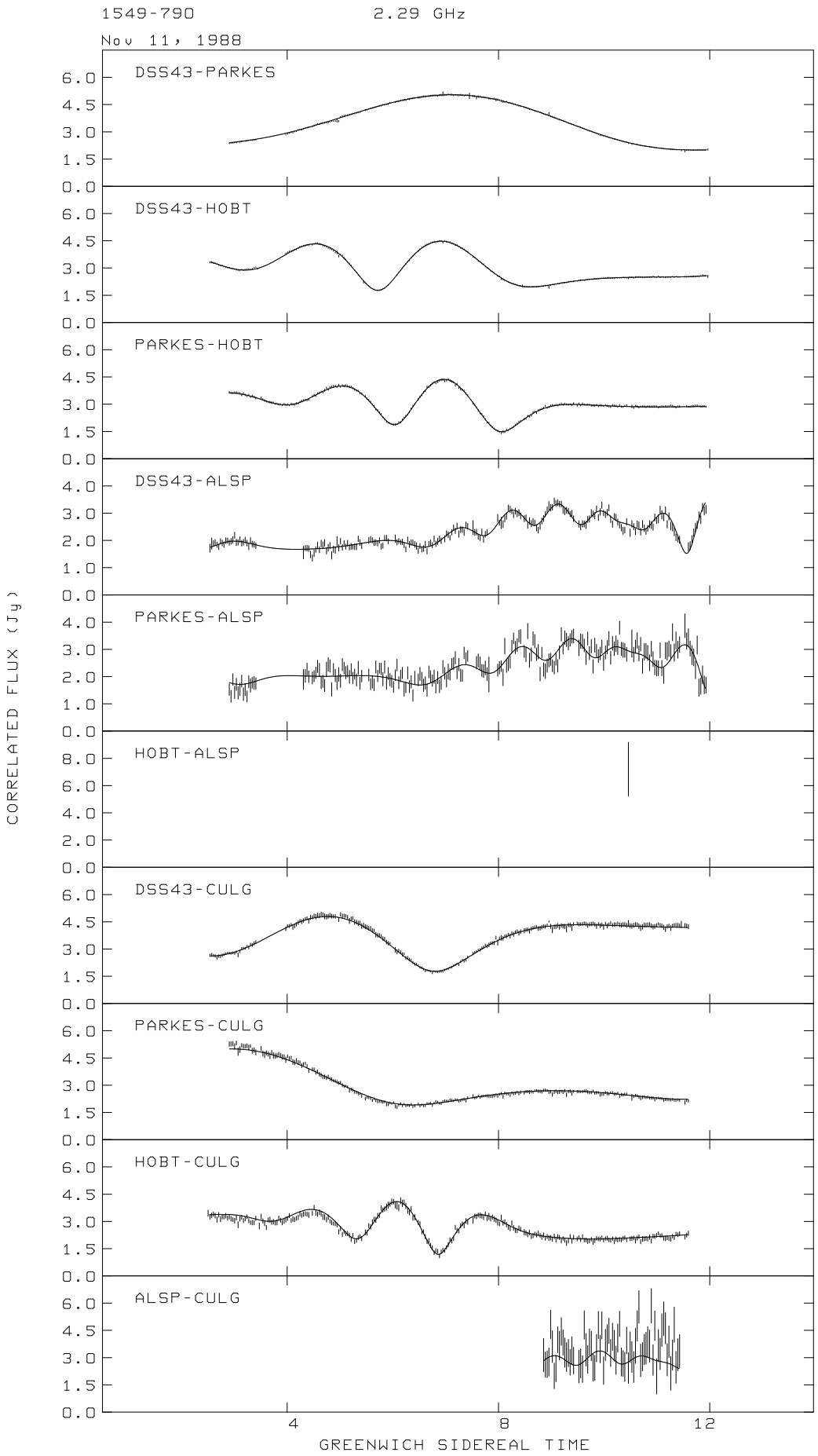
1549-790
2.29 GHz
Nov 11, 1988
DSS43-PARKES
DSS43-HOBT
PARKES-HOBT
DSS43-ALSP
PARKES-ALSP
HOBT-ALSP
DSS43-CULG
PARKES-CULG
HOBT-CULG
ALSP-CULG
CORRELATED FLUX (Jy)
GREENWICH SIDEREAL TIME
4
8
12

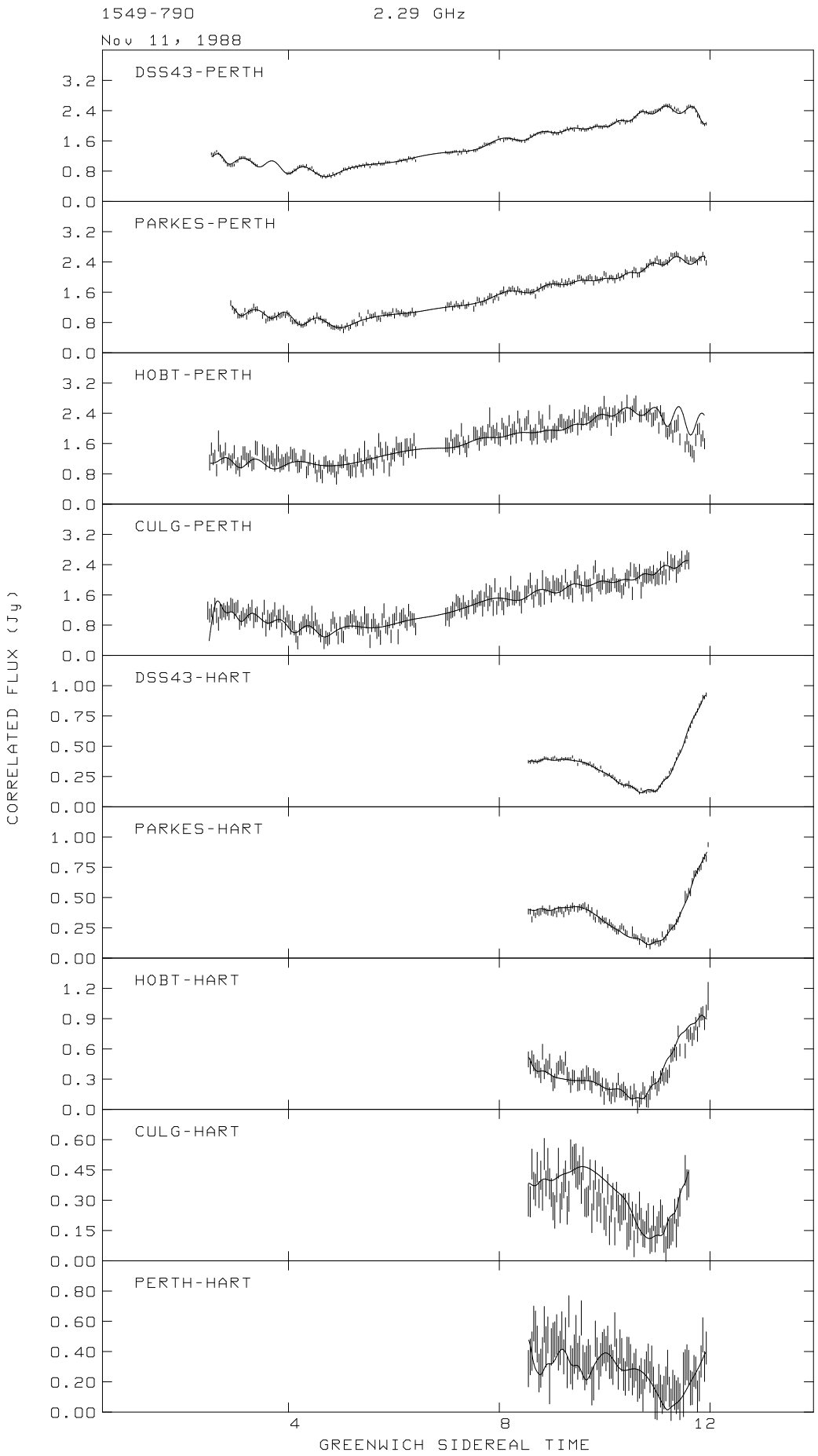
1549-790
2.29 GHz
Nov 11, 1988
DSS43-PERTH
PARKES-PERTH
HOBT-PERTH
CULG-PERTH
DSS43-HART
PARKES-HART
HOBT-HART
CULG-HART
PERTH-HART
CORRELATED FLUX (Jy)
GREENWICH SIDEREAL TIME
4
8
12

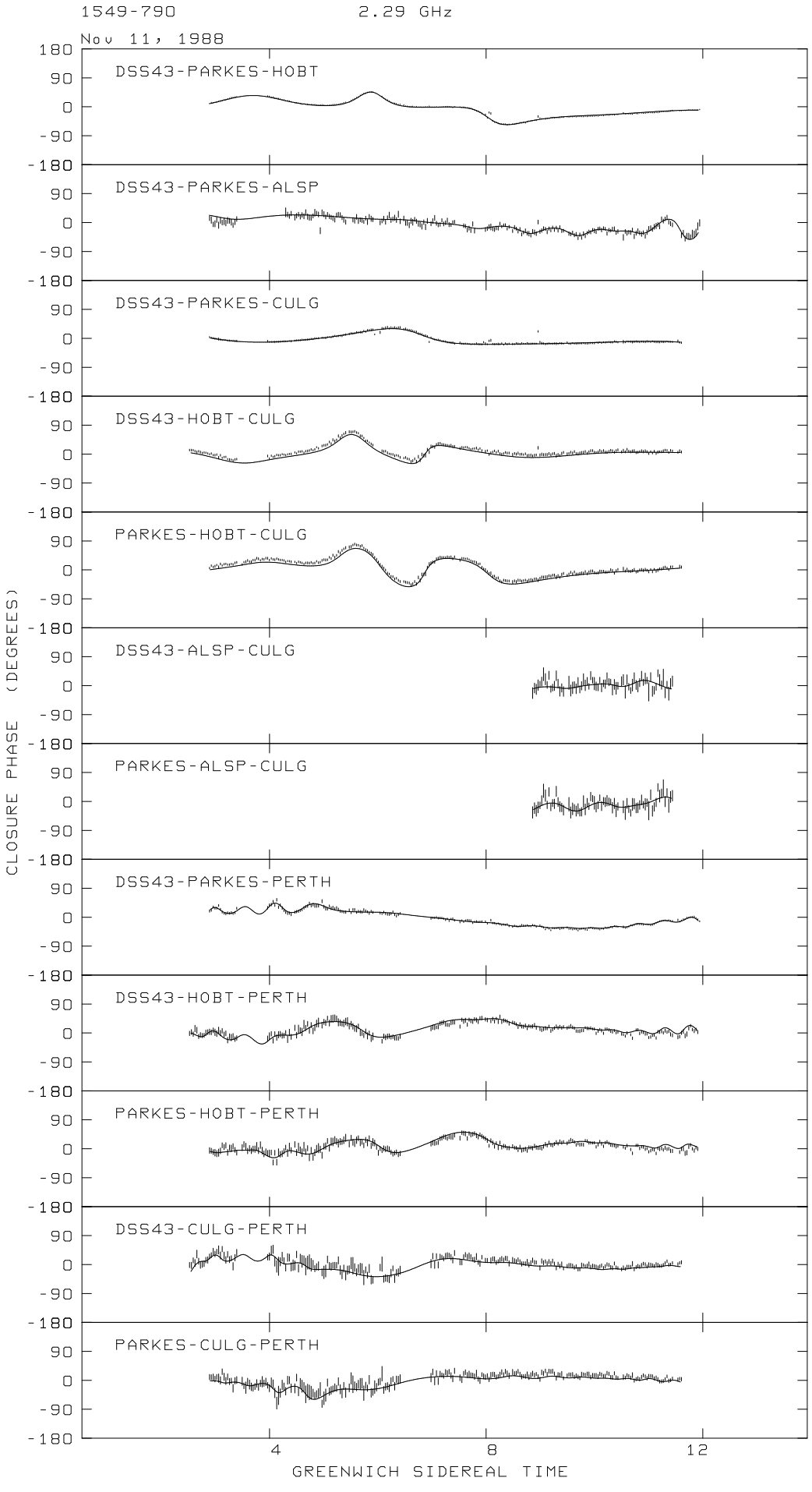
1549-790
2.29 GHz
Nov 11, 1988
DSS43-PARKES-HOBT
DSS43-PARKES-ALSP
DSS43-PARKES-CULG
DSS43-HOBT-CULG
PARKES-HOBT-CULG
DSS43-ALSP-CULG
PARKES-ALSP-CULG
DSS43-PARKES-PERTH
DSS43-HOBT-PERTH
PARKES-HOBT-PERTH
DSS43-CULG-PERTH
PARKES-CULG-PERTH
180
90
0
-90
-180
CLOSURE PHASE (DEGREES)
4
8
12
GREENWICH SIDEREAL TIME

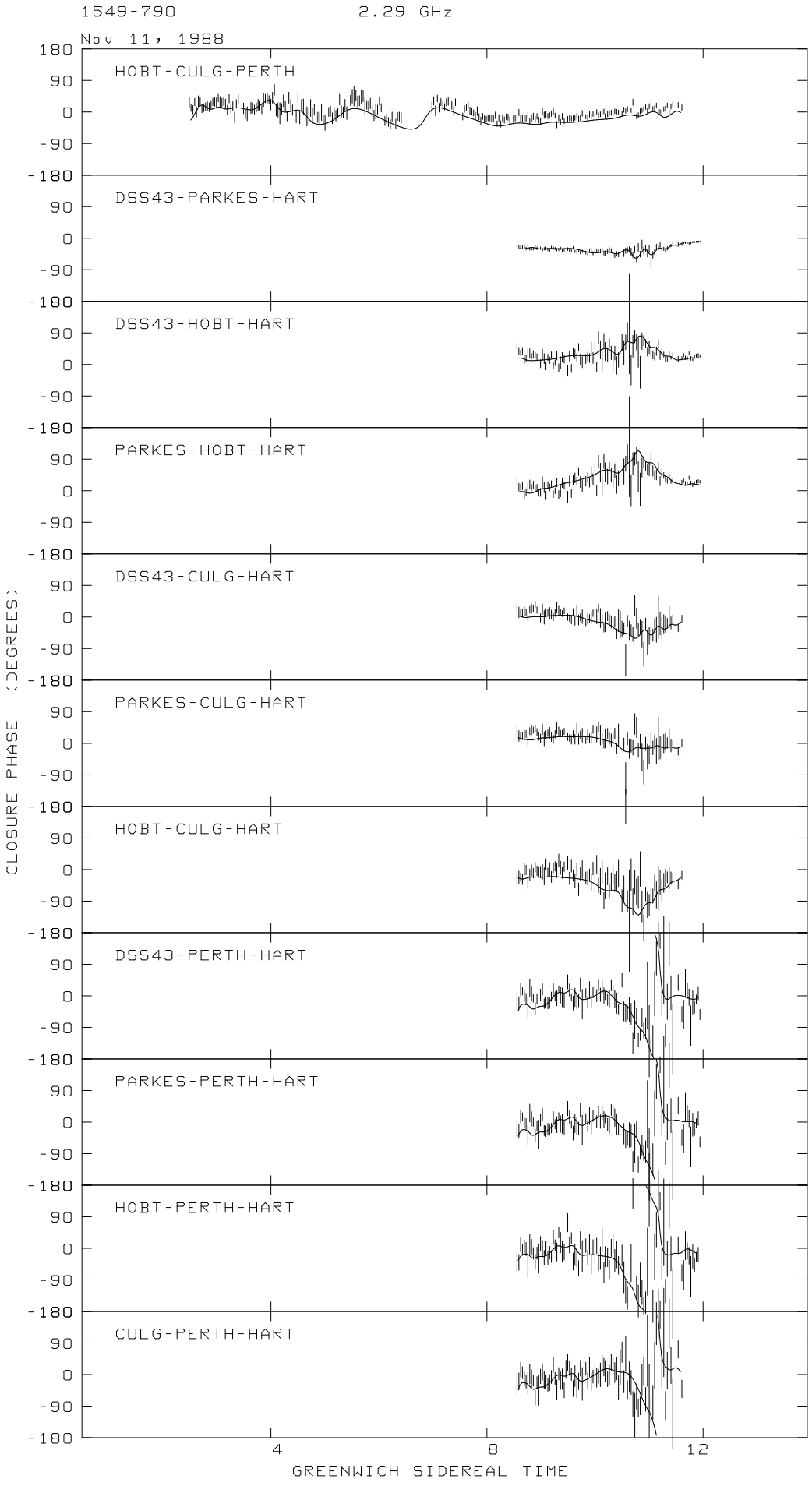
1549-790
2.29 GHz
Nov 11, 1988
HOBT-CULG-PERTH
DSS43-PARKES-HART
DSS43-HOBT-HART
PARKES-HOBT-HART
DSS43-CULG-HART
PARKES-CULG-HART
HOBT-CULG-HART
DSS43-PERTH-HART
PARKES-PERTH-HART
HOBT-PERTH-HART
CULG-PERTH-HART
180
90
0
-90
-180
CLOSURE PHASE (DEGREES)
4
8
12
GREENWICH SIDEREAL TIME

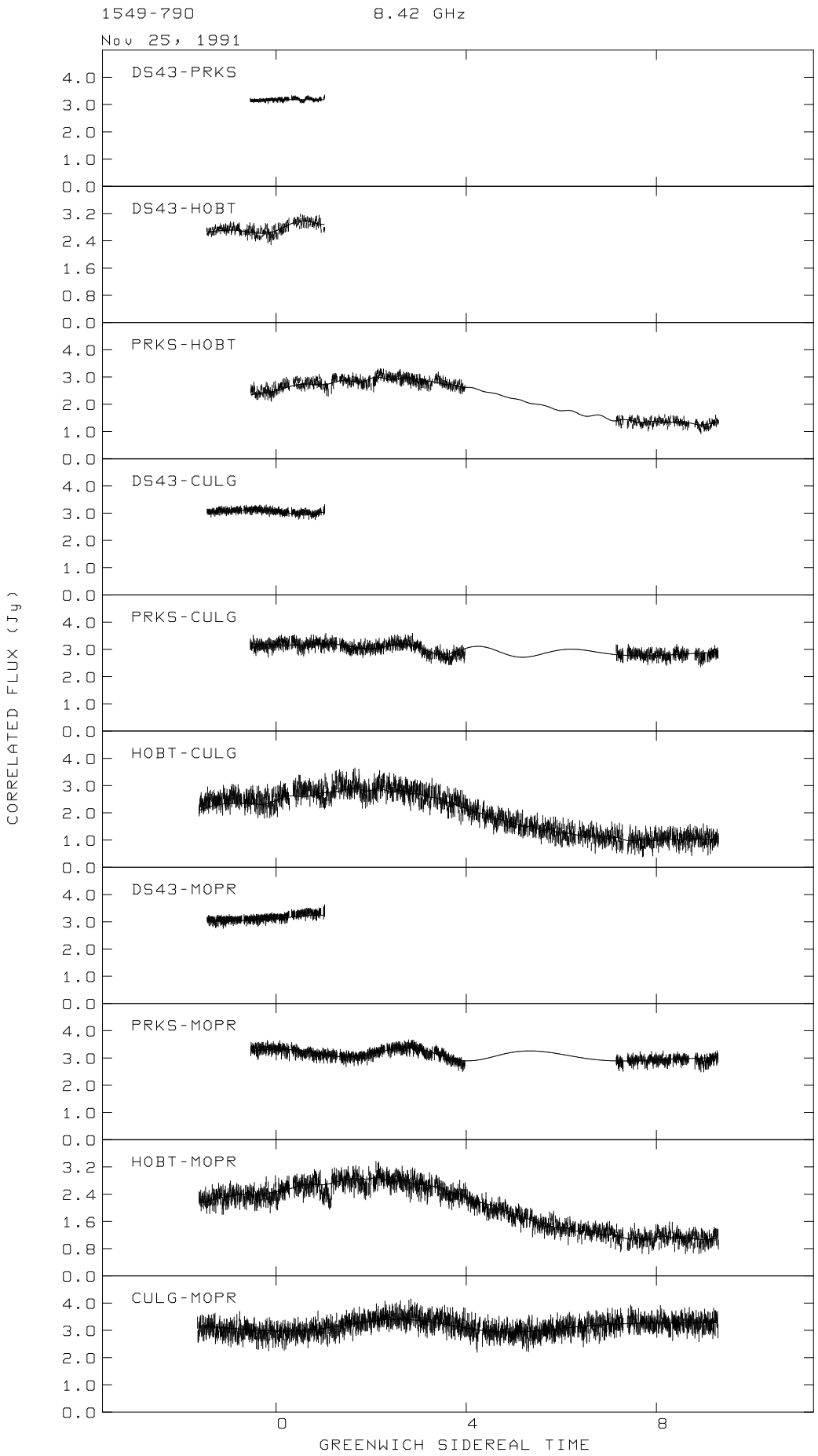
1549-790
8.42 GHz
Nov 25, 1991
DS43-PRKS
DS43-HOBT
PRKS-HOBT
DS43-CULG
PRKS-CULG
HOBT-CULG
DS43-MOPR
PRKS-MOPR
HOBT-MOPR
CULG-MOPR
CORRELATED FLUX (Jy)
GREENWICH SIDEREAL TIME
0
4
8

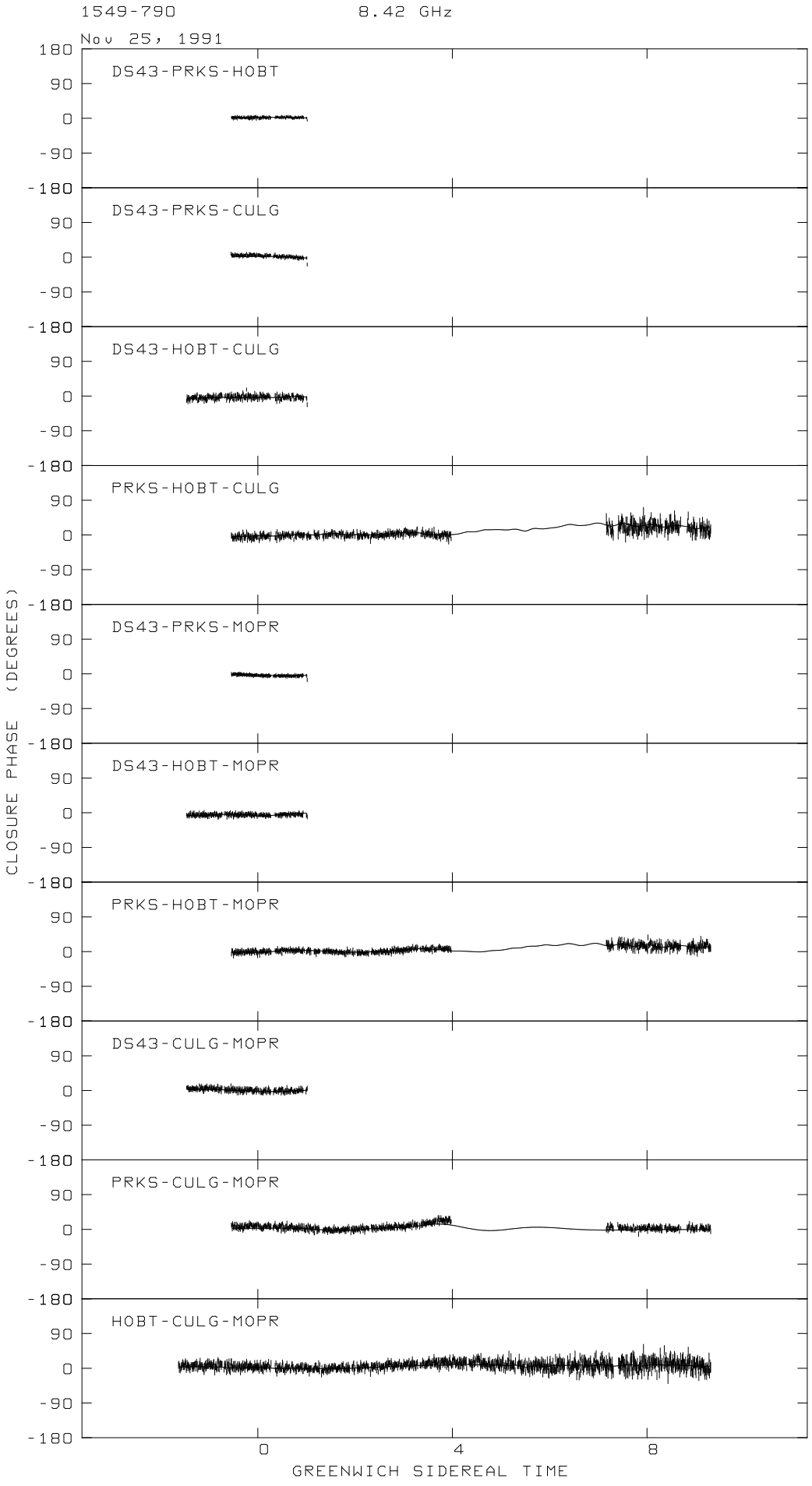
1549-790
8.42 GHz
Nov 25, 1991
DS43-PRKS-HOBT
DS43-PRKS-CULG
DS43-HOBT-CULG
PRKS-HOBT-CULG
DS43-PRKS-MOPR
DS43-HOBT-MOPR
PRKS-HOBT-MOPR
DS43-CULG-MOPR
PRKS-CULG-MOPR
HOBT-CULG-MOPR
180
90
0
-90
-180
CLOSURE PHASE (DEGREES)
0
4
8
GREENWICH SIDEREAL TIME

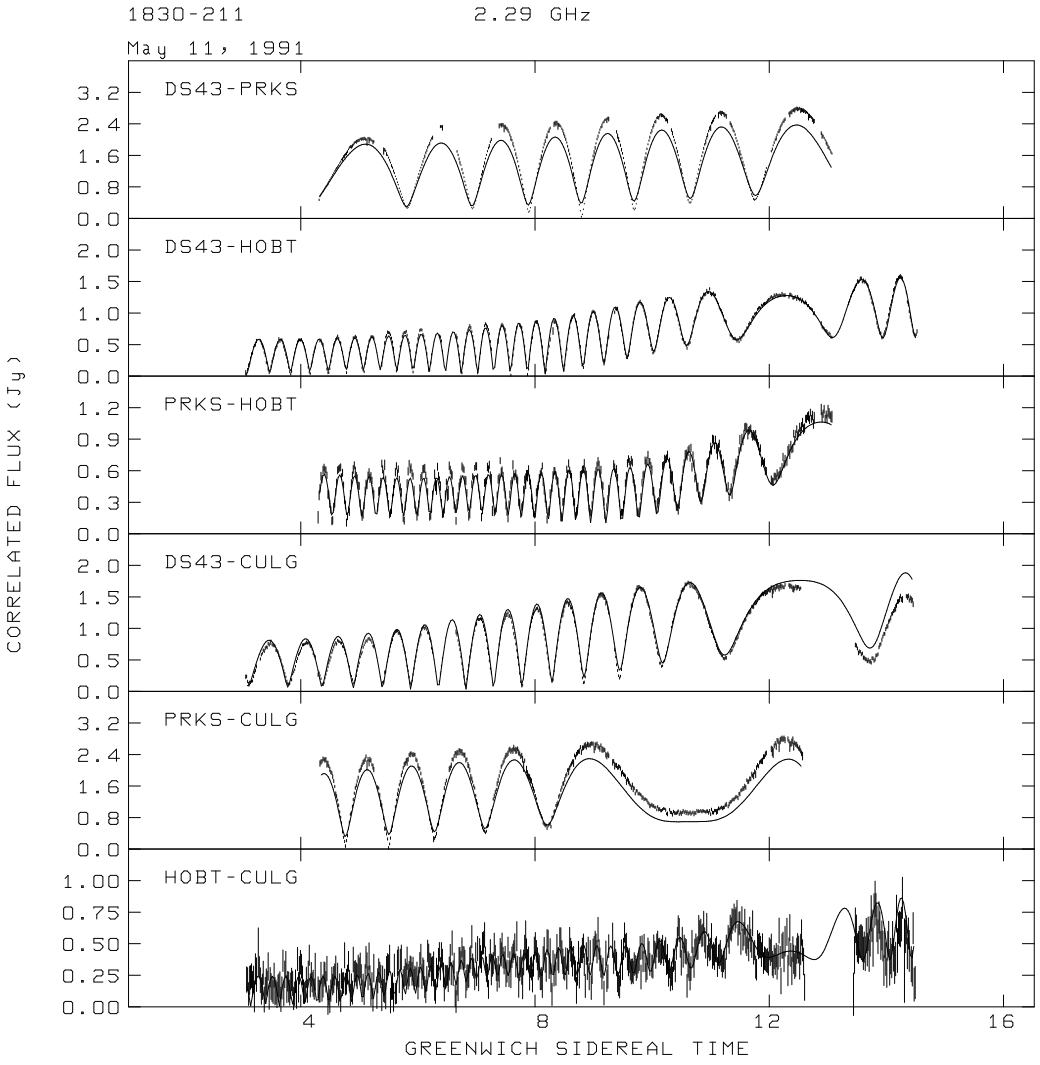
1830-211
2.29 GHz
May 11, 1991
DS43-PRKS
DS43-HOBT
PRKS-HOBT
DS43-CULG
PRKS-CULG
HOBT-CULG
CORRELATED FLUX (Jy)
GREENWICH SIDEREAL TIME

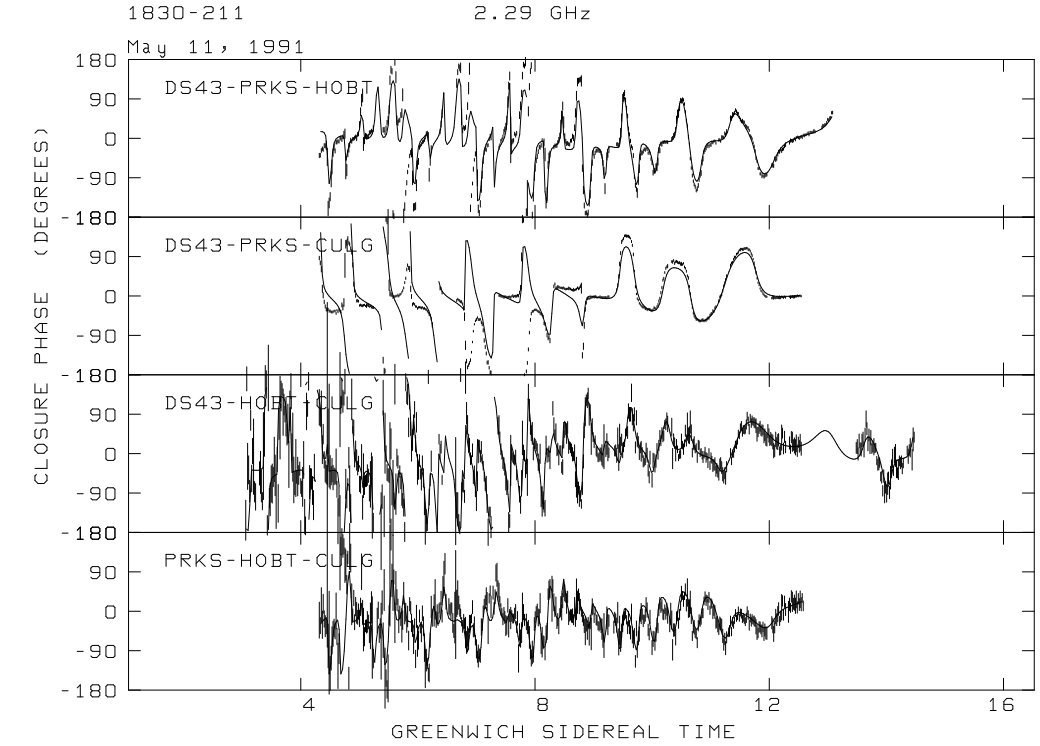
1830-211
2.29 GHz
May 11, 1991
DS43-PRKS-HOBT
DS43-PRKS-CULG
DS43-HOBT-CULG
PRKS-HOBT-CULG
CLOSURE PHASE (DEGREES)
GREENWICH SIDEREAL TIME

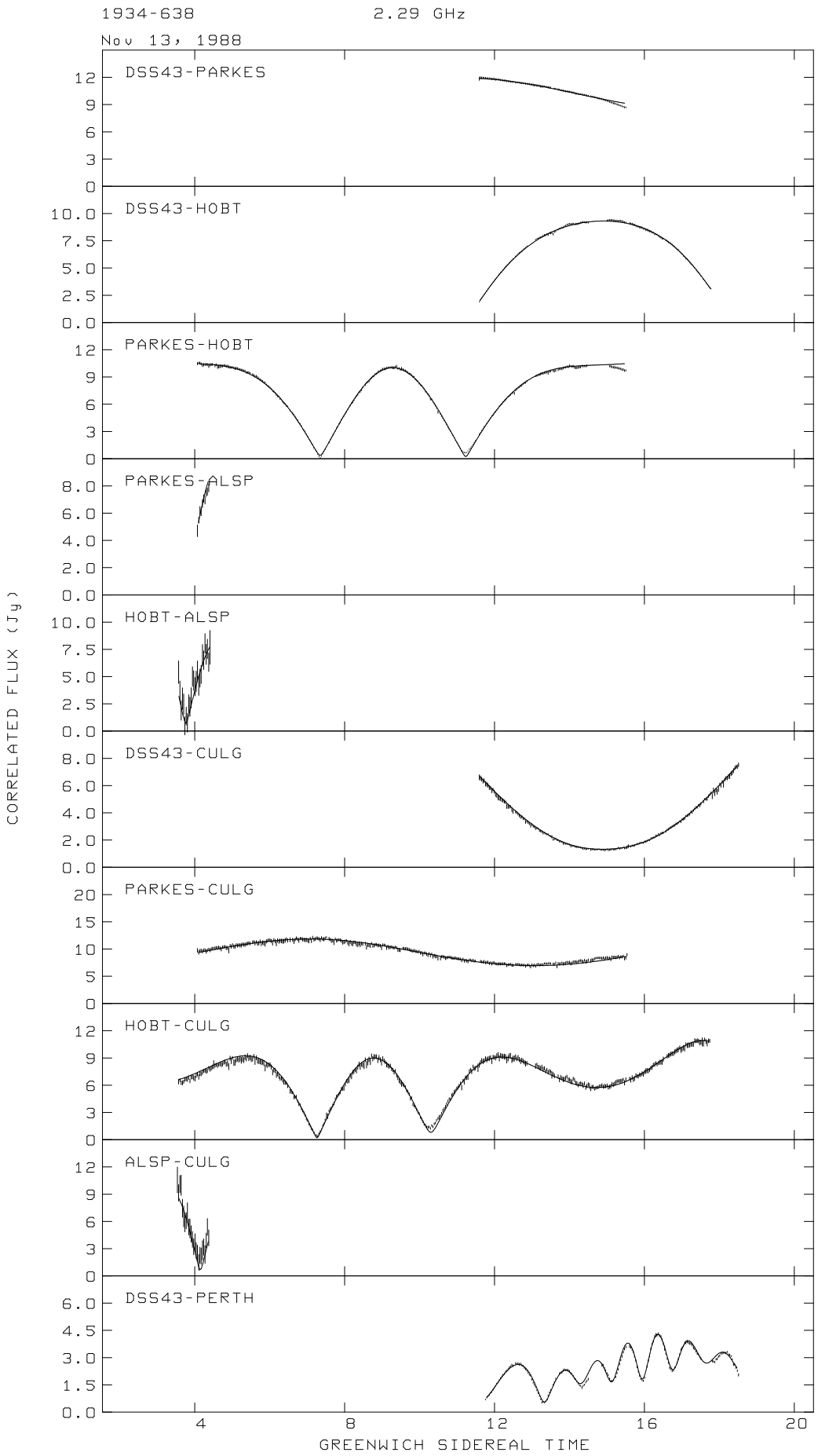
1934-638
2.29 GHz
Nov 13, 1988
DSS43-PARKES
DSS43-HOBT
PARKES-HOBT
PARKES-ALSP
HOBT-ALSP
DSS43-CULG
PARKES-CULG
HOBT-CULG
ALSP-CULG
DSS43-PERTH
CORRELATED FLUX (Jy)
GREENWICH SIDEREAL TIME

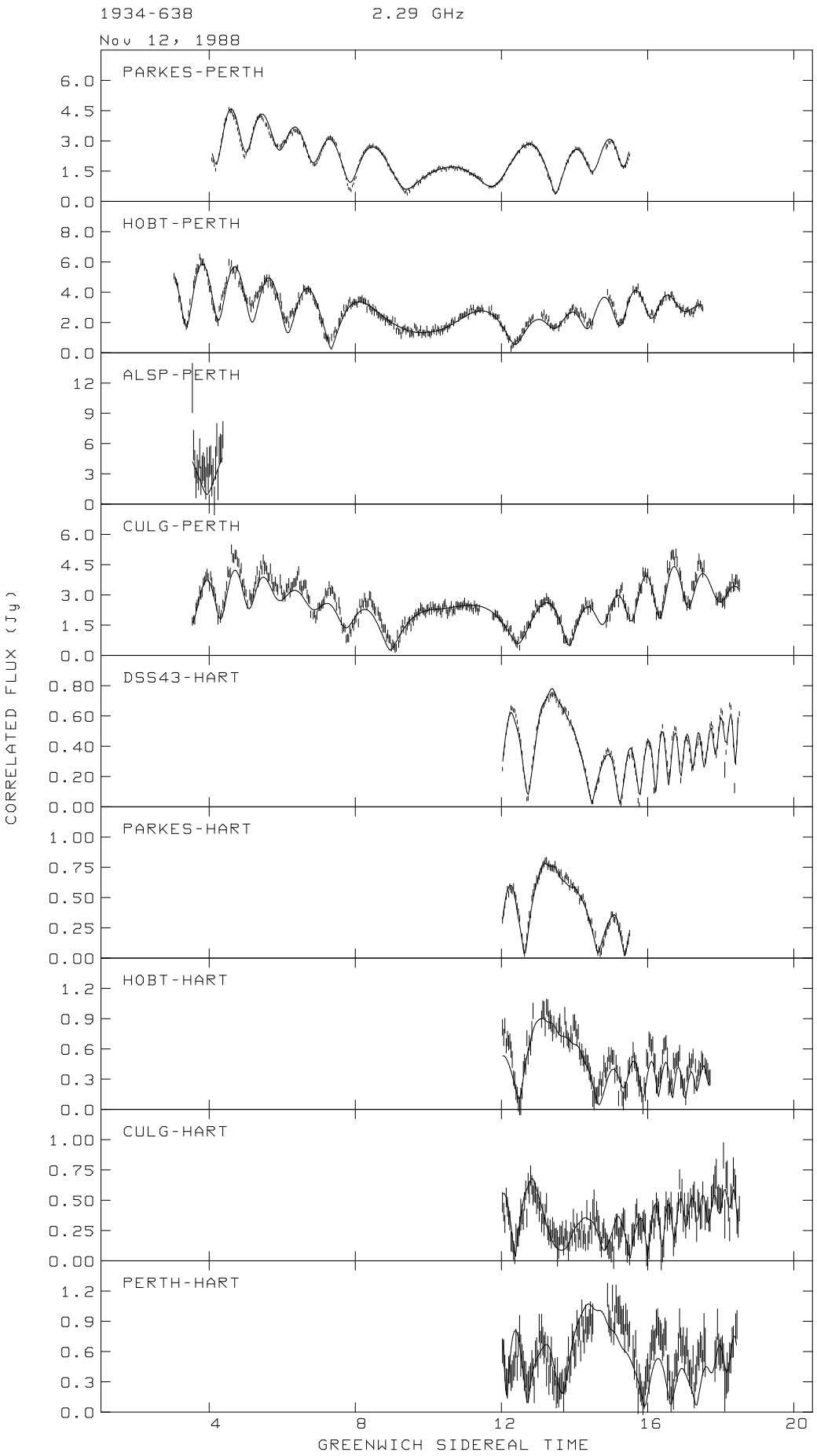
1934-638
2.29 GHz
Nov 12, 1988
PARKES-PERTH
HOBT-PERTH
ALSP-PERTH
CULG-PERTH
DSS43-HART
PARKES-HART
HOBT-HART
CULG-HART
PERTH-HART
CORRELATED FLUX (Jy)
GREENWICH SIDEREAL TIME
4
8
12
16
20

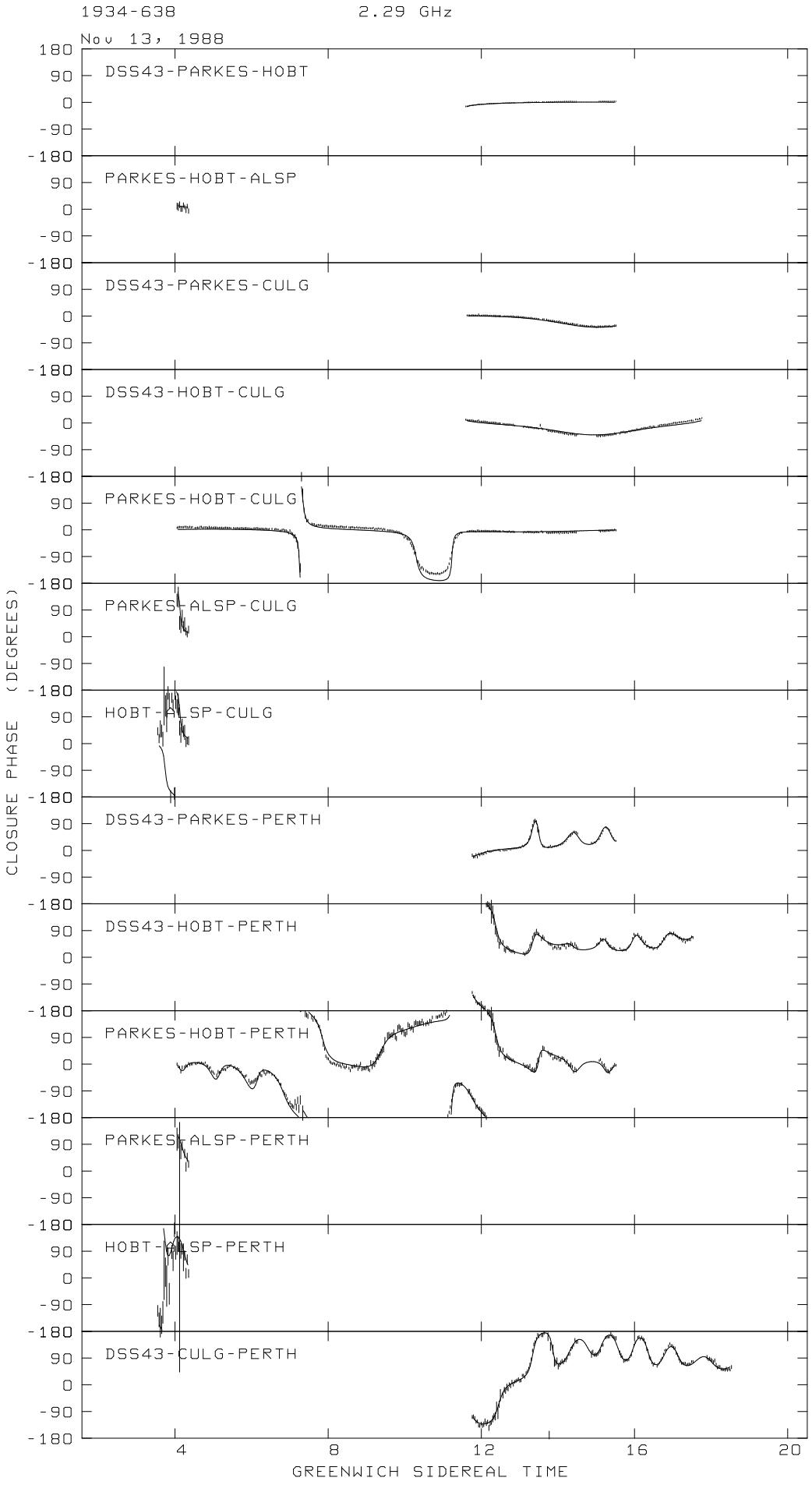
1934-638
2.29 GHz
Nov 13, 1988
DSS43-PARKES-HOBT
PARKES-HOBT-ALSP
DSS43-PARKES-CULG
DSS43-HOBT-CULG
PARKES-HOBT-CULG
PARKES-ALSP-CULG
HOBT-ALSP-CULG
DSS43-PARKES-PERTH
DSS43-HOBT-PERTH
PARKES-HOBT-PERTH
PARKES-ALSP-PERTH
HOBT-ALSP-PERTH
DSS43-CULG-PERTH
180
90
0
-90
-180
CLOSURE PHASE (DEGREES)
4
8
12
16
20
GREENWICH SIDEREAL TIME

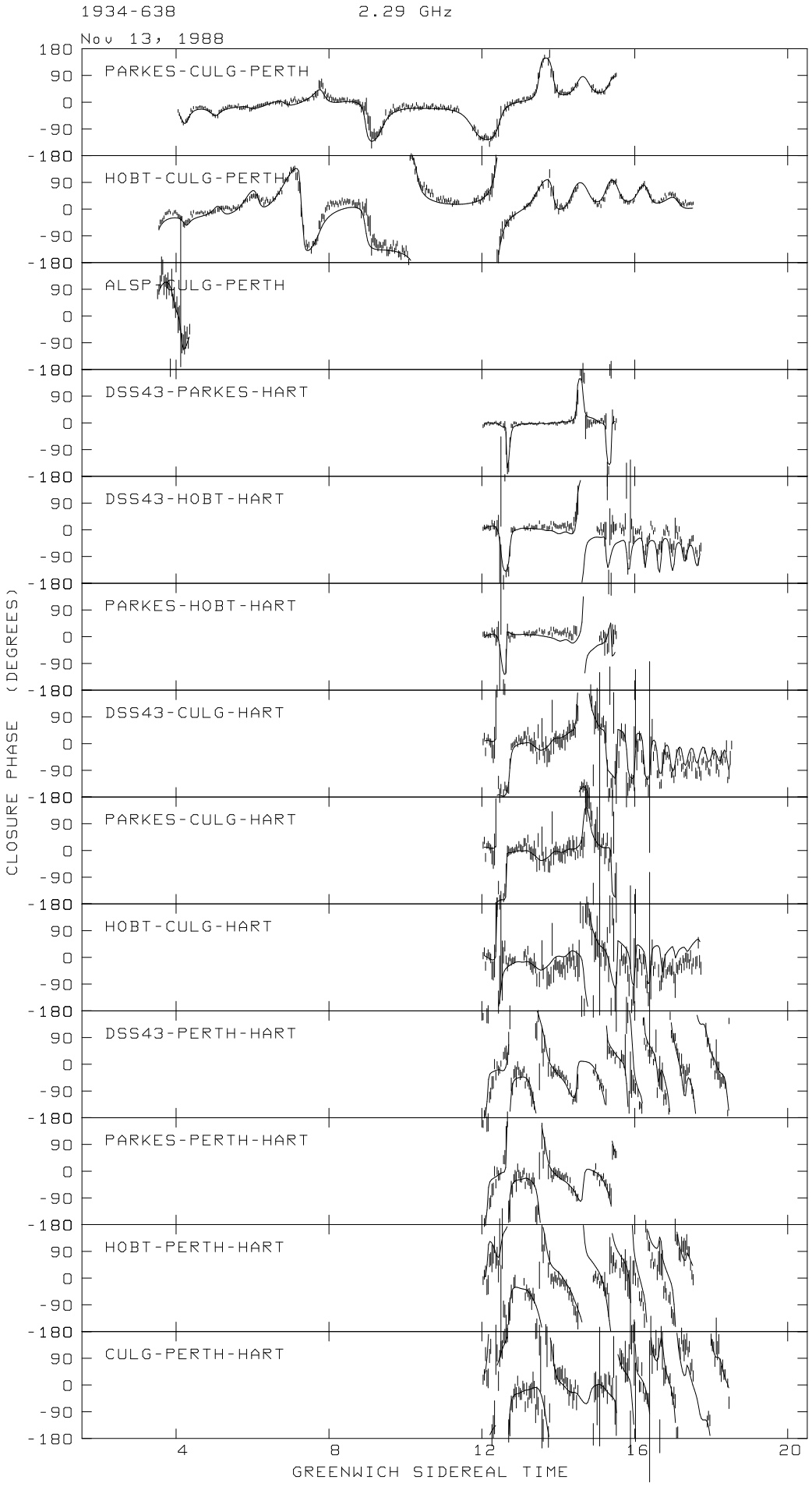
1934-638
2.29 GHz
Nov 13, 1988
PARKES-CULG-PERTH
HOBT-CULG-PERTH
ALSP-CULG-PERTH
DSS43-PARKES-HART
DSS43-HOBT-HART
PARKES-HOBT-HART
DSS43-CULG-HART
PARKES-CULG-HART
HOBT-CULG-HART
DSS43-PERTH-HART
PARKES-PERTH-HART
HOBT-PERTH-HART
CULG-PERTH-HART
180
90
0
-90
-180
CLOSURE PHASE (DEGREES)
4
8
12
16
20
GREENWICH SIDEREAL TIME

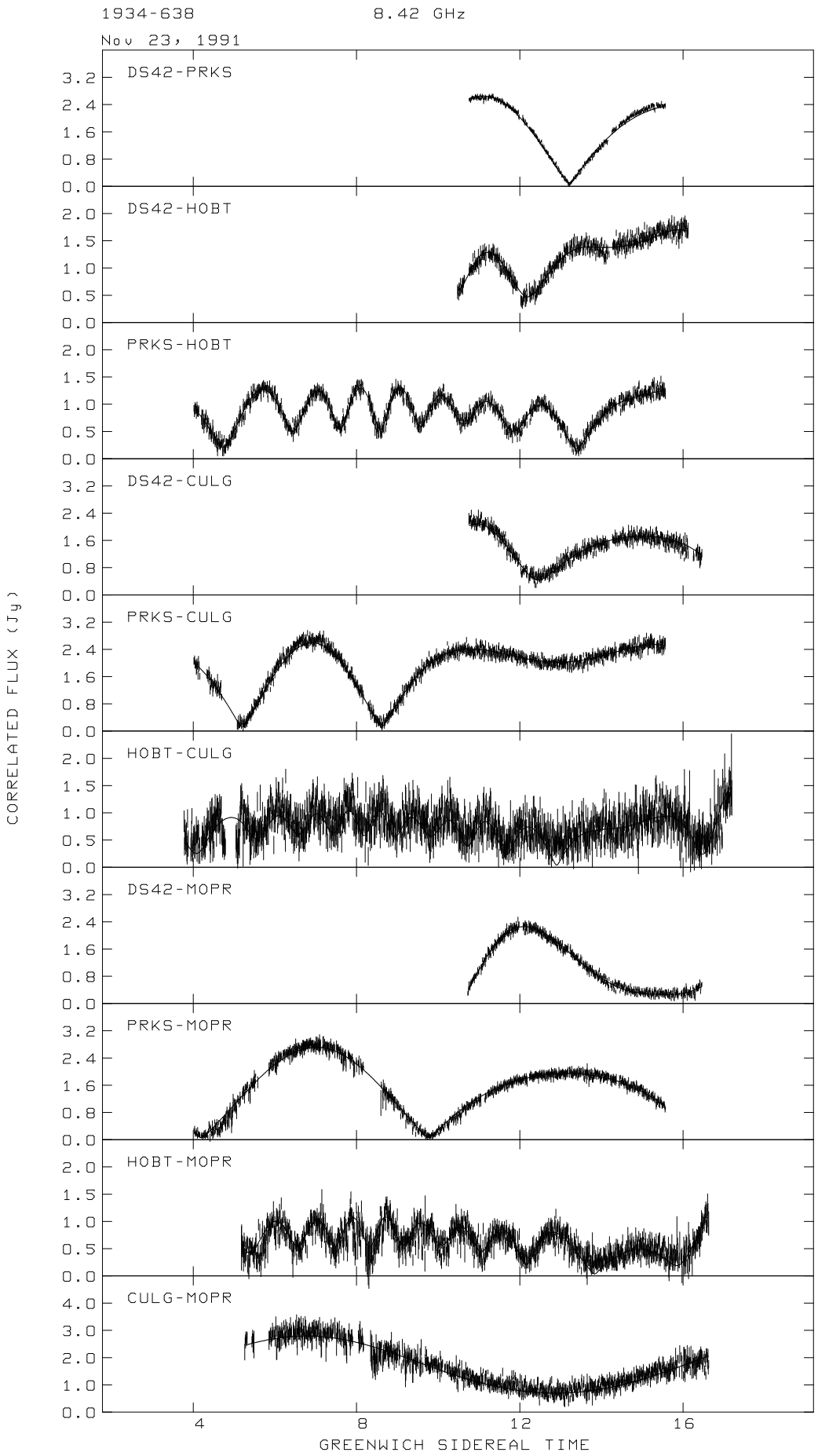
1934-638
8.42 GHz
Nov 23, 1991
DS42-PRKS
DS42-HOBT
PRKS-HOBT
DS42-CULG
PRKS-CULG
HOBT-CULG
DS42-MOPR
PRKS-MOPR
HOBT-MOPR
CULG-MOPR
CORRELATED FLUX (Jy)
GREENWICH SIDEREAL TIME
4
8
12
16

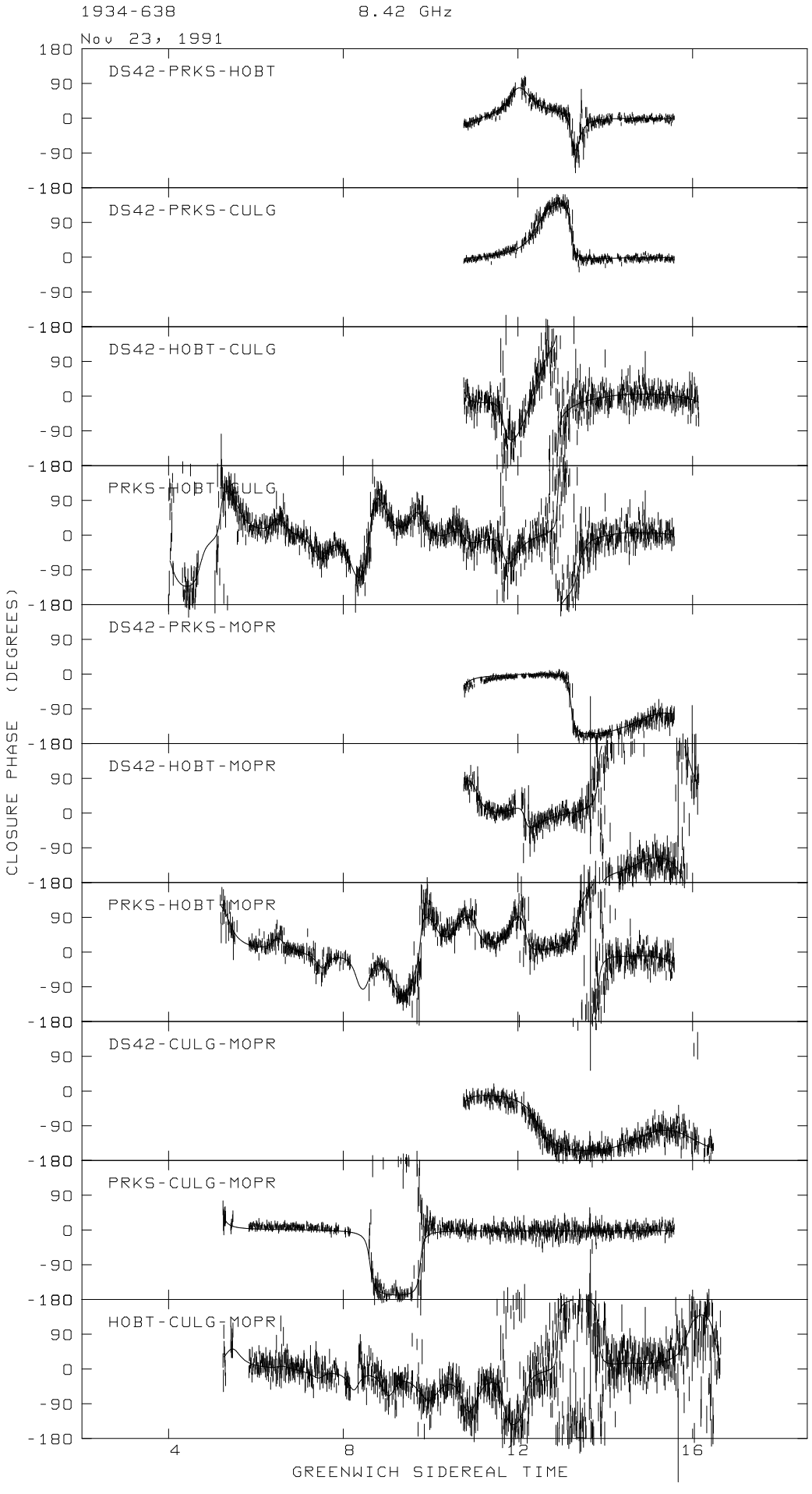
1934-638
8.42 GHz
Nov 23, 1991
DS42-PRKS-HOBT
DS42-PRKS-CULG
DS42-HOBT-CULG
PRKS-HOBT-CULG
DS42-PRKS-MOPR
DS42-HOBT-MOPR
PRKS-HOBT-MOPR
DS42-CULG-MOPR
PRKS-CULG-MOPR
HOBT-CULG-MOPR
180
90
0
-90
-180
CLOSURE PHASE (DEGREES)
4
8
12
16
GREENWICH SIDEREAL TIME

References

Baars, J., Genzel, R., Pauliny-Toth, I., and Witzel, A.: 1977, *Astron. Astrophys.* **61**, 99–106

Baars, J. and Hartsuijker, A.: 1972, *Astron. Astrophys.* **17**, 172–181

Batelaan, P., Goldstein, R., and Stelzreid, C.: 1970, *A Noise-Adding Radiometer for Use in the DSN*, Technical Report JPL Space Programs Summary 37–65, Vol.2, Jet Propulsion Laboratory, California Institute of Technology, Pasadena, California, 66–69

Baum, S., O'Dea, C., Murphy, D., and de Bruyn, A.: 1990, *Astron. Astrophys.* **232**, 19–26

Bolton, J., Clarke, M., and Ekers, R.: 1965, *Aust. J. Phys.* **18**, 627

Bolton, J., Gardner, F., and Mackey, M.: 1963, *Nature* **199**, 682–683

Bolton, J., Savage, A., and Wright, A.: 1979, *Aust. J. Phys. Astrophys. Suppl.* **46**, 1

Bracewell, R.: 1986, *The Fourier Transform And Its Applications*, McGraw Hill, second, revised Edition

Bracewell, R. and Roberts, J.: 1954, *Aust. J. Phys.* **7**, 615–640

Burbidge, E. and Burbidge, G.: 1972, *Astrophys. J.* **172**, 37

Burbidge, G. and Burbidge, E.: 1969, *Nature* **222**, 735

Cohen, M., Moffet, A., Romney, J., Schillizi, R., Shaffer, D., Kellerman, K., Purcell, G., Grove, G., Swenson, G., Yen, J., Pauliny-Toth, I., Preuss, E., Witzel, A., and Graham, D.: 1975, *Astrophys. J.* **201**, 249–255

Conway, J., Pearson, T., Readhead, A., Unwin, S., Xu, W., and Mutel, R.: 1992, *Astrophys. J.* **396**, 62–79

Cornwell, T. and Wilkinson, P.: 1981, *MNRAS* **196**, 1067–1086

Dent, W.: 1965, *Science* **148**, 1458–1460

Fanti, C., Fanti, R., Ficarra, A., Gregorini, L., Mantovani, F., and Padrielli, L.: 1983, *Astron. Astrophys.* **118**, 171–179

Fanti, R.: 1990, in C. Fanti, R. Fanti, C. O'Dea, and R. Schilizzi (eds.), *Compact Steep-Spectrum and GHz-Peaked Spectrum Radio Sources*, pp 218–221, Consiglio Nazionale delle Richerche Instituto di Radioastronomia - Bologna, Bologna, Italy

Fanti, R., Ficarra, A., Mantovani, F., Padrielli, L., and Weiler, K.: 1978, *Astron. Astrophys. Suppl. Ser.* **36**, 359–369

Fomalont, E. and Wright, M.: 1974, *Galactic And Extragalactic Radio Astronomy*, pp 256–290, Springer-Verlag

Gardner, F., Whiteoak, J., and Morris, D.: 1975, *Aust. J. Phys. Astrophys. Suppl.* **35**, 1–36

Gubbay, J., Legg, A., Robertson, D., and Craske, N.: 1971, *AJ* **76**, 965–969
Harnett, J., Haynes, R., Klein, U., and Wielebinski, R.: 1989, *Astron. Astrophys.* **216**, 39
Harnett, J., Haynes, R., Wielebinski, R., and Klein, U.: 1990, *Proc. Astron. Soc. Aust.* **8**, 257–260
Harnett, J., Klein, U., Haynes, R., and Wielebinski, R.: 1991, *Proc. Astron. Soc. Aust.* **9**, 266–268
Hewitt, A. and Burbidge, G.: 1993, *Astrophys. J., Suppl. Ser.* **87**, 451–947
Hodges, M., Mutel, R., and Phillips, R.: 1984, *AJ* **89**, 1327–1331
Högbom, J.: 1974, *Astron. Astrophys. Suppl. Ser.* **15**, 417–426
Jauncey, D., Reynolds, J., Tzioumis, A., Muxlow, T., Perley, R., Murphy, D., Preston, R., King, E., Patnaik, A., Jones, D., Meier, D., Bird, D., Blair, D., Bunton, J., Clay, R., Costa, M., Duncan, R., Ferris, R., Gough, R., Hamilton, P., Hoard, D., Kemball, A., Kesteven, M., Lobdell, E., Luiten, A., McCulloch, P., Murray, J., Nicolson, G., Rao, A., Savage, A., Sinclair, M., Skjerve, L., Taaffe, L., Wark, R., and White, G.: 1991, *Nature* **352**, 132–134
Jauncey, D., Savage, A., Preston, R., Morabito, D., Nicolson, G., and Tzioumis, A.: 1989a, *AJ* **98**, 54–63
Jauncey, D., White, G., Preston, R., Niell, A., Harvey, B., Morabito, D., Meier, D., Slade, M., Stolz, A., and Tzioumis, A.: 1989b, *AJ* **98**, 49–53
Jauncey, D., Wright, A., Peterson, B., and Condon, J.: 1978, *Astrophys. J.* **219**, L1
Jelley, J. and Cooper, B.: 1961, *Rev. Sci. Instrum.* **32(2)**, 166–175
Johnson, H.: 1966, *Ann. Rev. Astron. Astrophys.* **4**, 193–206
Jones, D., Jauncey, D., Preston, R., Reynolds, J., King, E., Meier, D., Tzioumis, A., Murphy, D., Nicolson, G., Ferris, R., Costa, M., Gough, R., Hoard, D., Amy, S., Blair, D., Campbell-Wilson, D., Clay, R., Edwards, P., Gwinn, C., Hamilton, P., Johnson, B., Jones, P., Kemball, A., Lobdell, E., Lovell, J., McAdam, W., McCulloch, P., Norris, R., Perlman, E., Sinclair, M., St. John, M., Skjerve, L., Wark, R., and White, G.: 1993, in R. Davis and R. Booth (eds.), *Sub-Arcsecond Radio Astronomy*, pp 150–151, Cambridge University Press
Jones, T. and Burbidge, G.: 1973, *Astrophys. J.* **186**, 791–799
Jones, T., O'Dell, S., and Stein, W.: 1974, *Astrophys. J.* **192**, 261–278
Kellermann, K.: 1966, *Aust. J. Phys.* **19**, 195–207
Kellermann, K.: 1974, in *Galactic and Extragalactic Radio Astronomy*, Chapt. 12, Springer-Verlag, Berlin, G.L. Verschuur and K.I. Kellermann (eds.)
Kellermann, K. and Owen, F.: 1988, in *Galactic and Extragalactic Radio Astronomy*, Astronomy and Astrophysics Library, Chapt. 13, Springer-Verlag, Berlin, Second Edition, G.L. Verschuur and K.I. Kellermann (eds.)
Kellermann, K. and Pauliny-Toth, I.: 1967, *Nature* **213**, 977–980
Kellermann, K. and Pauliny-Toth, I.: 1969, *Astrophys. J.* **155**, L71–L78
Kesteven, M., Bridle, A., and Brandie, G.: 1976, *AJ* **81**, 919–932
Kesteven, M., Bridle, A., and Brandie, G.: 1977, *AJ* **82(8)**, 541–556
Klein, M., Freiley, A., and Richter, P.: 1987, *DSN Radio Source List for Antenna Calibration*, Technical report, Jet Propulsion Laboratory, California Institute

of Technology, Pasadena, California, JPL D-3801 REV.B

Klein, M. and Stelzried, C.: 1976, *AJ* **81**, 1078–1083

Kochanek, C. and Narayan, R.: 1992, *Astrophys. J.* **401**, 461–473

Komesaroff, M., Roberts, J., Milne, D., Rayner, P., and D.J., C.: 1984, *MNRAS* **208**, 409–425

Kühr, H., Witzel, A., Pauliny-Toth, I., and Nauber, U.: 1981, *Astron. Astrophys. Suppl. Ser.* **45**, 367–430

Lang, K.: 1980, *Astrophysical Formulae*, Springer-Verlag, second Edition

Lanzetta, K., Wolfe, A., Turnshek, D., Lu, L., McMahon, R., and Hazard, C.: 1991, *Astrophys. J., Suppl. Ser.* **77**, 1

Large, M., Mills, B., Little, A., Crawford, D., and Sutton, J.: 1981, *MNRAS* **191**, 693–704

Lovell, J.: 1991, *Flux Density Variations In Compact Extragalactic Sources*, Honours Thesis, Physics Department, University of Tasmania

Mantovani, F., Junor, W., Fanti, R., Padrielli, L., Browne, I., and Muxlow, T.: 1992, *MNRAS* **257**, 353–367

Mantovani, F. and Padrielli, L.: 1990, in J. Zensus and T. Pearson (eds.), *Parsec Scale Radio Jets*, pp 230–235, Cambridge University Press, Cambridge, Great Britain

Mantovani, F., Padrielli, L., and Junor, W.: 1990, in C. Fanti, R. Fanti, C. O'Dea, and R. Schilizzi (eds.), *Compact Steep-Spectrum and GHz-Peaked Spectrum Radio Sources*, pp 174–181, Consiglio Nazionale delle Ricerche Instituto di Radioastronomia - Bologna, Bologna, Italy

Miley, G.: 1980, *Ann. Rev. Astron. Astrophys.* **18**, 165–218

Moran, J.: 1976, in M. Meeks (ed.), *Methods of Experimental Physics, Vol 12C*, pp 228–260, Academic Press, New York

Morganti, R., Killeen, N., and Tadhunter, C.: 1993, *MNRAS* **263**, 1023–1048

Murphy, D.W.and Jauncey, D., Preston, R., Reynolds, J., King, E., Meier, D., Tzioumis, A., Jones, D., Nicolson, G., Ferris, R., Costa, M., Gough, R., Hoard, D., Amy, S., Blair, D., Campbell-Wilson, D., Clay, R., Edwards, P., Gwinn, C., Hamilton, P., Johnson, B., Jones, P., Kemball, A., Lobdell, E., Lovell, J., McAdam, W., McCulloch, P., Norris, R., Perlman, E., Sinclair, M., St. John, M., Skjerve, L., Wark, R., and White, G.: 1993, in R. Davis and R. Booth (eds.), *Sub-Arcsecond Radio Astronomy*, pp 243–244, Cambridge University Press

Mutel, R., Hodges, M., and Phillips, R.: 1985, *Astrophys. J.* **290**, 86–93

Mutel, R. and Phillips, R.: 1987, in M. Reid and J. Moran (eds.), *The impact of VLBI on astrophysics and geophysics*, pp 73–74, Kluwer Academic Publishers

O'Dea, C.: 1990, *MNRAS* **245**, 20p–23p

O'Dea, C., Baum, S., and Stanghellini, C.: 1991, *Astrophys. J.* **380**, 66–77

O'Dea, C., Baum, S., Stanghellini, C., Morris, G., Patnaik, A., and Gopal-Krishna: 1990, *Astron. Astrophys. Suppl. Ser.* **84**, 549–562

Pearson, T.: 1991a, *Bull. Am. Astron. Soc.* **23**, 991–992

Pearson, T.: 1991b, *Introduction to the Caltech VLBI Programs*, Astronomy Department, California Institute of Technology

Penston, M. and Fosbury, R.: 1978, *MNRAS* **183**, 479

Perley, R.: 1982, *AJ* **87**, 859–880
Peterson, B. and Bolton, J.: 1972, *Astrophys. J.* **173**, L19
Phillips, R. and Mutel, R.: 1982, *Astron. Astrophys.* **106**, 21–24
Prestage, R. and Peacock, J.: 1983, *MNRAS* **204**, 355–365
Preston, R., Jauncey, D., Meier, D., Tzioumis, A., Ables, J., Batchelor, R., Faulkner, J., Gates, J., Greene, B., Hamilton, P., Harvey, B., Haynes, R., Johnson, B., Lambeck, K., Louie, A., McCulloch, P., Moorey, G., Morabito, D., Nicolson, G., Niell, A., Robertson, J., Royle, G., Skjerve, L., Slade, M., Slee, O., Stolz, A., Watkinson, A., Wehrle, A., and Wright, A.: 1989, *AJ* **98**, 1–26
Preston, R., Morabito, D., Williams, J., Faulkner, J., Jauncey, D., and Nicolson, G.: 1985, *AJ* **90**, 1599–1641
Rao, A. and Subrahmanyan, R.: 1988, *MNRAS* **231**, 229–236
Readhead, A. and Wilkinson, P.: 1978, *Astrophys. J.* **223**, 25–36
Reynolds, J., Jauncey, D., Russell, J., King, E., McCulloch, P., Fey, A., and Johnston, K.: 1994, *AJ*, Submitted
Rogers, A. and Moran, J.: 1981, *IEEE Trans. Instrum. Meas.* **IM-30(4)**, 283–286
Rudnick, L. and Jones, T.: 1982, *Astrophys. J.* **255**, 39–47
Russell, J., Reynolds, J., Jauncey, D., de Vegt, C., Zacharias, N., Ma, C., Fey, A., Johnston, K., Hindsley, R., Hughes, J., Malin, D., White, G., Kawaguchi, N., and Takahashi, Y.: 1994, *AJ* **107**, 379
Saikia, D., Singal, A., and Cornwell, T.: 1987, *MNRAS* **224**, 379–391
Savage, A., Jauncey, D., White, G., Peterson, B., Peters, W., Gulkis, S., and Condon, J.: 1990, *Aust. J. Phys.* **43**, 241–250
Schwab, F. and Cotton, W.: 1983, *AJ* **88(5)**, 688–694
Seielstad, G., Pearson, T., and Readhead, A.: 1983, *Publ. Astron. Soc. Pac.* **95**, 842–872
Shklovsky, J.: 1965, *Nature* **206**, 176–177
Simpson, C., Clements, D., Rawlings, S., and Ward, M.: 1993, *MNRAS* **262**, 889–892
Slee, O.: 1977, *Aust. J. Phys. Astrophys. Suppl.* **43**, 1
Slee, O. and Higgins, C.: 1973, *Aust. J. Phys. Astrophys. Suppl.* **27**, 1
Slee, O. and Higgins, C.: 1975, *Aust. J. Phys. Astrophys. Suppl.* **36**, 1
Slysh, V.: 1963, *Nature* **199**, 682
Stanghellini, C., Baum, S., O'Dea, C., and Morris, G.: 1990a, *Astron. Astrophys.* **233**, 379–384
Stanghellini, C., O'dea, C., Baum, S., and Fanti, R.: 1990b, in C. Fanti, R. Fanti, C. O'Dea, and R. Schilizzi (eds.), *Compact Steep-Spectrum and GHz-Peaked Spectrum Radio Sources*, pp 17–21, Consiglio Nazionale delle Ricerche Instituto di Radioastronomia - Bologna
Stanghellini, C., O'Dea, C., Baum, S., and Laurikainen, E.: 1993, **88**, 1–21
Tadhunter, C., Morganti, R., di Serego Alighieri, S., Fosbury, R., and Danziger, I.: 1993, *MNRAS* **263**, 999–1022
Taylor, G.: 1993, *The DIFMAP Cookbook*, Astronomy Deparment, California Institute of Technology
Thompson, A., Moran, J., and Swenson, G.: 1986, *Interferometry and Synthesis*

in Radio Astronomy, John Wiley and Sons Inc.

Tzioumis, A., Jauncey, D., Preston, R., Meier, D., Nicolson, G., Batchelor, R., Gates, J., Hamilton, P., Harvey, B., Haynes, R., Johnson, B., McCulloch, P., Moorey, G., Morabito, D., Niell, A., Robertson, J., Royle, G., Skjerve, L., Slade, M., Slee, O., Watkinson, A., Wehrle, A., and Wright, A.: 1989, *AJ* **98**, 36–43

Ulvestad, J., Johnston, K., Perley, R., and Fomalont, E.: 1981, *AJ* **86**, 1010–1035

van der Laan, H.: 1966, *Nature* **211**, 1131–1133

Véron, P., Véron-Cetty, M.-P., Djorgovski, S., Magain, P., Meylan, G., and Surdej, J.: 1990, *Astron. Astrophys. Suppl. Ser.* **86**, 543–553

Walker, R.: 1989, in M. Felli and R. Spencer (eds.), *Very Long Baseline Interferometry - Techniques and Applications*, pp 163–181, Kluwer Academic Publishers

Wall, J. and Peacock, J.: 1985, *MNRAS* **216**, 173–192

White, G.: 1992, *Proc. Astron. Soc. Aust.* **10**, 140–167

Wills, B.: 1975, *Aust. J. Phys. Astrophys. Suppl.* **38**, 1

Wright, A. and Otrupcek, R.: 1990, *PKSCAT90: The Southern Radio Source Database*, v1.01 Edition

Yentis, D., Cruddace, R., Gursky, H., Stuart, B., Wallin, J., MacGillivray, H., and Collins, C.: 1992, in H. MacGillivray and E. Thomson (eds.), *Digitised Optical Sky Surveys*, p. 67, Kluwer, Dordrecht

Yerbury, M.: 1975, *Rev. Sci. Instrum.* **46(2)**, 169–179